Fluid-structure interactions at small scales: collective effects, instabilities, and transport

Blaise Delmotte

INSTITUT POLYTECHNIQUE DE PARIS

ÉCOLE POLYTECHNIQUE

IP PARIS

Habilitation à Diriger des Recherches

Fluid-structure interactions at small scales: collective effects, instabilities, and transport

Habilitation à diriger des recherche de l'Institut Polytechnique de Paris
préparée à l'École Polytechnique

École doctorale n°626 ED IP Paris (ED-IPP)
Habilitation présentée et soutenue à Palaiseau, le 2 Octobre 2024, par

BLAISE DELMOTTE

Composition du Jury :

Elisabeth Guazzelli Directrice de recherche émérite, Matière et Systèmes Complexes	Rapportrice
Jacques Magnaudet Directeur de recherche, Institut Mécanique des Fluides de Toulouse	Rapporteur
Lorenzo Botto Associate Professor, TU Delft	Rapporteur
Denis Bartolo Professeur, École Normale Supérieure Lyon	Examinateur
Eric Clément Professeur, Sorbonne Université	Examinateur
Eric Lauga Professor, University of Cambridge	Examinateur

Contents

1 Introduction **1**

I Numerical modeling of complex suspensions **5**

2 Governing equations and modeling challenges **7**
2.1 Governing equations for the hydrodynamic problem 7
2.1.1 The mobility problem 9
2.2 Accounting for thermal fluctuations 9
2.3 (Partially) constrained kinematics 11
2.4 Governing equations for chemical interactions 13

3 Robust and efficient methods for modeling complex suspensions **17**
3.1 The rigid multiblob method: hydrodynamic and chemical interactions between colloidal particles with arbitrary shapes 18
3.1.1 Rigid multiblob model for the Stokes problem 18
3.1.2 Including thermal fluctuations 20
3.1.3 How to scale big and compute fast ? 23
3.1.4 Grid optimization: improving the accuracy of the RMB 25
3.1.5 Rigid multiblob model for the Laplace problem 28
3.2 Handling kinematic constraints in large suspensions 33
3.2.1 Constrained mobility problem 33
3.2.2 Validation example 35
3.2.3 Large scale simulations 37
3.3 The diffusio-phoretic Force Coupling Method 38
3.4 Perspectives and ongoing work 39

II Collective effects, instabilities and transport at small scales **41**

4 Active transport, instabilities and self-assembly in microroller suspensions **43**
4.1 Introduction 43
4.2 From one to two: a dynamical system insight on hydrodynamically-bound states 44
4.3 Density fluctuations and hydrodynamic transport by active layers 46
4.4 Unstable fronts and stable motile structures: the hydrodynamic genesis of colloidal creatures 49
4.4.1 Formation of a dense front 50
4.4.2 Transverse fingering instability 51
4.4.3 Hydrodynamic self-assembly 55
4.5 Individual and collective behavior above fluid-fluid interfaces 56

4.5.1 Individual motion . . . 58
4.5.2 Collective dynamics . . . 58
4.6 Hydrodynamic trapping enabled by thermal fluctuations . . . 60
4.7 Perspectives and ongoing work . . . 63

5 Motion of fibers in structured media **65**
5.1 Introduction . . . 65
5.2 Sedimentation of fibers in structured media . . . 66
5.2.1 Lateral displacement and trapping induced by a single obstacle . . . 67
5.2.2 Settling dynamics in a structured array of pillars: towards a sorting device 73
5.3 Advection of fibers in structured microchannels . . . 77
5.3.1 Dynamics of rigid fibers interacting with a triangular obstacle . . . 77
5.3.2 Towards an optimized separation of flexible fibers by deterministic lateral displacement in pillar arrays . . . 83
5.4 Perspectives and ongoing work . . . 91

6 The intriguing motion of *B. Paxillifer*: an exploratory study **95**
6.1 Introduction: we don't know much about *B. Paxillifer*... . . . 95
6.2 A toy model . . . 96
6.3 Data extraction and comparisons with experiments . . . 101
6.3.1 Extracting sliding motion from experiments . . . 101
6.3.2 Preliminary comparisons with experiments . . . 102
6.4 Perspectives . . . 104

7 Conclusions **107**

Bibliography **109**

CV **128**

Chapter 1

Introduction

This manuscript presents an overview of the work I have conducted and (co-)directed since completing my PhD in September 2015 and my arrival at LadHyX as a CNRS Researcher in October 2018. This research focuses on the collective effects, instabilities and transport phenomena that occur between immersed objects at the microscopic scale. To this end, I use a combination of mathematical modeling, numerical simulations, theoretical analysis and collaborate closely with experimentalists.

Regarding the modeling part, my approach is to develop mathematical and numerical methods to simulate the dynamics of suspensions, out-of-equilibrium systems, and more generally, interactions between immersed objects at low Reynolds numbers. My methodological objective is to produce tools that are sufficiently efficient to reach the macroscopic scale of a suspension, while maintaining a detailed description of the couplings (hydrodynamic, elastic, chemical, etc.) at the particle scale, whatever its shape, activity or mechanical properties (see Fig. 1.1).

I have employed these tools to investigate a range of phenomena including instabilities, wave propagation, and self-assembly in driven suspensions; locomotion in biological systems; the dynamics and sorting of elastic fibers in structured media; the motion of self-diffusiophoretic particles; or the rheology of Brownian suspensions. My work is driven by close collaborations with experimentalists and theoreticians. It lies at the interface between applied mathematics, fluid dynamics and soft matter. It is nourished by interactions with researchers in these different fields, with the constant aim of optimizing the resulting numerical methods and extending their fields of application to solve fundamental physical questions and application-oriented problems.

This document is structured around two principal axes. The first concerns the development of numerical methods for modeling complex suspensions, which is the focus of Part I. The second examines the physical phenomena that emerge in these systems and their potential applications, as described in Part II. Part I contains two chapters and Part II is divided into three chapters. The last section of each chapter is dedicated to some open questions that are either the focus of my ongoing research or that I would like to develop in the future.

The first chapter of Part I, Chapter 1, introduces the equations that govern the motion of complex suspensions at low Reynolds numbers and describes the associated modeling challenges. Complexity is introduced at multiple levels: in the shape of the particles, in the fluid through thermal fluctuations, in the motion of the particles with kinematic constraints or with additional couplings such as chemical interactions.

Chapter 2 outlines the methods I have co-developed to model such systems and to account for these complexities in large-scale simulations. The majority of these methods are based on the rigid multiblob framework which I (co-)developed during my stay at the Courant Institute. The

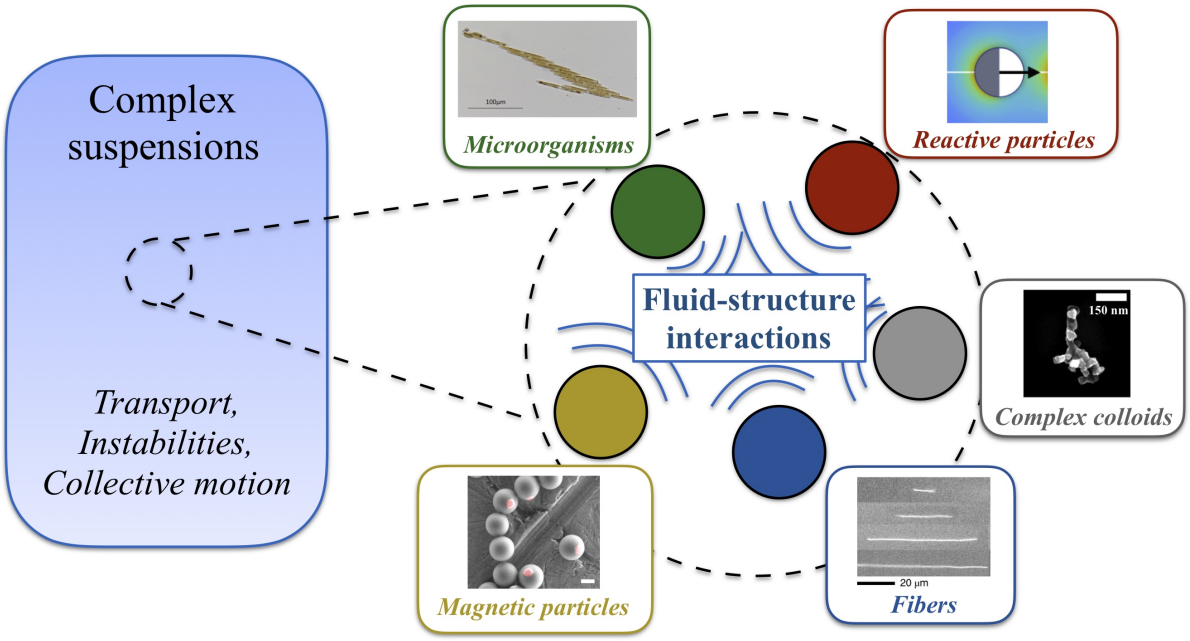

Figure 1.1: Graphical abstract of this HDR thesis. The macroscopic properties (stability, collective motion, transport properties, rheology,...) of complex suspensions are contingent upon fluid-structure interactions occurring at the scale of the constituents and dependent on their nature. Sources: iNaturalist (2017) (diatom), Rojas-Pérez *et al.* (2021) (reactive particle), Bourrianne *et al.* (2022) (colloid), Bielinski *et al.* (2024) (fibers), Driscoll *et al.* (2016) (magnetic particles).

work presented in this Chapter results from collaborations with applied mathematicians: Eric Keaveny (Maths Dept., Imperial College), Aleks Donev[1] (Courant Institute, NYU), Florencio Balboa-Usabiaga (Basque Center for Applied Mathematics) and Sébastien Michelin (LadHyX), with whom I co-supervised a PhD student (Francisco Rojas-Perez). The resulting codes are open source, publicly available and user-friendly with the aim of reaching a large community of developers and users.

The second part of the manuscript, referred to as Part II, focuses on collective effects and transport properties in systems where fluid-structure interactions play a major role. The three chapters it contains each represent a different project and are listed in order of completion.

The first system, described in Chapter 3, consists of colloidal torque-driven particles, called microrollers. In this system, strong hydrodynamic coupling between the particles gives rise to the formation of fast-moving layers, transverse instabilities and the self-assembly of stable motile structures. These phenomena are of fundamental interest to physicists and mathematicians, as well as having considerable potential for microfluidic and biomedical applications. This work was initiated during my post-doctoral stay at NYU from 2015 to 2018. It was conducted in collaboration with Aleks Donev on the modeling aspect and with Michelle Driscoll (Assist. Prof. Northwestern University) and Paul Chaikin (Professor, NYU) on the experimental aspect. To further investigate the potential of microrollers, Michelle Driscoll and I co-authored and secured

[1] A beloved friend who sadly passed away in 2023.

an NSF grant entitled "Magnetic microrollers as a platform for active transport" (Grant PMP-1706562), for which we were co-PIs from 2017 to 2021. I was personally responsible for the theoretical and modeling aspects of the project. Following the conclusion of the project, I have continued my collaboration with Michelle Driscoll to work on the trapping of microroller by obstacles. I have also investigated their collective dynamics near fluid-fluid interfaces separately.

Chapter 4 focuses on the motion of flexible fibers immersed in a viscous medium structured with obstacles. Despite the broad range of potential applications that it represents in biological, industrial and environmental processes, the transport of elastic fibers in structured media has received very little attention thus far. In this Chapter, we combine numerical simulations and laboratory experiments in order to identify the important mechanisms of fiber migration and trapping in structured environments. The goal is to use this fundamental knowledge to design efficient fiber sorting strategies that could be used for filtration, environmental assessments or biological diagnostics. In order to achieve these objectives, two different fields driving the fiber motion are considered: gravity in a quiescent fluid and pressure-driven flows in microfluidic chips. The sorting strategies based on sedimentation has recently been patented. The experimental part of the sedimentation project was conducted at LadHyX in collaboration with Camille Duprat (Professor, École Polytechnique), and the pressure-driven experiments are carried out at PMMH by Zhibo Li (PhD student) in collaboration with Anke Lindner (Professor U. Paris) and Olivia du Roure (Directrice de Recherche CNRS, PMMH). Numerical simulations were conducted by Ursy Makanga, a PhD student that I co-supervised with C. Duprat, Clément Bielinski, a post-doc working with me, and myself. This research is funded by my early-career grant (ANR-Jeune Chercheur) entitled "TransClog: Fiber Transport and Clogging in Structured Media" (ANR-20-CE30-0006) from 2020 to 2024.

Finally, Chapter 5 is an exploratory, and preliminary, study on the intriguing movement of *Bacillaria Paxillifer*, a diatom that can be found in freshwater and marine environments. This species in particular forms colonies of stacked rectangular cells that slide along each other while remaining parallel. The sliding motion between the cells appears to be somehow coordinated, allowing the structure to expand or contract in many different ways. This intriguing coordinated motion leads to beautiful and nontrivial conformations and trajectories at the scale of the colony. The variety of deformation sequences, their purpose, their mechanical origin, and the underlying fluid mechanics are not yet understood. Using numerical simulations, Chapter 5 proposes to address these questions with a simple toy model and through preliminary comparisons with experimental data. This work has been started in collaboration with Gabriel Amselem (Assist. Prof. École Polytechnique), who is in charge of the experimental part, and will be continued with Julien Le Dreff, who is finishing his Master internship and will start his PhD with me in October 2024.

For the sake of brevity and coherence[2], I have omitted other works completed during the 2015-2024 period. One study combines experiments, simulations and theory to investigate the collective sedimentation of a monolayer of colloidal particles above an incline (Sprinkle *et al.*, 2021). We found that collective sedimentation leads to the creation of a universal "triangular" inhomogeneous density profile, with a traveling density shock at the leading front moving in the

[2]In my view, the concept of "coherence" in research is more a stylistic exercise than a reflection of reality :-)

downhill direction. our theory shows that a simple Burgers equation reproduces this density profile without fitting parameters. The other work addresses the deformation of flexible fibers in sustained homogeneous isotropic turbulence (Sulaiman *et al.*, 2019). Through numerical simulations, we analyzed the deformation statistics of the fiber and identified two regimes based on the ratio of fiber length to persistence length, which represents the ratio of turbulent forcing to flexibility. The numerical results align with existing experimental data (Brouzet *et al.*, 2014).

Part I

Numerical modeling of complex suspensions

Chapter 2

Governing equations and modeling challenges

Contents

2.1 Governing equations for the hydrodynamic problem 7
2.1.1 The mobility problem 9
2.2 Accounting for thermal fluctuations 9
2.3 (Partially) constrained kinematics 11
2.4 Governing equations for chemical interactions 13

This Chapter introduces the equations that govern the motion of complex suspensions in viscous flows. Complexity is introduced at multiple levels of the system: in the shape of the particles, in the fluid through thermal fluctuations, in the motion of the particles with kinematic constraints or with additional couplings such as chemical interactions. We first introduce the governing equations of the hydrodynamic problem and then extend them to include thermal fluctuations. We then explain how the equations of motion are modified in the presence of kinematic constraints. Finally, we derive the governing equations for the chemical, phoretic, couplings between the suspended particles. At each step, we briefly discuss the main modeling challenges that will be addressed in the next Chapter.

2.1 Governing equations for the hydrodynamic problem

Let $\{\mathcal{B}_p\}_{p=1}^M$ be a set of M bodies immersed in a Stokes flow. The configuration of each body p is described by the location of a tracking point, $\boldsymbol{q}_p$, and its orientation represented by the unit quaternion $\boldsymbol{\theta}_p$, or in compact notation $\boldsymbol{x}_p = \{\boldsymbol{q}_p, \boldsymbol{\theta}_p\}$. The linear and angular velocities of the tracking point are $\boldsymbol{u}_p$ and $\boldsymbol{\omega}_p$. The external force and torque applied to a rigid body are $\boldsymbol{f}_p$ and $\boldsymbol{\tau}_p$. We will use the concise notation $\boldsymbol{U}_p = \{\boldsymbol{u}_p, \boldsymbol{\omega}_p\}$ and $\boldsymbol{F}_p = \{\boldsymbol{f}_p, \boldsymbol{\tau}_p\}$ as well, while unscripted vectors will refer to the composite vector formed by the variables of all the bodies, e.g. $\boldsymbol{U} = \{\boldsymbol{U}_p\}_{p=1}^M$. These bodies can have an active surface velocity $\boldsymbol{u}_s$, also called swimming gait, due to surface activity or prescribed deformations, such as phoresis (Anderson, 1989; Golestanian *et al.*, 2007) or ciliary motion (Blake, 1971*a*). The velocity and pressure, $\boldsymbol{v}$ and p, of the fluid with viscosity η are governed by the Stokes equations (Kim & Karrila, 1991)

$$-\boldsymbol{\nabla} p + \eta \boldsymbol{\nabla}^2 \boldsymbol{v} = \boldsymbol{0}, \tag{2.1}$$

$$\boldsymbol{\nabla} \cdot \boldsymbol{v} = 0, \tag{2.2}$$

while at the bodies surface the fluid obeys the boundary condition

$$\boldsymbol{v}(\boldsymbol{r}) = (\boldsymbol{\mathcal{K}}\boldsymbol{U}_p)(\boldsymbol{r}) + \boldsymbol{u}_s(\boldsymbol{r}) = \boldsymbol{u}_p + \boldsymbol{\omega}_p \times (\boldsymbol{r} - \boldsymbol{q}_p) + \boldsymbol{u}_s(\boldsymbol{r}) \text{ for } \boldsymbol{r} \in \partial\mathcal{B}_p, \tag{2.3}$$

where we have introduced the geometric operator $\boldsymbol{\mathcal{K}}$ that transforms rigid body velocities to surface velocities. Boundary conditions also apply at the bounding surface of the domain considered.

Since inertia does not play a role in Stokes flows the conservation of linear and angular momentum reduces to the balance of force and torque. For every body p the balance between hydrodynamic and external stresses is given by

$$\int_{\partial\mathcal{B}_p} \boldsymbol{\lambda}(\boldsymbol{r})\, \mathrm{d}S_{\boldsymbol{r}} = \boldsymbol{f}_p, \tag{2.4}$$

$$\int_{\partial\mathcal{B}_p} (\boldsymbol{r} - \boldsymbol{q}_p) \times \boldsymbol{\lambda}(\boldsymbol{r})\, \mathrm{d}S_{\boldsymbol{r}} = \boldsymbol{\tau}_p, \tag{2.5}$$

where $-\boldsymbol{\lambda}(\boldsymbol{r}) = \boldsymbol{\sigma} \cdot \boldsymbol{n}$ is the hydrodynamic traction exerted on the bodies by the fluid and $\boldsymbol{\sigma} = -p\boldsymbol{I} + 2\eta(\boldsymbol{\nabla}\boldsymbol{v} + \boldsymbol{\nabla}\boldsymbol{v}^T)$ is the fluid stress tensor. The adjoint of the geometric operator $\boldsymbol{\mathcal{K}}$ can be used to write the balance of force and torques for all bodies as

$$\boldsymbol{\mathcal{K}}^T\boldsymbol{\lambda} = \boldsymbol{F}. \tag{2.6}$$

In order to compute the trajectories of the immersed bodies, the equations of motion must be integrated in time. Some care is necessary to integrate the quaternion equations, therefore we discuss briefly some of their main properties (Delong *et al.*, 2015; Westwood *et al.*, 2022). A unit quaternion, $\boldsymbol{\theta} = [s, \boldsymbol{p}]$ with $s \in \mathbb{R}$ and $\boldsymbol{p} \in \mathbb{R}^3$, represents a rotation around a fixed axis: the finite rotation given by the vector $\boldsymbol{\gamma}$ has the associated unit quaternion

$$\boldsymbol{\theta}_{\boldsymbol{\gamma}} = \left[\cos(\gamma/2),\, \sin(\gamma/2)\boldsymbol{\gamma}/\gamma\right], \tag{2.7}$$

where $\gamma = \|\boldsymbol{\gamma}\|_2$. Unit quaternions can be combined by the quaternion multiplication

$$\boldsymbol{\theta}_3 = \boldsymbol{\theta}_2 \bullet \boldsymbol{\theta}_1 = \left[s_2 s_1 - \boldsymbol{p}_2 \cdot \boldsymbol{p}_1,\ s_2\boldsymbol{p}_1 + s_1\boldsymbol{p}_2 + \boldsymbol{p}_2 \times \boldsymbol{p}_1\right]. \tag{2.8}$$

Therefore, $\boldsymbol{\theta}_3$ represents the rotation obtained by the combination of a rotation $\boldsymbol{\theta}_1$ followed by a rotation $\boldsymbol{\theta}_2$. This product rule allows to write the kinematic equations of motion as

$$\frac{\mathrm{d}\boldsymbol{q}_p}{\mathrm{d}t} = \boldsymbol{u}_p, \tag{2.9}$$

$$\frac{\mathrm{d}\boldsymbol{\theta}_p}{\mathrm{d}t} = \frac{1}{2}\left[0, \boldsymbol{\omega}_p\right] \bullet \boldsymbol{\theta}_p = \boldsymbol{\Psi}_p\boldsymbol{\omega}_p. \tag{2.10}$$

$\boldsymbol{\Psi}_p$ is a 4×3 matrix

$$\boldsymbol{\Psi}_p = \frac{1}{2}\begin{bmatrix} -\boldsymbol{p}^T \\ s\boldsymbol{I} - \boldsymbol{p}^\times \end{bmatrix}, \tag{2.11}$$

where $\boldsymbol{p}^\times\boldsymbol{y} = \boldsymbol{p} \times \boldsymbol{y}$ for any vector $\boldsymbol{y}$[1].
Finally, the rotation matrix associated to the unit quaternion $\boldsymbol{\theta} = (s, \boldsymbol{p})$ is

$$\boldsymbol{R} = 2\left[\boldsymbol{p}\boldsymbol{p}^T + s\boldsymbol{p}^\times + \left(s^2 - \frac{1}{2}\right)\boldsymbol{I}\right]. \tag{2.12}$$

[1]In the following of the thesis we will omit the matrix $\boldsymbol{\Psi}$ in the equations of motion to simplify the notation. A detailed and rigorous version of these equations including $\boldsymbol{\Psi}$ can be found in (Delong *et al.*, 2015)

2.1.1 The mobility problem

Given the nonhydrodynamic forces and torques acting on the rigid bodies, $\boldsymbol{F}$, and the active motion on their surface $\boldsymbol{u}_s$, the equations (2.1)-(2.5) can be solved for the bodies velocities $\boldsymbol{U}$ and the tractions $\boldsymbol{\lambda}$. Since the Stokes equations are linear we can write the velocity of M rigid bodies as

$$\boldsymbol{U} = \boldsymbol{N}\boldsymbol{F} - \widetilde{\boldsymbol{N}}\boldsymbol{u}_s, \tag{2.13}$$

where $\boldsymbol{N} = \boldsymbol{N}(\boldsymbol{x})$ is the $6M \times 6M$ *body mobility matrix* that couple the forces and torques acting on the rigid bodies with their velocities, and $\widetilde{\boldsymbol{N}}$ is a linear operator ($\widetilde{\boldsymbol{N}} : L^2(S, \mathbb{R}^3) \to \mathbb{R}^{6M}$)[2], where S is the particle surface, which we will call *"slip mobility operator"*, mapping the surface motion to the particle velocities. As shown in (Swan *et al.*, 2011), which generalizes the work of Stone and Samuel (Stone & Samuel, 1996), $\widetilde{\boldsymbol{N}}$ can be obtained for a single particle using the Lorentz reciprocal theorem.

Modelling challenges:
Since, in Stokes flows, hydrodynamic interactions among particles decay slowly like the inverse of the distance, it is crucial to develop methods that can capture long-ranged hydrodynamic effects, while accounting for nontrivial boundary conditions on the particles' surface and still scale to tens or hundreds of thousands of particles. The Stokesian Dynamics (Brady & Bossis, 1988) and Boundary Element Methods (Pozrikidis, 1992) have been widely used to solve the many-body mobility problem in particle suspensions. These methods rely on Green's functions for steady Stokes flow to capture the effect of the fluid.
While the Stokesian dynamics framework works well for spherical particles, it has several notable technical difficulties: achieving near-linear scaling for many particle systems is technically challenging, handling nontrivial boundary conditions (bounded systems) is complicated and has to be done on a case-by-case basis and generalizations to complex particle shapes is difficult.
On the other hand, the Boundary Element Method suffers from convergence issues at small interparticle distances, requires special, and highly expensive, techniques to deal with the singularities distributed on the particle surfaces and is therefore limited to very few particles in dynamic simulations.

2.2 Accounting for thermal fluctuations

If the suspended particles are small enough, they will also move randomly due to thermal fluctuations in the surrounding fluid. In the overdamped limit, the effects of Brownian motion are captured through the inclusion of random velocities, turning the equations of motion into a

[2] $L^2(S, \mathbb{R}^3)$ is the space of vector-valued functions in $\mathbb{R}^3$, i.e. $\boldsymbol{u}_s$, defined on the manifold S (the particle surface) whose euclidean norm is square integrable on S, i.e. $\int_S \|\boldsymbol{u}_s\|_2^2 \mathrm{d}S < \infty$. I think this function space is a safe choice for $\boldsymbol{u}_s$, but it might not be the most appropriate...

system of stochastic differential equations given by the fluctuating Stokes equations

$$-\nabla p + \eta \nabla^2 \boldsymbol{v} = \boldsymbol{\nabla} \cdot \boldsymbol{\mathcal{Z}}, \tag{2.14}$$

$$\nabla \cdot \boldsymbol{v} = 0, \tag{2.15}$$

where the right hand side includes the divergence of a stochastic stress tensor $\boldsymbol{\mathcal{Z}}$ responsible for the thermal fluctuations or Brownian motion (Landau & Lifshitz, 1959; Fabritiis *et al.*, 2007). The stochastic stress tensor is delta correlated in space and time

$$\langle \mathcal{Z}_{ij}(\boldsymbol{x}, t) \rangle = 0, \tag{2.16}$$

$$\langle \mathcal{Z}_{ij}(\boldsymbol{x}, t) \mathcal{Z}_{kl}(\boldsymbol{x}', t') \rangle = 2\eta k_B T \left(\delta_{ik}\delta_{jl} + \delta_{il}\delta_{jk}\right) \delta(\boldsymbol{x} - \boldsymbol{x}')\delta(t - t'), \tag{2.17}$$

and the correlations magnitude depends on the thermal energy $k_B T$. The operator $\langle \cdot \rangle$ is an ensemble average.

The mobility problem formed by (2.14)-(2.15) together with the boundary conditions (2.3) and force-torque balance (2.4)-(2.5) leads to the (Itô) overdamped Langevin equations for the particle positions and orientations (Hinch, 1975; Noetinger, 1990; Roux, 1992)

$$\boldsymbol{U} = \boldsymbol{N}\boldsymbol{F} - \widetilde{\boldsymbol{N}}\boldsymbol{u}_s + \sqrt{2k_B T}\boldsymbol{N}^{1/2}\boldsymbol{Z} + k_B T \partial_{\boldsymbol{x}} \cdot \boldsymbol{N}, \tag{2.18}$$

where two additional terms appear on the right hand side.

The first is the random particle velocity increments due thermal agitation given by $\boldsymbol{U}_{th} = \sqrt{2k_B T}\boldsymbol{N}^{1/2}\boldsymbol{Z}$, with $\boldsymbol{N}^{1/2}$ being the square root of the mobility matrix, and $\boldsymbol{Z}$ is a vector of independent white noise processes. The dependence on the mobility matrix ensures that the fluctuation-dissipation theorem is satisfied, a necessary condition for the Boltzmann distribution to be recovered at equilibrium.

Along with the random velocities, the overdamped equations of motion require the inclusion of the thermal drift term, $k_B T \partial_{\boldsymbol{x}} \cdot \boldsymbol{N}$, which is the divergence of the mobility matrix with respect to the particle positions and orientations (Ermak & McCammon, 1978). This ensures that the stochastic differential equation with an Itô interpretation of the stochastic integral yields dynamics consistent with those of Smoluchowski's equation for the corresponding probability distribution. Neglecting this term in Brownian Dynamics simulations, which is sometimes the case in the literature, leads to erroneous equilibrium particle distributions (Delong *et al.*, 2014; Delmotte & Keaveny, 2015) and biases the dynamics of out-of-equilibrium systems (Sprinkle *et al.*, 2017; Leishangthem & Xu, 2024).

Modelling challenges:
Computing the square root of the mobility matrix $\boldsymbol{N}^{1/2}$ with classical linear algebra, such as Cholesky decomposition, is costly as it scales badly with the particle number $O(M^3)$. Though several methods have been introduced to accelerate the matrix square root computation (Fixman, 1986; Ando *et al.*, 2012, 2013; Chow & Saad, 2014), the inclusion of Brownian motion has often limited simulations to having very small particle numbers or ignoring completely hydrodynamic interactions between the particles.
The additional drift term $k_B T \partial_{\boldsymbol{x}} \cdot \boldsymbol{N}$ requires computing the divergence of the mobility matrix with respect to *all* the particle positions *and* orientations, which incurs a high computational cost and cannot be done analytically for complex particle shapes. This is done most efficiently using a well-designed time integration scheme that automatically accounts for the Brownian drift, yielding a numerical solution whose moments converge to the their true values as the time step size goes to zero. Fixman provides an early example of a midpoint scheme which, to leading order in the time step size, emits the Brownian drift term as part of its error expansion (Fixman, 1978; Grassia *et al.*, 1995). This scheme, however, relies on a resistance formulation, where the dense, long-ranged mobility matrix must be inverted, introducing costly additional linear systems.
In the past decade, significant advances have been made to compute these terms at a nearly linear computational cost ($O(M)$) in suspensions of spherical particle (Ando *et al.*, 2012, 2013; Delong *et al.*, 2014; Keaveny, 2014; Delmotte & Keaveny, 2015), but their generalization to nonspherical shapes has been lacking, and traditional methods for more complex shapes, such as the Boundary Element Method (Pozrikidis, 1992) or the Method of Regularized Stokeslet (Cortez, 2001), cannot handle thermal fluctuations.

2.3 (Partially) constrained kinematics

In a variety of scenarios, the movement of certain bodies is either wholly or partially constrained, while others are free to move. This phenomenon can be observed in systems comprising freely-flowing particles and immobile obstacles, such as suspensions flowing through porous media or in microfluidic chips structured by pillar arrays (see Sections 4.6, 5.2 and 5.3). In other cases, which encompass a diverse array of microscopic systems, small objects are locked by geometric constraints or connected by rigid bonds with exceedingly short relaxation timescales. Stiff bonds can be found in polymer chains, freely-jointed molecules (Sacanna *et al.*, 2010; McMullen *et al.*, 2018) or in molecules with bond angles. They can also be found in the hinges of multilink afticial microswimmers (Dreyfus *et al.*, 2005; Jang *et al.*, 2015; Liao *et al.*, 2019), in the hook connecting the flagellum to the cell body of bacteria (Berg & Anderson, 1973; Trachtenberg & Hammel, 1992), or in the form of adhesive forces between sliding cells in diatom colonies (Müller, 1782; Kapinga & Gordon, 1992; Gordon, 2016) (see Chapter 6). The use of kinematic constraints allows for the elimination of these fast degrees of freedom, thereby enabling larger time steps in numerical simulations.

In the majority of cases, the kinematic constraints mentioned above are holonomic, meaning that they depend only on the particle positions, orientations (and time t) and can be written in

the form

$$g(\boldsymbol{x}, t) = 0 \tag{2.19}$$

where $\boldsymbol{x} = \{\boldsymbol{q}, \boldsymbol{\theta}\}$ is a vector that collects all the particle positions and orientations. Examples of holonomic, scalar or vectorial, constraints are

- Prescribed position $\boldsymbol{q}_0(t)$ of a single body p:

$$\boldsymbol{g}(\boldsymbol{x}, t) = \boldsymbol{q}_p - \boldsymbol{q}_0(t) = \boldsymbol{0}, \tag{2.20}$$

- Prescribed orientation $\boldsymbol{\theta}_0(t)$ of a single body p:

$$\boldsymbol{g}(\boldsymbol{x}, t) = \boldsymbol{\theta}_p - \boldsymbol{\theta}_0(t) = \boldsymbol{0}, \tag{2.21}$$

- Prescribed distance $d(t)$ between body p and body q:

$$g(\boldsymbol{x}, t) = \frac{1}{2}\|\boldsymbol{q}_p - \boldsymbol{q}_q\|_2^2 - d(t)^2 = 0, \tag{2.22}$$

- Prescribed distance $d(t)$ between body p and body q along one specified direction $\boldsymbol{e}$ in the frame of body p:

$$g(\boldsymbol{x}, t) = (\boldsymbol{q}_p - \boldsymbol{q}_q) \cdot \boldsymbol{R}(\boldsymbol{\theta}_p) \cdot \boldsymbol{e}(t) - d(t) = 0, \tag{2.23}$$

  where $\boldsymbol{R}(\boldsymbol{\theta}_p)$ is the rotation matrix to the frame attached to body p, given in Eq. (2.12).

- Ball-and-socket joint between body p and body q:

$$\boldsymbol{g}_n(\boldsymbol{x}) = \boldsymbol{q}_p + \boldsymbol{R}(\boldsymbol{\theta}_p)\Delta\boldsymbol{l}_{np}(t) - \boldsymbol{q}_q - \boldsymbol{R}(\boldsymbol{\theta}_q)\Delta\boldsymbol{l}_{nq}(t) = \boldsymbol{0}, \tag{2.24}$$

  where $\Delta\boldsymbol{l}_{np}(t)$ is the vector from the body p to the hinge n in the body frame of reference. This vector is then rotated to the laboratory frame of reference by the rotation matrix $\boldsymbol{R}(\boldsymbol{\theta}_p)$. A constant vector $\Delta\boldsymbol{l}_{np} = \boldsymbol{c}$ represents a passive link, while $\Delta\boldsymbol{l}_{np} = \Delta\boldsymbol{l}_{np}(t)$ represents an active link. Section 3.2 and Chapter 6 provide examples of particles and microorganisms modeled with such constraints.

Following the classical framework of Lagrangian mechanics, a Lagrange multiplier is associated to each kinematic constraint in the equations of motion. In the context of immersed bodies at low Reynolds number, the inclusion of Lagrange multipliers results in the introduction of constraint forces $\boldsymbol{F}^C$ in the mobility problem (2.13)

$$\boldsymbol{U} = \boldsymbol{N}(\boldsymbol{F} + \boldsymbol{F}^C) - \widetilde{\boldsymbol{N}}\boldsymbol{u}_s. \tag{2.25}$$

In order to model suspensions with kinematic constraints, one has to solve the augmented mobility problem (2.25) together with the equations of motion (2.9)-(2.10) subject to a diversity of kinematic constraints (e.g. (2.20)-(2.24)) acting on a portion, or the totality, of the degrees of freedom in the system. Due to the nonlinearity of the kinematic constraints, this yields a nonlinear system of equations for the positions, orientations, as well as the constraint forces

associated with each constraint.

Modelling challenges:
Nonlinearities pose a challenge to integrate the equations of motion (2.9)-(2.10) for large suspensions (Featherstone, 1987; Schoeller *et al.*, 2021). They require using nonlinear solvers, usually relying on Newton's method, where one needs to compute a large and complex inverse Jacobian matrix at each iteration. Until now, this challenging task has limited numerical studies to small numbers of particles (Shum *et al.*, 2010; Shum & Yeomans, 2017; Walker *et al.*, 2019) or led to methods restricted to a specific type of constraint (Schoeller *et al.*, 2021).

2.4 Governing equations for chemical interactions

The individual and collective dynamics of self-propelled phoretic particles have attracted significant attention in recent decades (Moran & Posner, 2017; Stark, 2018; Illien *et al.*, 2017; Domínguez & Popescu, 2022; Zöttl & Stark, 2023).

Chemically-active phoretic colloids catalyze surface reactions to modify the concentration of chemical solutes surrounding them in order to self-propel, a phenomenon known as self-diffusiophoresis (Fig. 2.1). In doing so, they generate long-ranged hydrodynamic flows and chemical gradients that modify the trajectories of other particles. As a result, the dynamics of reactive suspensions is fundamentally governed by hydro-chemical interactions.

Owing to the small particle size ($O(1\mu\text{m})$) and the magnitude of the phoretic flows on their surface, the Péclet number characterizing the motion of the solute particles is small enough to neglect advection and consider only the diffusive part.

Thus, in the fluid domain the concentration of solute $c = c(\boldsymbol{r})$ diffuses according to the Laplace equation

$$D\boldsymbol{\nabla}^2 c = 0, \tag{2.26}$$

with diffusion coefficient D.

The immersed colloids activate chemical reactions on their surfaces to produce or consume solute. They are introduced as boundary conditions of the Laplace equation. The boundary conditions are imposed on the concentration fluxes, i.e. Robin boundary conditions, and to simplify the mathematical problem we only consider linear boundary conditions. In particular, we consider sinks that consume solute at a rate proportional to the local concentration, sources that produce solute at a constant flux or a linear combination of both (Golestanian *et al.*, 2007; Lu, 1998; Michelin & Lauga, 2014)

$$D\frac{\partial c}{\partial \boldsymbol{n}} \equiv D\boldsymbol{n}\cdot\boldsymbol{\nabla}c = kc - \alpha \quad \text{on } \partial\mathcal{B}_p, \tag{2.27}$$

where $\boldsymbol{n} = \boldsymbol{n}(\boldsymbol{r})$ is the surface normal on the colloids, $k = k(\boldsymbol{r}) > 0$ the surface reaction rate and $\alpha = \alpha(\boldsymbol{r}) > 0$ the surface production flux, both of which can vary over the colloidal surface. The minus sign in front of the production flux is included for convenience so positive values of α indicate production of solute. Since the reaction flux is proportional to the local concentration

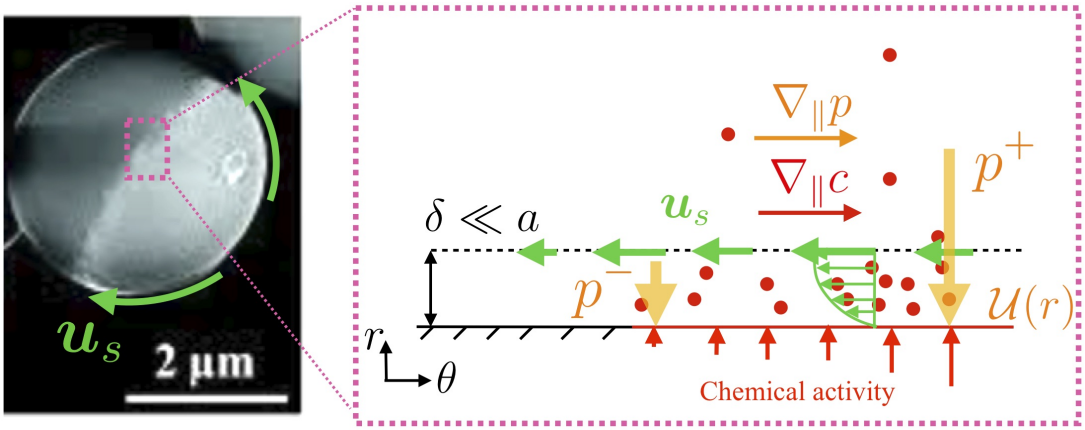

Figure 2.1: Self-diffusiophoresis a reactive particle. Left: close-up view of a spherical Janus particle (Theurkauff *et al.*, 2012). Right: close-up view of the particle surface. A particle with nonuniform surface chemical activity generates gradients of solute concentration $\boldsymbol{\nabla}_\parallel c$ (small red particles). The interaction force $-\boldsymbol{\nabla}\mathcal{U}$, here attractive, between the solute and the particle surface creates a tangential pressure gradient $\boldsymbol{\nabla}_\parallel p$ which induces a flow in the opposite direction. This flow can be modeled as a surface slip velocity $\boldsymbol{u}_s$ above a diffuse layer of thickness δ that is usually much smaller than the particle size $\delta \ll a$. The coefficient of proportionality between the concentration gradient $\boldsymbol{\nabla}_\parallel c$ and slip velocity $\boldsymbol{u}_s$ in (2.28) is called the mobility coefficient μ. It depends on the interaction potential, fluid viscosity, temperature, and position on the particle surface : $\mu = f(\mathcal{U}, k_B T, \eta, \boldsymbol{r})$.

while the concentration diffuses with a finite diffusion coefficient D, this boundary condition allows to model either diffusive-limited or reaction-limited systems. The balance between diffusion and reaction is characterized by the the Damkohler number, $\mathrm{Da} = kR/D$, which represents the ratio between the diffusive time over one colloidal radius, R^2/D, and the reaction time scale R/k. Thus, the Damkohler number is large for diffusive-limited systems and small for reaction limited systems (Bhalla *et al.*, 2013). Additional boundary conditions at the domain boundary, such as vanishing concentration at infinity, or zero flux at the domain walls, must be included to close the system.

Due to diffusiophoresis (see Fig. 2.1), the concentration gradients near the colloid surface lead to a slip velocity (Anderson, 1989; Marbach & Bocquet, 2019)

$$\boldsymbol{u}_s = \mu \boldsymbol{\nabla}_\parallel c = \mu \left(\boldsymbol{I} - \boldsymbol{n}\boldsymbol{n}^T \right) \boldsymbol{\nabla} c \quad \text{on } \partial\mathcal{B}_p, \tag{2.28}$$

where the coefficient of proportionality $\mu = \mu(\boldsymbol{r})$ is the surface mobility and $\boldsymbol{\nabla}_\parallel$ the surface gradient, i.e. the gradient projected to the surface tangent plane.

Modeling reactive suspensions requires solving first the Laplace problem (2.26), with Robin boundary conditions on the particle surfaces (2.27), in order to determine the concentration gradients on the particle surfaces $\boldsymbol{\nabla} c$, which are then used to compute the active slip (2.28) which is then added in the boundary conditions of the (fluctuating) Stokes mobility problem (2.18).

Modeling challenges:
The Laplace problem bear some similarities with the Stokes problem: interactions are long-ranged and boundary conditions are non-trivial on the particles' surface. Solving for the surface concentration gradients in large collections of (colloidal) reactive particles with arbitrary shapes and non-uniform catalytic surface properties is therefore challenging. Similarly to the Stokes problem, the preferred method for such systems is the Boundary Element, which does not handle thermal fluctuations and is restricted to very few particles in dynamic simulations.

Chapter 3

Robust and efficient methods for modeling complex suspensions

Contents

3.1 The rigid multiblob method: hydrodynamic and chemical interactions between colloidal particles with arbitrary shapes 18

3.1.1 Rigid multiblob model for the Stokes problem 18

3.1.2 Including thermal fluctuations 20

3.1.3 How to scale big and compute fast ? 23

3.1.4 Grid optimization: improving the accuracy of the RMB 25

3.1.5 Rigid multiblob model for the Laplace problem 28

3.2 Handling kinematic constraints in large suspensions 33

3.2.1 Constrained mobility problem 33

3.2.2 Validation example 35

3.2.3 Large scale simulations 37

3.3 The diffusio-phoretic Force Coupling Method 38

3.4 Perspectives and ongoing work 39

As explained in the previous Chapter the particle shape, hydrodynamic interactions, thermal fluctuations, constrained kinematics and chemical couplings pose multiple challenges to the modeling of complex particle suspensions. In this Chapter I present the methods I have co-developed with the aim to overcome these methodological barriers.

First, I present the framework of the rigid multiblob method (RMB), a versatile and efficient approach that I co-developed to model suspensions of rigid particles with arbitrary shapes. I then describe my contributions to account for hydrodynamic interactions, thermal fluctuations and phoretic effects in the RMB, as well as recent efforts to improve the accuracy and scalability of the method. I also introduce a new approach to handle kinematic constraints in complex suspensions, and its implementation in the RMB framework. Finally, I briefly present an alternative method based on regularized multipolar expansions for modelling hydrochemical couplings in suspensions of spherical particles.

At the end of each subsection, the main contributions and their relevance to the modeling challenges outlined in the Chapter 2 are briefly summarized.

3.1 The rigid multiblob method: hydrodynamic and chemical interactions between colloidal particles with arbitrary shapes

Collaborators: Florencio Balboa Usabiaga (Basque Center for Applied Mathematics (BCAM)), Aleksandar Donev (Courant Institute, NYU), Eric Keaveny (Imperial College)

In this section I present my contributions to the development of a unified, yet versatile, and scalable framework, based on the rigid multiblob model, for modeling hydrodynamic and phoretic interactions in large suspensions of arbitrarily shaped passive and active particles, taking into account thermal fluctuations and kinematic constraints. The whole framework is implemented, and continuously enriched by a large group of collaborators, in a GitHub repository (`https://github.com/stochasticHydroTools/RigidMultiblobsWall`) which is open source, publicly available and user-friendly. It has been actively used in the community, in combination with experiments and theory, to study a variety of systems involving (micro-)swimmers (Dombrowski *et al.*, 2019; Dombrowski & Klotsa, 2020; Westwood *et al.*, 2021; Gidituri *et al.*, 2023, 2024), active and passive colloids (Sprinkle *et al.*, 2020, 2021; Brosseau *et al.*, 2019, 2021; van der Wee *et al.*, 2023; Delmotte & Usabiaga, 2024), diffusing molecules (Długosz *et al.*, 2022, 2023), viruses (Moreno *et al.*, 2022), functionalized nanoparticles (Moreno-Chaparro *et al.*, 2023), Möbius strips (Moreno *et al.*, 2024), branched particles (Westwood *et al.*, 2022; Balboa Usabiaga & Ellero, 2024), fibers in structured environments (Makanga *et al.*, 2023, 2024*b*), coated drops (Gao *et al.*, 2023), magnetic spheres (Bililign *et al.*, 2022), chains (Yang *et al.*, 2020) or sheets (Wang *et al.*, 2023).

3.1.1 Rigid multiblob model for the Stokes problem

Related publication: Usabiaga *et al.* (2016)

In the rigid multiblob method (RMB), rigid bodies are discretized using a collection of minimally resolved spherical nodes of hydrodynamic radius a, also called "blobs", which are constrained to move as a rigid body. Figure 3.1 shows examples of various geometries discretized with the RMB.

Each blob is subject to a force, $\boldsymbol{\lambda}_i$, that enforces the rigid motion of the body. Thus, the integrals in the balance of force and torque (2.4)-(2.5) become sums over the blobs

$$\sum_{i\in\mathcal{B}_p} \boldsymbol{\lambda}_i = \boldsymbol{f}_p, \tag{3.1}$$

$$\sum_{i\in\mathcal{B}_p} (\boldsymbol{r}_i - \boldsymbol{q}_p) \times \boldsymbol{\lambda}_i = \boldsymbol{\tau}_p, \tag{3.2}$$

where $\boldsymbol{r}_i$ is the position of blob i belonging to body p ($\mathcal{B}_p$). The boundary condition on the particle surfaces (2.3), as in collocation methods (Pozrikidis, 1992), is evaluated at each blob

$$\boldsymbol{v}(\boldsymbol{r}_i) = \sum_j \boldsymbol{M}_{ij}\boldsymbol{\lambda}_j = \boldsymbol{u}_p + \boldsymbol{\omega}_p \times (\boldsymbol{r}_i - \boldsymbol{q}_p) + \boldsymbol{u}_s(\boldsymbol{r}_i) \text{ for all } i \in \mathcal{B}_p, \tag{3.3}$$

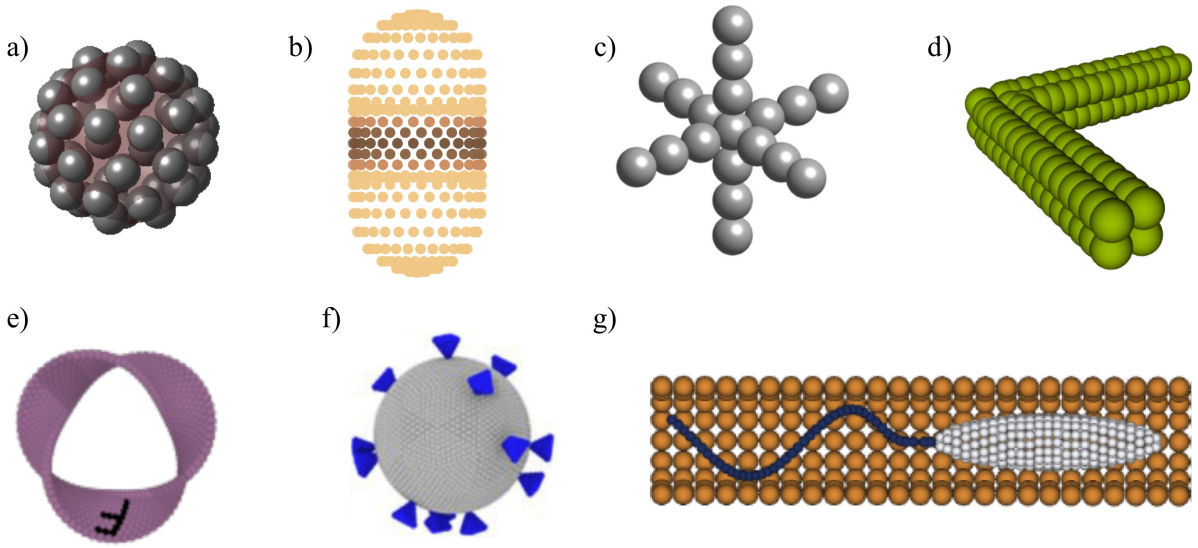

Figure 3.1: Examples of particles of various shapes discretized with the RMB model. (a) Sphere. (b) Smooth rod. (c) Branched particle. (d) Boomerang (Delong *et al.*, 2015). (e) Möbius strip (Moreno *et al.*, 2024). (f) HIV (Moreno *et al.*, 2022). (e) Bacterium in a pipe (Gidituri *et al.*, 2024).

where $\boldsymbol{v}(\boldsymbol{r}_i)$ is the fluid velocity at the position of blob i, $\boldsymbol{M}$ is the $3N_b \times 3N_b$ mobility matrix that mediates the hydrodynamic interactions between blobs, and N_b is the total number of blobs in the system. The term $\boldsymbol{M}_{ij}$ couples the force acting on the blob j to the velocity of blob i. Depending on the geometry of the domain under consideration, this matrix can be written explicitly if the Green's function of the problem is known, or its action can be computed with matrix-free methods relying on grid-based Stokes solvers, such as Immersed Boundary Methods (Peskin, 2002) or the Force Coupling Method (Maxey & Patel, 2001) (see Section 3.1.3.2). A well-known example of regularized Green's function is the Rotne-Prager-Yamakawa (RPY) approximation (Rotne & Prager, 1969; Wajnryb *et al.*, 2013), where the regularization is done by a double convolution of the Stokes Green's function, $\boldsymbol{\mathcal{G}}(\boldsymbol{r}, \boldsymbol{r}')$, with Dirac delta functions defined on the surface of a sphere of radius a:

$$\boldsymbol{M}_{ij} = \boldsymbol{M}(\boldsymbol{r}_i, \boldsymbol{r}_j) = \frac{1}{(4\pi a^2)^2} \int \delta(|\boldsymbol{r}' - \boldsymbol{r}_i| - a)\boldsymbol{\mathcal{G}}(\boldsymbol{r}', \boldsymbol{r}'')\delta(|\boldsymbol{r}'' - \boldsymbol{r}_j| - a)\mathrm{d}^3 r''\mathrm{d}^3 r'. \tag{3.4}$$

The well-known RPY mobility matrix was originally developed to provide a symmetric positive definite, pairwise approximation of the mobility matrix for a collection of spherical particles of equal radii in an unbounded domain (Wajnryb *et al.*, 2013). Extensions of the RPY matrix for particles of different radii (Zuk *et al.*, 2014), in a background shear flow (Wajnryb *et al.*, 2013), above a fluid-fluid interface (Delmotte, 2023) or a no-slip boundary (Swan & Brady, 2007) with arbitrary periodicities (Yan & Shelley, 2018; Yan & Blackwell, 2021), or in a spherical cavity (Aponte-Rivera & Zia, 2016) are available in the literature. Section 3.1.3.1 shows fast methods to compute the action of RPY tensor.

The whole linear system to solve the mobility problem is found by combining (3.1)-(3.3),

$$\begin{bmatrix} \boldsymbol{M} & -\boldsymbol{K} \\ -\boldsymbol{K}^T & \boldsymbol{0} \end{bmatrix} \begin{bmatrix} \boldsymbol{\lambda} \\ \boldsymbol{U} \end{bmatrix} = \begin{bmatrix} \boldsymbol{u}_s \\ -\boldsymbol{F} \end{bmatrix}. \tag{3.5}$$

In the linear system the matrix $\boldsymbol{K}$ is a discretization of the operator $\mathcal{K}$ introduced in Section 2.1: it transforms the rigid body velocities to blob velocities. The solution of (3.5) is

$$\boldsymbol{U} = \boldsymbol{N}\boldsymbol{F} - \boldsymbol{N}\boldsymbol{K}^T\boldsymbol{M}^{-1}\boldsymbol{u}_s \tag{3.6}$$

where $\boldsymbol{N} = \left(\boldsymbol{K}^T\boldsymbol{M}^{-1}\boldsymbol{K}\right)^{-1}$ and $\widetilde{\boldsymbol{N}} = \boldsymbol{N}\boldsymbol{K}^T\boldsymbol{M}^{-1}$ are the $6M \times 6M$ body mobility matrix and $6M \times 3N_b$ slip mobility operator given by the rigid multiblob model. The matrix $\widetilde{\boldsymbol{N}}$ maps the slip velocities to the forces applied on the surface nodes, through the blob resistance matrix $\boldsymbol{M}^{-1}$, then computes their resultant on each rigid body, through the operator $\boldsymbol{K}^T$, and multiply the resulting forces and torques by the body mobility matrix $\boldsymbol{N}$ to obtain the slip-induced body velocities in the suspension.

Key contributions:
The RMB allows to simulate suspensions of rigid bodies of arbitrary shape with active slip, without dealing with singularities, in a robust, simple and versatile framework. The RMB naturally interfaces with *any* fast method, either grid-based or relying on Green's functions, for computing hydrodynamic interactions between blobs (see Section 3.1.3). The linear system (3.5) can be solved efficiently with preconditioned iterative methods (see Section 3.1.3).

3.1.2 Including thermal fluctuations

Related publication: Westwood *et al.* (2022)

As explained in Section 2.2, two new terms appear in the equations of motion when thermal fluctuations are included: the random body velocities $\boldsymbol{U}_{\text{th}} = \sqrt{2k_BT}\boldsymbol{N}^{1/2}\boldsymbol{Z}$ and the spurious drift term $k_BT\partial_{\boldsymbol{x}} \cdot \boldsymbol{N}$. Both of these terms are challenging to account for with non-spherical particles and are computationally expensive. Below I present the formalism I have co-developed to handle these terms correctly and efficiently.

3.1.2.1 Stochastic particle velocities: $\boldsymbol{U}_{\text{th}} = \sqrt{2k_BT}\boldsymbol{N}^{1/2}\boldsymbol{Z}$

We found that the computation of the stochastic particle velocities can be readily incorporated into the system by including a random velocity at the blob level, $\boldsymbol{u}_{\text{th}}$, in the no-slip boundary conditions (3.3) (Sprinkle *et al.*, 2017; Westwood *et al.*, 2022). Specifically, we consider the fluctuating mobility problem

$$\begin{bmatrix} \boldsymbol{M} & -\boldsymbol{K} \\ -\boldsymbol{K}^T & \boldsymbol{0} \end{bmatrix} \begin{bmatrix} \boldsymbol{\lambda} \\ \boldsymbol{U} \end{bmatrix} = \begin{bmatrix} \boldsymbol{u}_s - \boldsymbol{u}_{\text{th}} \\ -\boldsymbol{F} \end{bmatrix}, \tag{3.7}$$

with the random blob velocity,

$$\boldsymbol{u}_{\text{th}} = \sqrt{2k_BT}\boldsymbol{M}^{1/2}\boldsymbol{Z}, \tag{3.8}$$

where $\boldsymbol{M}^{1/2}$ is the *square root* of the blob mobility matrix, i.e. $\boldsymbol{M}^{1/2}\left(\boldsymbol{M}^{1/2}\right)^T = \boldsymbol{M}$, and $\boldsymbol{Z}$ is a $3N_b \times 1$ white noise vector acting on the blobs, with covariance $\langle \boldsymbol{Z}(t)\boldsymbol{Z}^T(t')\rangle = \boldsymbol{I}\delta(t-t')$. This form of the noise term is equivalent to including a stochastic stress directly into the Stokes equation as in (2.14). Since with the RPY approximation and grid-based approaches the mobility $\boldsymbol{M}$ is positive definite, the stochastic velocity (3.8) is well defined. The covariance of the resulting rigid body velocities generated by the stochastic blob velocities, setting $\boldsymbol{F} = \boldsymbol{0}$ and $\boldsymbol{u}_s = \boldsymbol{0}$, is

$$\begin{aligned}
\langle \boldsymbol{U}\boldsymbol{U}^T\rangle &= \langle \boldsymbol{N}\boldsymbol{K}^T\boldsymbol{M}^{-1}\boldsymbol{u}_{\text{th}}\boldsymbol{u}_{\text{th}}^T\boldsymbol{M}^{-1}\boldsymbol{K}\boldsymbol{N}\rangle \\
&= (\boldsymbol{N}\boldsymbol{K}^T\boldsymbol{M}^{-1})\sqrt{2k_BT}\boldsymbol{M}^{1/2}\langle \boldsymbol{Z}\boldsymbol{Z}^T\rangle\boldsymbol{M}^{1/2}\sqrt{2k_BT}(\boldsymbol{N}\boldsymbol{K}^T\boldsymbol{M}^{-1})^T \\
&= 2k_BT\boldsymbol{N}\boldsymbol{K}^T\boldsymbol{M}^{-1}\boldsymbol{M}\boldsymbol{M}^{-1}\boldsymbol{K}\boldsymbol{N}\,\delta(t-t') \\
&= 2k_BT\boldsymbol{N}(\boldsymbol{K}\boldsymbol{M}^{-1}\boldsymbol{K}^T)\boldsymbol{N}\,\delta(t-t') \\
&= 2k_BT\boldsymbol{N}\,\delta(t-t'). \qquad (3.9)
\end{aligned}$$

Eq. (3.9) shows that the thermal noise is balanced by the viscous dissipation as required by the fluctuation dissipation balance. Thus the stochastic velocity we impose at the blob level (3.8) generates Brownian body velocities consistent with the Stokes equation. Equivalently, the square root of the body mobility matrix $\boldsymbol{N}^{1/2} = \boldsymbol{N}\boldsymbol{K}^T\boldsymbol{M}^{-1/2}$ satisfies the fluctuation dissipation balance with $\boldsymbol{N}^{1/2}(\boldsymbol{N}^{1/2})^T = \boldsymbol{N}$.

3.1.2.2 Drift term: $k_BT\partial_{\boldsymbol{x}}\cdot\boldsymbol{N}$

The second aspect of the computation is to account for Brownian drift when advancing the particle positions.
It has been shown (Delong *et al.*, 2014; Sprinkle *et al.*, 2017, 2019) that the drift can be incorporated using random finite differences (RFD), which a randomized version of the standard finite differences: given a Gaussian random vector, $\boldsymbol{W}$, such that $\langle \boldsymbol{W}\boldsymbol{W}^T\rangle = \boldsymbol{I}$, the divergence of the mobility matrix can be approximated as follows

$$k_BT\partial_{\boldsymbol{x}}\cdot\boldsymbol{N} = k_BT\left\langle \frac{\boldsymbol{N}(\boldsymbol{x}+\delta\boldsymbol{W}) - \boldsymbol{N}(\boldsymbol{x})}{\delta}\cdot\boldsymbol{W}\right\rangle + O(\delta^2), \qquad (3.10)$$

where δ a *small* number. This involves applying the mobility matrix $\boldsymbol{N}$, and thus solving the mobility problem (3.5), evaluated at randomly displaced positions/orientations $\delta\boldsymbol{W}$ to a random force/torque vector $k_BT\boldsymbol{W}$. RFD therefore requires at least one additional mobility solve of (3.5) per time-step compared to the deterministic setting.

Together with Eric Keaveny and his post-doc Tim Westwood, we developed a new midpoint scheme, called the "generalized Drifter-Corrector" (gDC), which *does not require* additional mobility solves compared to the deterministic case. The main idea behind the scheme is to advance to the mid-step using particle velocities obtained by orthogonally projecting the fluctuating velocities onto the space of rigid body motions. At the midstep, the full mobility problem (3.7) is solved and important factors based on the divergence of the projected fluctuating velocity are incorporated into the update. The gDC has the nice property that many of the additional computations needed to capture Brownian drift occur at the level of individual particles, and hence

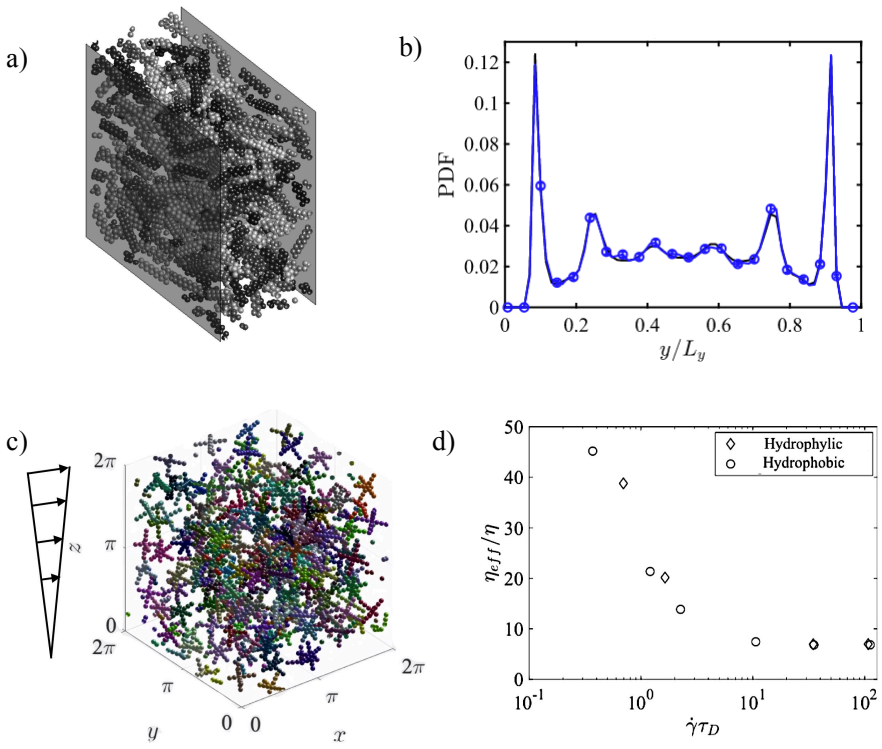

Figure 3.2: (a) Snapshot from a rod simulation with channel width $L_y = L/2$. Each rod has a randomly-selected greyscale coloring and the semi-transparent grey boundaries depict the locations of the boundaries. (b) The equilibrium distribution of rod positions between the channel walls. (c) Snapshot of the sheared branched particles in a periodic domain. Colors are chosen randomly. (d) Effective, shear-thinning, viscosity of both hydrophobic and hydrophilic suspensions with a particle volume fraction of 20% for different dimensionless shear rates.

naturally lend themselves to parallel computation and larger-scale simulation. As a result, the gDC scheme requires *a single mobility solve* per time step. The resulting scheme is weakly first-order accurate and, in practice, provides errors similar in magnitude to other schemes based on RFD (Sprinkle *et al.*, 2017), which are three-times more expensive. This significantly accelerates time integration for schemes built around grid-based solvers that can take advantage of the flows generated by a fluctuating stress. The gDC may also be used for matrix-based computations at a cost comparable to the existing state-of-the-art.

3.1.2.3 Large scale simulations

We have demonstrated the applicability of the scheme for larger-scale simulation by considering confined suspensions of rod-like particles, as well as the rheology of branched-particle suspensions. The second case is inspired by the experimental work of (Bourrianne *et al.*, 2022) on the rheology of highly textured silica particles (see Fig. 1.1). The discretization of a branched particle is shown in Fig. 3.1c. Figure 3.2a-b show a snapshot and the equilibrium distribution of rod-like particles in between two planes. Figure 3.2c-d show a suspension of branched parti-

cles in a shear flow together with the shear-thinning rheology of the suspension for two type of inter-particle potentials (hydrophobic and hydrophilic).

Key contributions:
Introducing the noise at the blob level allows to generate the correct Brownian velocity increments at the level of the bodies with arbitrary shapes. The random blob velocities can be computed with *any* fast method, either grid-based or Green's function-based (see Section 3.1.3). With our new scheme, the GDC, the drift term is computed with only one solve of the mobility problem (3.7) per time-step, which is three times less than other schemes with a similar accuracy.

3.1.3 How to scale big and compute fast ?

Related publications: Usabiaga *et al.* (2016); Westwood *et al.* (2022)

The linear system (3.7) needs to be solved efficiently to carry out dynamic simulations with large numbers of particles. To do so, two ingredients are crucial:

1. The size and condition number of the linear system (3.7) grows with the number of blobs N_b, it is therefore essential to use an iterative solver with a convergence rate that depends weakly on the number of particles. For that purpose we developed a block diagonal preconditioner applied to the iterative GMRES method. The resulting solver exhibits a convergence within a few iterations that is *independent* of the particle number M.

2. Hydrodynamic interactions between bodies are obtained directly from the matrix $\boldsymbol{M}$. The action of $\boldsymbol{M}$ on a vector is required to compute the deterministic velocities $\boldsymbol{U} = \boldsymbol{N}\boldsymbol{F} - \widetilde{\boldsymbol{N}}\boldsymbol{u}_s$, while the product $\boldsymbol{M}^{1/2}\boldsymbol{Z}$ is necessary to obtain the Brownian velocities $\boldsymbol{U}_{\text{th}}$. It is therefore essential to use and develop efficient methods to compute the action of $\boldsymbol{M}$ and its square root. In the following, I describe the approaches I have co-developed for the fast evaluation of $\boldsymbol{M}$ using Green's function and grid-based methods.

3.1.3.1 Fast hydrodynamics with Green's functions:

The computational cost of a mobility-vector products $\boldsymbol{M}\boldsymbol{\lambda}$ scales quadratically with the number of blobs ($O(N_b^2)$). In order to reduce this cost, we parallelize the RPY matrix-vector products on the shared memory of GPU's, which yields a linear scaling up to $N_b \sim 10^4 - 10^5$. We also use more sophisticated methods, such as the fast multipole methods (FMM) (Liang *et al.*, 2013) to achieve a linear scaling. For periodic domains, we use the positively split Ewald method (Fiore *et al.*, 2017; Fiore & Swan, 2018) or periodic FMM (Yan & Shelley, 2018; Yan & Blackwell, 2021) to compute the action of $\boldsymbol{M}$ on a vector.
To compute the action of $\boldsymbol{M}^{1/2}$ on the random vector $\boldsymbol{Z}$ we use the Lanczos algorithm (Ando *et al.*, 2012; Chow & Saad, 2014), This method iteratively approximates $\boldsymbol{M}^{1/2}\boldsymbol{Z}$ with a set of basis vectors of a vectorial space $\mathbb{K}$ that are linear combinations of the powers of the mobility matrix times the random vector: $\mathbb{K} = \text{span}\left\{\boldsymbol{Z}, \boldsymbol{M}\boldsymbol{Z}, \boldsymbol{M}^2\boldsymbol{Z}, ...\right\}$. The cost of the method therefore depends on the number of basis vectors, and thus mobility-vector products, required

to reach a given tolerance ε. Using our block-diagonal preconditioner, the convergence rate is independent of the number of blobs and a small number of iterations is required to reach a reasonable tolerance (typically 5 mobility-vector products for $\varepsilon = 10^{-5}$).

3.1.3.2 Fast hydrodynamics with matrix-free methods:

When there is no explicit expression for the Green's function of the system, we use matrix-free methods that rely on grid-based, parallelized, Stokes solvers such as the Force Coupling Method (FCM) with fluctuating hydrodynamics (Landau & Lifshitz, 1959; Keaveny, 2014; Delmotte & Keaveny, 2015).
With fluctuating FCM, the coupling between the blobs and the fluid is achieved through a forcing term $\boldsymbol{f}$ added to the fluctuating Stokes equations (2.14),

$$\boldsymbol{\nabla} p - \eta \boldsymbol{\nabla}^2 \boldsymbol{v} = \boldsymbol{\nabla} \cdot \boldsymbol{\mathcal{Z}} + \boldsymbol{f}, \tag{3.11}$$

$$\boldsymbol{\nabla} \cdot \boldsymbol{v} = 0. \tag{3.12}$$

The second term on the RHS of (3.11) is the blob forcing transferred to the fluid with a spreading operator $\mathcal{S}$,

$$\boldsymbol{f}(\boldsymbol{r}) = \mathcal{S}[\boldsymbol{\lambda}](\boldsymbol{r}) = \sum_{i=1}^{N_b} \boldsymbol{\lambda}_i \Delta_i(\boldsymbol{r}), \tag{3.13}$$

where the finite size of the blobs is accounted for with a Gaussian spreading envelope[1],

$$\Delta_i(\boldsymbol{r}) = (2\pi\sigma^2)^{-3/2} \exp\left(-\frac{\|\boldsymbol{r} - \boldsymbol{r}_i\|^2}{2\sigma^2}\right). \tag{3.14}$$

The length scale σ functions in a similar way to the blob radius, a, in the RPY tensor. The diagonal entries of the FCM mobility matrices will match those of the RPY tensor if $\sigma = a/\sqrt{\pi}$ (Maxey & Patel, 2001).

The fluid velocity, obtained after solving (3.11) and (3.12), is the sum of a deterministic part $\boldsymbol{v}^D$, due to the forcing $\boldsymbol{\lambda}$, and a fluctuating term $\boldsymbol{v}_{\text{th}}$, stemming from the fluctuating stress. We may express the total fluid velocity as

$$\boldsymbol{v} = \mathcal{L}^{-1}\left(\mathcal{S}\boldsymbol{\lambda} + \mathcal{D}\boldsymbol{\mathcal{Z}}\right) \tag{3.15}$$

$$= \boldsymbol{v}^D + \boldsymbol{v}_{\text{th}}, \tag{3.16}$$

where $\mathcal{S}$ is the spreading operator in (3.13), $\mathcal{L}^{-1}$ is the inverse Stokes operator (i.e. the fluid solver), and $\mathcal{D}$ the divergence operator applied to the fluctuating stress (Delong *et al.*, 2014).

The velocities of the blobs are then obtained from the fluid velocity using an averaging operator, $\mathcal{J}$, such that

$$\boldsymbol{u}_i = (\mathcal{J}[\boldsymbol{v}])_i = \int \boldsymbol{v}\Delta_i(\boldsymbol{r}) \mathrm{d}^3\boldsymbol{r} = \boldsymbol{u}_i^D + \boldsymbol{u}_{\text{th},i}, \quad i = 1, .., N_b, \tag{3.17}$$

[1]Other matrix-free methods, such as the Immersed Boundary Method (Peskin, 2002) use the exact same approach but with different kernels than a Gaussian function.

where $\mathcal{J} = \mathcal{S}^\star$ is adjoint to the spreading operator.

We see then that the FCM mobility matrix can be written as the composition of three linear operators: $\boldsymbol{M}_{FCM} = \mathcal{J}\mathcal{L}^{-1}\mathcal{S}$. Additionally, as demonstrated in (Keaveny, 2014; Delmotte & Keaveny, 2015) the velocity $\boldsymbol{u}_{\text{th}}$ satisfies the fluctuation—dissipation theorem with the covariance given by the FCM approximation of the mobility matrix,

$$\left\langle \boldsymbol{u}_{\text{th}}(t)\boldsymbol{u}_{\text{th}}(t')\right\rangle = 2k_BT\boldsymbol{M}_{FCM}\delta(t-t'), \tag{3.18}$$

where $\boldsymbol{u}_{\text{th}} = \sqrt{2k_BT}\boldsymbol{M}_{FCM}^{1/2}\boldsymbol{Z}(t)$, with $\boldsymbol{M}_{FCM}^{1/2} = \mathcal{J}\mathcal{L}^{-1}\mathcal{D}$.

Thus, we see that fluctuating FCM simultaneously computes the actions of $\boldsymbol{M}$ and $\boldsymbol{M}^{1/2}$ on $\boldsymbol{\lambda}$ and $\boldsymbol{Z}$, respectively, by considering solutions to the forced fluctuating Stokes equations.

The fluctuating FCM can be implemented with any kind of Stokes solver. This involves first evaluating the forcing, $\boldsymbol{f}(\boldsymbol{r})$, and the fluctuating stress, $\boldsymbol{\mathcal{Z}}$, on the grid. Next, the Stokes equations are solved with a Stokes solver (e.g. using Finite Volumes, Finite Elements, Finite Differences or a Spectral method). Finally, the trapezoidal rule is used to numerically integrate (3.17) to obtain the translational velocity for each of the blob making up the rigid bodies. Since our Stokes solvers are well-parallelized, the computational cost scales linearly with the number of blobs $O(N_b)$ (Delmotte *et al.*, 2015*b*; Hashemi *et al.*, 2023).

Key contributions:
For both Green's function- and grid-based approaches, we have fast, parallel, methods for computing hydrodynamic interactions between blobs and their random noise, with linear scaling $O(N_b)$. Thanks to our efficient preconditioned iterative solver, the rigid multiblob linear system (3.7) can be solved with just a few iterations, i.e. mobility-vector products $\boldsymbol{M}\boldsymbol{\lambda}$, independently of the number of blobs in the system. Therefore the linear scaling of the computational cost is preserved at the level of the rigid bodies $O(M)$, which allows for simulations of complex suspensions at a scale that had not been reached before.

3.1.4 Grid optimization: improving the accuracy of the RMB

Related publication: Delmotte & Usabiaga (2024)

In order to simulate a large number of complex particles, it is necessary to use as few blobs per particle as possible while maintaining a "reasonable" accuracy of the hydrodynamic interactions. Despite the regularization error induced by the regularized Green's function (3.4) that scales as the blob radius a, and thus as $N_b^{-1/2}$ (Delmotte & Usabiaga, 2024), it is possible to enhance the numerical accuracy for a given resolution through a grid optimization procedure. Once the number of blobs per particle and the quadrature used to mesh the particle surface have been chosen, two additional grid parameters can be tuned: the blob radius a and their position with respect to the actual particle surface. In fact, due to their finite size, the blobs do not have to lie on the actual particle surface. The distance of the blob centers relative to the particle surface is represented by a geometric parameter S, which represents the size scale of the discretized surface relative to the actual body surface: when $S = 1$ the surface of the grid coincides with the surface of the actual particle. If $S < 1$ ($S > 1$) the blobs are located in the interior (exterior)

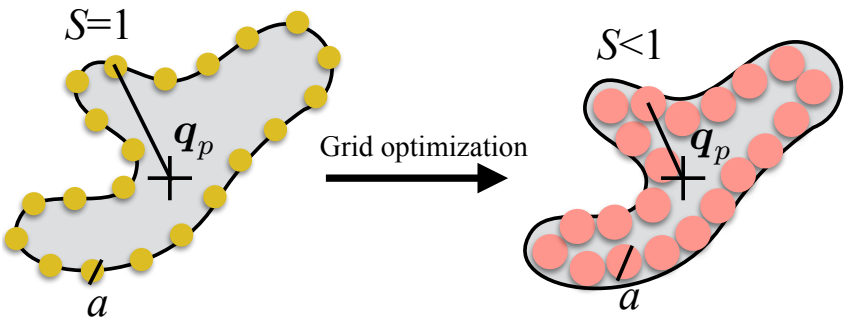

Figure 3.3: Sketch of the grid optimization procedure for a body with arbitrary shape (in grey) and position $\boldsymbol{q}_p$. Left: surface discretization of a body with arbitrary shape with N_b blobs of radius a (yellow disks) and size scale $S = 1$. Right: optimized grid with N_b larger blobs (red disks) positioned inside the actual body surface ($S < 1$).

of the actual surface (see Fig. 3.3). It is therefore important to optimize these geometric grid parameters in order to achieve a reasonable accuracy at a fraction of the computational cost associated with other methods, such as BEM.

3.1.4.1 Optimization procedure

The goal of the grid optimization is to find the values of the parameters S and a that best match the hydrodynamic response, i.e. the mobility $\boldsymbol{N}$ and the slip mobility operators $\widetilde{\boldsymbol{N}}$, of an isolated particle.

In our seminal work, this was done empirically and only for the mobility matrix $\boldsymbol{N}$ (Usabiaga *et al.*, 2016). More recently, Broms *et al.* (Broms *et al.*, 2023) wrote a formal minimization problem to match $\boldsymbol{N}$ in a systematic way. Inspired by their work, we proposed a new optimization strategy to match the slip mobility operator simultaneously (Delmotte & Usabiaga, 2024), which is outlined hereafter.

Let $\boldsymbol{N}_{ref}$ and $\widetilde{\boldsymbol{N}}_{ref}$ be the reference mobilities to be matched for a given body, which can be known analytically or calculated with a well-resolved discretization, and $\boldsymbol{N}(S, a)$ and $\widetilde{\boldsymbol{N}}(S, a)$ the operators obtained with the coarse mutliblob grid with parameters (S, a). $\boldsymbol{N}$ and $\boldsymbol{N}_{ref}$ have the same 6×6 shape regardless of the solution method used to compute them. However, $\widetilde{\boldsymbol{N}}$ and $\widetilde{\boldsymbol{N}}_{ref}$ have different sizes since their number of columns depends on the grid resolution, usually $N_{b,ref} \gg N_b$, regardless of the numerical method used to compute the reference solution. Nonetheless, their rank is identical: $r = 6$. Therefore these two operators can be decomposed with a singular value decomposition (SVD) and then compared using their 6 singular values $\boldsymbol{\Sigma} = \mathrm{diag}(\sigma_1, \cdots, \sigma_6)$.

Now that we have a way to measure the error between the coarse and reference mobility operators, we write the minimization problem to find the optimal grid parameters (S, a)[2]:

$$\min_{S,a} \left(\frac{\|\boldsymbol{N}_{ref} - \boldsymbol{N}(S,a)\|}{\|\boldsymbol{N}_{ref}\|} + \frac{\|\boldsymbol{\Sigma}_{ref} - \boldsymbol{\Sigma}(S,a)\|}{\|\boldsymbol{\Sigma}_{ref}\|} \right). \tag{3.19}$$

[2]The cost function is presented schematically; however, it is, in fact, more complex. For further details, see (Delmotte & Usabiaga, 2024).

The problem (3.19) is solved with a differential evolution algorithm (Storn & Price, 1997), which, due to its stochastic nature and to the small dimension of the parameter space, systemically converges to a global minimum[3].

3.1.4.2 Validation example

To illustrate the performance of the grid optimization, we show a validation example based on the swimming speed of a spherical squirmer of radius R in an unbounded domain with an axisymmetric slip distribution on its surface. More validation examples can be found in (Delmotte & Usabiaga, 2024). The spherical squirmer model consists of a spherical particle with a prescribed surface slip velocity, usually decomposed into series of spherical harmonics (Pak & Lauga, 2014). It has been extensively used to model the self-propulsion and flow generated by ciliated microorganisms (Lighthill, 1952; Blake, 1971*b*; Pedley, 2016).

With the multiblob method, the sphere surface is discretized with blobs located on geodesic grids (Swan & Wang, 2016), see Fig. 3.4a. In the original works of (Swan & Wang, 2016) and(Usabiaga *et al.*, 2016), the blob radius a is chosen so that neighboring blobs touch each other ($a/s = 0.5$, where s is the nearest-neighbor distance) and the geometric radius of the grid R_g is chosen in order to match the Stokes drag of an ideal sphere with radius R in an unbounded domain (i.e. $N_{\text{th}}^{UF} = 1/(6\pi\eta R)$). We denote this discretization as the "original grid". We also define the "optimized grid", parametrized by the doublet $(S = R_g/R, a)$, as the solution of the minimization problem (3.19).

We evaluate the hydrodynamic response of the sphere to a surface slip given, in the frame of the particle, by $\boldsymbol{u}_s = -\sin\theta \boldsymbol{e}_\theta$, where $\theta \in [0, \pi]$ is the angle between the position on the squirmer surface and its axis of symmetry $\boldsymbol{e}_z$. It is known from (Lighthill, 1952) that the resulting swimming speed is $\boldsymbol{U}_{\text{th}} = 2/3\boldsymbol{e}_z$.

Fig. 3.4b compare the propulsion speed from the different grids against the exact solution. Due to their regularization error, the grids converge slowly, as $\sim N_b^{-1/2}$, to the exact solution. The error of the original grid (green disks) always remains below 10% for all resolutions and below 6% above $N_b \geq 42$. Grid optimization (green triangles) further deceases the error which drops below 2% for $N_b \geq 42$. Note that an error of only 0.6% is obtained with an optimized coarse grid ($N_b = 42$), which is similar to the error obtained with a much finer grid ($N_b = 2400$) in the Regularized Stokeslet simulations of (Smith *et al.*, 2021).

Key contributions:
The grid optimization strategy is applicable to all particle shapes. As illustrated by the squirmer example, it significantly reduces the error compared to the original discretization, thereby enabling the simulation of slip-driven particles with coarse grids ($N_b = 42$) with a satisfactory degree of accuracy (2-3 digits).

[3]We found that gradient-based methods were much more sensitive to the initial guess and sometimes stopped at local minima.

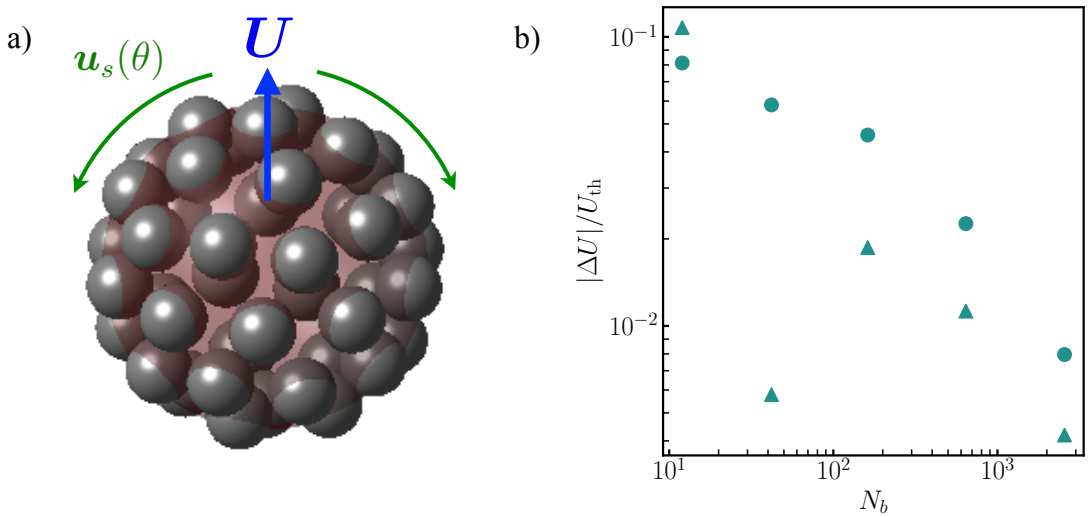

Figure 3.4: (a) Sketch of a squirmer discretized with $N_b = 42$ blobs with an axisymmetric slip velocity distribution. (b) Relative error of the propulsion speed of a squirmer as a function of the grid resolution N_b. Disks: original grid. Triangles: optimized grid.

3.1.5 Rigid multiblob model for the Laplace problem

Related publication: Delmotte & Usabiaga (2024)

3.1.5.1 Integral form of Laplace equations

Like Stokes, the Laplace equation (2.26) is an elliptic partial differential equations that can be written with an integral formulation at the particles' surfaces (Montenegro-Johnson *et al.*, 2015)

$$\left[\frac{1}{2}\boldsymbol{\mathcal{I}} - \boldsymbol{\mathcal{D}}\right] c = -\boldsymbol{\mathcal{S}}\left[\frac{\partial c}{\partial \boldsymbol{n}}\right] + c_\infty \quad \text{on } \partial\mathcal{B}, \tag{3.20}$$

where c_∞ is the background field evaluated at the particle surface, $\boldsymbol{\mathcal{S}}$ and $\boldsymbol{\mathcal{D}}$ are the single layer and double layer operators given by

$$\boldsymbol{\mathcal{S}}[c](\boldsymbol{x}) = \int_{\partial\mathcal{B}} G(\boldsymbol{x}-\boldsymbol{y})c(\boldsymbol{y})\,\mathrm{d}S_y, \tag{3.21}$$

$$\boldsymbol{\mathcal{D}}[c](\boldsymbol{x}) = \int_{\partial\mathcal{B}} T_i(\boldsymbol{x}-\boldsymbol{y})n_i(\boldsymbol{y})c(\boldsymbol{y})\,\mathrm{d}S_y, \tag{3.22}$$

where the integral is over all the colloidal surfaces: $\partial\mathcal{B} = \bigcup_{p=1}^{M}\partial\mathcal{B}_p$. $G(\boldsymbol{x},\boldsymbol{y})$ and $\boldsymbol{T}(\boldsymbol{x},\boldsymbol{y}) = \frac{\partial}{\partial \boldsymbol{y}}G(\boldsymbol{x},\boldsymbol{y})$ are the monopole and dipole Green's functions (or kernels) of the Laplace equation. In an unbounded domain, their expressions are

$$G(\boldsymbol{x},\boldsymbol{y}) = \frac{1}{4\pi}\frac{1}{r}, \tag{3.23}$$

$$T_i(\boldsymbol{x},\boldsymbol{y}) = \frac{1}{4\pi}\frac{r_i}{r^3}. \tag{3.24}$$

The double layer operator $\boldsymbol{\mathcal{D}}$ in (3.20) acts in the principal value sense and $\boldsymbol{\mathcal{I}}$ is the identity operator (Pozrikidis, 1992). The normal derivative of the concentration, $\partial c/\partial \boldsymbol{n}$, on the right hand side of (3.20) can be replaced with the boundary conditions on the colloids, Eq. (2.27), to rewrite the equation as

$$\left[\frac{1}{2}\boldsymbol{\mathcal{I}} - \boldsymbol{\mathcal{D}} + \boldsymbol{\mathcal{S}}\left[\frac{k}{D}\right]\right] c = \boldsymbol{\mathcal{S}}\left[\frac{\alpha}{D}\right] + c_\infty. \tag{3.25}$$

Since the surface parameters $k = k(\boldsymbol{r})$ and $\alpha = \alpha(\boldsymbol{r})$ define the boundary conditions, we have absorbing boundary conditions for ($k > 0$, $\alpha = 0$) and emitting boundary conditions for ($k = 0$, $\alpha > 0$). In general, it is possible to use $k, \alpha > 0$ to model a colloidal suspension of mixed sources and sinks.

Once the concentration is known, its gradient at the surfaces can be computed with the derivative of (3.25), i.e.

$$\frac{1}{2}\boldsymbol{\nabla} c = \boldsymbol{\nabla} c_\infty + \boldsymbol{\mathcal{L}}[c] - \boldsymbol{\mathcal{T}}\left[-\frac{k}{D}c + \frac{\alpha}{D}\right], \tag{3.26}$$

where

$$\boldsymbol{\mathcal{L}}_i[c](\boldsymbol{x}) = \int_{\partial\mathcal{B}} \frac{\partial T_i(\boldsymbol{x}-\boldsymbol{y})}{\partial x_j} n_j(\boldsymbol{y}) c(\boldsymbol{y})\, \mathrm{d}S_y, \tag{3.27}$$

$$\boldsymbol{\mathcal{T}}_i[c](\boldsymbol{x}) = \int_{\partial\mathcal{B}} T_i(\boldsymbol{x}-\boldsymbol{y}) c(\boldsymbol{y})\, \mathrm{d}S_y. \tag{3.28}$$

Then, we can use (2.28) to compute the active slip and solve the Stokes equations.

3.1.5.2 Rigid mutliblob discretization

Using the nodes of the optimized rigid multiblob grid as collocation points to solve the discretization of (3.25), we obtain the linear system

$$\left[\frac{1}{2}\boldsymbol{I}\boldsymbol{w}^{-1} + \boldsymbol{D} + \boldsymbol{S}\frac{\boldsymbol{k}}{D}\right]\boldsymbol{w}\boldsymbol{c} = \boldsymbol{S}\frac{\boldsymbol{w}\boldsymbol{\alpha}}{D} + \boldsymbol{c}_\infty, \tag{3.29}$$

where $\boldsymbol{I}$, $\boldsymbol{S}$ and $\boldsymbol{D}$ are $N_b \times N_b$ matrices corresponding to the discrete versions of the continuous operators introduced in (3.25). $\boldsymbol{c}$ and $\boldsymbol{\alpha}$ are $N_b \times 1$ vectors collecting the value of the concentration and the reaction flux at each node. Meanwhile, the reaction rate and the quadrature weights are arranged in the $N_b \times N_b$ diagonal matrices $\boldsymbol{k}$ and $\boldsymbol{w}$. The weight values $\boldsymbol{w}$ represent the surface area covered by the nodes. Once the surface concentration vector $\boldsymbol{c}$ is obtained after solving the linear system (3.29), we compute the concentration gradient on the nodes with

$$\frac{1}{2}\boldsymbol{\nabla}\boldsymbol{c} = \boldsymbol{\nabla}\boldsymbol{c}_\infty + \boldsymbol{L}\boldsymbol{w}\boldsymbol{c} + \boldsymbol{T}\left[\frac{\boldsymbol{w}\boldsymbol{k}\boldsymbol{c}}{D} - \frac{\boldsymbol{\alpha}}{D}\right], \tag{3.30}$$

where $\boldsymbol{L}$ and $\boldsymbol{T}$ are $3N_b \times N_b$ matrices corresponding to the discrete versions of the continuous operators introduced in (3.26).

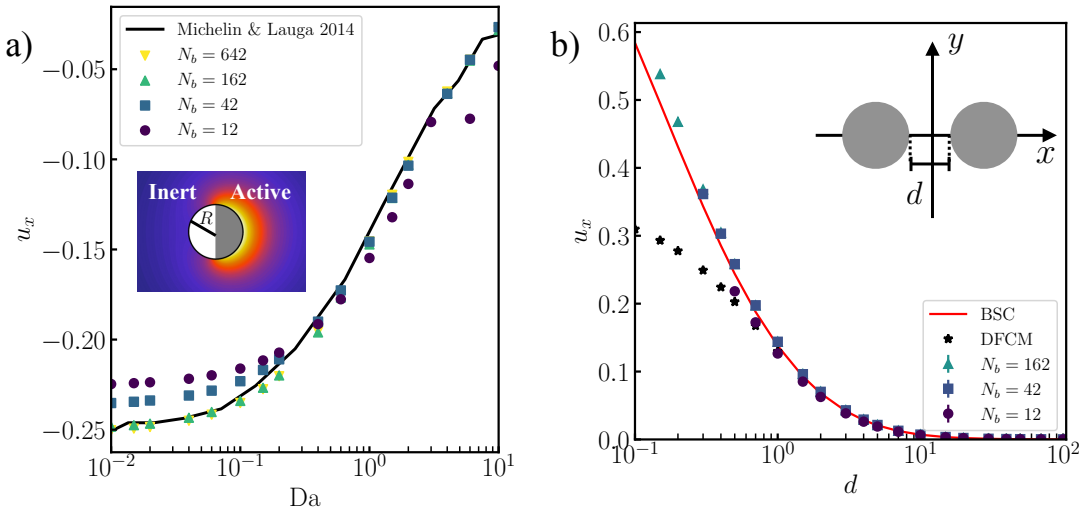

Figure 3.5: (a) Swimming speed for a Janus sphere as of function of the Damkohler number. Results for resolutions with different number of nodes, N_b, and comparison with the results of Michelin and Lauga (Michelin & Lauga, 2014). The results with 42 nodes agree well for high Da numbers and shows an error of about 5% for Da $\ll 1$; for finer resolutions the agreement is good for all Da numbers. Inset shows a the concentration field around a Janus particle (adapted from (Michelin & Lauga, 2014)). (b) Velocities along the x-axis for two spheres with uniform surface activity. The motion is symmetric thus we only show the velocity of one of them. The results for discretizations with $N_b = 12$, 42 and 162 are compared with DFCM and the exact solution computed in bispherical coordinates (BSC). Inset: sketch of the configuration.

Just like the hydrodynamic problem, our method naturally interfaces with fast methods, such as GPU parallelization or the Fast Multipole Method (Yan & Blackwell, 2020), for computing the action of the single and double layer operators, . To solve the linear system (3.29) we use an unpreconditioned GMRES solver, and found that the GMRES convergence is robust and scales well with the number of colloids.

Note that the Laplace kernels diverge when the source and target point coincide ($\boldsymbol{y} = \boldsymbol{x}$). For the sake of simplicity we did not introduce any kernel regularization to deal with this divergence, instead, we set the kernels diagonal terms to zero in both (3.29) and (3.30). Despite this approximation, the accuracy of this discretization remains reasonable at short distances, as shown in the next section.

3.1.5.3 Validation examples

We show two examples to evaluate the accuracy of the RMB model for the coupled Laplace-Stokes problem with optimized grids: a single reactive Janus particle at arbitrary Damkohler number Da $= kR/D$, and two reactive Janus particles with fixed emitting fluxes. More validation examples can be found in (Delmotte & Usabiaga, 2024)

Single reactive particle

Here we verify that our approach works for arbitrarily Da numbers by simulating a single Janus particle with an inert hemisphere and an active one and by comparing our results against those

of Michelin and Lauga (Michelin & Lauga, 2014). The surface mobility is set to $\mu(\boldsymbol{r}) = 1$ over the whole sphere; the background concentration is set to zero, $c_\infty = 0$, and the emitting fluxes and reaction rates are set to $\alpha = -1$ and $k = \mathrm{Da}D/R$ on the active hemisphere and $\alpha = k = 0$ on the passive one.

Fig. 3.5a shows the swimming speed of a Janus reactive particle as a function of the Damkohler number for several resolutions N_b. The general trend is recovered by all our discretizations. For low Da numbers the concentration cannot diffuse as fast as it is consumed and an asymmetric concentration profile is formed around the sphere. That asymmetry creates surface concentration gradients and consequently a surface slip that induces a swimming speed. As the Da number increases, and the concentration diffuses faster, the concentration asymmetry is reduced which leads to weaker concentration gradients and a swimming speed that tends to zero for $\mathrm{Da} \gg 1$. A more careful comparison against the results of Michelin and Lauga shows that our results agree well with a resolution of $N_b = 162$ nodes or more. For 42 nodes we obtain a good agreement for $\mathrm{Da} > 1$ and an error of about 5% for $\mathrm{Da} \ll 1$.

Two uniform particles

In our second test we consider colloids with a uniform emission flux and mobility, $\alpha = 1$ and $\mu = 1$, on their surfaces (see inset of Fig. 3.5b). We compare our results with those obtained by the Diffusiophoretic Force Coupling Method (DFCM), which relies on truncated multipolar expansions (see Section 3.3 and (Rojas-Pérez *et al.*, 2021)), and the exact solution computed in bispherical coordinates (BSC).

We show in Fig. 3.5b the velocity for one of the colloids as a function of the gap d between the two colloids[4]. Close colloids generate a concentration gradient in their gap which induces a phoretic speed u_x. As the particles are moved apart the magnitude of the concentration gradient decreases and the speed decays to zero. We observe that our lowest resolution, $N_b = 12$, is accurate down to gaps of one colloidal radius, $d = 1$, just as the DFCM. For higher resolutions, but still small number of blobs, the solution remains accurate for smaller gaps, down to $d \approx 0.1$ for $N_b = 42$, and it surpasses the accuracy of the DFCM.

3.1.5.4 Large scale simulations

Using the capacities offered by our new framework, we turn to the simulation of larger and more complex systems. Both examples explore new physical problems that, to the best of our knowledge, have not been addressed with numerical simulations before.

First we study the collective swimming of phoretic and Brownian Janus smooth rods on an incline. It has been shown that a single particle can exhibit gravitaxis by tilting against the incline and swimming uphill against very steep slopes (Brosseau *et al.*, 2021). Here we investigate the effect of hydrochemical interactions on a whole suspension. We find that hydrochemical attraction suppresses gravitaxis and observe the emergence of small clusters that rearrange dynamically due to thermal fluctuations (see Fig. 3.6). These clusters rotate, translate or remain still, while sedimenting along the incline.

[4]Since the discretized colloids are not perfectly isotropic, see Fig. 3.1a, we only compute the solution down to distances where the nodes, of radius a, of the different colloids start to overlap. This way the results do not depend on the relative orientation of the colloids. Since the node radius decreases for finer grids, higher resolutions overlap at a smaller gap size.

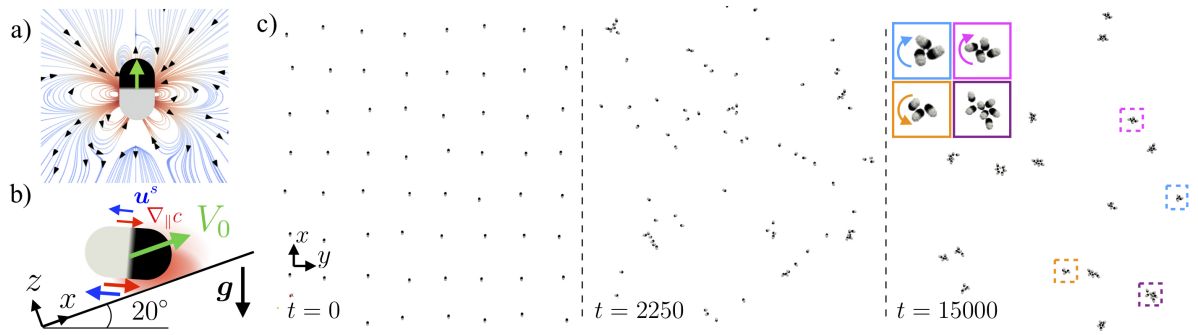

Figure 3.6: (a) Flow field around a phoretic Janus smooth rod. (b) Sketch of the self-propulsion and tilting mechanisms of a phoretic gravitactic rod above an incline with angle $\alpha = 20°$. Red and blue arrows represent concentration gradients and slip velocities respectively. (c) Snapshots of the simulation over time. Insets in the last panel: close-up view on some clusters, colored arrows show their rotation direction if any.

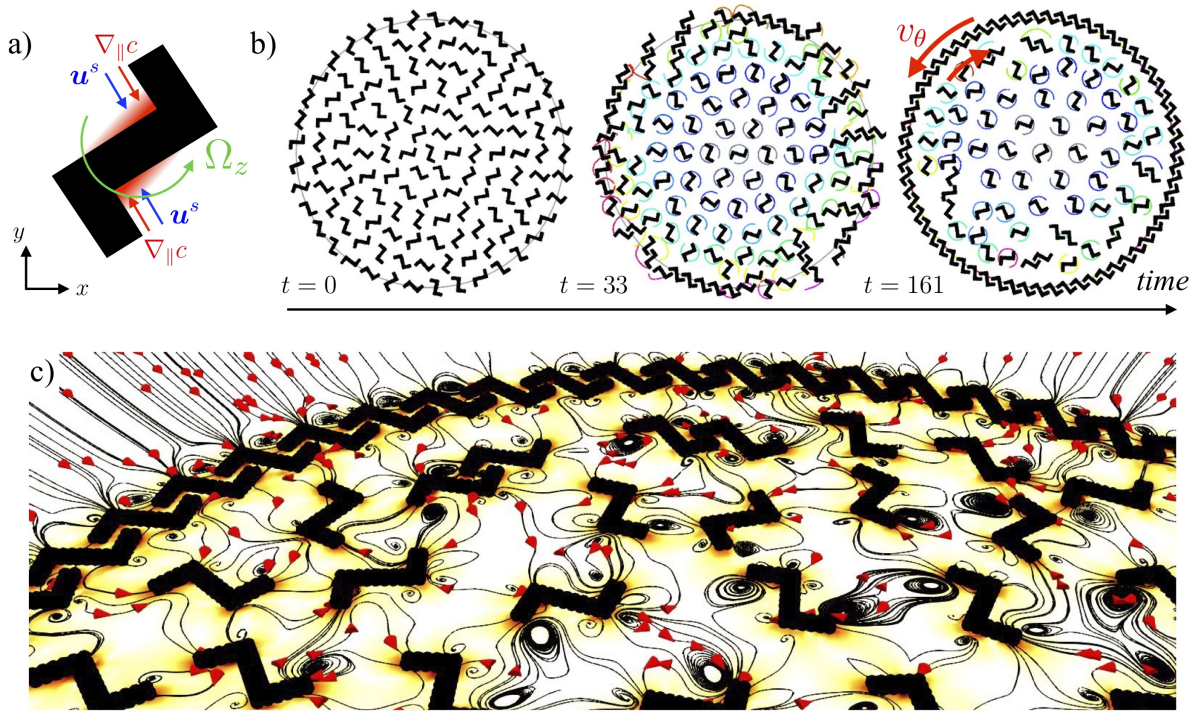

Figure 3.7: (a) Geometry of a chiral particle and schematic of the self-rotation mechanism. (b) Snapshots of the simulation at three different times. Light grey circle: confining disk of radius $R = 10$. Colored lines: trajectory of the tip of the arms over the last rotation period. Red arrows: azimuthal motion, v_θ, of the particles at the periphery. (c) Flow field around the chiral particles. Color-scale from white to dark red: magnitude of the velocity field. Black lines with red arrows: streamlines.

The second simulation, inspired by recent experimental work (Zhang *et al.*, 2019; Brooks *et al.*, 2019; Kumar *et al.*, 2022), consists of a large collection of chiral particles with uniform surface properties confined by a harmonic potential above a no-slip wall. Thanks to its chi-

rality, a single particle rotates by itself and stirs the surrounding fluid due to self-phoresis. We show that a large collection of such particles exhibit nontrivial collective behaviours, such as the coexistence of an outer rim and an inner crystal rotating in opposite directions (see Fig. 3.7).

Key contributions:
Our method can simulate large suspensions of phoretic particles of arbitrary shape accounting for thermal fluctuations at all Damkohler numbers. It employs second-layer formulations, regularized kernels and a grid optimization strategy to solve the coupled Laplace-Stokes equations with reasonable accuracy at a fraction of the computational cost associated with traditional numerical methods Our framework is not limited to diffusiophoresis, i.e. solute concentration fields. It broadly applies to any scalar field that satisfies elliptic equations, such as temperature or electric potential. With minor modifications, our code can be used to study the dynamics of thermophoretic or electrophoretic particle suspensions.

3.2 Handling kinematic constraints in large suspensions

Collaborator: Florencio Balboa Usabiaga (BCAM)
Related publication: Balboa Usabiaga & Delmotte (2022)

3.2.1 Constrained mobility problem

As explained in Section 2.3, handling nonlinear holonomic constraints in large suspensions of bodies with arbitrary shape is challenging. However, when the constraints are holonomic their time derivatives are *linear* in the velocities of the rigid bodies. Therefore the time derivative of these constraints, also called Pfiaffian form, can be written compactly as a constraint equation on the particle *velocities*

$$\dot{\boldsymbol{g}} = \boldsymbol{C}\boldsymbol{U} - \boldsymbol{B}(t) = \boldsymbol{0}, \tag{3.31}$$

where the matrix $\boldsymbol{C} = (\partial \dot{\boldsymbol{g}}/\partial \boldsymbol{U})$ is the constraints' Jacobian. Table 3.1 provides the Jacobian matrix $\boldsymbol{C}$ and $\boldsymbol{B}$ vector of the time derivative of constraints (2.20)–(2.24).

Each constraint exerts a force and torque on the rigid bodies which in the case of passive links, $\boldsymbol{C}\boldsymbol{U} = \boldsymbol{B}(t) = 0$, generate no work (Goldstein *et al.*, 2001). This condition is enough to determine the structure of the constraint generalized forces,

$$\boldsymbol{F}^C = \boldsymbol{C}^T \boldsymbol{\phi} \tag{3.32}$$

where $\boldsymbol{\phi}$ is a Lagrange multiplier homogeneous to a force (Delmotte *et al.*, 2015*a*). It is easy to verify that the generated power, $dW = \boldsymbol{U} \cdot \boldsymbol{F}^C = \boldsymbol{\phi} \cdot \boldsymbol{B}(t)$, indeed vanishes for passive constraints and that the constraint forces do not exert any net force or torque on the whole articulated body.

Adding the constraint forces, $\boldsymbol{F}^C = \boldsymbol{C}^T \boldsymbol{\phi}$, in the mobility relation (3.6), and inserting the velocity constraint (3.31) yields the linear system for the Lagrange multipliers $\boldsymbol{\phi}$ and particle

Equation $\boldsymbol{g}(\boldsymbol{x},t)$	Pfiaffian form $\dot{\boldsymbol{g}}(\boldsymbol{x},t)$ (3.31)
(2.20)	$\boldsymbol{C}_p = [\boldsymbol{I}_{3\times3} \;\; \boldsymbol{0}_{3\times3}]$ $\boldsymbol{B}(t) = \dot{\boldsymbol{q}}_0(t)$
(2.21)	$\boldsymbol{C}_p = [\boldsymbol{0}_{4\times3} \;\; \boldsymbol{\Psi}_p]$ $\boldsymbol{B}(t) = \dot{\boldsymbol{\theta}}_0(t)$
(2.22)	$\boldsymbol{C}_{pq} = [(\boldsymbol{q}_p - \boldsymbol{q}_q)^T \;\; \boldsymbol{0}_{1\times3} \;\; -(\boldsymbol{q}_p - \boldsymbol{q}_q)^T \;\; \boldsymbol{0}_{1\times3}]$ $B(t) = \dot{d}_{pq}(t)$
(2.23)	$\boldsymbol{C}_{pq} = \left[\boldsymbol{e}_p^T \;\; \left(\boldsymbol{e}_p \times (\boldsymbol{q}_p - \boldsymbol{q}_q)\right)^T \;\; -\boldsymbol{e}_p^T \;\; \boldsymbol{0}_{1\times3}\right]$ $B(t) = \dot{d}_{pq}(t)$
(2.24)	$\boldsymbol{C}_n = \left[\boldsymbol{I}_{3\times3} \;\; -\Delta\boldsymbol{l}_{np}^{\times} \;\; -\boldsymbol{I}_{3\times3} \;\; \Delta\boldsymbol{l}_{nq}^{\times}\right]$ $\boldsymbol{B}(t) = \boldsymbol{R}(\boldsymbol{\theta}_q)\dot{\Delta}\boldsymbol{l}_{nq}(t) - \boldsymbol{R}(\boldsymbol{\theta}_p)\dot{\Delta}\boldsymbol{l}_{np}(t)$

Table 3.1: Jacobian matrix $\boldsymbol{C}$ and $\boldsymbol{B}$ vector of the time derivative of constraints (2.20)–(2.24).

velocities $\boldsymbol{U}$

$$\begin{bmatrix} -\boldsymbol{N}\boldsymbol{C}^T & \boldsymbol{I} \\ \boldsymbol{0} & \boldsymbol{C} \end{bmatrix} \begin{bmatrix} \boldsymbol{\phi} \\ \boldsymbol{U} \end{bmatrix} = \begin{bmatrix} \boldsymbol{N}\boldsymbol{F} - \widetilde{\boldsymbol{N}}\boldsymbol{u}_s \\ \boldsymbol{B} \end{bmatrix}, \tag{3.33}$$

where $\boldsymbol{I}$ is a $6M \times 6M$ identity matrix. Any method to solve the Stokes problem, and therefore to apply the mobility matrix $\boldsymbol{N}$, can be used with (3.33).

In the absence of constraints, $\boldsymbol{C} = \boldsymbol{0}$, we can write the velocity of the rigid bodies as $\widehat{\boldsymbol{U}} = \boldsymbol{N}\boldsymbol{F} - \widetilde{\boldsymbol{N}}\boldsymbol{u}_s$. Then, when the bodies are constrained, the velocity can be written as

$$\begin{aligned} \boldsymbol{U} &= \widehat{\boldsymbol{U}} + \boldsymbol{N}\boldsymbol{C}^T\boldsymbol{\phi}, \\ &= \left[\boldsymbol{I} - \boldsymbol{N}\boldsymbol{C}^T\boldsymbol{G}\boldsymbol{C}\right]\widehat{\boldsymbol{U}} + \boldsymbol{N}\boldsymbol{C}^T\boldsymbol{G}\boldsymbol{B}(t), \end{aligned} \tag{3.34}$$

where $\boldsymbol{G} = \left(\boldsymbol{C}\boldsymbol{N}\boldsymbol{C}^T\right)^{-1}$ is the *constraint resistance matrix*. Both lines of (3.34) are enlightening. The first line shows that the unconstrained velocity is rectified by the flow generated by the constraint forces. It also shows that the linear system becomes a *mixed mobility-resistance problem*, as the constraint forces, $\boldsymbol{\phi}$, are unknowns of the linear system. The second line shows that for passive constraints, i.e. $\boldsymbol{B}(t) = 0$, the constrained velocity can be found by projecting $\widehat{\boldsymbol{U}}$ to the space of admissible velocities. Note that the matrix $\boldsymbol{Q} = \boldsymbol{I} - \boldsymbol{N}\boldsymbol{C}^T\boldsymbol{G}\boldsymbol{C}$ is a projection operator, i.e. $\boldsymbol{Q}^2 = \boldsymbol{Q}$.

With the rigid multiblob model presented above, the whole linear system to solve the constrained mobility problem is found by combining (3.1)-(3.3), (3.31) and (3.32)

$$\begin{bmatrix} \boldsymbol{M} & -\boldsymbol{K} & \boldsymbol{0} \\ -\boldsymbol{K}^T & \boldsymbol{0} & \boldsymbol{C}^T \\ \boldsymbol{0} & \boldsymbol{C} & \boldsymbol{0} \end{bmatrix} \begin{bmatrix} \boldsymbol{\lambda} \\ \boldsymbol{U} \\ \boldsymbol{\phi} \end{bmatrix} = \begin{bmatrix} \boldsymbol{u}_s \\ -\boldsymbol{F} \\ \boldsymbol{B} \end{bmatrix}. \tag{3.35}$$

This linear system has the same structure as the unconstrained problem (3.5), which allows to use the same preconditioned iterative solver (see Section 3.1.3). While resistance problems

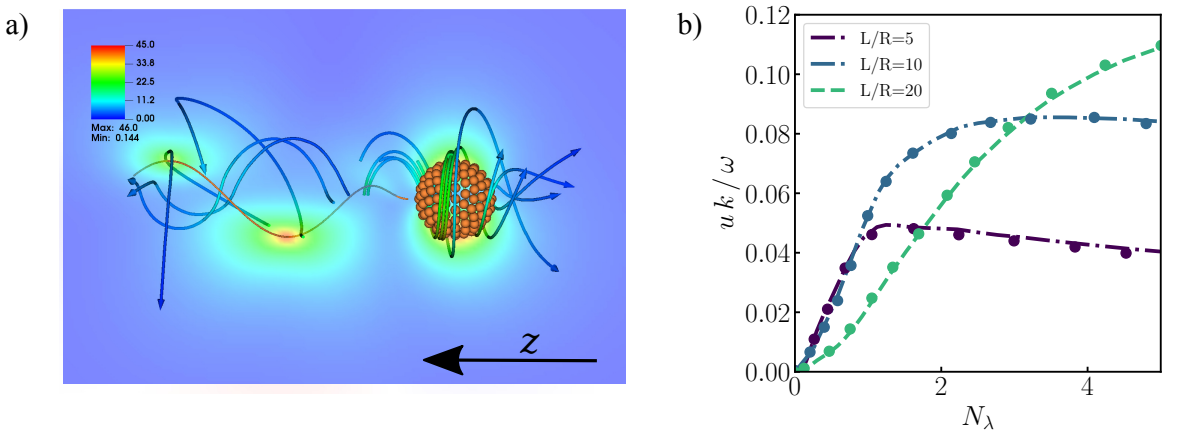

Figure 3.8: (a) Streamlines around an swimming bacterium in free space and slice of the velocity magnitude. (b) Swimming speed of the bacterium normalized by the helical wave speed ω/k, with k the wavenumber of the helical wave. Dashed line: RMB with kinematic constraints. Symbols: (Higdon, 1979*a*).

are known to scale poorly with the particle number, the iterative solver for the *mixed mobility-resistance problem* (3.33) is not sensitive to the system size, therefore allowing to study large suspensions of constrained bodies with quasilinear computational cost.

Additionally, constraint violations, e.g. due to discrete time-integration errors, are prevented by correcting the particles' positions and orientations at the end of each time-step. Our correction procedure, based on a nonlinear minimization algorithm, has negligible computational cost and preserves the accuracy of the time-integration scheme.

3.2.2 Validation example

To validate the method, we consider the motion of a swimming bacterium and compare our results with those of Higdon (Higdon, 1979*a*). More examples can be found in (Balboa Usabiaga & Delmotte, 2022). The bacterium is formed by a spherical body of radius $R = 1\,\mu$m and a single helical flagellum of length $L = 10\,\mu$m, see Fig. 3.8a. We discretize the spherical body with 162 blobs of radius $a = 0.131\,\mu$m and the flagellum with only 38 blobs. The effective thickness of the flagellum is $h \approx a$. We incorporate two ball-and-socket links (2.24) between the spherical body and the flagellum,

$$\boldsymbol{g}_n(\boldsymbol{x}) = \boldsymbol{q}_{\text{body}} + \boldsymbol{R}(\boldsymbol{\theta}_{\text{body}})\Delta\boldsymbol{l}_{n\,\text{body}} - \left[\boldsymbol{q}_{\text{flagellum}} + \boldsymbol{R}(\boldsymbol{\theta}_{\text{flagellum}})\Delta\boldsymbol{l}_{n\,\text{flagellum}}\right] = \boldsymbol{0}, \tag{3.36}$$

$$\Delta\boldsymbol{l}_{1\,\text{body}} = (0,0,R+a), \quad \Delta\boldsymbol{l}_{1\,\text{flagellum}} = (0,0,-a), \tag{3.37}$$

$$\Delta\boldsymbol{l}_{2\,\text{body}} = (0,0,2R+a), \quad \Delta\boldsymbol{l}_{2\,\text{flagellum}} = (0,0,R-a), \tag{3.38}$$

the first keeps the flagellum attached at the body surface while the second, at an arbitrary distance from the first but aligned along the same direction, fixes the axis of rotation. The flagellum is rotated by prescribing a constant angular velocity ω of the tail relative to the body.

Figure 3.8a shows the streamlines around a bacterium together with the magnitude of the velocity field. It can be observed that the flagellum and the spherical body rotate in opposite directions, as required for a torque-free swimmer. In Figure 3.8b we plot the swimming speed normalized by the wave speed, ω/k, as a function of the number of wavelengths N_λ for different normalized flagellum lengths L/R. Our results agree are in excellent agreement with those of Higdon (Higdon, 1979*a*) and show the optimal value of N_λ increases with the flagellum length L/R.

3.2.3 Large scale simulations

The versatility of our method, combined with fast methods to evaluate hydrodynamic interactions (cf. Section 3.1.3), allowed us to study a plethora of large constrained systems within a unified framework. Its robustness and scalability were used to investigate the motion of sedimenting fibers in arrays of obstacles (cf. Section 5.2), to explore the locomotion modes of a model microswimmer inspired by the diatom colony *Bacillaria Paxillifer* (cf. Chapter 6), and to simulate large suspensions of bacteria interacting near a no-slip boundary, which we show in more details below.

To demonstrate the capabilities of our method we simulate a suspension with $M = 100$ bacteria swimming above a no-slip wall. Most numerical studies on bacterial suspensions use either continuum formulations (Saintillan & Shelley, 2008; Lushi, 2016), minimal models based on regularized Stokes dipoles (Lushi *et al.*, 2014) or methods such as Lattice Boltzmann or Multiparticle Collision Dynamics that work at finite Schmidt and Reynolds numbers (Scagliarini & Pagonabarraga, 2022; Qi *et al.*, 2022). Instead, we solve the Stokes flow around the whole bacteria, each discretized with 200-blobs (body + flagellum). This is a large system with $N_b = M \times 200 = 20,000$ blobs and $61,800$ unknowns. We consider two types of boundary conditions: a semi-infinite system only bounded by the wall and a system with periodic boundary conditions (PBC) in the directions parallel to the wall. We include a short range steric repulsion between the bacteria and between the bacteria with the wall to prevent overlaps. To compute the hydrodynamic interactions between the blobs above a no-slip wall we use a Fast Multipole implementation of the wall-corrected RPY tensor, available in the library STKFMM (Yan & Shelley, 2018; Yan & Blackwell, 2020), that enables PBC along the lateral directions. In both cases the computational cost scales quasilinearly with the total number of blobs which allows to run long simulations. The angular velocity of the flagellum is set to $\omega = 100\,\mathrm{Hz}$ and the time step to $\Delta t = 0.005\,\mathrm{s}$, which corresponds to 12 steps per flagellum rotation. We simulate the system for 2500 time steps, which takes about 12h on a 28-core computer.

Figure 3.9 shows a few snapshots of the bacterial suspension. Initially, the bacteria form a square lattice and are oriented towards the wall with small perturbations in their orientations. They start swimming towards the wall but the monolayer soon becomes unstable and forms dense clusters. In the unbounded domain a single cluster is formed, while with PBC the suspension exhibits more complex patterns. Additionally, in the unbounded domain the cluster preserves the tendency of bacterium to swim in circles near walls (Maeda *et al.*, 1976) due to the torque dipole created by the opposite rotation of body and flagellum and the hydrodynamic interactions with the wall (Lauga *et al.*, 2006). With PBC the strong interactions between neighbor bacteria suppress this effect. At longer times the flow created by the bacteria destroys the monolayer:

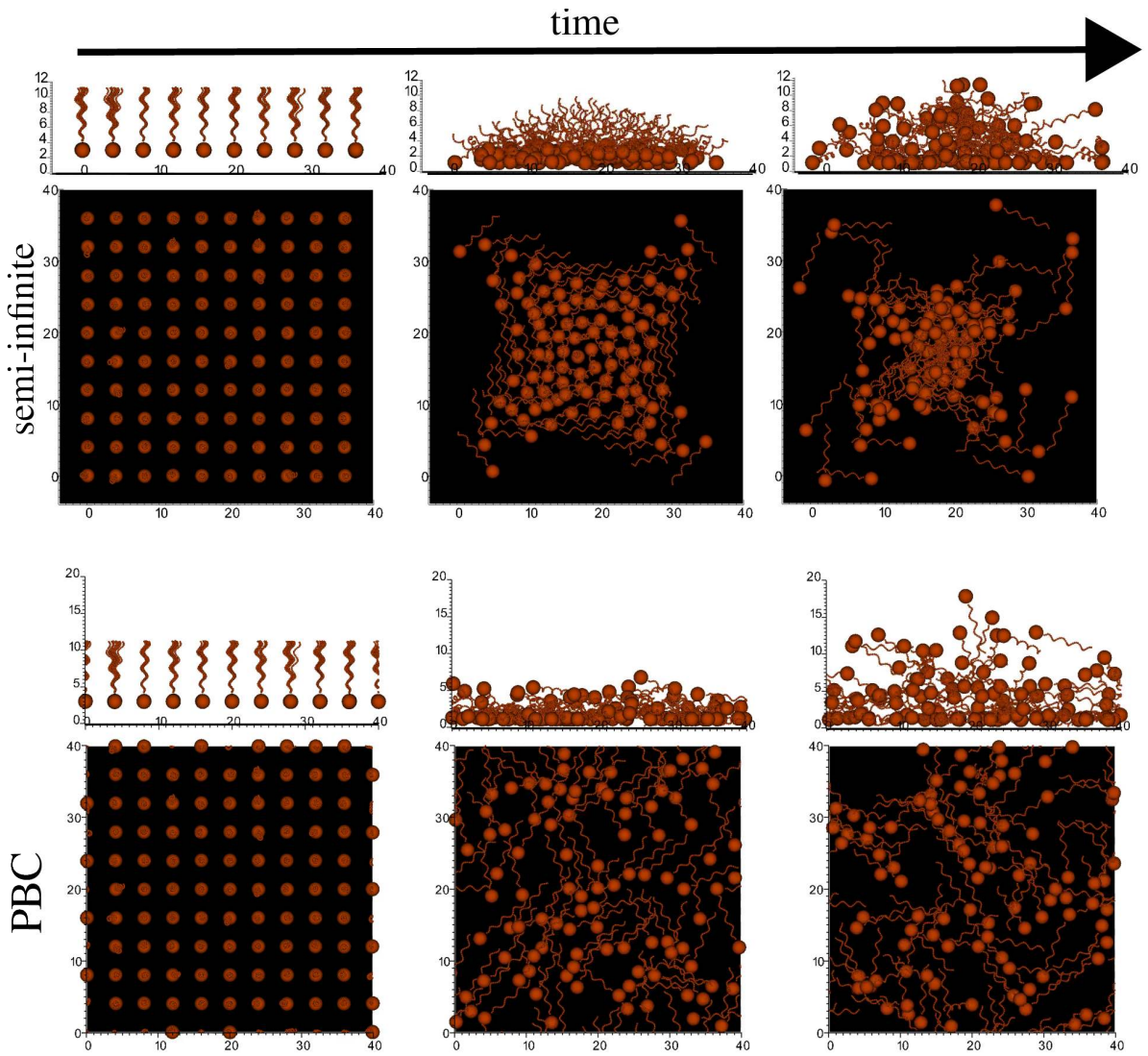

Figure 3.9: Top and lateral views of a suspension of $N = 100$ bacteria above a no-slip wall at times 0, 5 and 12 s. Top row: semi-infinite domain only bounded by the wall. Bottom row: periodic boundary conditions (PBC) in the directions parallel to the wall.

some bacteria reorient away from the wall, while others stay tilted towards it.

Our model, which includes both effects as well as the steric interactions and collisions between bacteria, opens a window to explore the stability of microswimmer suspensions beyond continuum model approximations.

Key contributions:
Our velocity formulation of the constraints between bodies enables to write the mixed resistance-mobility problem as a single linear system. This linear system is solved with a preconditioned iterative solver that couples effectively with any numerical method to compute hydrodynamic interactions between rigid bodies. Interestingly, the solver convergence is independent of the system size and constraint type, therefore allowing to simulate large suspensions in a scalable fashion. Our tool can handle different populations of constrained bodies simultaneously where both passive and time-dependent constraints are directly read from a simple input file. Thanks to its simplicity and flexibility, the user can readily use it to study physical and biological systems involving large collections of constrained bodies.

3.3 The diffusio-phoretic Force Coupling Method

Collaborator: Sebastien Michelin (LadHyX)
Student involved: Francisco Rojas-Pérez (PhD)
Related publication: Rojas-Pérez *et al.* (2021)

Most current methods to model phoretic suspensions of *spherical* particles rely on the Green's functions of the Laplace operator: either to approximate the signatures of spherical particle in the far-field, which is only valid in the very dilute limit in simple geometries, or to discretize the surface of complex particles with monopoles (3.23) and dipoles (3.24) densities, which requires handling singular integrals (see Section 3.1.5).

To overcome these limitations, we proposed a regularized mutipole framework, directly inspired by the Force Coupling Method (FCM) (cf. Section 3.1.3), to model phoretic suspensions. Our approach, called Diffusio-phoretic FCM (DFCM), relies on grid-based volume averages of the concentration field to compute the particle surface concentration moments. These moments define the chemical multipoles of the diffusion (Laplace) problem and provide the swimming forcing of the Stokes equations.

Unlike far-field models based on singularity superposition, DFCM accounts for mutually-induced dipoles. The method improves over far-field approximations for a wide range of inter-particle distances. The resulting framework can readily be implemented into efficient CFD solvers, allowing for large scale simulations of semi-dilute diffusio-phoretic suspensions in arbitrary geometries.

We used the method to characterize the collective motion of Janus colloids as a function of their surface chemical properties (mobility μ and activity α), see Fig. 3.10. Depending of the values taken by these microscopic parameters, the macroscopic response can exhibit markedly different behaviors (gas-like phase, co-existing dynamic clusters, full aggregation,...).

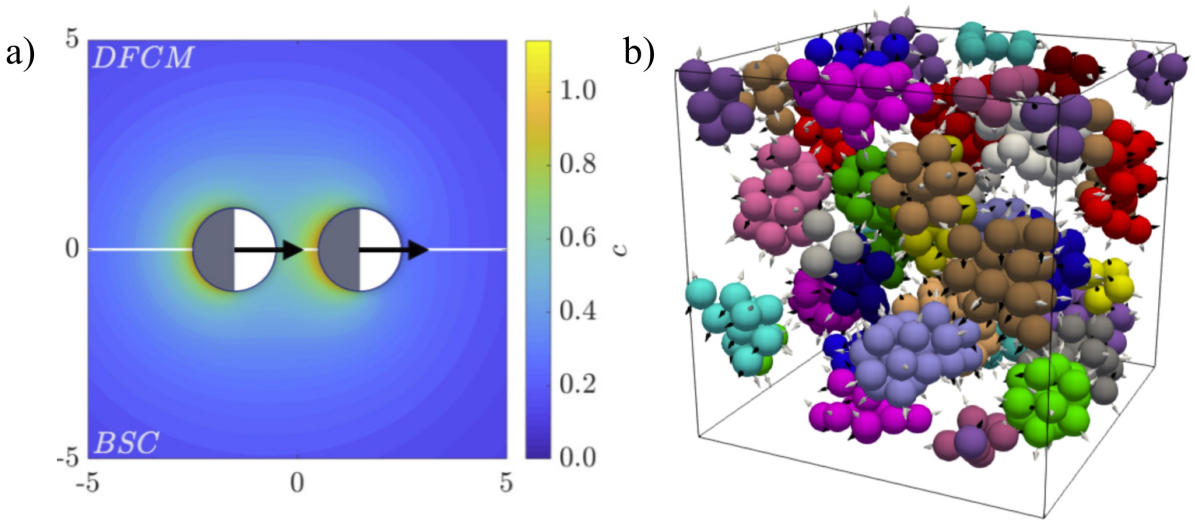

Figure 3.10: (a) Disturbance of the concentration field induced by two Janus particle. Top: DFCM solution. Bottom: exact solution obtained with bispherical cooprdinates (BSC). (b) Self-organisation of a suspension of unforced Janus phoretic particles into moving clusters.

3.4 Perspectives and ongoing work

- **Grid optimization for the Laplace problem.** The grid optimization presented in Section 3.1.4 only focuses on the hydrodynamic response of the particles. However, the optimal grid for the Stokes problem might not always be optimal for the Laplace problem. In future work we plan to optimize the grid for both problems simultaneously or to use a different grid for each problem. The idea would be to match the exact linear operators of the Laplace problem. Since only the tangential component of the surface gradient $\boldsymbol{\nabla}_{\parallel}\boldsymbol{c} = [\boldsymbol{I} - \boldsymbol{nn}]\,\boldsymbol{\nabla c} = \boldsymbol{P}_{\parallel}\boldsymbol{\nabla c}$ has an effect on the hydrochemical coupling through the slip velocity $\boldsymbol{u}_s = \mu\boldsymbol{\nabla}_{\parallel}\boldsymbol{c}$, we will only focus on the operator that relate the tangential surface gradients with the forcing terms. This operator, denoted $\boldsymbol{G}$, can be written explicitly[5] and satisfies

$$\boldsymbol{\nabla}_{\parallel}\boldsymbol{c} = \boldsymbol{G} \cdot \underbrace{\begin{bmatrix} \frac{\boldsymbol{\alpha}}{D} \\ \boldsymbol{c}_{\infty} \\ \boldsymbol{\nabla c}_{\infty} \end{bmatrix}}_{\boldsymbol{f}_{\boldsymbol{\nabla}}} \tag{3.39}$$

  where $\boldsymbol{G} = [\boldsymbol{G}_{\alpha}, \boldsymbol{G}_{\infty}\,\boldsymbol{G}_{\boldsymbol{\nabla}_{\infty}}]$ is a $3N_b \times 5N_b$ matrix that gives the tangential surface gradients induced by the forcing terms in $\boldsymbol{f}_{\boldsymbol{\nabla}}$, namely the surface fluxes and background field. Its size depends on the number of grid points.
  The goal of grid optimization is to match the action of the operator $\boldsymbol{G}_{ref}$ obtained with a reference grid, independently of a specific forcing $\boldsymbol{f}_{\boldsymbol{\nabla}}$. However, direct comparison between $\boldsymbol{G}$ and $\boldsymbol{G}_{ref}$ is impossible due to the difference in the number of nodes ($N_{b,ref} \gg N_b$).

[5] See Appendix D of (Delmotte & Usabiaga, 2024) for the full expression.

One alternative is to compare moments of $\boldsymbol{\nabla}_{\|}\boldsymbol{c}$, such as the mean:

$$\overline{\boldsymbol{\nabla}_{\|}\boldsymbol{c}} = \overline{\boldsymbol{G}} \cdot \boldsymbol{f}_{\boldsymbol{\nabla}} \tag{3.40}$$

where $\overline{\boldsymbol{G}}$ is a $3 \times 5N_b$ matrix. Using singular value decomposition of $\overline{\boldsymbol{G}}$, one can define the relative error between the three singular values of $\overline{\boldsymbol{G}}$ and $\overline{\boldsymbol{G}}_{ref}$, as in Section 3.1.4

$$E_{\overline{\boldsymbol{G}}} = \|\boldsymbol{\Sigma}^{\overline{\boldsymbol{G}}}_{ref} - \boldsymbol{\Sigma}^{\overline{\boldsymbol{G}}}\| / \|\boldsymbol{\Sigma}^{\overline{\boldsymbol{G}}}_{ref}\|. \tag{3.41}$$

The error on the mean, $E_{\overline{\boldsymbol{G}}}$, and on higher moments, could either be minimized separately to optimize the grid for the Laplace problem only, or it could be added to the cost function (3.19) to optimize the grid for the whole hydrochemical problem.

- **Smart quadratures for the rigid multiblob discretization.** While the use of the regularized Green's function (3.4) simplifies the generation of the Brownian noise, Eq. (3.8), and makes the rigid multiblob method robust, its error convergence rate is relatively slow with respect to the number of blobs ($\sim N_b^{-1/2}$). In order to evaluate the effect of the regularization in the continuous setting, i.e. prior to discretization, one may consider the flow induced by a known force density on a body's surface, $\boldsymbol{\lambda}$, with the regularized Green's function (3.4)

$$\boldsymbol{v}(\boldsymbol{x}) = \int \boldsymbol{M}(\boldsymbol{x},\boldsymbol{y})\boldsymbol{\lambda}(\boldsymbol{y})\,\mathrm{d}S_y = \int \boldsymbol{\mathcal{G}}(\boldsymbol{x},\boldsymbol{y})\boldsymbol{\lambda}(\boldsymbol{y})\,\mathrm{d}S_y + \int \Delta\boldsymbol{M}(\boldsymbol{x},\boldsymbol{y})\boldsymbol{\lambda}(\boldsymbol{y})\,\mathrm{d}S_y, \tag{3.42}$$

where $\Delta\boldsymbol{M}(\boldsymbol{x},\boldsymbol{y}) = \boldsymbol{M}(\boldsymbol{x},\boldsymbol{y}) - \boldsymbol{\mathcal{G}}(\boldsymbol{x},\boldsymbol{y})$ is the difference between the RPY mobility (3.4) and the Green's function of the Stokes equation. The first term in the right hand side is the exact flow predicted by the Stokes equation. Thus, even before the discretization step, the method introduces a regularization error in the flow. The *correction* kernel scales with the blob radius, a, as

$$\Delta\boldsymbol{M}(\boldsymbol{x},\boldsymbol{y}) \sim \begin{cases} a^2 & \text{for } |\boldsymbol{x}-\boldsymbol{y}| > 2a, \\ a & \text{for } |\boldsymbol{x}-\boldsymbol{y}| \leq 2a. \end{cases} \tag{3.43}$$

Accordingly, given that the discretization employs a number of blobs $N_b \sim 1/a^2$, the convergence rate of the error scales as $\sim N_b^{-1/2}$ for self interactions, i.e. for the self-mobility matrices of the bodies. Even though the grid optimization strategy, outlined in Section 3.1.4, allows to improve the accuracy, we are not aware of any quadrature rule that can cancel such error for arbitrary force distributions. One of the key challenges I would like to address in the future is the development of a quadrature rule that can balance the regularization error to achieve a higher convergence rate for the rigid multiblob method.

Part II

Collective effects, instabilities and transport at small scales

Chapter 4

Active transport, instabilities and self-assembly in microroller suspensions

Contents

4.1 Introduction . . . 43
4.2 From one to two: a dynamical system insight on hydrodynamically-bound states . . . 44
4.3 Density fluctuations and hydrodynamic transport by active layers . . . 46
4.4 Unstable fronts and stable motile structures: the hydrodynamic genesis of colloidal creatures . . . 49
4.4.1 Formation of a dense front . . . 50
4.4.2 Transverse fingering instability . . . 51
4.4.3 Hydrodynamic self-assembly . . . 55
4.5 Individual and collective behavior above fluid-fluid interfaces . . . 56
4.5.1 Individual motion . . . 58
4.5.2 Collective dynamics . . . 58
4.6 Hydrodynamic trapping enabled by thermal fluctuations . . . 60
4.7 Perspectives and ongoing work . . . 63

Funding: NSF grant "Magnetic microrollers as a platform for active transport" (Grant PMP-1706562). PI: Aleks Donev. Co-PIs: Michelle Driscoll and Blaise Delmotte. 2017-2020

4.1 Introduction

Collaborators: Michelle Driscoll (Northwestern University), Aleksandar Donev (Courant Institute, NYU), Paul Chaikin (Center for Soft Matter Research, NYU), Florencio Balboa Usabiaga (BCAM)

When a colloidal particle is rotated in close proximity to a wall (e.g. by a magnetic field), it exhibits a forward movement and generates advective flows that are significantly stronger than its self-induced velocity, v_0, over large distances relative to its size. This straightforward assertion regarding a single torque-driven particle has significant implications at the collective level.

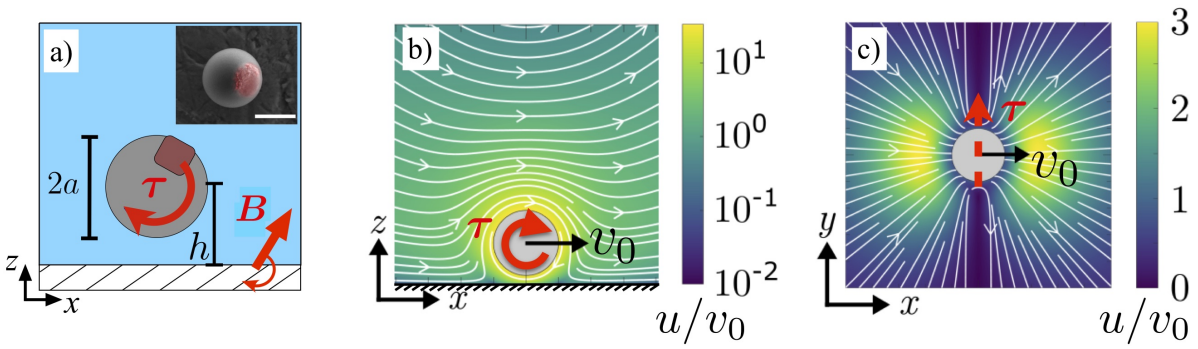

Figure 4.1: (a) SEM and schematic of the polymer colloids with an embedded magnetic cube, indicated in red (scale bar is 1 μm). A rotating magnetic field, $\boldsymbol{B}$, with angular frequency f directs particle rotation. (b)-(c), Calculated streamlines around a rotating particle ($h = 0.98$ μm) in the plane perpendicular (b) and parallel (c) to the rotation direction. Flow velocity is normalized by single particle translation velocity v_0 and its magnitude is shown by the colorbar.

When a group of these microrollers is driven, the strong hydrodynamic coupling between the particles leads to the formation of fast-moving layers, transverse instabilities and the self-assembly of stable motile structures. These phenomena are of fundamental interest to physicists and mathematicians, as well as having great potential for microfluidic and biomedical applications.

Using experiments, theory and numerical simulations, my collaborators and I have combined our efforts to elucidate the multitude of phenomena that emerge within this system, to explore their evolution in various environments and to assess their potential for flow pumping and particle transport. In lieu of a chronological account of the project, this chapter presents the phenomena observed in the system with increasing complexity.

4.2 From one to two: a dynamical system insight on hydrodynamically-bound states

Related publications: Driscoll *et al.* (2016); Delmotte (2019)

The microrollers we study are spherical rotating colloidal particles, with typical radius $a \approx 0.5 - 2\mu$m. They are confined by gravity at an average equilibrium height above a bottom wall resulting from the competition between gravity and thermal fluctuations: $h = a + k_B T/mg \approx 1 - 3.5\mu$m, where m is the excess mass of a roller.

In experiments, the microrollers are realized by applying a rotating magnetic field $\boldsymbol{B}$ (where the axis of rotation is directed along the y-axis parallel to the bottom wall) to suspended colloidal particles with a small permanent magnetic moment $\boldsymbol{m}$ (see Fig. 4.1a). The resulting torque $\boldsymbol{\tau} = \boldsymbol{m} \times \boldsymbol{B}$ drives the particle rotation about the y-axis. Inter-particle magnetic interactions are small compared to thermal energy ($< 0.1\ k_B T$) and to hydrodynamic forces (Mason number = viscous forces/magnetic forces ≈ 500). Hydrodynamics is therefore the dominant inter-particle interaction in this system, which is distinctly different from many other systems of rotating

magnetic particles, where dynamics is found to be a strong function of inter-particle magnetic interactions(Sing *et al.*, 2010; Martinez-Pedrero *et al.*, 2015; Grzybowski *et al.*, 2000; Snezhko, 2016). Finally, in contrast with experiments on Quincke rollers (Bricard *et al.*, 2013), the rotation direction is prescribed and does not arise from the system dynamics.

The asymmetric flow field created by the rotation of these microrollers leads to their propulsion: velocity gradients induced by the rotation are stronger on the bottom part of the sphere near the no-slip wall than on the top, where the velocity slowly decays to zero at infinity, which results in a translational motion parallel to the floor (see Fig. 4.1b). As shown in Fig. 4.1c, a microroller also induces transverse flows in the plane parallel to the floor. Since these particles are suspended at a finite height ($h/a \sim O(1)$), they do not roll on the chamber floor. Unlike heavier rollers which are very close to the floor ($h/a \ll 1$) (Bricard *et al.*, 2013; Karani *et al.*, 2019; Chamolly *et al.*, 2020; Demirörs *et al.*, 2021; Bozuyuk *et al.*, 2022), the velocity of the fluid at the surface of these microrollers is *orders of magnitude* higher than the self-induced velocity v_0 of the microrollers themselves (see colorbars of Fig. 4.1b-c). As a result, a microroller generates advective flows much stronger than v_0 over long distances compared with its size. Therefore we expect collective translation to dominate over self-induced translation.

However, adding a second microroller next to the other does not only enhance their translational speed, but also produces periodic orbits than can be characterized with a simple dynamical system approach.

Consider a pair of coplanar, non-Brownian, microrollers above an infinite solid wall in a fluid with viscosity η. The two particles are spherical with radius a, mass m and coordinates (x_i, y_i, z_i), $i = 1, 2$, where $y_1 = y_2$, and the no-slip boundary is located at $z = 0$. Each particle is subject to an external torque $\tau = \tau_1 = \tau_2$ along the y-axis. Using the translational invariances of the system, this simple model makes it possible to work in a three-dimensional phase space and thus to easily characterize and visualize the different trajectories and fixed points of the associated dynamical system. The corresponding, dimensionless, reduced equations of motion for the state vector $\mathbf{x} = (x_{12}, z_{12}, z_C)$ are given by

$$\dot{\mathbf{x}} = \begin{bmatrix} \dot{x}_{12} \\ \dot{z}_{12} \\ \dot{z}_C \end{bmatrix} = \boldsymbol{\mu}^{U\tau} + B^{-1}\mathbf{M}^{UF} \cdot \begin{bmatrix} \mathbf{F}_1 \\ \mathbf{F}_2 \end{bmatrix}, \tag{4.1}$$

where $x_{12} = x_1 - x_2$, $z_{12} = z_1 - z_2$ are the relative positions, and $z_C = (z_1 + z_2)/2$ is the height of the center of mass. $\boldsymbol{\mu}^{U\tau}$ is a 3×1 vector of scalar mobility functions that relate the torque applied on the particles along the y-axis, τ, to the velocity of the system in phase space $\dot{\mathbf{x}}$. $\mathbf{M}^{UF}$ is the 3×4 mobility matrix that relates the gravitational forces applied on the particles $\mathbf{F}_i$ to $\dot{\mathbf{x}}$. $\boldsymbol{\mu}^{U\tau}$ and $\mathbf{M}^{UF}$ contain the self-induced effects as well as hydrodynamic interactions between the particles above a no-slip wall. These functions have analytical expressions in the far field (Swan & Brady, 2007) and depend exclusively on the geometric parameters of the system: $\mathbf{x}$ and a.

Despite its apparent simplicity, we find that this system exhibits a wide variety of complex behaviors that are controlled by a dimensionless parameter $B = U_\tau/U_g = \tau/mga$, which com-

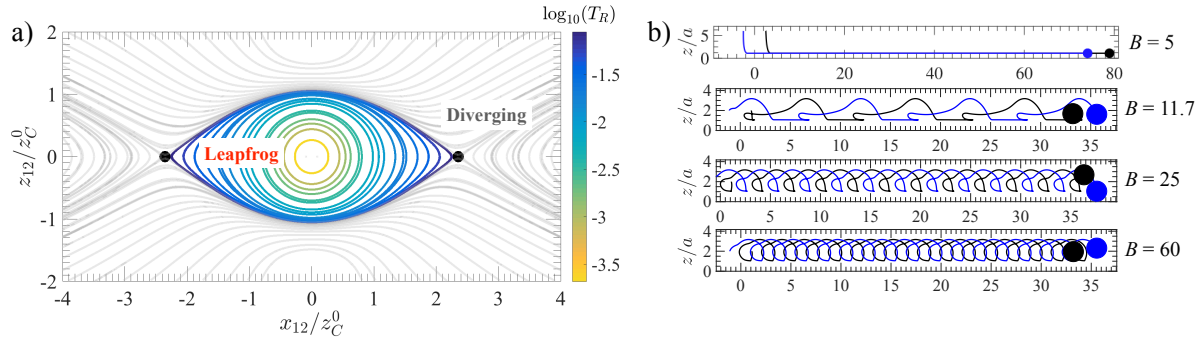

Figure 4.2: (a) Trajectories of microrollers in phase space in the limit $B = \infty$ colored by their period T_R. Grey trajectories diverge. The black circles represent the saddle points ($x_{12}^*/z_C^0 = \pm 2.357$, $z_{12}/z_C^0 = 0$, $z_C/z_C^0 = 1$), where z_C^0 is the initial height of the center of mass, that lie on the separatrix between neutrally stable leapfrog orbits and unstable states. (b) Trajectories in the (x, z)-plane for $B = 5 - 500$, where $B^* \approx 11.7$ is the critical value for the onset of leapfrog motion.

pares the flow induced by the external torque on a microroller $U_\tau \sim \tau/\eta a^2$ to its settling speed due to gravity $U_g \sim mg/\eta a$. In Fig. 4.1b, we can clearly see two regions, on the left near the roller and above to the right, where the streamlines induced by the microroller go upward and can overcome the effect of gravity on a second microroller.

In the limit $B \to \infty$, active particles can be considered as neutrally buoyant and the phase space is divided into two regions: a region with neutrally stable periodic leapfrog trajectories, and a region of diverging trajectories (see Fig. 4.2a).

For finite values of B, the system exhibits various attractors whose existence and stability depend on B. In particular, the leapfrog motion only exists above a critical value $B^* \approx 11.7$, for which active flows can overcome gravity (see Fig. 4.2b). This leapfrog motion is a unique limit cycle whose basin of attraction increases with B. Even though our hydrodynamic interactions are not fully resolved and overestimate particle mobilities, we conjecture that more resolved solutions would not affect the existence of this threshold value, but only shift B^* to a higher value.

We have also discovered the existence of an another stable state appearing at $B = 59.5$, where a particle at the rear lifts another particle up at the front. This fixed point undergoes a Hopf bifurcation at $B = 77$, where the trajectories follows a limit cycle, and then disappears at $B = 95.5$. The existence of this fixed point is also of importance since, before self-assembling into clusters, microrollers at the front are lifted up the floor by the others at the rear. This study therefore helps to better understand the transport and self-assembly mechanisms of active particles.

4.3 Density fluctuations and hydrodynamic transport by active layers

Related publications: Delmotte *et al.* (2017*b*); Driscoll *et al.* (2016); Driscoll & Delmotte (2018)

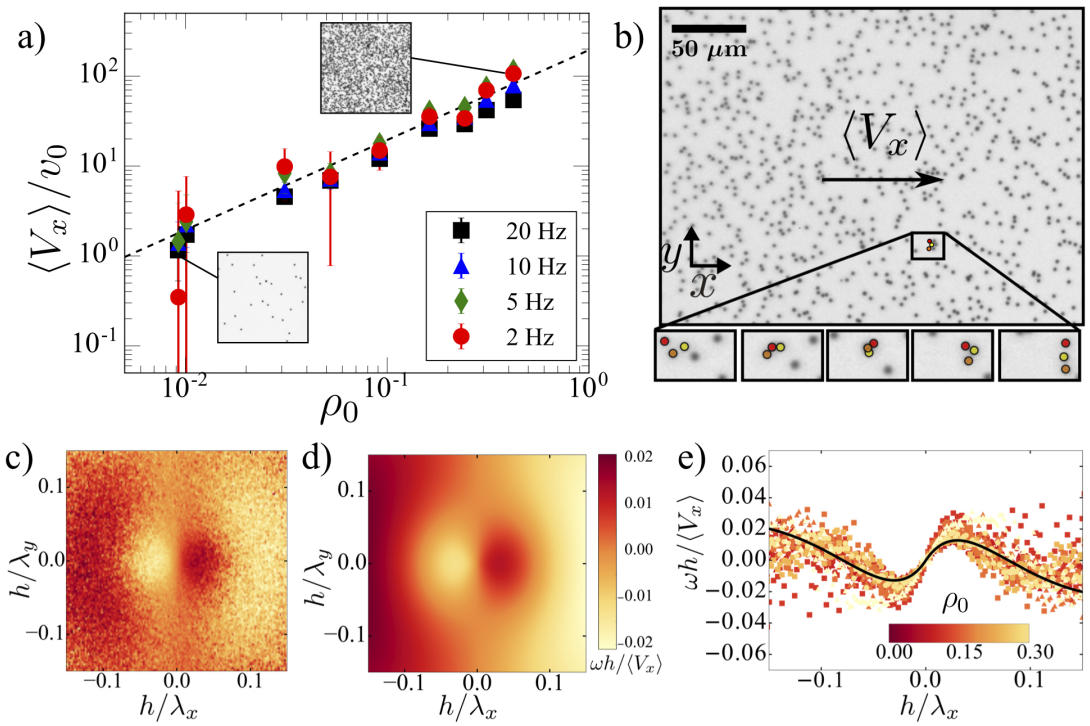

Figure 4.3: (a) Normalised particle velocity measured in experiments, $\langle V_x \rangle / v_0$, vs. area fraction, ρ_0 for various rotation frequencies f. Insets show pictures of the system at the highest and lowest ρ_0. Dashed-line: best linear fit. (b) Microroller suspension at $\rho_0 = 0.09$. The magnified inset shows the formation and breakup of an individual cluster (images 1 s apart). (c) Normalized experimental dispersion curve $\omega h/\langle V_x \rangle$ obtained for $\rho_0 = 0.25$ and $f = 10$ Hz, where the wavenumbers are normalized by $h/2\pi$. (d) Normalized theoretical dispersion curve obtained from Eq. (4.8). (e) Normalized dispersion for $k_y = 0$. Symbols indicate experimental measurements, curve is the theoretical result. Symbol color indicates density, and symbol shape indicates frequency, ■ : $f = 5$ Hz, ●: $f = 10$ Hz, ▲ : $f = 20$ Hz).

The enhanced translation and leapfrog orbits observed for particle pairs lead to strong collective flows and density fluctuations in large uniform suspensions of microrollers.

Our experimental observations and simulations showed that uniform suspensions of microrollers form active motile carpets. Both simulations, experiments and theory show that the collective speed of the suspension is very large compared to the self-induced velocity (up to $\langle V_x \rangle / v_0 \approx 100$) and increases linearly with the particle are fraction ρ_0: $\langle V_x \rangle / v_0 \sim \rho_0$ (see Fig. 4.3a). Inside these fast moving carpets, we observe particle density fluctuations: small clusters of particles form and break up continuously in a propagative fashion (Fig. 4.3b).

To better understand these density fluctuations, we introduced a minimal continuum model. This model neglects out of plane motion in the vertical $\hat{\boldsymbol{z}}$-direction. Using a mean-field approach, we considered the microroller suspension as an infinite sheet of rotlets (point-torque singularities). The rotlet density $\rho(x, y, t)$, is distributed at a fixed height $z = h$. The value of h used in the model is the gravitational height from the experiments $h = a + k_B T/mg = 1\mu m$. A point

rotlet located at $(x', y'; h)$ induces a fluid velocity $\boldsymbol{v}(x, y; h)$ given by:

$$\begin{aligned} v_x(x, y; h) &= K_x\left(x - x', y - y'; h\right) \\ &= Sh\frac{(x-x')^2}{[(x-x')^2+(y-y')^2+4h^2]^{5/2}} \end{aligned} \tag{4.2}$$

$$\begin{aligned} v_y(x, y; h) &= K_y\left(x - x', y - y'; h\right) \\ &= Sh\frac{(x-x')(y-y')}{[(x-x')^2+(y-y')^2+4h^2]^{5/2}}, \end{aligned} \tag{4.3}$$

where $S = 6\tau/(8\pi\eta)$ in m^3, $\eta = 10^{-3}$ Pa·s is the dynamic viscosity of water and K_x and K_y are the hydrodynamic interaction kernels, i.e. Green's functions, given by (Blake & Chwang, 1974). The conservation law for the rotlet density is

$$\frac{\partial \rho}{\partial t} + \nabla \cdot (\boldsymbol{u}\rho) = 0, \tag{4.4}$$

which, in the (x, y)-plane coinciding with the sheet, simplifies to

$$\frac{\partial \rho(x, y, t)}{\partial t} = -\frac{\partial\left(\rho u_y\right)}{\partial y} - \frac{\partial\left(\rho u_x\right)}{\partial x}, \tag{4.5}$$

where $u_x(x, y)$ and $u_y(x, y)$ are the local velocities due to nonlocal hydrodynamic interactions with rotlets at other positions in the sheet,

$$u_x(x, y) = K_x * \rho, \tag{4.6}$$

$$u_y(x, y) = K_y * \rho. \tag{4.7}$$

We note that u_x and u_y are finite because the kernels K_x and K_y are not singular. Linearizing (4.5) about the uniform density state and looking for plane wave solutions $\rho = \tilde{\rho}e^{i(\boldsymbol{k}\cdot\boldsymbol{x}+\omega t)}$, we obtained the following dispersion relation (in the frame moving with the mean suspension velocity $\langle V_x\rangle = \langle u_x\rangle$):

$$\omega(k_x, k_y) = k_x \langle V_x\rangle \exp(-2hk)(1 - 2hk), \tag{4.8}$$

which is purely real.

Our experimental and theoretical dispersion curves are in excellent agreement (see Fig. 4.3c-e). They exhibit a dispersive behavior: due to far-field hydrodynamics, density waves propagate freely in all directions and their speed and direction of propagation change with the wavenumber k_x and k_y.

A similar behavior had been observed in strongly-confined driven suspensions, such as droplets in Hele-Shaw cells (Desreumaux *et al.*, 2013), where the local flow field around a particle is always quasi-two-dimensional (q2D) and can be modeled as a potential dipole (Cui *et al.*, 2004; Beatus *et al.*, 2012; Brotto *et al.*, 2013). Even though the microcroller-induced flow field is quite different from the dipolar one, the spectrum we measure is qualitatively similar: ω is symmetric about the axis $k_y = 0$ and antisymmetric about the axis $k_x = 0$. Indeed, the rotlet and source dipole flows share axial symmetry about the orientation axis (here $\hat{\boldsymbol{x}}$) and they are

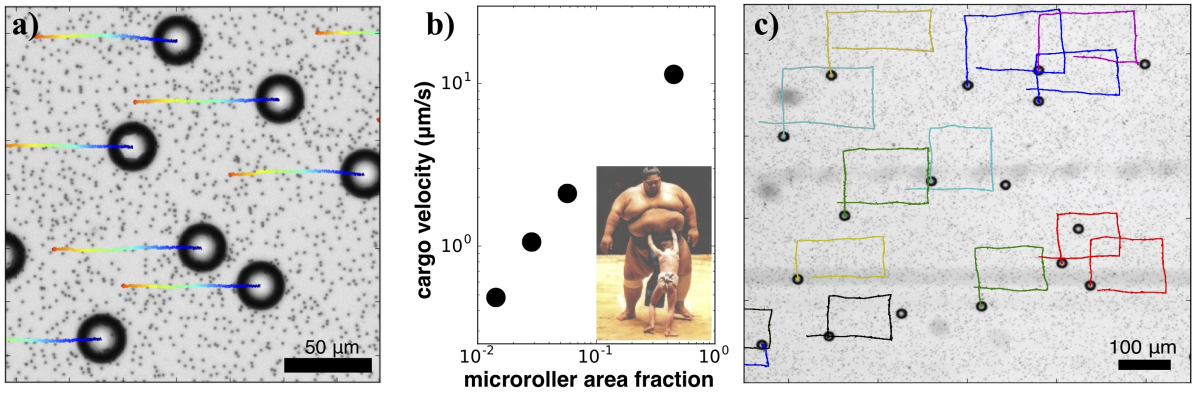

Figure 4.4: (a) Transport of large passive cargo particles (glass beads that are 20 times bigger than rollers!) by a uniform suspension. Colored lines indicate cargo particle tracks; total time is 20s. (b) Cargo velocity as a function of microroller area fraction. (c) Guided transport in a uniform suspension by varying the direction of the rotating magnetic field over time. Colored lines indicate the tracks of selected passive particles; total time 460 seconds.

both attractive at the rear and repulsive at the front of the particle, which are the essential features needed to observe this propagative dynamics. Our model and experiments therefore show that related but quite different structure formation can emerge from a fundamentally different system, with a different particle-induced flow field and a different type of confinement. This contrasts with the prediction that only dipolar hydrodynamic perturbations can generate such dynamics (Desreumaux *et al.*, 2013).

In addition to their dispersive behaviour, active carpets generate strong flows above them. By varying the direction of the magnetic field, these active layers can be used for the guided transport of large passive cargoes, such as glass beads, that are not sensitive to the magnetic field (see Fig. 4.4). The ability to transport passive particles over macroscopic distances, as well as to guide them, suggests that rollers are a promising candidate system for controlling both microscopic mixing and large scale transport for particle micromanipulation, fluid pumping and drug delivery in microfluidic and biological systems (Driscoll & Delmotte, 2018).

4.4 Unstable fronts and stable motile structures: the hydrodynamic genesis of colloidal creatures

Related publications: Driscoll *et al.* (2016); Delmotte *et al.* (2017*a*,*b*); Balboa Usabiaga *et al.* (2017)

When the suspension is not uniformly distributed it undergoes a cascade of instabilities: it evolves in the form of a very dense front that rapidly destabilizes to emit fingers whose tips can detach and form compact, self-sustained, motile structures propagating at high speeds. These colloidal creatures form a stable state of the system. Combining experiments, large scale numerical simulations and continuum models, we have explained the predominant role of hydrodynamic collective effects in the development of these colloidal creatures. Our work

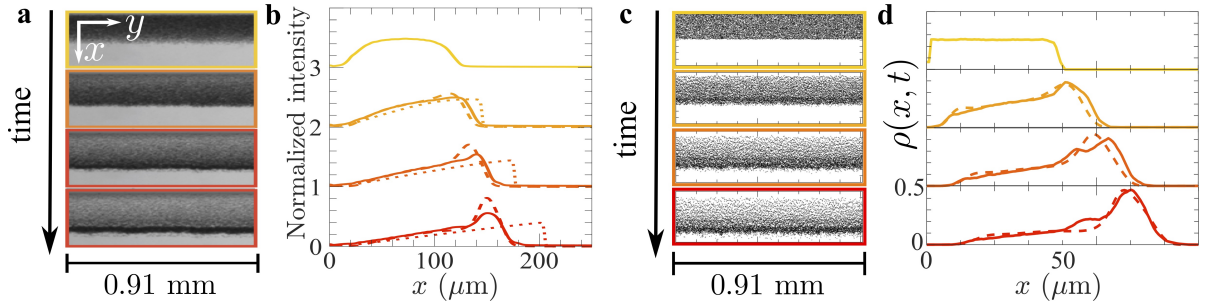

Figure 4.5: **a**, Experiment: formation of the shock front, images are 400 ms apart. **b**, Solid line: normalized experimental intensity measurements for the images in **a**. Each curve represents the mean intensity, with the mean taken in the $\hat{\boldsymbol{y}}$-direction. Dashed line: nonlocal hydrodynamic model (4.9). Dotted line: local Burgers model (4.10). The curves are vertically displaced from each other for clarity. **c**, Top view of a three dimensional Brownian Dynamics simulation, images are 640 ms apart. **d**, Solid line: density, $\rho(x,t)$, from the simulations averaged over four realizations. Dashed-line: nonlocal hydrodynamic model (4.9).

has shown that the transverse instability and the resulting self-assembly are predominantly controlled by a geometric parameter: the height of the particles in relation to the wall.

4.4.1 Formation of a dense front

In a second set of experiments, instead of a uniform distribution, we initially localize the particles in a narrow strip on one side of the chamber. After the rotating field is turned on, the particle distribution changes dramatically, organizing into a shock front, see Fig. 4.5a. Shock-like structures have been observed in other driven suspension systems (Beatus *et al.*, 2009; Champagne *et al.*, 2011; Lefauve & Saintillan, 2014; Tsang & Kanso, 2016), where density shock waves are formed due to local (Champagne *et al.*, 2011; Beatus *et al.*, 2009) or nonlocal (Lefauve & Saintillan, 2014; Tsang & Kanso, 2016) hydrodynamic interactions. However, in all of these cases, the shock evolves into a Burgers-like shape: the shock front continually steepens and a sharp discontinuity in density is observed. Here, we observe something quite different: the shock in this microroller system evolves to have a finite width. To understand the origin of this finite-width shock, we turn again to a continuum model, representing the microroller suspension as a continuum sheet of rotlets. We can assume the rotlet density to be uniform along the $\hat{\boldsymbol{y}}$-direction (see Fig. 4.5a). Thus, after integrating Eq. (4.5) over the $\hat{\boldsymbol{y}}$-direction we obtain the one-dimensional *nonlocal* conservation equation

$$\frac{\partial \rho}{\partial t} = -\frac{\partial \left[\rho \left(K * \rho\right)\right]}{\partial x}, \tag{4.9}$$

where

$$K(x-x';h) = \int_{-\infty}^{+\infty} K_x(x-x',y;\,h)dy = \frac{4Sh}{3}\frac{(x-x')^2}{\left[(x-x')^2+4h^2\right]^2}.$$

Since the kernel K is symmetric with respect to $x-x'$, the flow induced by a uniform strip of rotlets (i.e. a rectangular function) will be stronger at the center than at the edges, which

will lead to an accumulation of particles towards the leading edge. We note that, in the long wavelength limit, the *nonlocal* model (Eq. (4.9)) can be approximated by the *local* inviscid Burgers' equation:

$$\frac{\partial \rho(x,t)}{\partial t} = -\frac{\pi S}{3}\frac{\partial \rho(x,t)^2}{\partial x}. \tag{4.10}$$

The height of the sheet in the continuum model, $h = 2.62$ μm, is taken from the time-averaged particle height measured in 3D simulations. Comparisons between the numerical solution of (4.9) with experiments and large Brownian dynamics simulations shows quantitative agreement (see Fig. 4.5a-d). The nonlocal model accurately captures both the bump-like shape and the dynamics of the shock, while the Burger's approximation predicts the propagation of a discontinuity with a different speed. Overall, these results demonstrate that the width of the shock front is intrinsically selected by the nonlocal nature of the hydrodynamic interactions, and is set by the average height from the wall h[1].

4.4.2 Transverse fingering instability

Once formed, the front quickly becomes unstable in the direction transverse to propagation, leading to the appearance of density fluctuations that continue to grow as fingers (see Fig. 4.6a).

To understand the mechanisms behind this instability, we first tried to reproduce it with numerical simulations, and then gradually simplified the system by reducing its complexity and the number of physical ingredients.

In order to reproduce the instability we performed 3D numerical simulations using the numerical tools we developed for performing many-body Brownian dynamics simulations (cf. Chapter 3). As in the experiments, the gravitational height is controlled by the Brownian diffusion in the direction perpendicular to the wall. Our initial conditions are obtained by sampling the equilibrium Gibbs-Boltzmann distribution of a two-periodic suspension with a periodic cell in the $x-y$ directions using a Monte Carlo method, which is similar to the experiments where the particles reach an approximately quasi-steady equilibrium configuration in a narrow strip. The only parameter which is varied between the simulations is the gravitational height by changing the excess mass of the roller.

Our numerical simulations with more than 30 000 active colloidal rollers show that the thermal fluctuations set the characteristic height of the colloids above the wall in the initial condition. This characteristic height in turn controls the time scale and wavelength for the development of the fingering instability which is dominated by active flows (Pe$\sim O(10-10^2)$). As shown in Fig. 4.6b-c, our stochastic simulations are in quantitative agreement with the experimental measurements. The predominant wavelength in our stochastic simulations is $\lambda_{num} = 98\mu$m for $h_g = 1.5a$ and $\lambda_{num} = 140\mu$m for $h_g = 3.5a$, which is in good agreement with the fastest growing mode measured in the experiments for similar gravitational heights: $\lambda_{exp} \approx 95\mu$m and $\lambda_{exp} \approx 160\mu$m, respectively.

[1] In the case of a colloidal monolayer of particles sedimenting down an incline, where self-induced effects dominate over collective effects, we found that the Burgers approximation works remarkably well to describe the particle density profile (Sprinkle *et al.*, 2021)

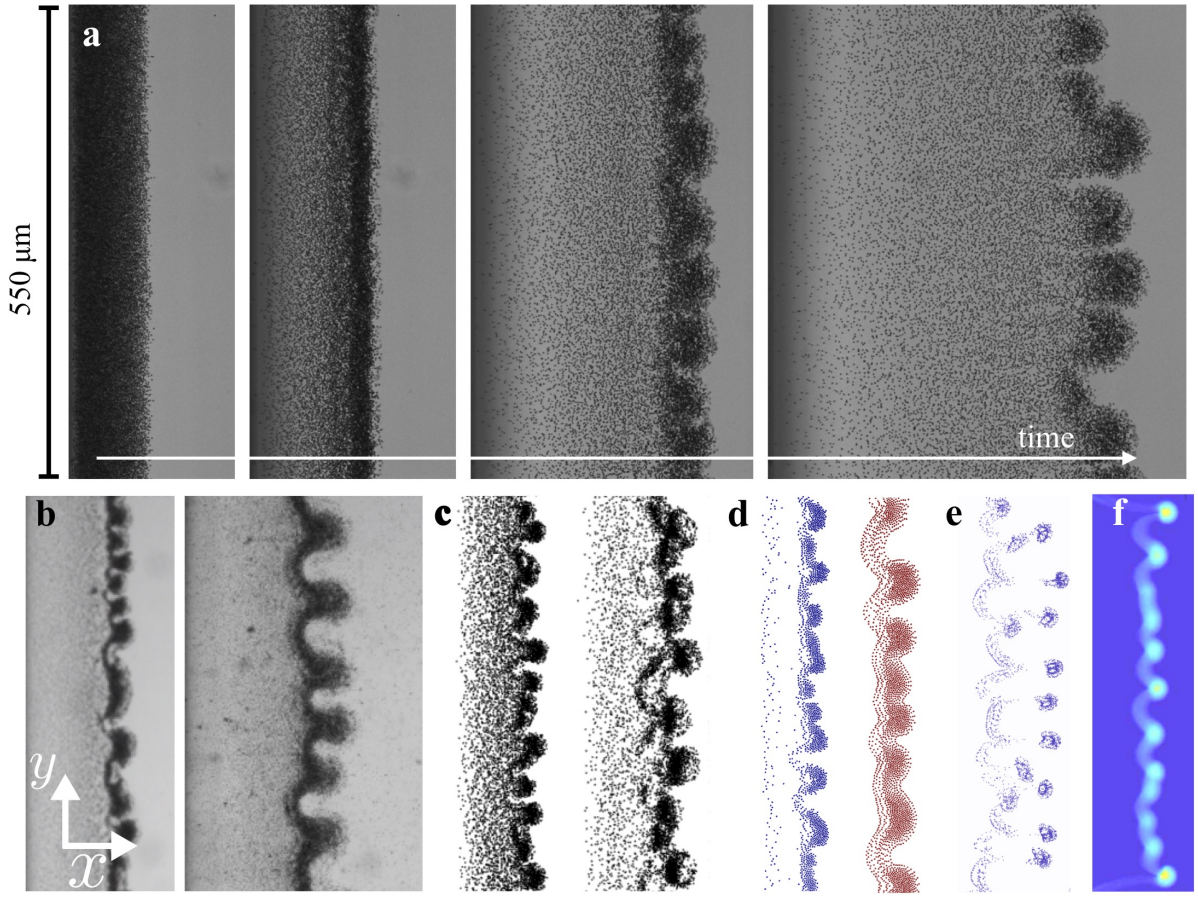

Figure 4.6: Fingering instability. **a**, Time evolution of the instability in the experiment (top view). All images are 0.55 mm tall. **b**, Experiments with two different gravitational heights: Left: $h_g = 1$ μm (left) and $h_g = 2.5$ μm (right). **c**, 3D Brownian Dynamics simulations using same parameters as in the experiments. **d**, Quasi-2D simulations without Brownian motion. Left: particle height $h = 1.97$ μm. Right: $h = 3.94$ μm. **e**, Quasi-2D simulation of discrete rotlet singularities with no steric repulsion. **f**, Quasi-2D simulations of the mean-field model (4.5).

Experiments and high-fidelity simulations show that the particle height is an important control parameter that sets the wavelength of the instability. To test the assumption, we simplify the system in our simulations by restricting the rollers to a fixed height h in a plane parallel to the wall. This simplified system reproduces the instability in the plane: the shock forms, the transverse instability develops with a wavelength set by the height (see Fig. 4.6d).

We further removed *all* non-hydrodynamic effects and simplified the system to its bare minimum by simulating instead a collection of point rotlet singularities without any steric repulsion. Again, numerical simulations show that *both* the fingering instability and clustering are reproduced with only this one ingredient: planar hydrodynamic interactions in the vicinity of a no-slip boundary (see Fig. 4.6e). These discrete simulations are corroborated with numerical simulations[2] of the mean-field model (4.5), which also show remarkable visual agreement with

[2]The nonlocal mean-field equation (4.5) is solved numerically with a third-order-space second-time finite

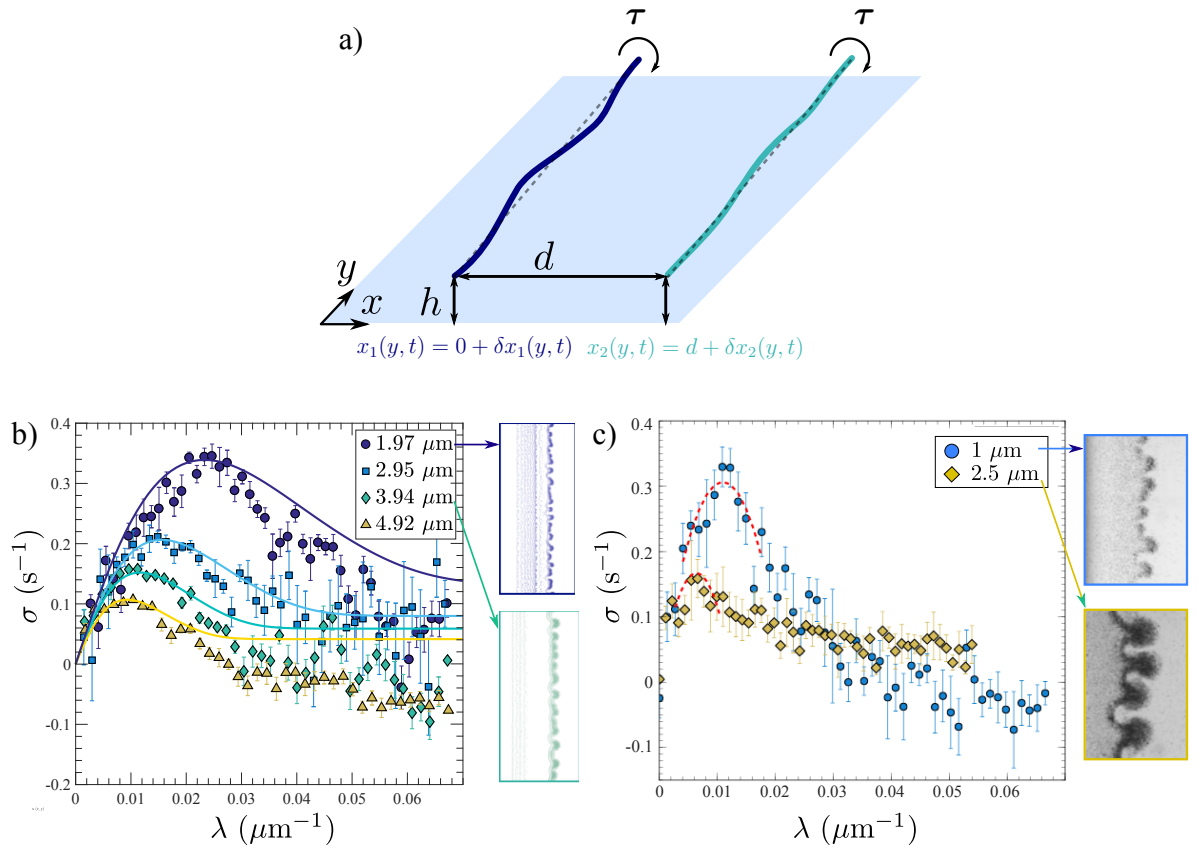

Figure 4.7: (a) Sketch of the two infinite lines. The rotlet densities are rotating with a constant torque, $\boldsymbol{\tau}$, about the y-axis and interact hydrodynamically in the xy-plane at a height h above the floor. (b) Stability diagram. Symbols: quasi-2D particle simulations for $h = 1.97-4.92$ μm. Solid lines: theoretical predictions from the two-line model for the growth rate σ_1 for $d = 9.5h$. The pictures on the right show snapshots of the fingering instability at two different heights $h = 1.97, 3.94$ μm. (c) Experimental stability diagram for gravitational heights $h_g = a + k_B T/mg = 1, 2.5$ μm. The pictures on the right show snapshots of the fingering instability.

experiments, see Fig. 4.6f.

Overall, these results show that the instability is controlled by far-field hydrodynamic interactions in the *plane parallel to the floor*, but they do not provide a clear physical picture of the instability mechanism. Nonlinear phenomena such as the shock formation do not elucidate the exact mechanisms at play behind the transverse instability of the front that forms the fingers.

In order to gain further insight, I derived a minimal model, consisting of two lines of rotlets. This model is analytically tractable while retaining the essential elements required to reproduce the instability.

Consider two infinite lines of rotlets, labeled $\mathcal{L}_1$, at the rear, and $\mathcal{L}_2$, at the front, driven

volume method optimally designed for hyperbolic scalar conservation equations (Bell *et al.*, 1988; May *et al.*, 2011), where convolution products due to hydrodynamic interactions (4.7) are evaluated with a Riemann sum on GPUs for efficiency. The code I developed is accessible on GitHub: `https://github.com/stochasticHydroTools/ConvolutionAdvection/tree/master/ConvolutionAdvectionBDS`

by a torque around the y axis at a fixed height h in a plane parallel to the fluid-fluid interface (see Fig. 4.7a). We denote $x_1(y,t)$ and $x_2(y,t)$ their position and $\rho_1(y,t) \equiv \rho(x_1(y,t),y,t)$ and $\rho_2(y,t) \equiv \rho(x_2(y,t),y,t)$ their rotlet densities. The model is governed by the equations of motion of each line together with the conservation of rotlets along their length:

$$\begin{aligned} \frac{\partial x_i(y,t)}{\partial t} &= u_x(x_i(y,t),y) \\ \frac{\partial \rho_i(y,t)}{\partial t} &= -\frac{\partial[\rho_i(y,t)u_y(x_i(y,t),y)]}{\partial y} \end{aligned} \quad , i = 1,2, \tag{4.11}$$

where length and time have been rescaled with $l_c = h$ and $t_c = 8\pi\eta l_c^3/\tau$ respectively. These four PDEs are nonlinear and nonlocal. The velocity at a given point (x_i, y) along a line $\mathcal{L}_i$ is given by the sum of the flows induced by each line,

$$u_x(x_i,y) = \sum_{j=1}^{2} \int_{-\infty}^{+\infty} K_x(x_i - x_j, y - y')\rho_j(y')\mathrm{d}y', \tag{4.12}$$

$$u_y(x_i,y) = \sum_{j=1}^{2} \int_{-\infty}^{+\infty} K_y(x_i - x_j, y - y')\rho_j(y')\mathrm{d}y'. \tag{4.13}$$

The base state of this system corresponds to two straight lines with uniform rotlet densities ($\rho_i(y,t) = \rho_0$) translating at a steady speed, so that their position are constant in the moving frame ($x_1(y,t) = 0$, $x_2(y,t) = d$), where d is the initial distance between the two lines.

We perturb the system about the base state

$$x_1(y,t) = 0 + \delta x_1(y,t) \tag{4.14}$$

$$x_2(y,t) = d + \delta x_2(y,t), \tag{4.15}$$

$$\rho_1(y,t) = \rho_0 + \delta\rho_1(y,t) \tag{4.16}$$

$$\rho_2(y,t) = \rho_0 + \delta\rho_2(y,t), \tag{4.17}$$

where $\delta x_1, \delta x_2 \ll \min(d,h)$ and $\delta\rho_1, \delta\rho_2 \ll \rho_0$.

After Taylor expanding the functionals in Eqs. (4.11)-(4.13) to obtain the linearized equations, and looking for periodic solutions of the form

$$\mathbf{u} = (\delta x_1, \delta x_2, \delta\rho_1, \delta\rho_2) = \tilde{\mathbf{u}}\, e^{iky+\sigma t},$$

where $k = 2\pi/\lambda$ is the wavenumber and

$$\tilde{\mathbf{u}} = (\delta\tilde{x}_1, \delta\tilde{x}_2, \delta\tilde{\rho}_1, \delta\tilde{\rho}_2),$$

we obtain an eigenvalue problem with four analytical solutions $\sigma_1(k), .., \sigma_4(k)$[3]. The first two eigenvalues are real and of opposite sign $\sigma_1 = -\sigma_2$. The two others are imaginary and conjugate $\sigma_3 = \bar{\sigma}_4$.

Figure 4.7b compares the growth rate $\sigma = \sigma_1(k)$ of the two line model with our quasi-2D particle simulations, where the microrollers are restricted to the xy-plane, at several heights

[3]Full expressions of the dispersion relation and its solutions are provided in (Delmotte *et al.*, 2017*a*)

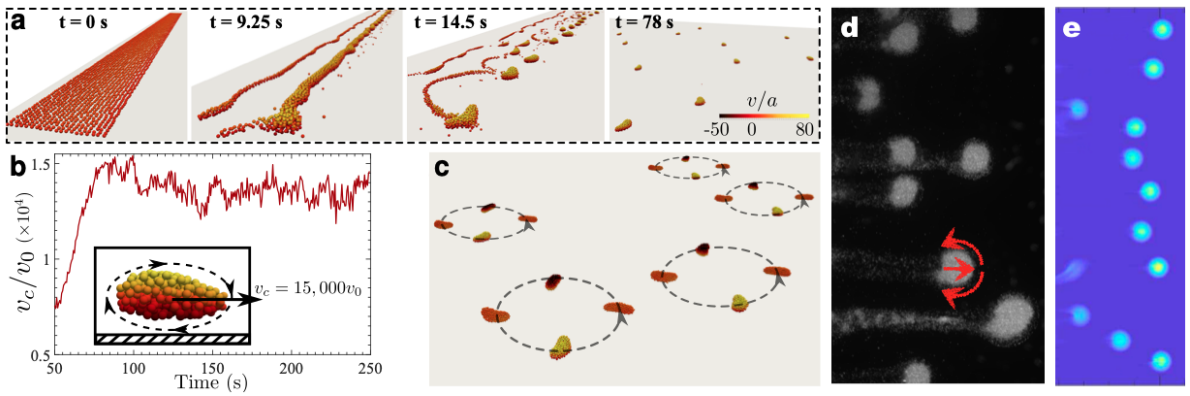

Figure 4.8: Stable motile structures. **a**, Time evolution of the instability. Color bar indicates translational velocity in radii/s and the camera position changes dynamically. $t = 0$ s: 8000 rollers are initially randomly distributed on a strip. $t = 9.25$ s: a compact front appears and starts to destabilise. $t = 14.5$ s: the fingertips start to detach from the front and form clusters. $t \geq 78$ s: the clusters reach a stable steady state in which they translate autonomously at a constant speed. **b**, Time evolution of normalised translational velocity of a cluster, v_c/v_0, where v_0 is the velocity of a roller at the same centre of mass height. Inset: side view of the cluster at $t = 78$ s, as indicated by the arrows particles rotate about the centre of mass of the critter. **c**, Circular periodic trajectory of five clusters rotating counter-clockwise in response to slowly changing the axis of rotation. The period of the trajectory is $T = 40$ s and a frame is shown every $T/4$. **d**, Emergence of stable motile clusters in experiments (top view). Red arrows indicate the recirculation of the flow field in the plane parallel to the floor. **e**, Detachment of motile clusters in quasi-2D numerical simulations of the mean-field model.

$h = 1.97 - 4.92$ μm. Two parameters must be adjusted in the two-line model to match these simulations: the distance between the two lines d to match the fastest growing wavelength $\lambda_{\max}$, and the strength S (or ρ_0) to match the magnitude of the maximum growth rate $\sigma_{\max}$. Setting $d/h = 9.5$ matches $\lambda_{\max}$ quantitatively for all the simulated heights, which shows that the instability wavelength depends linearly on h. The experimental stability diagrams in Fig. 4.7c are qualitatively similar: they have a well-defined fastest growing mode $\lambda_{\max}$ which increases with the particle height.

Thus the two-line model contains the essential physical ingredients to capture the fingering instability observed in the simulations and in the experiments. Its simplicity allows to study the physical meaning of each term in the governing equations in order to understand the mechanisms at play. A careful analysis of the terms involved in the stability analysis show that *both* the advective flow induced by one line on the other *and* self-induced transverse motion must be present to generate the fingering instability. As shown in Section 4.5, without transverse flow there is no transverse instability in the suspension.

4.4.3 Hydrodynamic self-assembly

Due to the increased density of particles in the shock region, the fingertips are much denser and, due to collective effects, move much faster than the rest of the suspension. If the particles are maintained high enough away from the wall, the fingertips break off to form self-sustained,

compact clusters made of hundreds or thousands of particles (Fig. 4.8a). These colloidal creatures rotate around their center of mass and translate with a speed 15,000 times faster than a single roller would at the same center of mass height (Fig. 4.8b). They form a natural stable state of the system: they move at a constant speed, do not lose particles (in the absence of thermal fluctuations), and are not observed to dissolve. We further explore their stability by changing the direction (but not the magnitude) of the external torque $\boldsymbol{\tau}$ periodically in time. The clusters follow the prescribed circular trajectory (Fig. 4.8c). Similar structures to the clusters were obtained experimentally when h_g was increased (by using lighter particles), although in the experiment they continually lose some particles as they move (Fig. 4.8d). In our 3D simulations, the compact clusters are extremely robust, suggesting they may be an attractor in the system dynamics – similar cluster appear regardless of the initial conditions.

As illustrated in Fig. 4.8d, the flow field in the frame moving with the center of mass of a cluster exhibits a recirculation zone whose size matches the cluster width. The closed streamlines observed in this flow field are responsible for the self-sustained and compact clusters. This is demonstrated by the numerical simulations of the 2D mean-field model (4.5) in the plane parallel to the floor (Fig. 4.8e): the detached clusters remain compact for an extended period of time due to the in-plane recirculation. As seen in studies of sedimenting particle clouds (Metzger *et al.*, 2007), the chaotic nature of the recirculating flow inside a cluster can lead to the loss of particles. However, in experiments and 3D simulations, additional circulation in the xz-plane limits particle loss (see inset of Fig. 4.8b). Clusters smaller than the width of the recirculation zone in the xy-plane, which is related to the wavelength of the fingering instability and proportional to the height above the wall, can form and remain stable, while larger ones break up by shedding excess particles. These clusters thus form solely from hydrodynamic interactions with neither the attractive nor repulsive potential interactions required for other physical/chemical systems, nor the sense/response interactions of living systems. Thanks to the strong recirculating flow they induce, these stable motile structures could also be used for mass transport and/or mixing in microfluidic environments.

4.5 Individual and collective behavior above fluid-fluid interfaces

Related publication: Delmotte (2023)

We have just shown that above a rigid wall, hydrodynamic interactions between microrollers induce a variety of collective motions such as periodic leapfrog orbits, the formation of fast moving layers, the emergence of dense fronts, and the growth of a fingering instability that releases stable motile clusters. Despite the rich and well documented dynamics observed above rigid boundaries, little is known about their collective behavior near interfaces.

We consider the motion of small torque-driven spherical particles with radius a suspended in a fluid with dynamic viscosity η_{in} above a fluid-fluid interface (Fig. 4.9a). The outer fluid on the other side of the interface has dynamic viscosity η_{out} which can vary from zero (e.g. air) to $+\infty$ (a rigid wall). We denote $\xi = \eta_{out}/\eta_{in}$ the viscosity ratio between the two fluids across the interface. Here we only consider particles with large contact angles that are not adsorbed to the

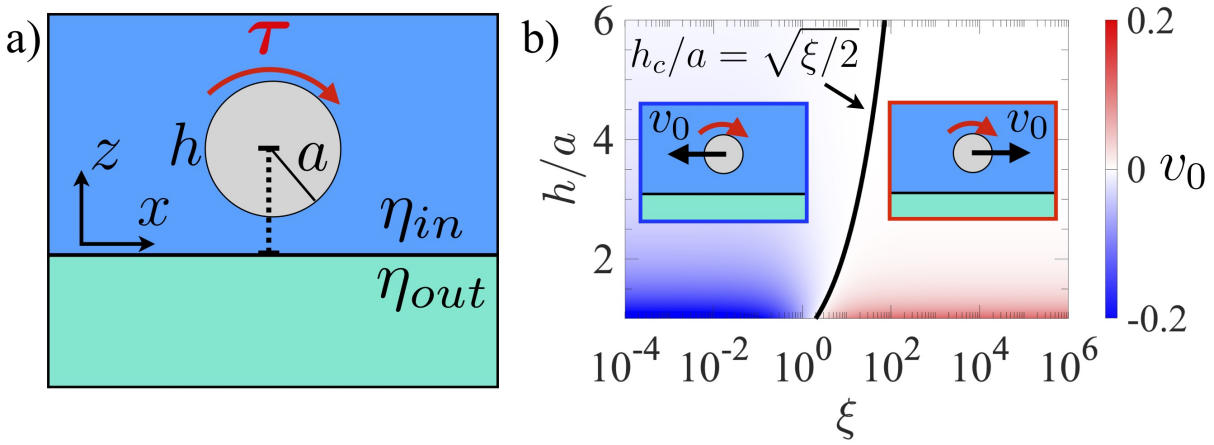

Figure 4.9: a) Schematic of a torque-driven particle above a fluid-fluid interface. b) Self-induced velocity of the particle v_0 in response to a constant torque τ as a function of $\xi = \eta_{out}/\eta_{in}$ and normalized height h/a.

surface (such as paramagnetic beads above air/water surfaces (Martinez-Pedrero *et al.*, 2015)). In typical experiments the particles are micron-sized ($a = O(1)\mu$m) and suspended in water ($\eta_{in} = 10^{-3}$Pa·s). They rotate in synchrony with an external magnetic field with frequency $f = O(10)$Hz thanks to a magnetic torque aligned with the $y-$axis denoted τ. The corresponding capillary number is $\mathrm{Ca} = \eta_{in}u/\gamma \approx 10^{-6} - 10^{-5}$, where $u = \omega a = 2\pi f a$ is the maximal fluid velocity, reached on the particle surface due to the no-slip condition, and $\gamma = O(10^{-2})$N/m is the typical surface tension between the two phases. Owing to the very small value of Ca and to the small size of the particles, the interface can be approximated as flat and nondeformable for all values of ξ (Lee *et al.*, 1979). In this limit, one can compute the flow field around the particles using the Green's function $\boldsymbol{G}$ of the Stokes equations which, by linearity, is given by (Swan & Brady, 2007):

$$\boldsymbol{G} = 1/(\xi+1)\boldsymbol{G}^{FS} + \xi/(\xi+1)\boldsymbol{G}^{W} \tag{4.18}$$

where $\boldsymbol{G}^{FS}$ is the Green's function of a domain bounded by a flat free-surface and $\boldsymbol{G}^{W}$ a domain bounded by a flat no-slip wall, both of which have known analytical expressions based on image systems (Blake & Chwang, 1974; Lee *et al.*, 1979)[4]. Using the Faxen formulae for the motion of a spherical particle in a non-uniform flow (Kim & Karrila, 1991), one obtains the far-field (RPY) pairwise mobility matrix $\boldsymbol{M}$.

By integrating the expression of $\boldsymbol{G}$ and $\boldsymbol{M}$ into to the theoretical and numerical tools developed earlier, I investigated the dynamics of microrollers near fluid-fluid interfaces. I showed how the viscosity ratio across the interface, ξ, modifies the flow around the spinning particles, with strong consequences on their individual and collective motion.

[4]Note that if the interface is not flat, e.g. near a small droplet, (4.18) involves additional terms that cannot be written as simple linear combinations of $\boldsymbol{G}^{FS}$ and $\boldsymbol{G}^{W}$ (Fuentes *et al.*, 1989).

4.5.1 Individual motion

At the individual level, ξ controls the direction and speed of a single microroller. In the far-field, the self-induced velocity of a single microroller above the interface, is given by

$$v_0(\xi, h/a) = \frac{1}{4}\left(\frac{a}{h}\right)^2\left[-\frac{1}{\xi+1} + \frac{\xi}{\xi+1}\frac{1}{2}\left(\frac{a}{h}\right)^2\right], \tag{4.19}$$

where the velocity has been normalized by $\tau/8\pi\eta a^2$. Interestingly, the sign of the velocity in (4.19) depends both on the viscosity ratio *and* the particle height (Fig. 4.9b). Below a critical value $\xi_c = 2$ the velocity is always negative, even though the applied torque is clockwise, and decays as $(a/h)^2$ for $\xi = 0$. This surprising backward motion has already been observed experimentally (Martinez-Pedrero *et al.*, 2015) and is due to the fact there is no velocity gradient at the free-surface underneath. The particle therefore experiences a stronger viscous stress on its upper side, where velocity gradients are more pronounced compared to the lower side. As a result, the particle "rolls" on the liquid above, which exerts greater resistance against rotational motion, resulting in a backward movement. When $\xi \geq \xi_c$, there is a critical height $h_c = \sqrt{\xi/2}a$ at which viscous stresses balance between both sides such that the particle rotates in place, i.e. $v_0(\xi > \xi_c, h_c) = 0$. v_0 is positive below h_c and negative above. In the limit of a no-slip wall, $\xi \to +\infty$, v_0 is always positive and decays as $(a/h)^4$. These results show that both the direction and speed of a rotating particle can be controlled with the viscosity ratio.

4.5.2 Collective dynamics

We further explore the dynamics at the collective level where large collections of particles interact. We investigate the effect of the viscosity ratio using 3D Stokesian dynamics simulations that include both hydrodynamic and steric interactions between tens of thousands of microrollers above the interface. Fig. 4.10a shows the time evolution of 10,000 microrollers initially lying on a monolayer with area fraction $\phi = 0.65$, at a given height $z_C^0/a = 1.2$, for various viscosity ratios $\xi \in \{0, 0.5, 1.5, 5, +\infty\}$. In the case of a no-slip wall, $\xi = +\infty$, the strips evolves as described in Section 4.4. The rollers inside the fingertips perform a treadmill motion that follows the clockwise rotation of the torque. A few particles are occasionally shed from the front and lifted up by flow of the rotating structures. When $\xi = 5$ the suspension behaves similarly with a slower forward motion. At a critical value $\xi \approx 1.5$, the suspension treadmills without translating, but the transverse instability still occurs in place, leading to a lateral separation of the particles. Below that threshold, the suspension self-assembles into a long roll treadmilling clockwise but moving backwards. When $\xi = 0.5$ the roll is wavy due to the transverse instability, but evolves at a significantly slower rate, and sporadically sheds particles from the rear. In the free-surface limit ($\xi = 0$), the transverse instability is suppressed and the roll remains straight and stable. It does not shed any particle because, in this regime, the streamlines of the flow induced by the microrollers are closed regardless of the separation distance.

In order to better understand the effect of ξ on the transverse instability, we use the simple two-line model described in 4.4.2. This model contains all the essential ingredients to faithfully reproduce the fingering instability above a no-slip wall and naturally extends to fluid-fluid interfaces by using the linear combination of Green's functions in (4.18). After carrying a linear

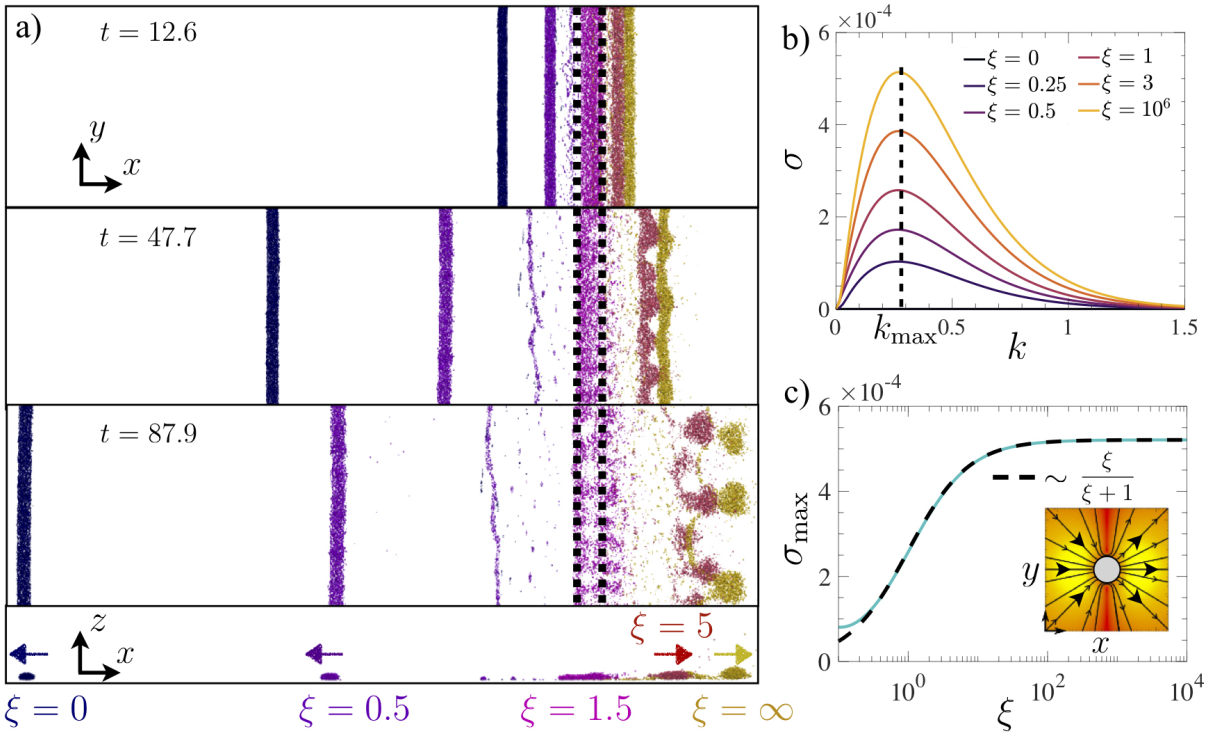

Figure 4.10: a) Time-evolution of 10,000 microrollers initially uniformly distributed in a monolayer (delimited by the black dotted lines) above the interface. Each color corresponds to a different value of $\xi \in \{0, 0.5, 1.5, 5, +\infty\}$ simulated independently. Bottom panel: side view at $t = 87.9$. Arrows: direction of motion. b) Growth rate of the two line model (4.11)–(4.13) for various ξ. Dashed line: fastest growing mode $k_{\max}$. c) Maximum growth rate (solid cyan line) as a function of ξ. Dashed black line: prefactor $\sim \xi/(\xi + 1)$ due to the transverse flows generated above a no-slip boundary (inset).

stability analysis of the system around the base state, we obtain an analytical expression for the growth rate $\sigma(k, \xi)$, plotted in Fig. 4.10b. First, we notice that an identical fastest growing mode is selected for all values of ξ, as seen by the clear bump at $\lambda_{\max} = 2\pi/k_{\max} = 23$. The corresponding growth rate, $\sigma_{\max}$, increases with ξ. The increase of $\sigma_{\max}$ is quantified in Fig. 4.10c, and shows a plateau at large ξ. A detailed analysis of the two-line model shows that the growth rate of the transverse instability is proportional to the transverse flow u_y in (4.11). Since the microrollers do not induce transverse flows above a free surface ($u_y^{FS} = 0$), $\sigma_{\max}$ scales as $\xi/(\xi + 1)$, which is the prefactor of the no-slip wall contribution $\boldsymbol{G}^W$ in (4.18) (see inset of Fig. 4.10c). Overall the two-line model highlights the crucial role of these transverse flows and exhibits a good agreement with the simulations in the sense that, for a given particle height, ξ only changes the growth rate of the instability without affecting much the dominant wavelength. However since the height of the particles is kept constant in the model, it cannot capture the slight increase of the wavelength with ξ that is observed on Fig. 4.10a.

The nature of the interface does not only affect the direction of motion of the suspension and the growth of the transverse instability, but also the shape and structure of the emerging clusters.

We study these changes from a macroscopic point of view using the mean field model (4.4) but in the xz-plane *perpendicular* to the interface. The distribution of microrollers $\rho(\boldsymbol{x},t)=\rho(x,z,t)$ in the (x,z)-plane obeys the following conservation equation

$$\frac{\partial\rho(x,z,t)}{\partial t} = -\frac{\partial\left(\rho u_x\right)}{\partial x}-\frac{\partial\left(\rho u_z\right)}{\partial z}, \tag{4.20}$$

where, as before, the velocities in the flux term arise from the long-ranged hydrodynamic interactions between microrollers in the (x,z)-plane, e.g. $u_x(\boldsymbol{x},t)=\int K_x(\boldsymbol{x}-\boldsymbol{x}')\rho(\boldsymbol{x}',t)\mathrm{d}\boldsymbol{x}'$. Above a no-slip boundary located at $z=0$, the kernel is given by (Blake & Chwang, 1974)

$$\begin{aligned} K_x(x-x',z-z') \sim & (z-z')\left(\left[(x-x')^2+(z-z')^2\right]^{-3/2}-\left[(x-x')^2+(z+z')^2\right]^{-3/2}\right) \\ & +6z(x-x')^2\left[(x-x')^2+(z+z')^2\right]^{-5/2} \end{aligned} \tag{4.21}$$

$$\begin{aligned} K_z(x-x',z-z') \sim & (x-x')\left(\left[(x-x')^2+(z+z')^2\right]^{-3/2}-\left[(x-x')^2+(z-z')^2\right]^{-3/2}\right) \\ & +6z(z+z')(x-x')\left[(x-x')^2+(z+z')^2\right]^{-5/2} \end{aligned} \tag{4.22}$$

The conservation equation (4.20) is solved numerically and the rollers are initially uniformly distributed ($\rho=\rho_0$) over a thin strip of aspect ratio $\Gamma=L/H=9.4$ near the interface. After some time, the system reaches a quasi-steady state where a main cluster emerges and translates at a steady speed. Fig. 4.11 shows a snapshot of the microroller density at the same dimensionless time in the quasi-permanent regime for various values of ξ together with the density $\rho(x_C,z)$ and velocity profiles $u_x(x_C,z)$ at the central cross-section of the cluster. The cluster is delimited by the iso-value $\rho=0.4\rho_0$ (red line).

As in the discrete particle simulations, the velocity of the cluster is fastest and backwards for $\xi=0$, vanishes around $\xi\approx 1.1$, where the cluster treadmills in place, and increases forward beyond. The shape of the cluster evolves from a near-hemisphere of aspect ratio $\Gamma=3.1$ at $\xi=0$, to a "pancake" shape ($\Gamma=8.4$) at $\xi=1.1$, and becomes circular when ξ increases further ($\Gamma=2$ and $\Gamma=1.4$ for $\xi=5$ and $\xi=+\infty$). In addition to the shape, ξ controls the particle distribution inside the cluster. The distribution is uniform at $\xi=0$ ($\rho\approx\rho_0$) and becomes more peaked as ξ increases, with a maximum $\rho_{\max}\approx 3.8\rho_0$ reached at $\xi=+\infty$. These changes in concentration, together with the boundary condition at the interface underneath, determine the velocity profile within the cluster. At $\xi=0$, the treadmilling motion is fastest near the bottom interface, where the slip condition allows for large velocities. As ξ increases, the particles concentrate at the center and the no-slip condition becomes stronger, which shifts the maximum velocity upwards and generates a rigid-body motion near the core.

4.6 Hydrodynamic trapping enabled by thermal fluctuations

Related publication: van der Wee *et al.* (2023)

All the phenomena described in the previous sections occur above smooth infinite surfaces. To realize the full potential of the system for microfluidic applications, it is necessary to develop an understanding of how their transport is modified by an environment structured by obstacles.

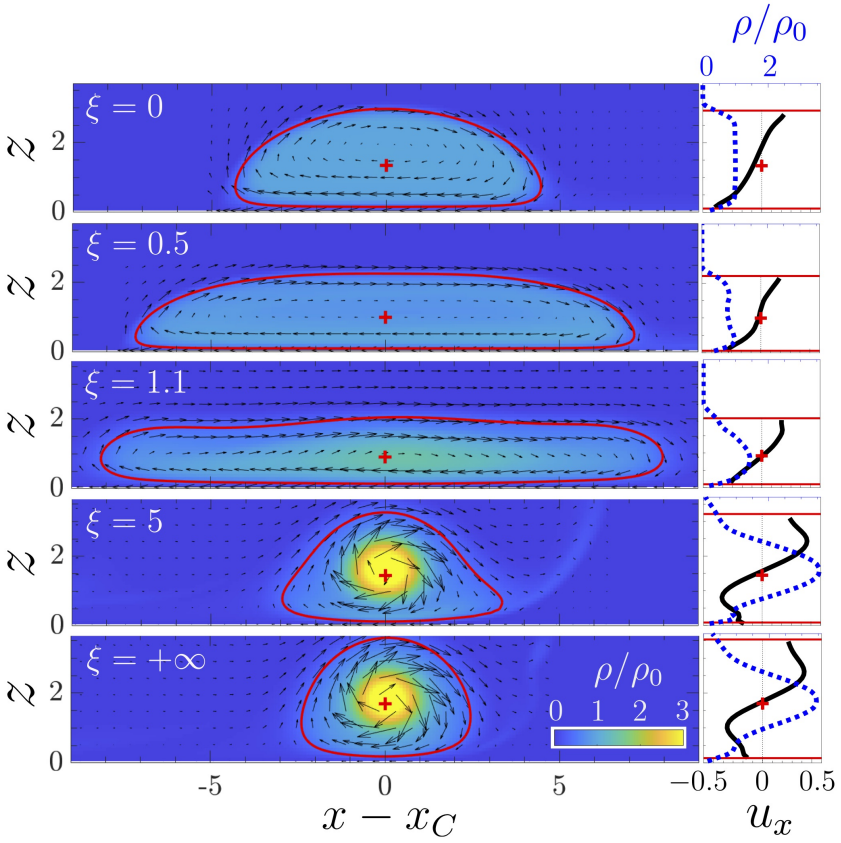

Figure 4.11: Particle density distribution $\rho(\boldsymbol{x}, t)$ obtained from the mean-field model (4.20) at $t = 1418$ (quasi-steady state) in the (x, z)-plane for various $\xi \in \{0, 0.5, 1.5, 5, +\infty\}$. Black arrows: flow field. Solid red line: $\rho/\rho_0 = 0.4$. Red cross: position of the COM (x_C, z_C). Side panels: density (dotted blue line) and velocity (solid black line) profiles at $x = x_C$.

As the interaction of a single microswimmer with obstacles is very sensitive to its flow field (Spagnolie *et al.*, 2015; Takagi *et al.*, 2014; Simmchen *et al.*, 2016; Wykes *et al.*, 2017; Hoeger & Ursell, 2021; Takaha & Nishiguchi, 2022; Ketzetzi *et al.*, 2022), we can expect the microroller to similarly exhibit unique interactions with obstacles due to its particular flow field, as well as its prescribed direction.

We combined experiments and numerical simulations to study the interaction of a microroller with a cylindrical obstacle of radius R on a rigid floor. The microroller radius is $a = 1\,\mu$m. In the simulations, the obstacle surface is discretized with blobs satisfying a zero-velocity constraint (cf. Section 3.2), the microroller surface is discretized with rigidly connected blobs (cf. Section 3.1.1), and thermal thermal fluctuations are included as explained in Section 3.1.2. Fig. 4.12a-b shows an experimental and simulated trajectory of the microroller as it gets trapped in the wake of the obstacle. In this system, we observe trapping of the microroller in the wake of the obstacle *only* in the presence of thermal fluctuations. As illustrated in the histograms of the particle position Fig. 4.12c-d, in the absence of thermal fluctuations, the microroller always passes-by the obstacle while it spends a considerable amount time in the wake if Brownian motion is taken

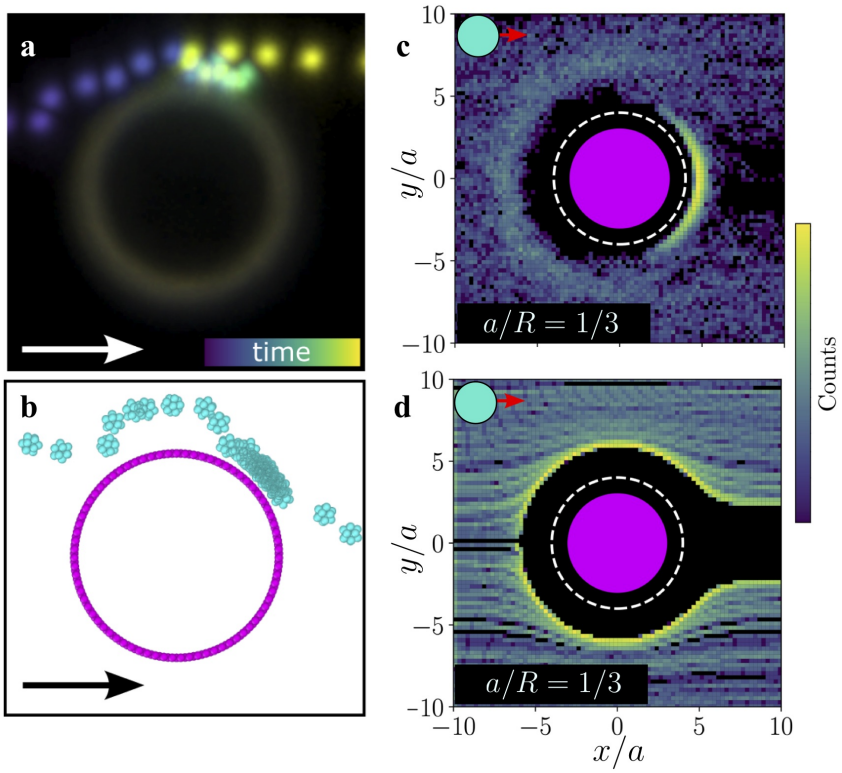

Figure 4.12: The interaction of microrollers with cylindrical obstacles in experiments and simulations. (a) Temporal projection of a fluorescence microscopy image sequence of microrollers interacting with cylindrical obstacles ($H = 20$ µm, $R = 14.4$ µm), where the microroller is trapped and eventually released. (b) Temporal projections of simulations of microrollers approaching cylindrical obstacles ($R = 10$ µm $= 10a$) where also the microrollers gets trapped and eventually released. The arrows denote the direction of propagation of the microrollers. (c)-(d) 2D histograms (log-scale) of the $[x,y]$ coordinates of a microroller interacting with a cylindrical obstacle of radius $R = 3a$ with (c) and without (d) thermal fluctuations. The solid magenta circle denotes the obstacle, the white dashed line the position of the roller at contact with the obstacle.

into accounted.

To understand the mechanism of this trapping, we characterize the velocity of the roller around the obstacle and find saddle points up- and downstream of the obstacle, which are connected by a separatrix encircling the obstacle (see Fig. 4.13a). Near the upstream saddle point the roller is repelled from the obstacle, whereas downstream the roller is drawn towards the obstacle, causing it to get trapped by an attractor (stable node), whose basin of attraction is delimited by the separatrix.

The existence of the saddle points has a purely hydrodynamic origin. At the typical height measured in simulations, the flow induced by the microroller is one to two orders of magnitude greater than the self-induced velocity v_0: on the roller surface the fluid velocity reaches $u \approx 30v_0$ and $u \approx 5v_0$ a few radii away along the x-axis (see Fig. 4.1a). As a result, when the obstacle is separated from the microroller at a given distance d_x along the x-axis, it needs to cancel strong horizontal and vertical flows on its surface in order to satisfy the no-slip condition $\boldsymbol{u} = 0$ for

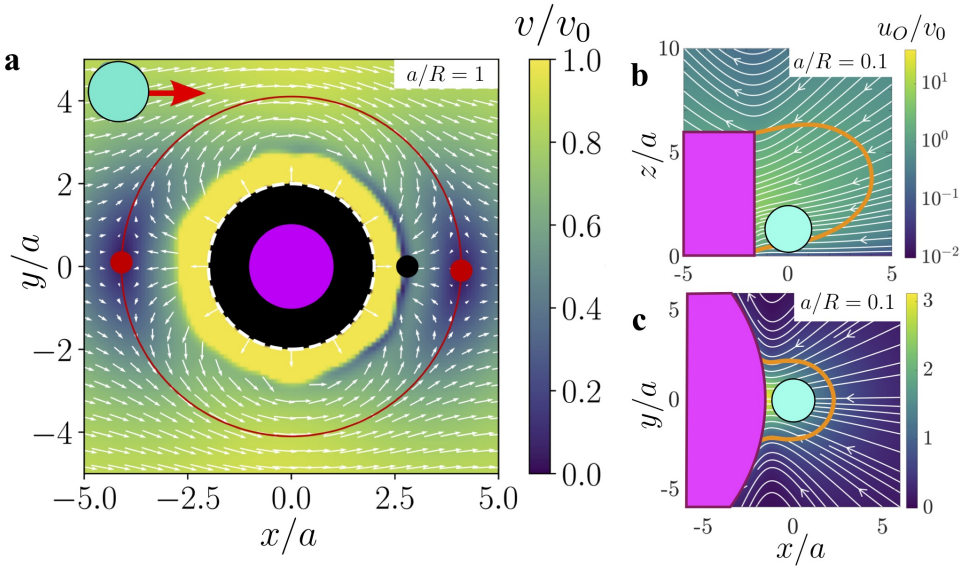

Figure 4.13: (a) The roller velocity field v normalized by the bulk velocity in the absence of obstacle v_0 with the roller velocity directions and critical points annotated. The two saddle points are annotated with ● on top of which a circle is plotted indicating the separatrix. The stable node (or attractor) is indicated by ●. In this plot with also plotted the velocity inside the zone that is dominated by the electrostatic repulsion, where we measured velocities much larger than the bulk velocity v_0. Solid magenta disk: obstacle with radius $R = a$. Black region: overlap region. (b)-(c) Fluid velocity field induced by the traction forces on the surface of the cylinder for a relative size $a/R = 0.1$ in the $x - y$ plane (b) and $x - z$ plane (c). Solid orange line: iso-contour $u_x = -v_0$, for which the fluid velocity induced by the cylinder balances the self-induced velocity of the roller v_0. If the microroller lies inside that region, it will be attracted towards the obstacle.

the fluid velocity. To do so, it exerts a surface force distribution (called traction forces) that generates a velocity field, u_O, opposite to the one induced by the microroller (see Figs. 4.13b-c). Owing to the high magnitude of the surface velocities and to their slow decay, the flow reflected by the cylinder is able to overcome the translation of the microroller at speed v_0. The large the obstacle radius, the stronger the reflected flow. This explains why the rollers are attracted to the obstacle at the rear and, by symmetry, repelled at the front. The saddle points therefore correspond to the separation distances at which the cylinder-induced velocity on the microroller exactly balances v_0. At the location of the attractor (stable node), hydrodynamic attraction is balanced by electrostatic repulsion between the obstacle and the roller.

The trapping mechanism we find is therefore quite unique: to enter the basin of attraction of the obstacle, the particle must cross the separatrix and noise, here thermal fluctuations, is the only means to do so.

4.7 Perspectives and ongoing work

- **Are the motile clusters steady traveling solutions of the microroller conservation equation ?** In the experiments and particle simulations the clusters emerging from the transverse instability seem to remain stable at very long times. My numerical sim-

ulations of the mean-field, nonlocal, conservation equation confirm this hypothesis. One of my current goals is to determine the structure of these steady traveling solutions. My preliminary mathematical analysis of (4.20)-(4.22) shows that steady-state traveling solutions, $\rho_\infty(X,Z) = \rho(x - c_x t, z - c_z t)$, where c_x and c_z are the components of the traveling velocity, must obey the following properties:

- owing to the symmetries of the hydrodynamic kernel (K_x, K_z), the steady traveling solution moves at a constant positive speed along the $x-$direction ($c_x > 0$) with no vertical motion ($c_z = 0$),
- the traveling solution is fore-aft symmetric with respect to its center of mass X_C: $\rho_\infty(X - X_C, Z) = \rho_\infty(X_C - X, Z)$,
- the flow induced by the microroller distribution in the moving frame is tangential to the iso-density lines ($\rho_\infty = cte$)

$$\boldsymbol{u}(X,Z) \cdot \boldsymbol{\nabla}\rho_\infty = 0. \tag{4.23}$$

In the future, I would like to extend this analysis to 3D and to find these steady travelling solutions using variational calculus, based on a Lagrangian involving (4.23), instead of time-advanced numerical simulations. The emergence of steady traveling solutions in nonlocal PDEs has driven significant attention and these results would be of interest to a wide community of mathematicians and theoretical physicists.

- **Experiments near interfaces or hydrophobic surfaces.** My theoretical and numerical work on the individual and collective motion of microrollers above fluid-fluid interfaces is begging for experimental validation. However, these are not easy to perform as most particles wet fluid-fluid interfaces. However, our results could be generalized to solid interfaces with a finite slip length (Lauga & Squires, 2005), which are found in many experimental systems, such as hydrophobic surfaces. Experiments with such materials should be easier to perform and could deepen our understanding of collective motion near complex interfaces.

- **Microrollers as active surfactant molecules:** In this work I considered particles lying *above* the interface, i.e. with large contact angles. In many cases the particles wet the outer fluid and get adsorbed at the interface. Adsorbed active particle layers can be used as active surfactants to modulate interfacial properties in emulsions or films, or to pump and mix flows in the surrounding fluids (Fei *et al.*, 2017, 2020). Up to now, the hydrodynamics of torque-driven particles straddling fluid-fluid interfaces is still not well-understood (Maldarelli *et al.*, 2022) and should deserve more attention given their exciting applications.

Chapter 5

Motion of fibers in structured media

Contents

5.1 Introduction 65
5.2 Sedimentation of fibers in structured media 66
5.2.1 Lateral displacement and trapping induced by a single obstacle 67
5.2.2 Settling dynamics in a structured array of pillars: towards a sorting device 73
5.3 Advection of fibers in structured microchannels 77
5.3.1 Dynamics of rigid fibers interacting with a triangular obstacle 77
5.3.2 Towards an optimized separation of flexible fibers by deterministic lateral displacement in pillar arrays 83
5.4 Perspectives and ongoing work 91

Funding: ANR grant "TransClog: Fiber Transport and Clogging in Structured Media" (ANR-20-CE30-0006). PI: Blaise Delmotte. 2021-2024.

5.1 Introduction

The transport of fibers through complex environments, such as porous and structured media, occurs in a variety of systems. Small fibers, such as micro-plastic fibers released from washing machines (up to 700000 per wash!!! (Napper & Thompson, 2016)), may propagate in soil or cause pollution of aquatic habitats and need to be filtered efficiently (Re, 2019; Engdahl, 2018). When flowed through small cracks in natural rocks, flexible fibers may buckle, leading to the eventual clogging and closure of small paths (D'Angelo *et al.*, 2010). This phenomenon is employed in petroleum engineering to prevent proppant flowback (Howard *et al.*, 1995). Similar clogging may happen in the vascular system, where biofilm streamers may form in irregular channels, detach, transport and ultimately remain attached and clog small vessels or structures such as stents (Rusconi *et al.*, 2010; Drescher *et al.*, 2013). Other industrial processes rely on the trapping of the fibers on obstacles, e.g. in papermaking where the fibers accumulate on the wires of a fabric through which a suspension is drained in order to form the paper sheet (Vakil & Green, 2011; Lundell *et al.*, 2011). Interactions with obstacles are also used in microfluidic particle sorting devices based on the so-called deterministic lateral displacement (DLD) technique, which was initially developed for rigid spherical particles (Huang *et al.*, 2004; McGrath *et al.*, 2014; Salafi *et al.*, 2019). DLD uses successive collisions with pillars in a background flow to sort particles based on their size or mechanical properties. It has been successfully extended to separate DNA

fragments (Wang *et al.*, 2015; Chen *et al.*, 2015), pathogenic bacteria (Beech *et al.*, 2018), cells (Kabacaoğlu & Biros, 2018; Loutherback *et al.*, 2012; Holm *et al.*, 2019), and blood parasites (Holm *et al.*, 2011). However, the separation or filtration of flexible fibers, such as micro-plastics, by size and/or rigidity using obstacles has not yet been reported and would be beneficial for environmental assessments or decontamination.

Understanding how elastic structures navigate in a fluid embedded with interacting obstacles is therefore essential to study the physics of biological, industrial and environmental processes. In contrast to polymers, the transport of elastic fibers in structured media has received very little attention so far (Chakrabarti *et al.*, 2020*a*), despite the broad range of potential applications that it represents. Indeed, it remains a difficult task due to the intricate couplings between fibers and obstacles that involve elastic, hydrodynamic, contact and physico-chemical forces.

The objective of the TransClog project (ANR-20-CE30-0006) is to combine numerical simulations and laboratory experiments in order to identify the important mechanisms of fiber migration and trapping, at both the individual and collective levels, in structured environments. This fundamental knowledge will then used to design efficient fiber sorting strategies.

In order to achieve these goals, two different fields driving the fiber motion are considered: gravity in a quiescent fluid and pressure-driven flows in microfluidic chips. In the following sections, I will present our results obtained in the gravity-driven case and then with pressure-driven flows.

In the gravity-driven case, the obstacles can either trap or reorient sedimenting fibers upon contact. After reorientation, a fiber drifts sideways while relaxing back to its equilibrium shape. The resulting lateral displacement is large relative to the fiber length and strongly depends on its mechanical and geometrical properties. We show how these effects can be leveraged to propose a new strategy to sort particles based on their size and/or elasticity. This approach has been patented (Makanga *et al.*, 2024*a*) and has the major advantage of being simple to implement and totally passive.

In a pressure-driven flow, richer dynamics emerges from fiber-obstacle interactions, where pole-vaulting is also observed. However, since flexible fibers deform and can barely migrate across streamlines, the shape and arrangement of obstacles must be carefully optimized to maximize lateral displacement. The resulting pillar networks can efficiently sort fibers by length and/or stiffness in microfluidic chips.

Although based on different mechanisms, both approaches can be used for fiber separation depending on the context, the scale of the system under consideration and operational constraints.

5.2 Sedimentation of fibers in structured media

Collaborators: Camille Duprat (LadHyX)
Students involved: Ursy Makanga (PhD), Mohammadreza Sepahi (Master intern)

When subjected to external forces such as gravity or centripetal acceleration, the trajectories of a fiber are strongly influenced by its flexibility and orientation relative to the direction of the force. For instance, due to its drag anisotropy, a rigid fiber settling in a quiescent fluid oriented

at an angle with the force will experience a drift as it settles down, resulting in significant lateral displacements. During the settling process, flexible fibers undergo significant deformations and reorientations, which profoundly impact their transport (Saggiorato *et al.*, 2015; Marchetti *et al.*, 2018; Cunha *et al.*, 2022). The equilibrium shape of a fiber subject to gravity in a viscous fluid results from the balance between viscous and internal elastic stresses, which is quantified by the so-called elasto-gravitational number

$$Be = F^G L^2/EI = WL^3/EI, \tag{5.1}$$

where $F^G = WL$ is the gravity force, W the weight per unit length of the fiber, E its Young's modulus and $I = \pi a^4/4$ its second moment of inertia. In the rigid case, $Be \ll 1$, the fiber keeps its initial shape, while in the flexible regime, $Be \gg 1$, it bends due to its own hydrodynamic disturbances. The fiber will thus adopt a more or less pronounced "U" shape, depending on Be, oriented perpendicularly with the direction of gravity, independently of its initial configuration Indeed, a flexible fiber bends due to its own hydrodynamic disturbances, which leads to a torque that reorients the fiber perpendicularly to gravity, thus reducing its lateral drift compared to the rigid case (Xu & Nadim, 1994; Li *et al.*, 2013). As we explain below, the presence of an obstacle will modify the deformation and orientation of the fiber, thereby influencing its trajectory and lateral displacement.

5.2.1 Lateral displacement and trapping induced by a single obstacle

Related publication: Makanga *et al.* (2023)

By means of numerical simulations, experiments and analytical predictions, we investigate the dynamics of flexible fibers settling in a viscous fluid embedded with obstacles of arbitrary shapes. First we consider the prototypical case of a single flexible fiber settling in a quiescent fluid embedded with a fixed obstacle with various cross-sections.

5.2.1.1 Setup and methods

In experiments, homemade elastic fibers, with controlled geometrical and mechanical properties, are released in a large tank which has a rectangular cross-section ($L_1 = 60$ cm, $L_2 = 40$ cm) and height $H = 80$ cm, filled with silicone oil ($\rho = 970$ kg/m^3, $\eta = 0.97$ Pa.s). A 3D-printed obstacle of width 1 cm and spanning the entire depth of the tank is held against the walls in the center of the tank. Fibers are initially held in the upper part of the tank by tweezers in a shape close to their equilibrium configuration (see Fig. 5.1a). It ensures that equilibrium is reach before interacting with the obstacles. Fibers are released by slightly opening the tweezers simultaneously to avoid large flow disturbances. Typically, the fiber settling velocity is 0.5 mm/s, corresponding to Reynolds numbers $Re \sim 10^{-2}$.

In the simulations, the fiber is discretized with M_F blobs along its centerline that are linked together by elastic forces to account for the internal tension and bending forces (see Fig. 5.1b). Twisting of the fiber is neglected. The discretized stretching free energy of a fiber made of M_F

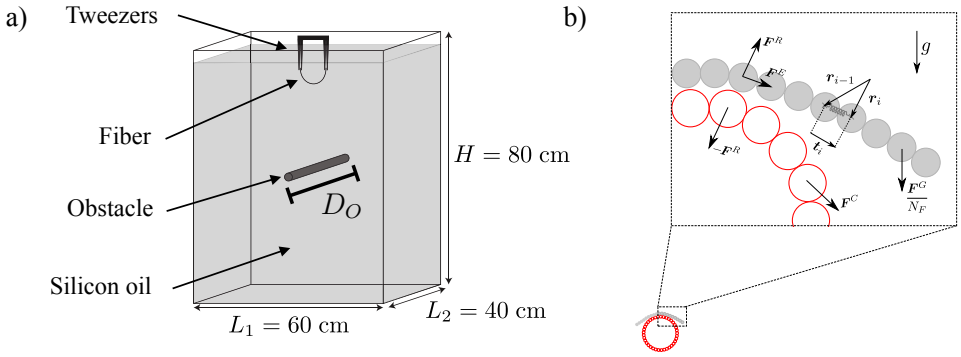

Figure 5.1: (a) Experimental setup. (b) Sketch of the numerical model, showing the discretized fiber (gray), an obstacle slice (red) and the various non-hydrodynamic forces at play.

blobs is given by (Marchetti *et al.*, 2018)

$$H^S = \frac{S}{4a} \sum_{i=2}^{M_F} \left(|\boldsymbol{t}_i| - 2a \right)^2 , \tag{5.2}$$

where the tangential vector is defined as $\boldsymbol{t}_i = \boldsymbol{r}_i - \boldsymbol{r}_{i-1}$, $S = \pi E a^2$ is the stretching modulus with E being the Young's modulus. On the other hand, the bending free energy in its discretized form is given by (Marchetti *et al.*, 2018)

$$H^B = \frac{B}{2a} \sum_{i=2}^{M_F - 1} \left(1 - \hat{\boldsymbol{t}}_{i+1} \cdot \hat{\boldsymbol{t}}_i \right) . \tag{5.3}$$

where $B = EI = \pi E a^4/4$ is the bending modulus, and $\hat{\boldsymbol{t}}_i$ the unit tangential vector, $\hat{\boldsymbol{t}}_i = \boldsymbol{t}_i / |\boldsymbol{t}_i|$. The total elastic potential $H = H^S + H^B$ is the sum of the stretching and bending free energies. The internal elastic forces are obtained by taking the gradient of H with respect to the blob positions:

$$\boldsymbol{F}^E = -\nabla_{\boldsymbol{r}} H.$$

In addition to internal elastic forces, the fibers experience a uniform gravitational force $\boldsymbol{F}^G = -m\boldsymbol{g}$ as well as a contact force with the obstacle surface $\boldsymbol{F}^R$, here modeled as a repulsive force between the fiber blobs and the obstacle blobs. Due to the roughness of the obstacle surface that is made of blobs, this force has a component normal to the fiber centerline F_n^R and a tangential component F_τ^R that acts as an effective friction force: $\boldsymbol{F}^R = F_\tau^R \hat{\boldsymbol{t}} + F_n^R \hat{\boldsymbol{n}}$.

The obstacle surface is discretized with M_O blobs that are constrained to remain fixed, i.e. with a zero-velocity constraint: $\boldsymbol{C}\boldsymbol{U} = \boldsymbol{0}$, where $\boldsymbol{C} = [\boldsymbol{0}_{3M_O \times 3M_F} \ \boldsymbol{I}_{3M_O \times 3M_O}]$ is a block matrix which selects the obstacle blobs to which the kinematic conditions apply (cf. Section 3.2).

Thanks to the generic and versatile framework of the constrained RMB (cf. Section 3.2), the fiber and obstacle blobs are treated identically in the linear system (3.33). Hydrodynamic interactions between all the blobs of the system are accounted for with the RPY mobility tensor in an unbounded domain.

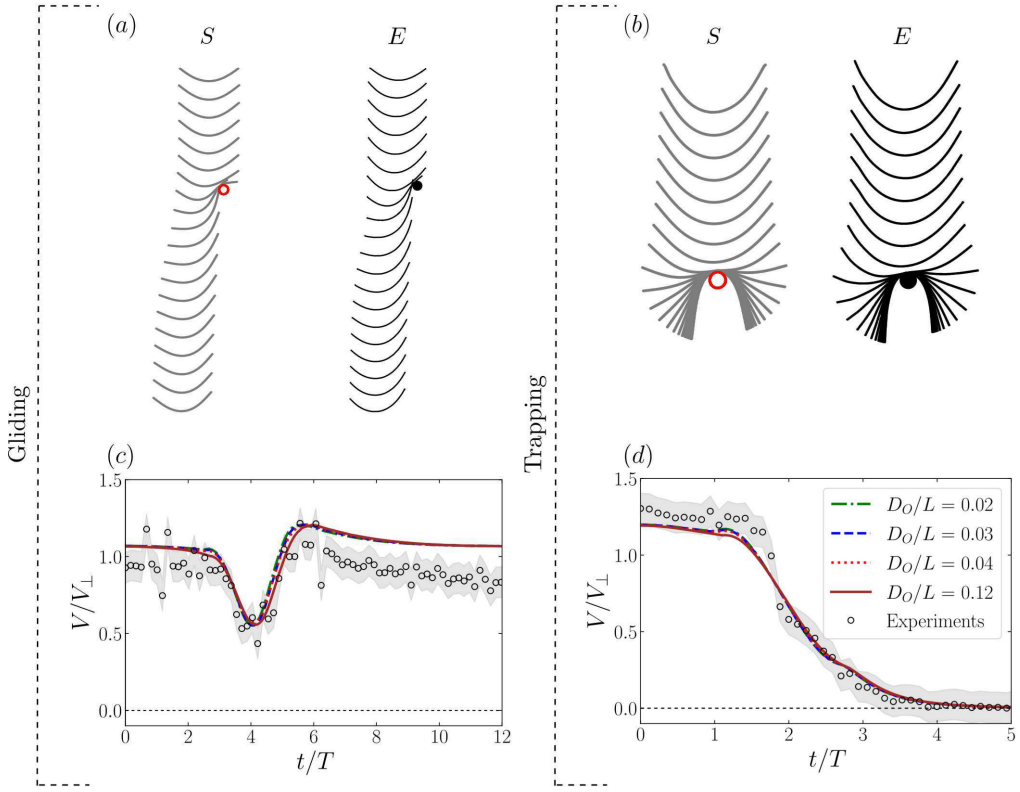

Figure 5.2: $(a-b)$ Numerical (S) and experimental (E) chronophotographies of a flexible fiber ($Be \approx 200$) settling against an obstacle in a viscous fluid. $(c-d)$ Evolution of the total velocity of the center of mass of the fiber as function of dimensionless time in experiments (circles with grey shaded error bars) and numerical simulations (lines) for various depths of the obstacle.

5.2.1.2 Validation

In the sedimentation process, the presence of the obstacle leads to two main outcomes that depend on the mechanical and geometrical properties of the system: the fiber can either glide along the obstacle and then drift sideways while relaxing to its equilibrium shape (see Fig. 5.2(a)) or remain trapped around it (see Fig. 5.2(b)). These events results from the complex interplay between internal elastic stresses, contact forces and hydrodynamic interactions with the embedded rigid obstacle.

Fig. 5.2 shows numerical and experimental realizations of the gliding and trapping events for a semi-flexible fiber ($Be \approx 200$) settling against an obstacle (the complete set of parameters is provided in the Appendix of (Makanga *et al.*, 2023)). In the simulations, the initial position of the fiber centerline and its mechanical properties are directly extracted from the experiments.

As shown by the chronophotographies in panels $(a)-(b)$, the simulations agree qualitatively well with experiments for both events. In addition, the time evolution of the settling speed, reported in panels $(c)-(d)$, shows excellent quantitative agreement, thus confirming the adequacy of our method to capture fiber-obstacle interactions in a viscous fluid.

5.2.1.3 Analysis of the trapping states

In the absence of surface roughness, steric forces with the obstacle are exclusively directed along the normal of the fiber centerline. In this regime, trapping is only possible for symmetric configurations where the gravity forces balance on both sides of the fiber. However, surface asperities appear both in experiments and simulations: even though the elastic fibers are smooth, the 3D-printer has a finite resolution and defects might occur, while the simulated obstacles and fibers have a roughness $\delta/a \approx 0.1$ (see (Makanga *et al.*, 2023)). Surface roughness generates friction directed along the fiber centerline. These tangential forces can balance asymmetric gravity forces and thus prevent the fiber from slipping away from the obstacle. The trapping probability and trapping configurations are obviously highly sensitive to the details of the surface roughness. However, we did not try to match the experimental roughness in the simulations. The focus was, for a given roughness value, to understand the mechanisms that lead to the observed trapping states.

In order to investigate the trapping state, we systematically varied the obstacle shape, fiber deformability Be and initial position to generate a PDF of the trapping modes on the pillars shown in Fig. 5.3a.

In the stiff limit ($Be = 10$), fibers barely deform and cannot conform to the obstacle shape. The trapping configurations are determined by the equilibrium between the tilt induced by the lever arm due to gravity and the friction forces at the contact points with the obstacle. Consequently, the trapping probability of the fiber decreases as the tip of the obstacle narrows, and is highest for the widest contact region (i.e. for the downward-pointing triangle in panel (a)). This competition between lever arm and friction at the tips of the obstacle gives rise to strongly asymmetric trapping states for upward-pointing triangles (panel (e)).

In the highly flexible regime, $Be = 1000$, the fiber conforms to the obstacle shape and its freely hanging extremities are aligned with the gravitational field. Such alignment with gravity induces a tangential load along the fiber centerline, which competes with friction in the high curvature regions of the obstacle. As a result, the fiber is mostly trapped by obstacles with high curvatures (panels (a) and (e)), and easily slips away from smooth obstacles (panels (b-d)).

To further quantify the main differences between the stiff and flexible limits, we measure the total tangential (i.e. frictional) component of the resultant steric force, F_τ^R, acting on the fiber against an upward-pointing triangle as a function of the relative length ξ (see Fig. 5.3c). First we notice that, regardless of the rigidity, the friction force is small for short relative lengths ($\xi \leq 1$) because the fiber rests on the base of the triangle. When $\xi > 1$, the rigidity makes a big difference since the contact with the obstacle becomes more and more localized along the fiber. In the rigid case ($Be = 10$), the tilt induced by the lever arm effect increases with ξ, and so does the friction force to counterbalance the resulting tangential motion. In the flexible regime ($Be = 1000$), as soon as the fiber extremities stick out of the obstacle ($\xi > 1$), they align with gravity and generate a strong tangential load (i.e. a pulley effect). As a result the friction force jumps suddenly, by a factor 24, between $\xi = 1$ and $\xi = 2$ and is at least twice larger than the friction on the rigid fiber. This is illustrated for $\xi = 2$ in the close-up views of Fig. 5.3d, where

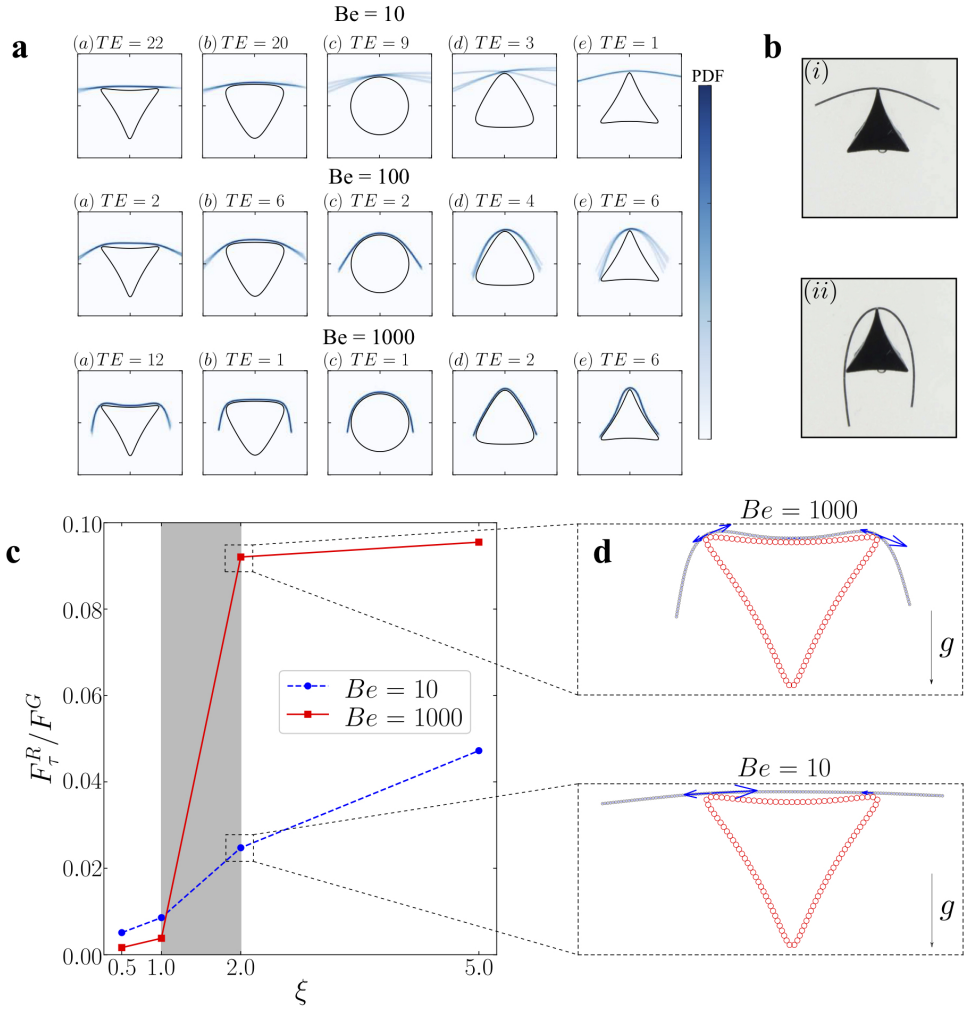

Figure 5.3: **a.** Probability distribution of the trapping configurations of the fiber around the obstacle, for $\xi = 2$, various shapes and values of Be. TE is the percentage of trapping events. **b.** Asymmetric trapping events observed in experiments. **c.** Evolution of the tangential component (frictional force) of the contact force scaled by the gravitational force as a function of ξ for a stiff and flexible fiber $Be = 10 - 1000$ on an upward-pointing triangle. The close-up views in **d.** show the corresponding distributions of the tangential component of the steric force along the fiber centerline (blue arrows).

the larger compliance of the flexible fiber leads to an extra frictional contact near the right edge of the triangle compared to the rigid one. For longer flexible fibers ($\xi = 5$), the curvature near the edges of the obstacle saturates and so does the friction force.

In the semi-flexible regime ($Be = 100$), shown in Fig. 5.3a, the fiber is flexible enough to promotes alignment of the extremities with gravity but cannot conform to obstacles with high curvatures. Consequently, the trapping probability is more evenly distributed among the various obstacle shapes.

As shown in Fig. 5.3b, some of the exotic, asymmetric, trapping states observed in numerical simulations with non-circular obstacles have also been reported in experiments. This good agreement with experiments suggests that the effective friction coefficient in our simulations is at least equal or larger than the experimental one. Finally, for the range of parameters considered, our analysis shows that trapping is overall minimized with smooth circular obstacles. These findings will be used in the design of fiber sorting devices where trapping or long residence times are undesired.

5.2.1.4 Obstacle-induced lateral displacement

The gliding motion along the obstacle induces a tilt of the fiber centerline with respect to gravity, measured at the midpoint, denoted $\theta(t)$ (see Fig. 5.4(a)). Here, the origin of time ($t = 0$) is taken when the fiber leaves the obstacle, i.e. when there is no contact anymore. This tilt induces a lateral drift as the fiber reorients back to its horizontal equilibrium shape. We define this lateral shift, δx, as the lateral displacement of the fiber center of mass between a given starting time, here $t = 0$, and the final equilibrium state.

In the elongated limit ($\varepsilon = 2a/L \ll 1$), the velocity and lateral displacement of weakly flexible fibers ($Be \ll 1$) with initial orientation $\theta(0)$ has been computed analytically by Li *et al.* (Li *et al.*, 2013) using slender body theory (Keller & Rubinow, 1976; Johnson, 1980; Tornberg & Shelley, 2004). Their approach is based on a multiple-scale analysis (Hinch, 1991; Bender & Orszag, 1999) where they identify two relevant independent timescales in the fiber dynamics: the time for the fiber to settle its length L, of order $\mathcal{O}(1)$, and the time to reorient toward its equilibrium configuration, which is much slower and of order $\mathcal{O}(Be^{-1})$. In the case of a fiber with uniform thickness, mass and bending stiffness, they found an analytical expression for the lateral shift given by:

$$\frac{\delta x}{L} = \frac{c_0}{2CBe}\beta_0, \tag{5.4}$$

where

$$\beta_0 = \frac{\pi}{2} - \theta(0), \tag{5.5}$$

$$C = \frac{7}{400} + c_0^{-1}\left(\frac{1813 - 300\pi^2 + 630\ln(2)}{18000}\right). \tag{5.6}$$

and $c_0 = \ln(1/\varepsilon^2 e)$. Holding β_0 constant in Eq.(5.4), we observe that the lateral shift is inversely proportional to the elasto-gravitational number Be and the larger displacements are achieved for very stiff fibers, $Be \to 0$. The lateral shift is also proportional to the initial angle β_0 by holding Be constant. We also notice that, $\delta x = 0$ when $\theta(0) = \pi/2$: a fiber whose unit tangent at the midpoint is initially oriented perpendicular to the direction of gravity, will not experience a drift motion, as expected.

Figure 5.4(b) shows a typical trajectory of the midpoint of a rigid fiber with $Be = 10$, $\xi = 2$, after it has hit an upward-pointing triangular obstacle. The black solid line corresponds to the numerical simulation of the full system and the red dashed line to the theoretical prediction with the initial tilt angle taken from the numerics (here $\theta(0) = 0.38 \approx \pi/8$). While the two curves show some discrepancies at short time when the fiber reorients, their lateral shift matches

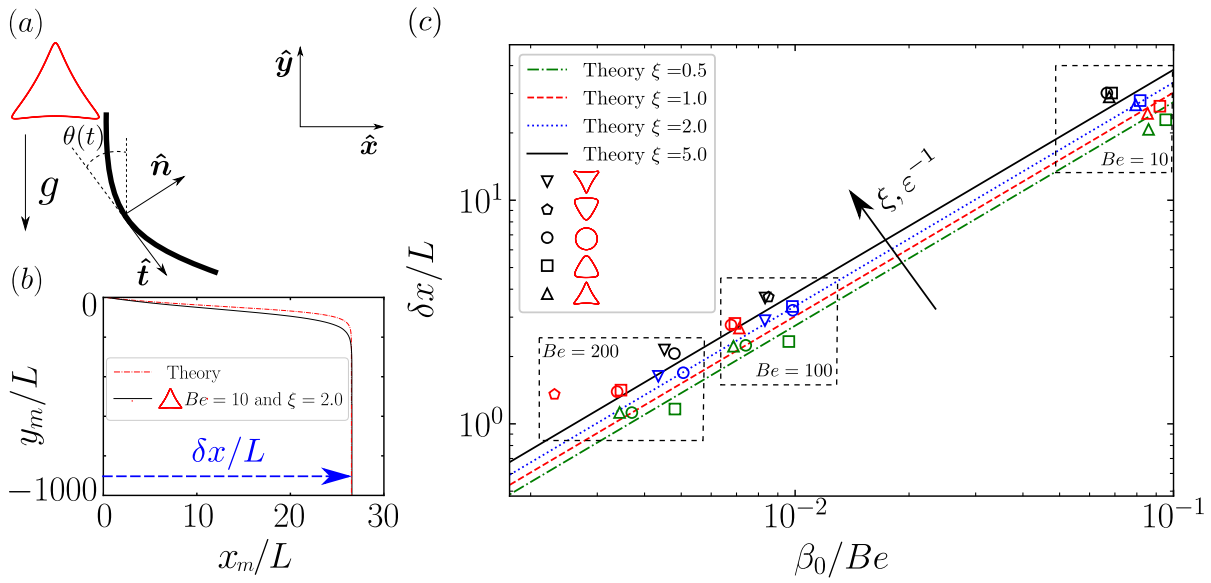

Figure 5.4: (a) Illustration of a fiber as it exits an obstacle. θ: tilt angle of the fiber centerline with respect to gravity, measured at the midpoint. (b) Results from numerical simulations (black solid line) and from theoretical predictions (red dash-dot line) showing the trajectory of the center of mass of the fiber for $Be = 10$ and $\xi = 2$. (c) Scaled lateral shift $\delta x/L$ versus β_0/Be. Comparison of the theoretical predictions (lines) with numerical results (symbols) for various fiber lengths ξ and obstacle shapes.

exactly at long times when equilibrium is reached.

Fig. 5.4(c) compares the predicted lateral shift in Eq. (5.4) with numerical simulations for a large number of realizations involving different obstacle shapes and relative length $\xi = 0.5, \ldots, 5$. As before, the initial tilt angle in Eq. (5.5) is taken from the simulations after hitting the obstacle. These results show that (i) the good agreement between theory and simulations hold until $Be = 200$ despite the small deformation approximation, (ii) for a given value Be, the obstacle shape has a marginal effect on β_0 and therefore on $\delta x/L$, (iii) the scaling with Be^{-1} leads to large lateral displacement (up to $\delta x \approx 30L$ for $\beta_0/Be \approx 0.1$).

Our findings demonstrate that an obstacle can reorient a settling fiber, thereby deviating its trajectory. This reorientation and subsequent lateral motion are strongly influenced by the geometrical and mechanical properties of the fiber, as quantified by the elasto-gravitational number, Be. Consequently, this obstacle-induced lateral displacement under gravity can be exploited to passively sort fibers by length, L, and/or rigidity, E.

5.2.2 Settling dynamics in a structured array of pillars: towards a sorting device

Patent: Makanga *et al.* (2024*a*)
Ongoing work: Makanga *et al.* (2024*b*)

The objective of this study is to investigate the potential of lateral dispersion with obstacles arranged in a lattice to sort fibers according to their flexibility and/or length. Rather than pursuing a systematic parametric exploration or optimization of the system, our aim is to provide a proof of concept for a novel passive sorting strategy.

Our first numerical simulations conducted on periodic arrays of pillars with circular cross-section have yielded encouraging results, which are outlined in the following section.

5.2.2.1 Setup and methods

The array of pillars is arranged in a hexagonal lattice, which we characterize by the structural angle, $\phi_s = \pi/6$, and the lattice spacing relative to the width of the pillars, d/ω.

In our model, a unit lattice cell contains the equivalent of two pillars, while the computational domain consists of 2×2 unit cells, thus including the equivalent to 8 pillars, plus the fiber. Therefore the total number of blobs in the computational domain is $M = M_F + 8M_O$. The mobility matrix is given by the Rotne-Prager-Yamakawa (RPY) hydrodynamic tensor which we evaluate in a triply periodic domain, made of four unit cells with eight pillars, with the Positively-Split-Ewald (PSE) method (Fiore *et al.*, 2017; Pérez Peláez, 2022) for a fast computation of its action on a given vector.

5.2.2.2 Preliminary results

Figure 5.5 shows an example of fibers with identical lengths sorted by rigidity ($Be = 10$, 100, 1000) for a given lattice spacing $d/\omega \approx 3.5$ and relative length $\xi = L/\omega = 2.36$. The stiffest fiber migrates laterally across the lattice (displacement mode), while the more flexible ones exhibit no average displacement from the direction of gravity (zig-zag mode). These long-time trajectories are periodic. In the zigzag mode, there is no average displacement from the direction of gravity, the fiber center of mass oscillates around a quasi-straight line. Conversely, in the displacement mode, there is a net displacement from the direction of gravity, the fiber center of mass follows a cyclical skew bumping path with period $n = 3$. From this period, we can define the migration angle of the fiber $\phi = \tan^{-1}\left(\frac{\tan(\phi_s)}{n}\right) = 0.36\phi_s$.

Our first analyses indicate that these long-time trajectories are related to the early scattering dynamics between the fibers and the obstacles. The scattering dynamics are contingent upon the fiber deformability Be, its length relative to the obstacle width $\xi = L/\omega$ and on the lattice spacing d/ω. We denote θ_c the angle of the fiber with respect to gravity when it touches an obstacle and $x_c \in [-\omega/2, \omega/2]$ the x-position of the fiber extremity with respect to the obstacle center at contact. We define two type of scattering events by analogy with electrostatic interactions:

- *In-scattering*: the contact angle and the contact point are unlike-charged, i.e. (θ_c^+, x_c^-) or (θ_c^-, x_c^+), referred to as "In" events in Fig. 5.6a. In this case the fiber will remain within the same column.

- *Out-scattering*: the contact angle and the contact point are like-charged, i.e. (θ_c^+, x_c^+) or (θ_c^-, x_c^-), referred to as "Out" events in 5.6a. In this case, the fiber will migrate sideways across the lattice.

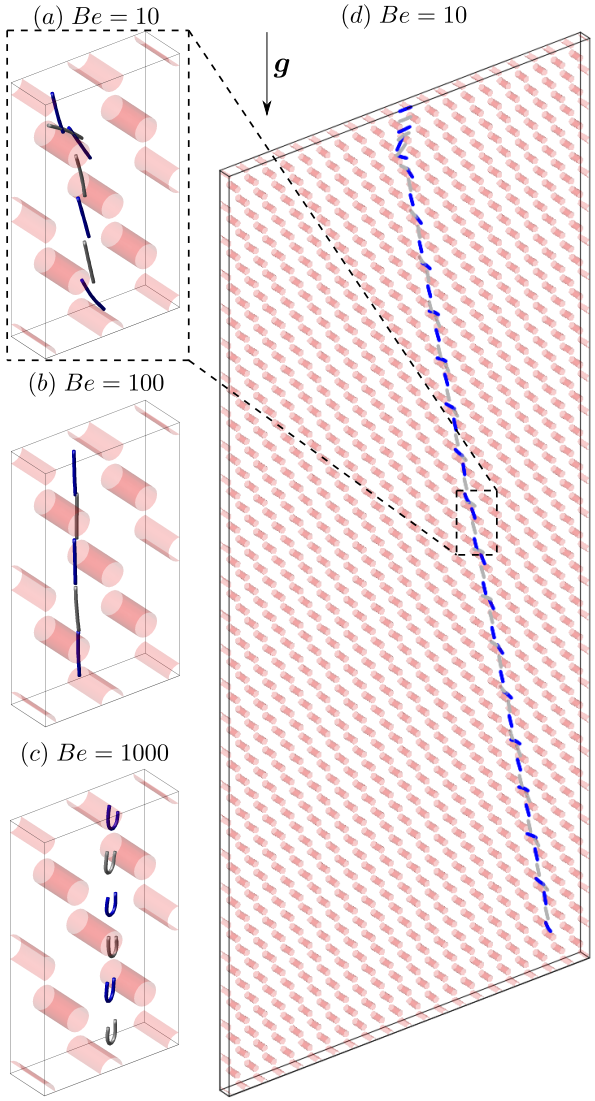

Figure 5.5: Chronophotographs of a flexible fiber settling through an array of obstacles. The time step between two consecutive frames (shown with alternative colors: blue and gray) is $\Delta t = 3T$, where $T = L\eta/W$ is the characteristic settling time. The snapshots are taken at long times for a fixed value of the relative length, $\xi = 2.36$, and various values of the elastogravitational number: (*a*) $Be = 10$, (*b*) $Be = 100$, and (*c*) $Be = 1000$. The panel (*d*) shows the unwrapped trajectory of the fiber for $Be = 10$. For the latter, the considered time interval is $0 \leq t/T \leq 300$.

In the limit of large lattice spacing $d/L > 1$ and small deformations $Be \ll 1$, we have extended the theory of Li *et al.* (2013), briefly presented in Section 5.2.1.4, to predict the position of the fiber extremities relative to the obstacle surface. Given the initial angle of the fiber θ_0 (e.g. when it exits a previous obstacle) and the initial position of its extremity relative to the obstacle center $\boldsymbol{R}_O(0)$, we can predict x_c and θ_c, and thus whether the fiber will migrate laterally or not.

Fig.5.6b shows the predicted position of the contact point as a function of θ_0 (normalized

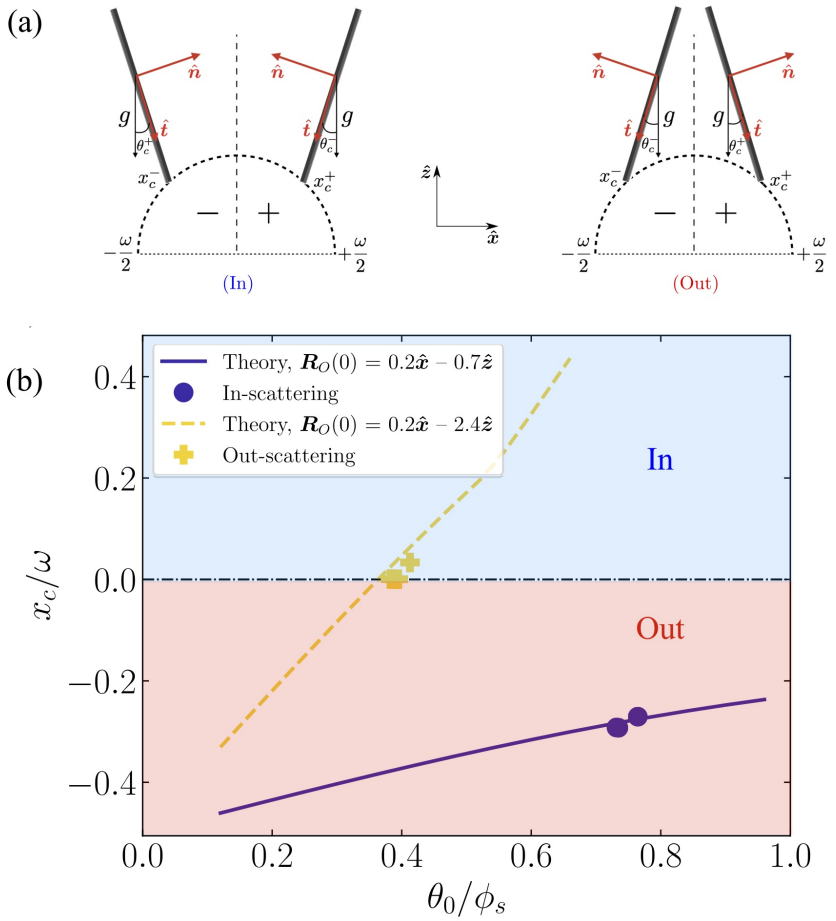

Figure 5.6: (a) Schematic of the two modes of scattering induced by fiber-pillar interactions. (b) Position of the contact point x_c/ω versus the initial angle θ_0/ϕ_s for various initial positions $\boldsymbol{R}_O(0)$. Lines: theoretical prediction. Markers: numerical simulations with $Be = 10$ and $\varepsilon^{-1} = 15$ ($\xi = 2.36$).

by the structural lattice angle: $\pi/50 \leq \theta_0 \leq \pi/6$) for two initial positions $\boldsymbol{R}_O(0)$ taken from numerical simulations. These theoretical curves are compared with the scattering events obtained from the simulation of the rigid fiber that migrates across the lattice shown in Fig. 5.5a ($Be = 10$ and $\xi = 2.36$). Although further comparisons are needed, the numerical results are in good agreement with the theoretical predictions, thus confirming the adequacy of our simple theoretical model to predict the scattering process experienced by the fiber at short times, in the limit of small deformations and large lattice spacings. For a given geometry of the array, i.e. lattice arrangement and spacing, these findings may be used to predict in which mode of migration the trajectory of an elongated particle will fall at long times. For instance, array geometries that are designed such that the distance between two obstacles of successive rows is $\boldsymbol{R}_O(0) \cdot \hat{\boldsymbol{x}} \leq 0.2$ and $\boldsymbol{R}_O(0) \cdot \hat{\boldsymbol{z}} \geq -0.7$ will only lead to "In" scattering events *regardless of the exit angle* θ_0, and therefore to a zigzag mode, see Fig.5.6b. On the contrary, if the vertical distance from the next row of obstacle is $\boldsymbol{R}_O(0) \cdot \hat{\boldsymbol{z}} = -2.4$, it can either move sideways ("Out" event) or fall downward ("In" event) depending on θ_0.

Overall, our combination of theory, numerical simulations, and experiments offers valuable insights into the design of gravity-based sorting devices for a range of applications, including biomedical, microfluidic, and environmental. Our proof of concept is patented (Makanga *et al.*, 2024*a*).

5.3 Advection of fibers in structured microchannels

Collaborators: Anke Lindner (PMMH), Olivia du Roure (PMMH)
Students involved: Clément Bielinski (Post-Doc), Zhibo Li (PhD)

When the buoyancy forces of suspended fibers are too small to cause significant movement, they can be guided and sorted using a background flow. When freely transported in a viscous flow, a fiber may deform in response to viscous forces (Du Roure *et al.*, 2019). These deformations might help the fiber migrate across the flow streamlines, e.g. through buckling (Wandersman *et al.*, 2010; Quennouz *et al.*, 2015), bending or coiling (Xue *et al.*, 2022). In the presence of obstacles, flexible fibers may thus deform, stretch, buckle, vault and tumble due to the flow generated by the obstacles, which will modify their trajectory as well as their transport time (Sabrio & Rasoulzadeh, 2022; Kawale *et al.*, 2017; Chakrabarti *et al.*, 2020*a*). The presence of obstacles might thus affects the long-time transport properties of fibers, such as dispersion, and can serve as a base for sorting devices.

This is what we explore in the next sections. First, I describe our fundamental work on the interaction between a rigid fiber and a triangular obstacle in a microchannel. Our findings show that direct contact between the fibers and the pillar results in a rich variety of fiber dynamics and significantly enhances cross-streamline migration (Section 5.3.1). However, the resulting lateral displacement remains relatively small compared to the sedimentation case and decreases drastically with increasing fiber flexibility. To overcome these limitations, we utilize pillar arrays in microfluidic chips (Section 5.3.2). By integrating a comprehensive analysis of the flow field within the array with an optimization algorithm, we develop an effective fiber sorting strategy in pressure-driven flows.

5.3.1 Dynamics of rigid fibers interacting with a triangular obstacle

Related publication: Li *et al.* (2024)

In this work, we combine microfluidic experiments and numerical simulations to study the interactions of a rigid fiber with an individual equilateral triangular pillar in a microfluidic channel.

5.3.1.1 Setup and methods

We consider a microchannel of width $W_{ch} = 800\,\mu m$, height $H_{ch} = 40\,\mu m$, and length $L_{ch} = 20\,mm$ with a pressure driven flow (forced with syringes in experiments). See Fig. 5.7a for a detailed sketch of the experimental setup. A triangular pillar with the same depth H_{ch} as the

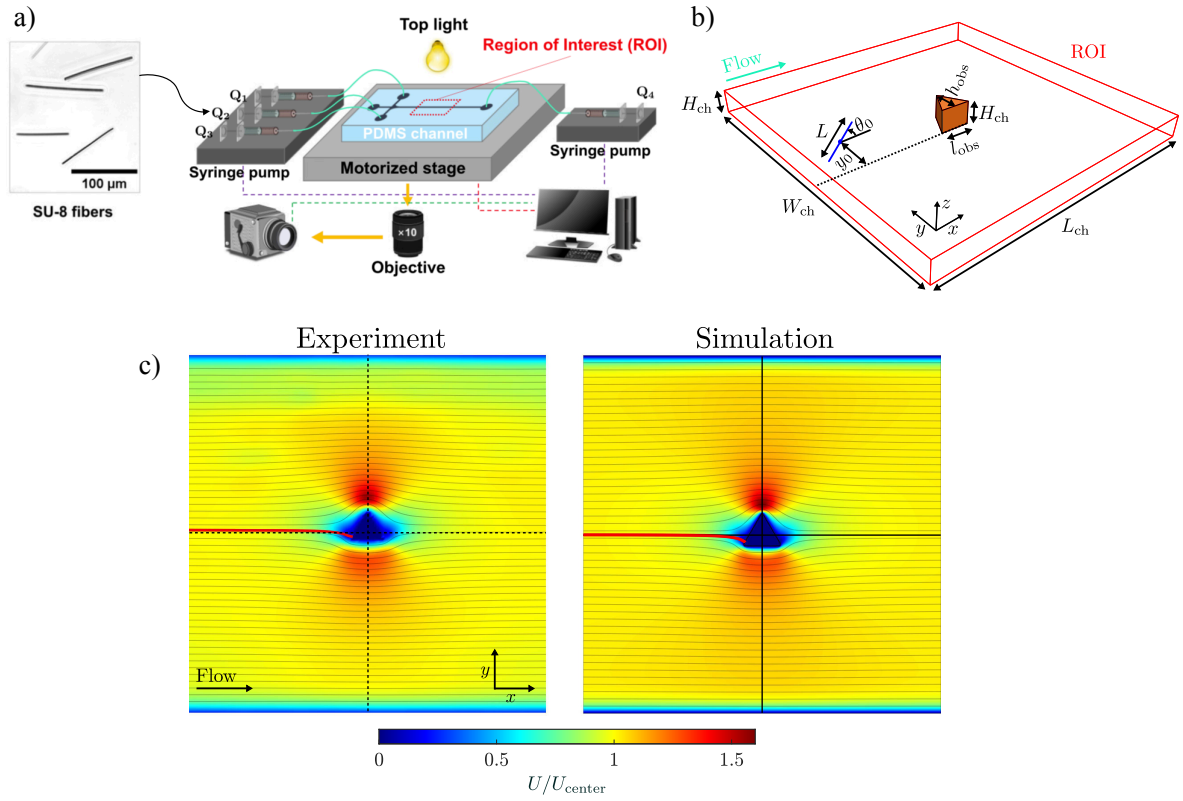

Figure 5.7: (a) A detailed sketch of the experimental setup showing the SU-8 fibers, microfluidic channel, flow control, and data acquisition. (b) Zoom in on the region of interest (ROI) showing the main geometrical parameters of the study (figure not to scale). (c) Normalized velocity magnitude and streamlines obtained experimentally by micro-PIV (left) and computed by LBM simulation (right). The thick red line is the flow separatrix.

channel is placed in the middle of the microchannel. Its base is aligned with the flow direction and the triangle is of height $h_{obs} = 75\,\mu m$ and base $l_{obs} = 2h_{obs}/\sqrt{3}$ (see Fig. 5.7b).

Rigid fibers are delivered from the inlet into a narrow band in the center of the channel width increasing the probability of their interaction with the obstacle. In the experiments, the rigid fibers are prepared by shearing an emulsion of SU-8 polymer droplets in a glycerol-ethanol mixture and exposing the stretched droplets to ultraviolet (UV) light.

In simulations, the background flow in the microchannel around the obstacle is computed with a CFD code using the Lattice-Boltzmann method (LBM)[1] (Succi, 2001; Krueger *et al.*, 2016). Perturbations of the flow induced by the fibers are accounted for with the RPY mobility matrix providing the hydrodynamic interactions between of the blobs connecting the fiber centerline. Similarly to the sedimentation case in Section 5.2, a contact force between the fiber and the obstacle surface is introduced in order to prevent artificial overlaps and is calibrated to match the experimental dynamics. More details on the numerical method are provided in (Li *et al.*, 2024).

[1] Any other approach to solve for the Stokes flow (Boundary Element Method, Finite-Volume,Spectral Methods...) would have been equally effective.

The flow field computed by the LBM is shown in Fig. 5.7c and compared to micro-PIV measurements in the midplane of the experimental channel in the neighborhood of the pillar (only a portion of the channel is represented here). The main features of the experimental flow are well captured by the simulation. The velocity is zero along the bounding walls ($y = 0$ and $800\,\mu$m) and on the pillar surface. The fluid is sharply accelerated right above and below the pillar and it is almost uniform far away from the pillar. The confinement of the flow in the shallow Hele-Shaw like channel leads to a localization of the flow disturbance close to the obstacle and to a strong acceleration zone at the apex of the triangle. The red thick line is the flow separatrix which separates the streamlines going above and below the obstacle.

5.3.1.2 Fiber dynamics

The dynamics of rigid fibers is investigated as a function of their length L, initial angle with respect to the flow direction θ_0 and lateral position y_0 at the channel entry. A lateral position of $y_0 = 0$ corresponds to the position of the base of the triangle (see Fig. 5.8d). We thus refer to increasing y_0 as positioning the fiber "higher" whereas decreasing y_0 corresponds to positioning the fiber "lower" along the triangle. More than 200 experiments and 1300 numerical simulations have been performed with a single isolated fiber for various initial conditions. Four different fiber dynamics have been observed both experimentally and numerically, with excellent quantitative agreement, depending on θ_0, y_0 and L:

- "Below" (Fig. 5.8a): the fiber follows a mostly symmetric trajectory and goes below the pillar without touching it.
- ‘"Above" (Fig. 5.8b): the fiber follows a mostly symmetric trajectory which goes above the pillar without touching it.
- "Pole-vaulting" (Fig. 5.8c): the fiber establishes contact with the obstacle and pole-vaults, resulting in an asymmetric trajectory where the fiber does not go back to its initial configuration (θ_0, y_0) far away downstream.
- "Trapping"(Fig. 5.8d): the fiber gets trapped at the left tip of the pillar and finds an equilibrium position that results from the balance of the hydrodynamic forces exerted on the fiber on both sides of the contact point.

The dependence of the fiber dynamics with the initial conditions is shown more broadly on Fig. 5.9a which compares the fiber dynamics observed experimentally (open symbols) and obtained numerically (closed symbols) for a large number of initial configurations (θ_0, y_0), and for fiber length $0.5l_{\text{obs}} \leq L \leq 1.5l_{\text{obs}}$ in the experiments and $L = 0.8l_{\text{obs}}$ in the simulations, which is the average length of the fibers in the experiments. The black dashed line indicates the position of the flow separatrix far away from the pillar. It separates the “Below” and “Above” dynamics well. The situation is more complex close to the separatrix, where the fibers may interact directly with the pillar. Here, the four dynamics coexist and the behavior of the fibers is strongly dependent on their initial angle. In both simulations and experiments, all the trapping events are located very close to the flow separatrix and the pole-vaulting events are observed for the same range of values of (θ_0, y_0).

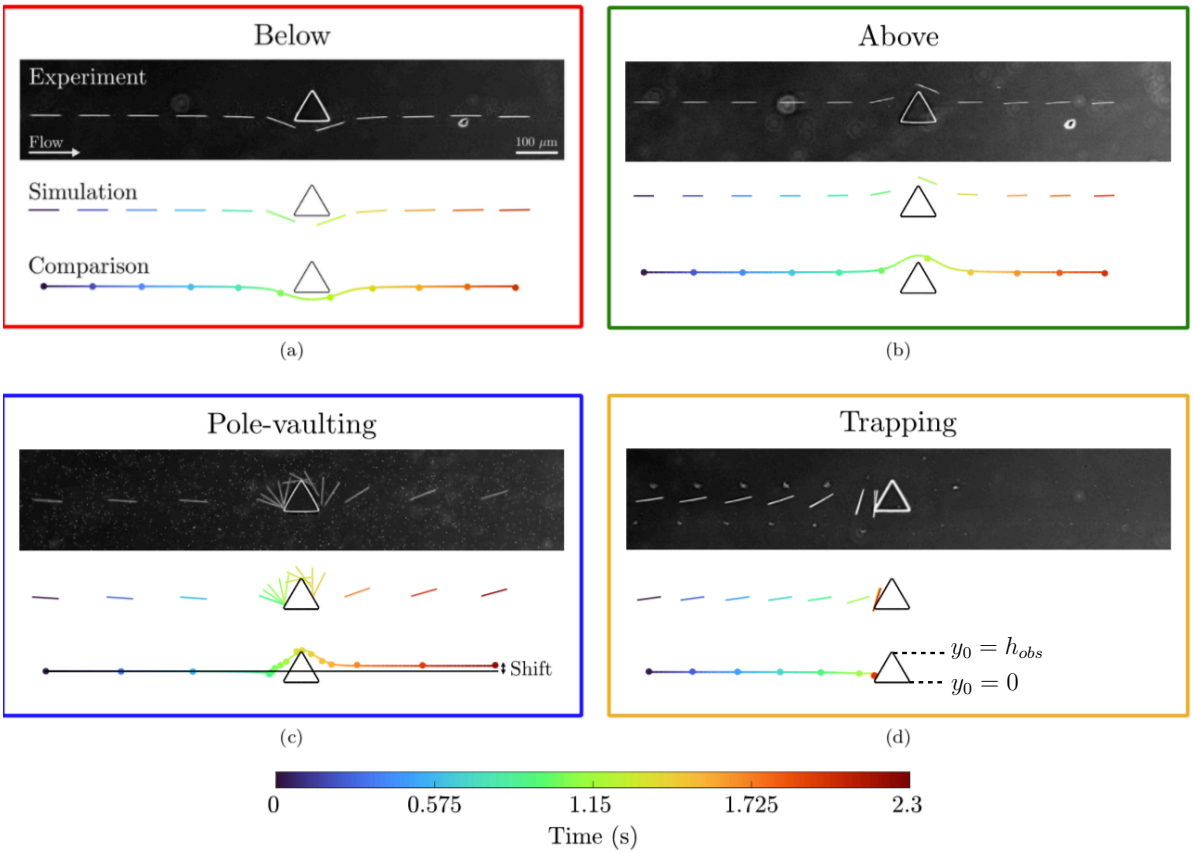

Figure 5.8: The four different fiber dynamics observed experimentally and accurately reproduced by simulations. The first line of each panel shows images from the experiments, the second line represents the chronophotograph of the simulation and the third line compares the trajectories of the fiber center of mass in the experiment (dots) and in the simulation (solid line). The colors in the two last rows of each panel indicate the time with the color-code indicated at the bottom of the figure. All figures share the same scale bar ($100\,\mu$m).

5.3.1.3 Effect of contact on fiber dynamics and cross-streamline migration

To understand how contact with the pillar affects the fiber dynamics we report in Fig. 5.9b the fiber dynamics obtained for the range of contact conditions reached in experiments (open symbols) and simulations (closed symbols). The fibers are released at the channel entry within the range of initial conditions: $-10° \leq \theta_0 \leq 10°$ and $0 \leq y_0/h_{\rm obs} \leq 1$. The four fiber dynamics occupy well distinct regions in the $(\theta_{\rm c}, y_{\rm c})$ space. Pole-vaulting events occur when $\theta_{\rm c} \lesssim 0$ and $0.05 \lesssim y_{\rm c}/h_{\rm obs} \lesssim 0.5$. The "Below" dynamics is obtained for both positive and negative contact angles, and up to $y_{\rm c}/h_{\rm obs} = 0.4$. The "Above" and "Below" domains are well separated by a thin region of trapping events, which reveals the existence of an equilibrium contact configuration between these two dynamics. There are also some trapping events for $y_{\rm c}/h_{\rm obs} \approx 0$ and $\theta_{\rm c} \leq -30°$. For those cases, the fiber rotates and slides around the left apex of the pillar, and it finds an equilibrium position where it remains trapped. There is an overall good agreement between the dynamics obtained experimentally and numerically. Interestingly, several contact configurations

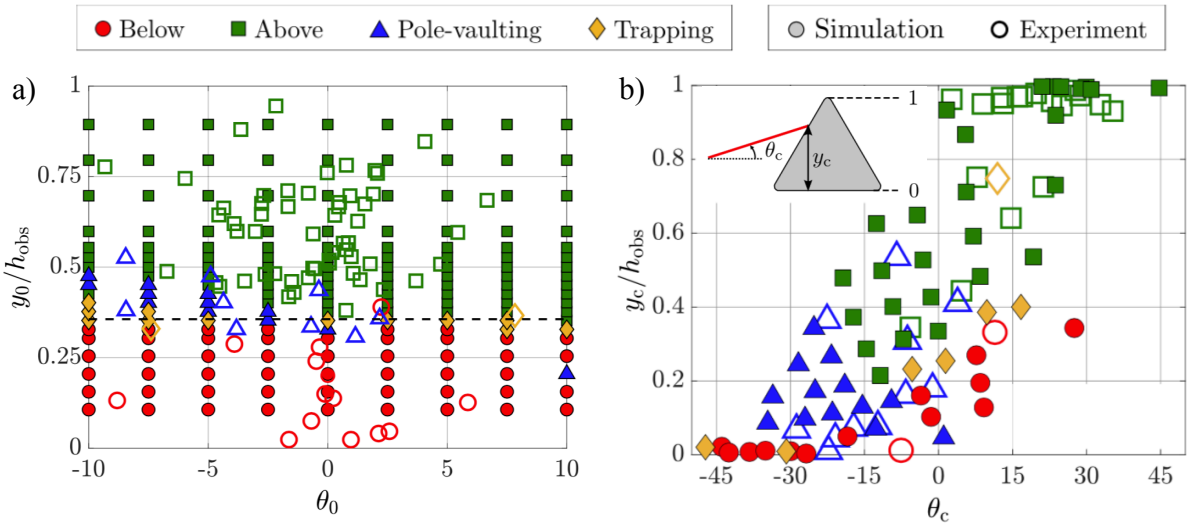

Figure 5.9: (a) Effect of the fiber initial configuration on the resulting dynamics. The fiber lengths are $0.5l_{obs} \leq L \leq 1.5l_{obs}$ in the experiments and $L = 0.8l_{obs}$ in the simulations (filled symbols), which is the average length of the fibers in the experiments (open symbols). The dashed line represents the position of the flow separatrix at the entrance of the channel.(b) Phase diagram representing the dynamics of fibers initially located far away from the pillar as a function of their contact configuration θ_c and y_c. Open symbols: experiments; closed symbols: simulations at $L/l_{obs} = 1$. Inset: definition of the contact angle θ_c and the contact position y_c.

cannot be reached and no data is observed in the top left and bottom right corners of the plot. The mapping between the contact configurations and the initial conditions

$$(\theta_c, y_c) = f(\theta_0, y_0, L) \tag{5.7}$$

is complex due to the triangular obstacle that disturbs the flow field in its vicinity and the coupling of the fiber orientation and position due to its elongated shape. A thorough sensitivity analysis of the mapping is carried out in the Appendix D of (Li *et al.*, 2024). Overall, our findings show that small differences in the initial conditions lead to strong differences in the fiber trajectories and orientation close to the obstacle due to the finite size effects of the fiber in the complex disturbance flow field around the obstacle. This explains why in the region close to the flow separatrix very different fiber dynamics can be observed.

The different fiber dynamics and contact with the pillar also induce a lateral drift of the fiber. The lateral displacement is quantified by

$$\delta = \frac{y_f - y_0}{h_{obs}} \tag{5.8}$$

where y_0 and y_f are respectively the initial (upstream) and final (downstream) lateral positions of the fiber center of mass at equilibrium far away from the pillar, and h_{obs} is the pillar height. Note that due to the symmetry of the streamlines, lateral displacement is only observed in the case of *cross-stream migration*.

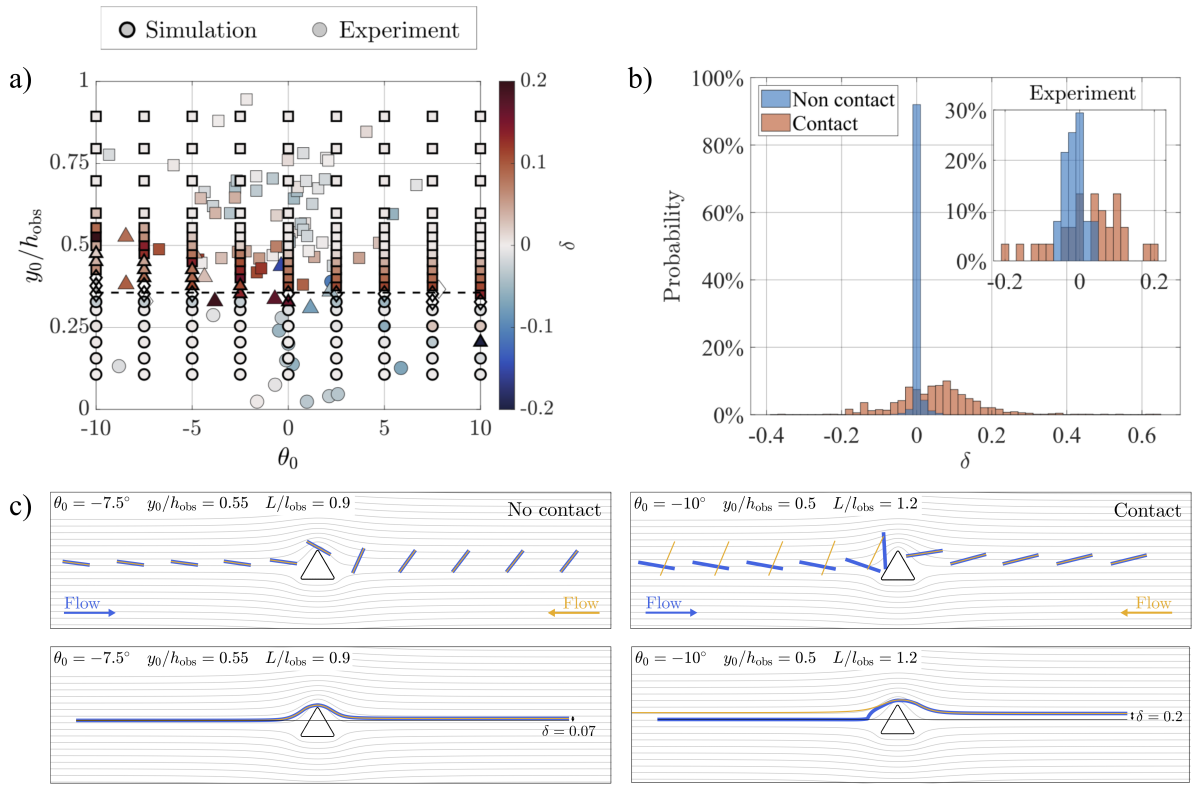

Figure 5.10: (a) Effect of the fiber initial configuration and length on the lateral displacement δ. The fiber lengths are $0.5l_{obs} \leq L \leq 1.5l_{obs}$ in the experiments (thin edges) and $L = 0.8l_{obs}$ in the simulations (thick edges), which is the average fiber length in the experiments. The dashed line represents the position of the flow separatrix at the entrance of the channel. (b) Probability of δ with and without contact in the simulations. Inset shows the experimental probabilities. Initial conditions are: $-10° < \theta_0 < 10°$, $0 < y_0/h_{obs} < 1$, and $0.5 < L/l_{obs} < 1.5$ both in the experiments and simulations. (c) Typical example of chronophotographs and trajectories in the absence (left) and presence (right) of contact (blue: flow from left to right, yellow: flow from right to left). No contact: reversibility of the fiber motion is shown by the superimposition of blue and yellow trajectories. Small lateral deviation, δ, is obtained. Contact: irreversibility of the fiber motion (blue and yellow trajectories do not superimpose), and larger lateral displacement is observed.

Figure 5.10a shows the influence of the initial condition on the lateral displacement. It compares experimental data (thin edges) and simulated data (thick edges) at $L = 0.8l_{obs}$ (the mean fiber length in the experiments), varying θ_0 and y_0. The fiber dynamics are coded by the same symbols as in Fig. 5.9. The darker the color, the larger the deviation. This figure provides a link between the fiber dynamics and the lateral displacement. The "Pole-vaulting" dynamics leads to strong lateral deviations, while the "Above" and "Below" dynamics result in very small deviations, with the exception of initial conditions close to the flow separatrix (indicated by the dashed line in panel 5.10a). Most lateral displacements are positive meaning that the fiber will be deviated towards larger y positions, but some negative (and rather small) lateral deviations are observed in particular for negative initial angles θ_0. The lateral displacements obtained in the simulations are in rather good agreement with those observed experimentally. In the

experiments, δ is also larger close to the flow separatrix, i.e. in the range $0.3 \leq y_0/h_{\text{obs}} \leq 0.55$ where the fibers strongly interact with the pillar, and it is rather small outside this range, where the fibers do not or weakly interact with the pillar.

Significant lateral displacement is only observed for fibers released close to the separatrix that thus pass very close to or touch the obstacle. This enhancement is quantified in Fig. 5.10b showing the probability distribution of lateral displacements with and without contact. In the absence of contact, both simulations and experiments exhibit a peaked distribution around $\delta = 0$. When contact occurs, the distributions widen significantly: the standard deviation σ_δ increases by a factor 13 in the simulations (from $\sigma_\delta \approx 0.0085$ to ≈ 0.11) and by a factor 3.5 in the experiments (from $\sigma_\delta \approx 0.026$ to ≈ 0.092).

By reversing the flow after the fiber has passed the obstacle in the simulations we have tested the reversibility of the trajectories (Fig. 5.10c). The trajectories where no contact between the fiber and the obstacle occurs remain reversible as required for flows at vanishing Reynolds numbers whereas trajectories with contact are not reversible. Contact thus strongly modifies the nature of the trajectories. The good agreement between experimental and simulated trajectories in the case of contact confirms that contact properties but also the occurrence of contact are correctly captured by the effective approach of the simulations and reasonably well detected by our visual observations.

Altogether, these results confirm that contact strongly enhances lateral displacements. However, we would like to stress that contact is *not necessary* to induce asymmetric fiber trajectories and cross-stream migration. As shown above and in Fig. 5.10c, δ can reach non-zero, yet small, values in the absence of contact, without breaking the reversibility of the Stokes equations. It is well-known from Faxen's laws that a finite object can migrate across streamlines in the presence of a shear gradient if the flow has some curvature in the direction normal to the streamlines (Kim & Karrila, 1991; Rallabandi *et al.*, 2017). For instance, the trajectory of a sphere transported by a uniform flow around a spherical obstacle is fore-aft symmetric, but deviates from the streamlines as it approaches the obstacle, where the flow is curved, and follows them back as it moves away. The situation is more complex for fibers whose orientation also strongly influences the flow sampled by the object. Changes in orientation allow the fiber to jump across streamlines asymmetrically with respect to the obstacle but the trajectory remains reversible. When direct contact occurs between fiber and obstacle, as shown in Fig. 5.10c, stronger cross-stream migration is observed, leading to larger deviations, and the trajectory becomes irreversible.

5.3.2 Towards an optimized separation of flexible fibers by deterministic lateral displacement in pillar arrays

Ongoing work: Bielinski *et al.* (2024)

As shown in the previous section, the lateral displacement induced by the interaction between a single rigid fiber and an obstacle in pressure-driven flows is small compared to the sedimentation case: $\delta < 0.2h_{obs} \approx 0.2L$ in pressure-driven flows (see Fig. 5.10a) whereas $\delta \approx 30L$ for weakly flexible sedimenting fibers (see Fig. 5.4(c)).

Hereafter, we first evaluate the effect of flexibility on the lateral displacement with a single pillar, and then use pillar arrays to develop an effective fiber sorting strategy for pressure-driven

flows.

5.3.2.1 The interaction of a flexible fiber and a triangular pillar

In order to investigate the effect of fiber flexibility in this simple, fundamental, setting, we inject actin filaments in the microchannel. The synthesis of actin filaments is based on a well-controlled and reproducible protocol detailed extensively in Liu *et al.* (2018). Filaments have typical lengths of 5 to 50 μm, diameters of 5 to 9 nm and a persistence length of $\ell_p = 17 \pm 1\,\mu$m, as measured by analysis of thermal-fluctuation-induced conformational changes (Liu, 2018). The obstacle size for this set of experiments is $h_{obs} \approx 38\mu$m.

In an ambient flow, the deformability of a flexible fiber is measured by the elasto-viscous number (Young & Shelley, 2007):

$$\bar{\mu} = \frac{8\pi\eta\dot{\gamma}L^4}{EIc_0} \tag{5.9}$$

which compares the characteristic timescale for elastic relaxation of the fiber, $t_{el} = \frac{8\pi\eta L^4}{EIc_0}$, with the timescale of the imposed flow $t_{flow} = \dot{\gamma}^{-1}$ and serves as an effective measure of the strength of viscous forces compared to elastic restoring force. The limit $\bar{\mu} \to 0$ corresponds to a rigid fiber, the buckling threshold is near $\bar{\mu} = 153$ (Chakrabarti *et al.*, 2020*b*), and the limit $\bar{\mu} \to \infty$ corresponds to a floppy fiber. Due to their small flexural rigidity, the actin filaments used in experiments are highly deformable ($\bar{\mu} \sim O(10^3 - 10^6)$).

Fig. 5.11a-b show two instances of an actin filament interacting with a triangular pillar, demonstrating an excellent agreement between experimental and simulation results. For these two cases, the initial filament configurations in the simulation are extracted directly from experimental observations. Figure 5.11c presents the lateral displacement of the actin filaments from the experimental data, taking into account their initial position and contour length L. Since the mechanical properties are consistent across all filaments, an identical contour length corresponds

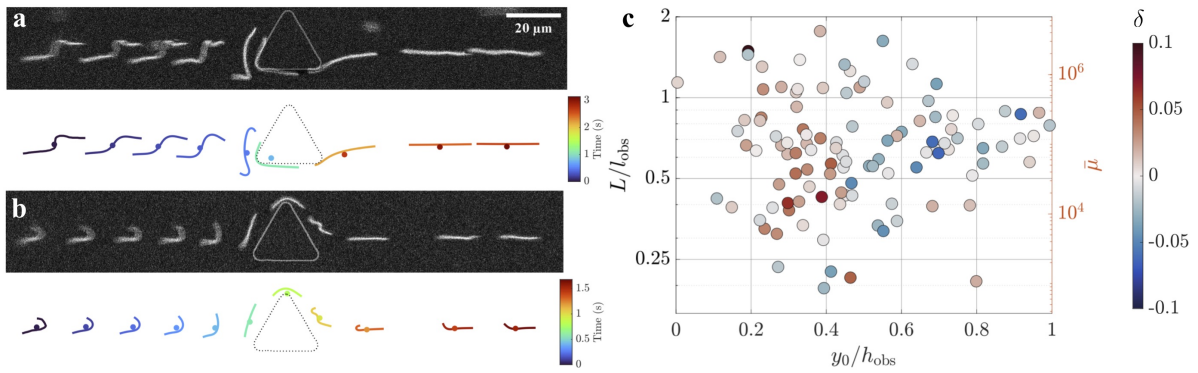

Figure 5.11: (a)-(b) Actin filaments interacting with the pillar in experiments and simulations showing 'Below' and 'Above' modes. The flow is from left to right. Grey images: experiments. Colored shapes: simulation results. Colored dots in lower panel: center-of- mass of the filaments as measured from the experiments to show the good match with simulations. Color map: time. (c) Lateral displacement δ (colorbar) as a function initial position y_0/h_{obs} and contour length L/l_{obs} (or elastoviscous number $\bar{\mu} \sim L^4$).

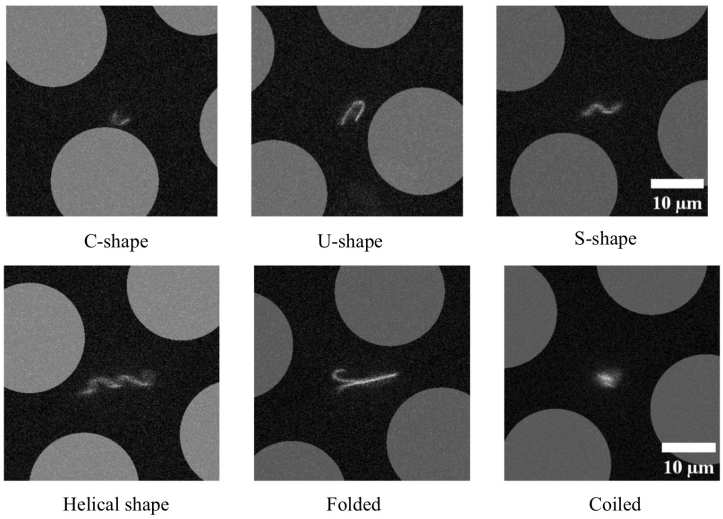

Figure 5.12: 2D (top row) and 3D (bottom row) deformations of actin filaments in a pillar array (Li, 2023).

to an identical elastoviscous number, as demonstrated on the right y-axis. From the data presented in the figure, it is apparent that approximately 95 % of cases exhibit a lateral displacement of $\delta < 0.05 h_{obs}$, which is smaller than the rigid case. The reduction in the lateral displacement is due to the inherent flexibility of these filaments, which leads to large deformations, compliance with streamlines, and a drastic reduction in cross-streamline migration

5.3.2.2 Flow, Poincaré maps and migration modes in periodic pillar arrays

To further illustrate the difficulties posed by flexible filaments, we present the diverse range of two-dimensional (2D) and three-dimensional (3D) morphologies that an actin filament can adopt within a pillar array in Fig. 5.12. These fiber deformations exhibit all the morphologies previously observed in simple flows, such as shear and compressional flows (Chelakkot *et al.*, 2012; Nguyen & Fauci, 2014; Du Roure *et al.*, 2019; Chakrabarti *et al.*, 2020*b*). This diversity of shapes affects the apparent contour length of the filament and its interactions with the flows and obstacles. Consequently, the sorting of flexible fibers by length represents a significant challenge.

Hereafter we combine experiments and numerics to investigate the feasibility of deterministic lateral displacement (DLD) with pillar arrays to sort highly flexible fibers by length. Then we outline an optimization strategy based on the pillar arrangement with the aim of improving the sorting efficiency.

In order to investigate the motion of fibers in pillar arrays we first consider a simple geometry consisting of a periodic lattice of rotated square units. We denote G_x and $G_y (= G_x)$ the spacing between two adjacent pillars, R the pillar radius, $\lambda = G_x + 2R$ the size of the unit cell and α the relative angle between the lattice axes and the direction of the incident flow (see Figure 5.13a).

Figure 5.13b shows the simulated and experimentally measured flow in a unit cell with dimensions $G_x = 13.5\mu$m, $R = 8.3\mu$m, $\lambda = 30.1\mu$m, for various angles α. For $\alpha = 0°$ the flow has two axial symmetries. One axial symmetry is also preserved for $\alpha = 45°$, while for intermediate values in-between, the flow does not have any symmetries.

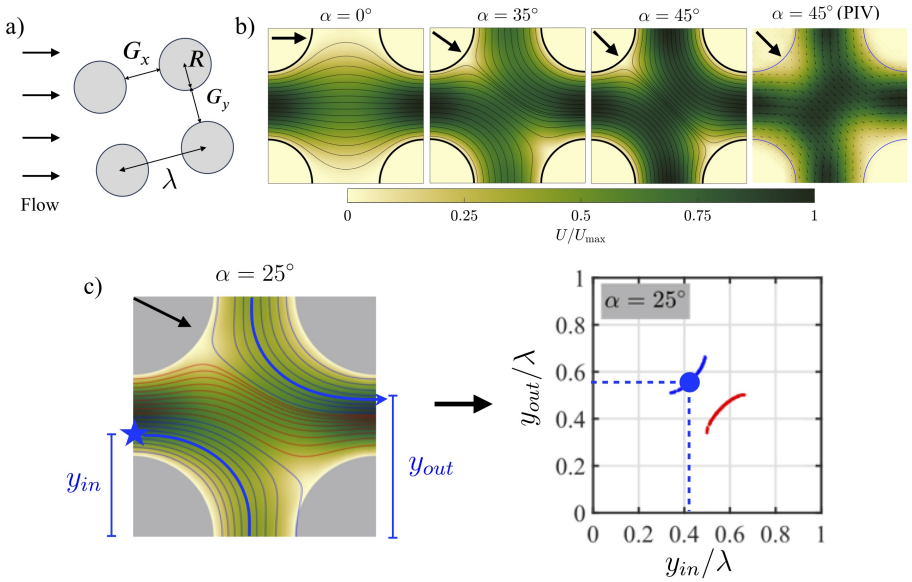

Figure 5.13: (a) Unit cell of a rotated square lattice. (b) Simulated and experimentally measured flow field in the unit cell for $\alpha = 0°, 35°, 45°$. (c) Definition of the Poincaré first recurrence map for a fluid tracer in a unit cell with a lattice angle $\alpha = 25°$. Left: flow field with two group of streamlines (red and blue lines). The thick blue line is the trajectory of a fluid tracer following a blue streamline. Right: Poincaré map for all the flow streamlines. Blue disk: position of the fluid tracer following the thick blue streamline.

In order to characterize the motion of particles in the unit cell, we use Poincaré first recurrence maps: for a given unit cell, we report the $y-$position at the outlet, y_{out}, as a function of the $y-$position at the inlet y_{in}. Figure 5.13c shows an example of Poincaré map obtained for fluid tracers in a unit cell with $\alpha = 25°$. Figure 5.14 shows the experimental and simulated maps for fluid tracers and the fiber center of mass as a function of α for various fiber lengths $L \in [5; 50\mu\text{m}]$. When the flow is symmetric ($\alpha = 0°, 45°$), the fibers do not interact with the pillars and follow the streamlines. When the symmetry is broken, longer fibers start to deviate from the streamlines. This effect is particularly enhanced at $\alpha = 35°$ where fibers with $L \geq 40\mu\text{m} = 1.3\lambda$ follow a different path than shorter ones.

In order to understand the fiber motion associated to the enhanced dispersion at $\alpha = 35°$, we visualize the trajectory and chronophotograph of a short ($L = 9.6\mu\text{m} = 0.32\lambda$) and long ($L = 48\mu\text{m} = 1.6\lambda$) fiber in Fig. 5.15a-b. The initial configuration of the fiber in the simulations is extracted directly from the experiments. The first two lines of each panel respectively represent the experimental and numerical chronophotographs, and the third line compares the trajectories of the fibers center of mass in the simulation (solid line) and in the experiment (dots). The time is indicated by the colorbar. There is a very good agreement between experiments and simulations in both panels. The deformation of the fiber is well captured by the simulations, the trajectories almost overlap and the timescales are in close match.

The short fiber experiences strong deformations as it is transported by the flow due to velocity gradients. It adopts a U-shape just below the first pillar, and then unfolds and recovers a C-shape further away downstream. It passes freely in between the pillars, in a zig-zag mode,

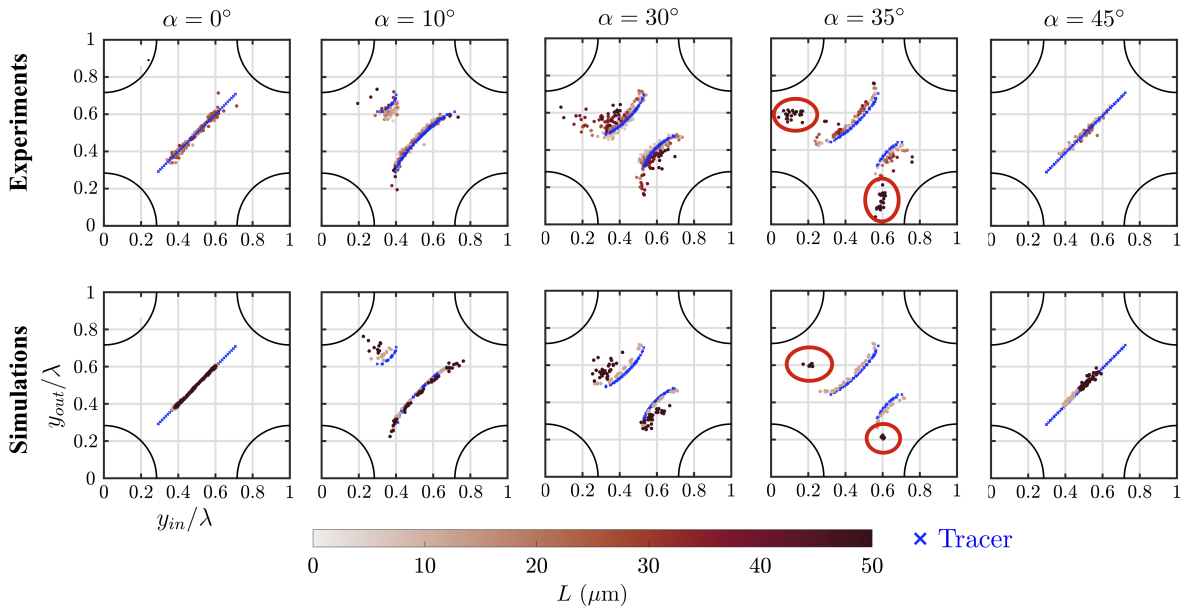

Figure 5.14: Poincaré maps of the fibers center-of-mass in the experiments (top) and simulations (bottom) at various lattice tilt angles α. The colors indicate the contour length of the fibers. Blue crosses show the Poincaré maps of tracer particles following the streamlines computed from simulations. Quarter circles in each corner of the plots represent the pillars in a unit cell.

with no visible direct contact, and it mostly acts as a tracer particle following the streamlines.

In contrast, the long fiber closely interacts with the pillars and direct contact occurs. The long fiber has short periods of trapping during which it partially wraps around the pillars before being released in the ambient flow and migrate laterally in a displacement mode. As shown by Fig. 5.15c-d, this partial wrapping state allows the long fiber to sample the flow of a different group of streamlines with its freely hanging tail, and thus to migrate laterally across the lattice, while the short fiber remains in the same group of streamlines.

5.3.2.3 Fiber separation in microfluidic chips

These periodic zig-zag and displacement modes at $\alpha = 35°$ can be used to separate fibers over long trajectories. To evaluate the sorting potential of the system, we flow fibers in a microfluidic chips with a pillar array expanding over 9 mm along the channel. In the experiments, a dilute suspensions of polydispersed actin filament suspensions is delivered into an approximately $200\,\mu$m wide band close to one channel side by flow focusing. Multiple field-of-views are set across the channel width at 9 mm downstream from the beginning of the pillar array, through which we could get the statistics of the fiber lengths and positions[2] (see Fig. 5.16a). In the simulations, we perform an ensemble average for each length, where each realization is initialized in the same unit cell with different initial conditions taken from the experiments.

Figure 5.16b shows the simulated average trajectories of 50 short fibers of length $L = 12\,\mu$m

[2]Because of the limited field of view, the fibers could not be tracked individually in experiments. My collaborators at PMMH are actively working on it.

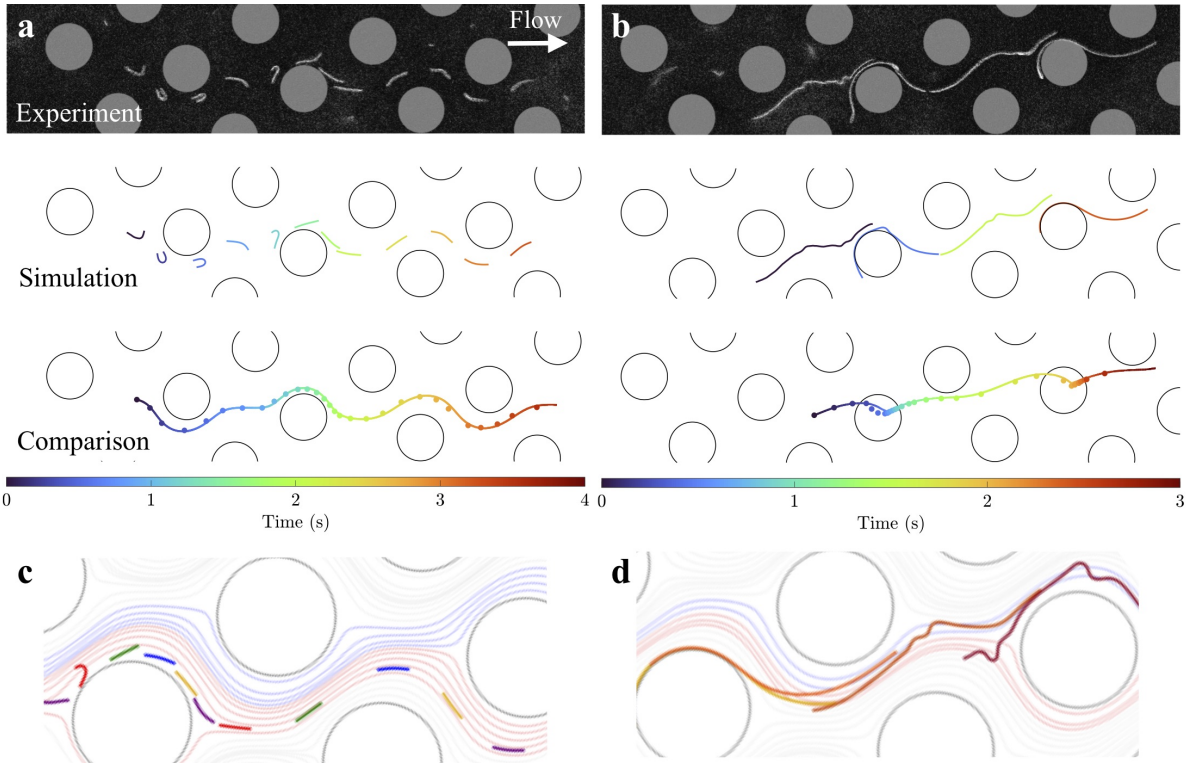

Figure 5.15: (a)-(b) Comparisons between experiments and simulations with a lattice angle of $\alpha = 35°$. The first line shows images from the experiment, the second line is the chronophotograph from the simulation, and the third line represents the simulated (solid line) and experimental (dots) trajectories of the fiber center of mass. Colors indicate time. Fiber length is $L = 9.6\mu$m in (a) and $L = 48\mu$m in (b). (c)-(d) Close-up view of simulated fiber motion with streamlines. Red (blue) streamlines go below (above) the next incident pillar.

$= 0.4\lambda$ and 50 long fibers of length $L = 48\,\mu\text{m} = 1.6\lambda$. At long times, we observe a relative lateral motion with an angle of approximately $\beta \approx 7°$ between the trajectories of short and long fibers, which represents a vertical separation of about $9 \times \tan\beta \approx 1.1$ mm at the exit of the array. The trajectories of long fibers exhibit a larger standard deviation compared to short ones because they need a longer transient regime before reaching a steady and periodic motion. However it remains relatively small compared to the length of the lattice, which ensures the robustness of the separation between short and long fibers.

In order to assess the range of lengths for which fibers can be sorted, we report the lateral displacement y_f measured at the outlet of the lattice as a function of the fiber length $L \in [5; 90\mu m] = [0.17; 3]\lambda$ in Fig. 5.16c. In the simulations, below a critical length $L_c \approx 40\mu$m $= 1.3\lambda$, the lateral migration of fibers increases moderately with their length ($y_f < 500\mu$m). In this regime, denoted regime I, their motion is dominated by the zig-zag mode with an increasing fraction of intermittent displacement modes for larger fibers. Above the critical length ($L > L_c$), the lateral displacement abruptly jumps to a high plateau ($y_f \geq 1300\mu$m). This regime II corresponds to a pure, periodic, displacement mode. However, for fibers with length $L \gtrsim 70\mu$m $= 2.3\lambda$, the lateral migration drops down to a plateau ($y_f \lesssim 600\mu$m). In this regime III, the

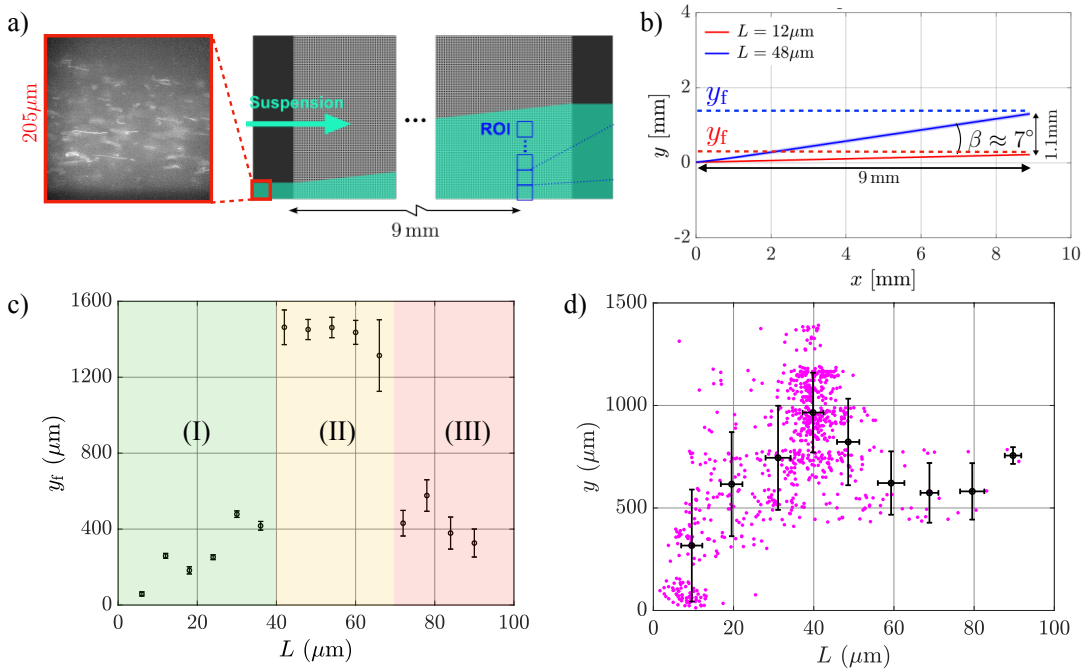

Figure 5.16: Fiber separation in a a rotated square lattice with $\alpha = 35°$. a) Sketch of DLD experiments in which the actin filament suspension is focused into a 200 μm band close to the side wall before going to the pillar array. b) Simulated average trajectory of 50 short fibers of length $L = 12\,\mu$m (red) and 50 long fibers of length $L = 48\,\mu$m (blue). Shaded areas correspond to the standard deviation. c) Lateral displacement of the fiber center of mass in the simulations at $x = 9$mm. Data are averaged over 50 runs with different initial fiber configurations for each length. d) Lateral displacement of the fiber center of mass in the experiments at $x = 9$mm.

fiber motion switches between displacement and zig-zag modes intermittently with no clear periodic patterns. We are currently working actively to explain these transitions. Our current interpretation, which needs to be improved, is that fibers in regime I are too short to systemically sample the flow from the other groups of streamlines, which prevents them from migrating. Above the critical length L_c, the fibers are long enough to sample a sufficient portion of the other group while wrapping around the obstacles, which always drives them into the basin of attraction of the periodic displacement mode. However, if the fiber is too long, it becomes more deformable ($\bar{\mu} \sim L^4$), better conforms to the streamlines and therefore follow them more, leading to frequent zig-zag motion.

Preliminary experimental results, shown in Fig. 5.16d, exhibit the same trends: the lateral displacement increases with the fiber length up to a value after which it decreases and then plateaus. However, instead of an abrupt jump near the critical length, we observe a more continuous increase. As can be seen from the error bars, more statistics are needed to conclude on the experimental observations. Nevertheless, these preliminary results provide an encouraging proof of concept for fiber sorting in microchannels with pillar arrays.

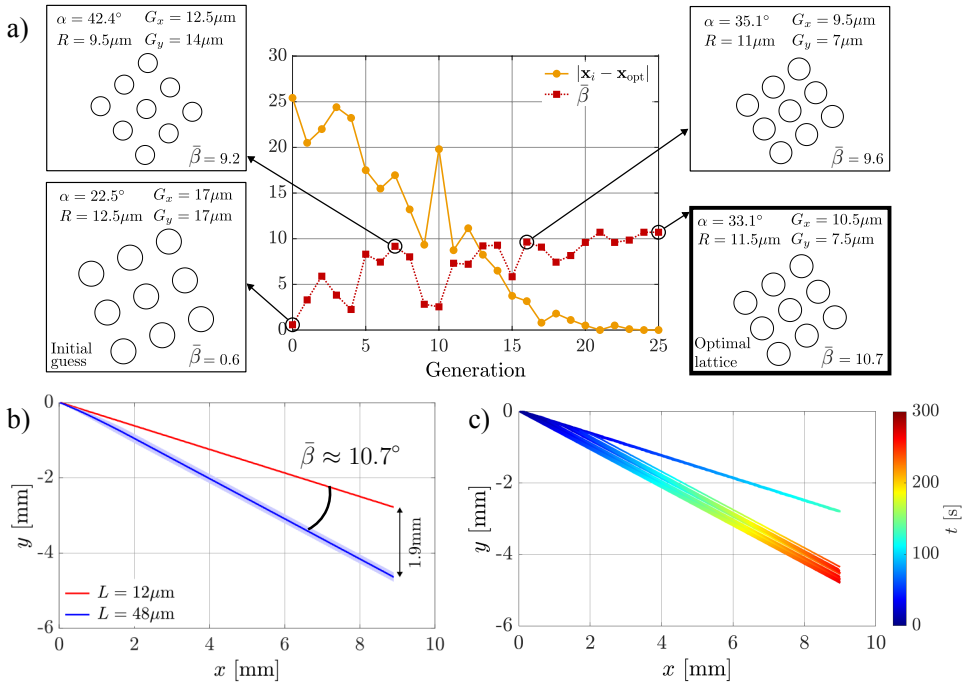

Figure 5.17: a) Convergence of the optimization algorithm. Yellow: distance $|\mathbf{x}_i - \mathbf{x}_{\text{opt}}|$ between the best guess of the ith generation and the optimal configuration $\mathbf{x}_{\text{opt}}$. Red: values of the objective function $\bar{\beta}$ at each iteration. Snapshots of lattices at generations 0 (initial guess), 7, 16 and 25 (optimal lattice) are shown (at the same scale) along with the values of their geometrical parameters. b) Simulated average trajectories of 50 short fibers of length $L = 12\,\mu$m (red) and 50 long fibers of length $L = 48\,\mu$m (blue) in the optimal lattice. Shaded areas correspond to the standard deviation. c) Simulated trajectories (50 long and 50 short fibers) colored by time. Top trajectories correspond to short fibers, as in (b).

5.3.2.4 Optimization of the pillar array

So far, our sorting results have been obtained with a rotated square array, where the orientation with respect to the flow α was chosen empirically based on the Poincaré maps (Fig. 5.14). In order to optimize the lattice in more systematic fashion, we seek the optimal set of geometric parameters, $\boldsymbol{X} = \{\alpha, G_x, G_y, R\}$, that maximizes $\bar{\beta}$, the mean relative angle of migration between short and long fibers across the array:

$$\bar{\beta}(\boldsymbol{X}) = \frac{1}{N_S N_L} \sum_{i=1}^{N_S} \sum_{j=1}^{N_L} |\beta_{ij}(\boldsymbol{X})| T_i T_j, \quad T_i = \begin{cases} 0 & \text{if trapping} \\ 1 & \text{else} \end{cases} \tag{5.10}$$

where $N_S = N_L = 4$ is the number of realizations for each type fiber (long "L" and short "S"), β_{ij} is the relative migration angle at long time between a realization i of a short fiber and a realization j of a long fiber, and T_i is a penalization function to prevent trapping in the lattice. $\bar{\beta}$ is maximized with a stochastic optimization algorithm, called covariance matrix adaptation evolution strategy (CMA-ES) (Hansen & Ostermeier, 2001). Figure 5.17a illustrates the convergence of the algorithm, accompanied by snapshots of lattices throughout the optimization process. The optimal unit cell, thus far, has been found to be rectangular ($G_x \neq G_y$), and the

average angle has been shown to be improved by 51% in comparison to our empirical choice ($\bar{\beta} \approx 10.7°$ vs. $\bar{\beta} \approx 7.1°$), see Fig. 5.17b. In addition to improving the spatial separation, the optimized array also separates the long and short fibers in time: shorter fibers exit the array approximately three times earlier than the long ones, see Fig. 5.17c. Overall, the optimized lattice improves the robustness of the sorting device by increasing both the DLD performances and the chromatographic separation between long and short flexible fibers. We are currently testing the optimized lattice experimentally.

5.4 Perspectives and ongoing work

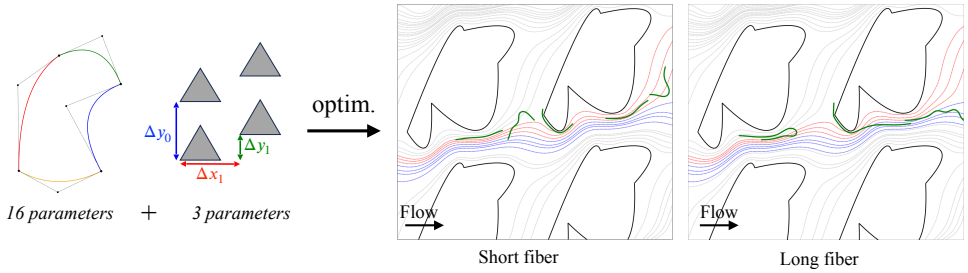

Figure 5.18: Preliminary results on shape optimization with 19 parameters (16 for the shape and 3 for the lattice spacings). Right: motion of a short and long fiber in the optimized lattice. Red and blue lines represent different group of streamlines.

- **Obstacle arrangement and shape optimization.** We are currently adding more geometric degrees of freedoms in the optimization of the pillar array to check if separation can be further improved in microchannels. Figure 5.18 shows an example with a set of 19 geometric parameters: the arrangement is controlled by 3 lattice spacings and the obstacle shape is parametrized with 4 Béziers curves, which represents 8 control points with 2 coordinates each. Starting from a circular cylinder, the current stage of the optimization algorithm leads to a more intricate shape with a small appendage that longer fibers can wrap to move across groups of streamlines. These preliminary results are encouraging and will be verified experimentally in future work. However, geometric constraints, such as the maximum curvature, will be added for practical microfabrication purposes. The setup could also be further optimized by using multiple arrays with different cell size λ in series to more finely sort fibers by length.

- **Sorting fiber suspensions: effect of fiber-fiber interactions.** We will probe the robustness and throughput of the proposed gravity-based and microfluidic-based sorting strategies. Combining experiments and simulations we will investigate the motion of semi-dilute and concentrated suspensions in structured and disordered media. In these regimes, fiber-fiber hydrodynamic interactions and contact forces may affect their relative motion, their clogging probability, their trajectories and thus the sorting efficiency of the system. Through this work we will also address more fundamental questions regarding the stability, velocity and density fluctuations in fiber suspensions in structured media. Our preliminary

simulations, which involve thousands of sedimenting fibers in a structured lattice (see Fig. 5.19), indicate that the mean settling speed, velocity fluctuations and the formation of streamers are significantly modified by the presence of obstacles (Herzhaft & Guazzelli, 1999; Saintillan *et al.*, 2005; Metzger *et al.*, 2005; Gustavsson & Tornberg, 2009).

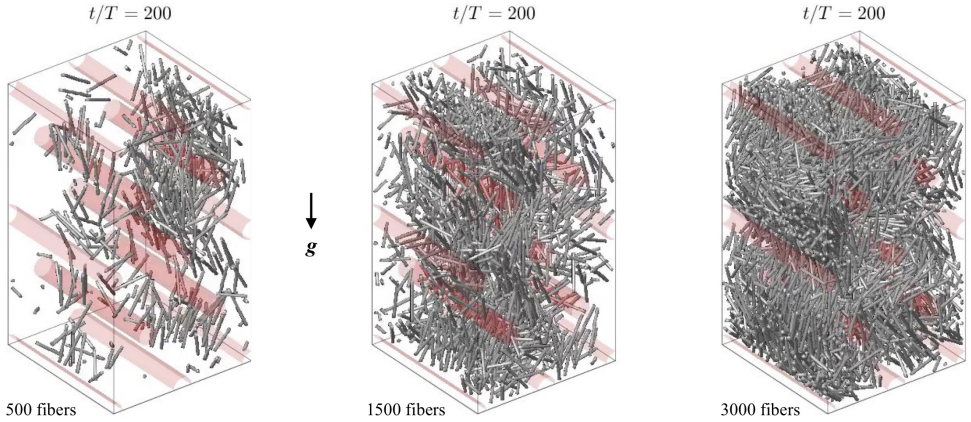

Figure 5.19: Snapshots of preliminary simulations of a suspension of rigid fibers sedimenting in a hexagonal lattice at three fibers volume fractions $\phi \approx 1$, 5, 10%. Streamers and fibers in the back-flow regions either zig-zag or move along the diagonals of the lattice.

- **Fiber migration in idealized gels: effect of elasticity and physico-chemical interactions.** Elongated parasites, such as Spirochetes (lime disease) and Plasmodium (malaria), navigate migrate in human tissues and mucus (Douglas *et al.*, 2015; Paul *et al.*, 2002; Johnson, 1977). Their typical size (3-50 microns) is comparable to the pore size of mucus (0.1-10 microns) (Murgia *et al.*, 2018). Translocation of particulate matter, such as microorganisms, viruses, or pharmaceutical carriers, through these elastic barriers is an active field of research (Murgia *et al.*, 2018; Boegh & Nielsen, 2015; Kirch *et al.*, 2012). Interacting gels, such as mucus, can filter particles based on their size and shape, but also with physico-chemical, namely electrostatic, interactions: particles with specific surface properties might engage in strong interactions with the hydrogel structure and thereby get trapped, whereas molecules with different properties might be able to escape retention (Lieleg & Ribbeck, 2011). The discrimination between various filtering effects is of primary importance to evaluate the barrier function of artificial and natural gels.

  To address these fundamental questions, I aim to investigate the motion of flexible fibers in an idealized poro-elastic medium made of rigid posts elastically tethered in space (see Fig. 5.20). Physico-chemical interactions between fibers and posts will be accounted for with electrostatic potentials. In the absence of fibers, all the tethers would stretch, and the obstacles would remain oriented with the flow. We expect collisions, potential interactions and hydrodynamic interactions to reorient obstacles, dynamically change the structure of the porous medium and thus the fiber trajectories. Two main dimensionless parameters will be varied to investigate fiber motion in this model system: the stiffness of the tether relative to the bending stiffness of the fiber, and the strength of the interaction potential relative to the viscous drag on the fiber.

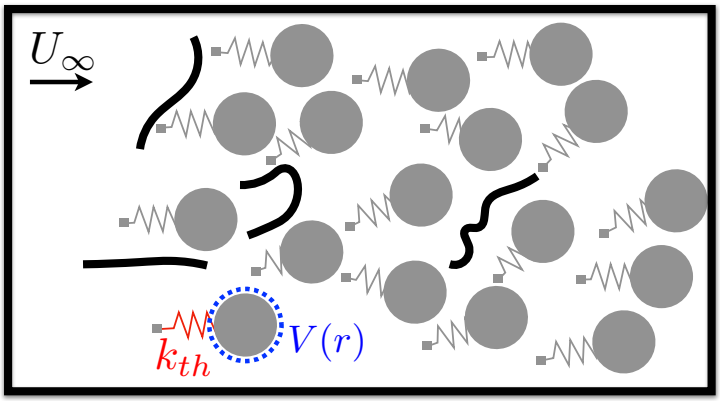

Figure 5.20: Schematic of elastic fibers migrating across an elastic medium made of interacting obstacles elastically tethered in space. k_{th}: tether stiffness. $V(r)$: electrostatic interaction potential.

Chapter 6

The intriguing motion of *B. Paxillifer*: an exploratory study

Contents

6.1 Introduction: we don't know much about *B. Paxillifer*... 95
6.2 A toy model 96
6.3 Data extraction and comparisons with experiments 101
6.3.1 Extracting sliding motion from experiments 101
6.3.2 Preliminary comparisons with experiments 102
6.4 Perspectives 104

Collaborator: Gabriel Amselem (LadHyX)
Student involved: Julien le Dreff (PhD, starting in October 2024)

6.1 Introduction: we don't know much about *B. Paxillifer*...

Diatoms are among the most abundant microalgae found in both oceanic and freshwater environments worldwide. They generate about 20 to 50 percent of the oxygen produced on the planet each year and constitute nearly half of the organic material found in the oceans. While some species sediment and drift passively with ambient flows, others employ various strategies for foraging or self-propulsion. One pennate species in particular, called *Bacillaria Paxillifer*, forms colonies of stacked rectangular cells that slide along each other while remaining parallel. Colonies of *Bacillaria Paxillifer* are phototactic and motile. They mostly live and move on substrates such as sediment beds, but also actively deform at fluid-fluid interfaces or when suspended in the bulk. Cells are rectangular in shape with typical length $L \approx 60 - 100\mu$m, height and width $H \approx W \approx 5 - 10\mu$m (see Fig. 6.1a). These cells are glued together by an adhesive substance, called mucilage, that they excrete through lateral grooves, called raphes, where they attach and slide relative to each other. The sliding motion between cells seems to be somehow coordinated, allowing the structure to expand or contract in many different ways. This intriguing coordinated motion leads to beautiful and nontrivial conformations and trajectories at the scale of the colony (Müller, 1782; Kapinga & Gordon, 1992; Gordon, 2016; Harbich, 2023), see Fig. 6.1b. However, the literature on diatom locomotion and *B. Paxillifer* in particular is indeed very scarce. So far, the diversity of deformation sequences, their purpose, their mechanical origin and the underlying fluid mechanics remain a mystery.

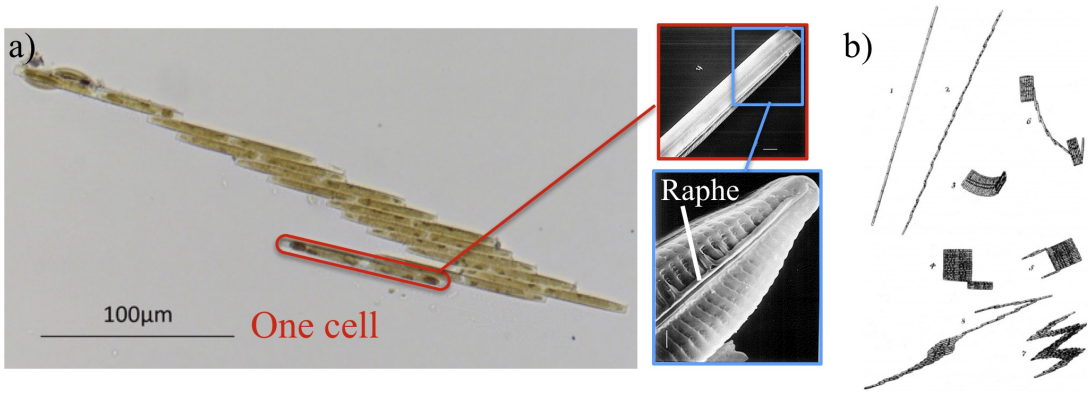

Figure 6.1: (a) Microscope view of a colony made of $M = 12$ rod-like cells (iNaturalist, 2017). The close-up views are SEM images showing a single cell and the raphe (i.e. lateral groove) that is found on both sides (Kapinga & Gordon, 1992). (c) Drawing of the various configurations observed by O.F Müller, who discovered the species *Bacillaria Paxillifer* in 1782 (Müller, 1782).

In collaboration with Gabriel Amselem, who initially introduced me to this topic, we initiated a study on the motion of this fascinating microorganism through simulations and experiments. Based on encouraging preliminary results, we decided to hire a PhD student, Julien le Dreff, who will start working on this topic in October 2024.

In the following, I present our preliminary simulation and experimental work on *B. Paxillifer*. The first section focuses on a toy model inspired by the seemingly periodic oscillations of the colony that have been observed in some cases under the microscope (Harbich, 2023). Our preliminary results show that the cell aspect ratio L/H and the phase shift between pairs of oscillating cells control their swimming speed and direction in a complex way. Above a critical cell aspect ratio, that is close to the one measured in nature, we found the existence of an optimal swimming mode with propulsion *in the direction* of the deformation wave and a wavelength *five times longer* than the colony: $\lambda \approx 5L_c$, where L_c is the length of the colony. Below that critical value we recover the optimal dynamics found for flagellated swimmers: propulsion is in the direction opposite to the wave and the optimal wavelength is close to the length of the colony $\lambda \approx L_c$ (Brokaw, 1965; Higdon, 1979*a*,*b*; Dresdner *et al.*, 1980; Spagnolie & Lauga, 2010; Tam & Hosoi, 2011; Lauga & Eloy, 2013; Lauga, 2020).

In the second section, I briefly present our efforts to combine experiments and simulations. I describe our method for extracting sliding motions from experimental videos and then using them as kinematic constraints in simulations. The resulting motion of the colony is then compared with the experiments.

6.2 A toy model

Ongoing work: Le Dreff & Delmotte (2024)

Our model swimmer inspired by *Bacillaria Paxillifer* is made of N_{rods} rigid rods connected together by kinematic constraints. Each rod is discretized with blobs distributed along its

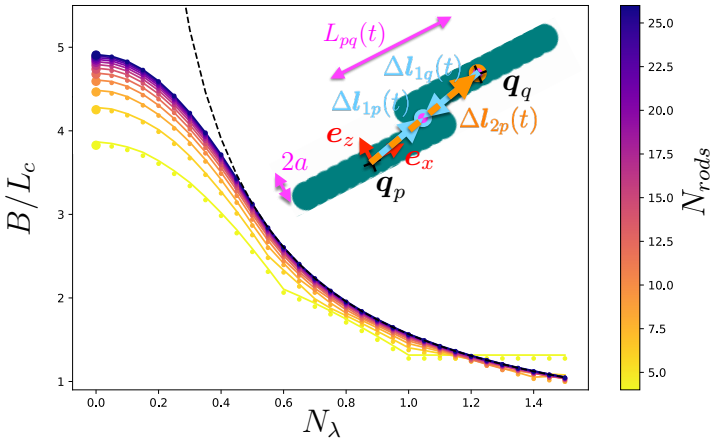

Figure 6.2: Amplitude of the sliding wave traveling along the colony as a function of N_λ for various colony size N_{rods}. Solid lines: theoretical prediction Eq. (6.6). Dots: amplitude measured in simulations. Black dashed line: amplitude in the limit of infinitely long colony $B \to A/\sin(\Delta\phi/2)$. Inset: Schematic of the two links enforcing the kinematic sliding constraint between two adjacent rods p and q. Cyan arrows: connections to link 1 (6.2). Orange arrow: connection to link 2 (6.3). Magenta circles: location of the links. The basis vectors represent the local frame attached to body p.

centerline with a spacing chosen to match highly accurate predictions of the rod mobility coefficients (Bringley & Peskin, 2008; Usabiaga *et al.*, 2016). The length of the stacked colony is $L_c = N_{rods} \times H$. Using the framework presented in Section 3.2 to handle kinematic constraints, we prescribe a tangential periodic sliding motion and a constant normal distance between adjacent rods. To enforce both of these kinematic constraints, we use two active, co-linear, ball-and-socket links (2.24) between each pair of adjacent rods p and q (see inset of Fig. 6.2):

$$\boldsymbol{g}_n(\boldsymbol{x}) = \boldsymbol{q}_p + \boldsymbol{R}(\boldsymbol{\theta}_p)\Delta\boldsymbol{l}_{np} - \left[\boldsymbol{q}_q + \boldsymbol{R}(\boldsymbol{\theta}_q)\Delta\boldsymbol{l}_{nq}\right] = \boldsymbol{0}, \; n = 1, 2, \tag{6.1}$$

$$\Delta\boldsymbol{l}_{1p} = 0.5L_{pq}(t)\boldsymbol{e}_x + 0.5H\boldsymbol{e}_y, \quad \Delta\boldsymbol{l}_{1q} = -\Delta\boldsymbol{l}_{1p}, \tag{6.2}$$

$$\Delta\boldsymbol{l}_{2p} = L_{pq}(t)\boldsymbol{e}_x + H\boldsymbol{e}_y, \quad \Delta\boldsymbol{l}_{2q} = \boldsymbol{0}, \tag{6.3}$$

$$\text{with } L_{pq}(t) = A\sin(2\pi ft + \phi_n), \tag{6.4}$$

where $A = 1.8L$ is the sliding amplitude estimated from typical experimental videos, and $\phi_n = (n-1)\Delta\phi, n = 1, \ldots, N_{rods} - 1$, is the local phase, $\Delta\phi$ being the phase shift between two adjacent pairs of sliding rods. The first equation (6.1) is the ball-and-socket constraint for the two links. Eqs. (6.2) and (6.3) provide the time-dependent position of the active links with respect to the position of the tracking point of the adjacent rods p and q. Eq. (6.4) provides the temporal variations of the tangential distance, i.e. the sliding motion, between two adjacent rods. The location of the second link in eq. (6.3) is arbitrary as long as it lies on the axis connecting $\boldsymbol{q}_p$ and $\boldsymbol{q}_q$ and does not coincide with the first link[1]. This relative sliding motion can be seen as a deformation wave in the frame oriented with the colony: $y(x_n + ct) \sim B\sin(k(x_n + ct))$ with amplitude B, wave number $k = 2\pi/\lambda = (N_{rods} - 1)\Delta\phi/L_c$, speed $c = 2\pi f/k$ along the

[1]We could also have used a constraint which prescribes the normal distance (i.e. (2.23) with $\boldsymbol{e} = \boldsymbol{e}_y$ and $d(t) = H$) together with a prescribed tangential motion (i.e. (2.23) with $\boldsymbol{e} = \boldsymbol{e}_x$ and $d(t) = L_{pq}(t)$). The result is identical.

$-x$ direction, and discrete horizontal positions $x_n = (n-1)H$, $n = 1, .., N_{rods}$. We define the number of wavelengths along the colony as $N_\lambda = L_c/\lambda$. In the limit $N_\lambda \to 0$ the colony extends and contracts synchronously ($\Delta\phi = 0$). Unlike typical traveling waves, where the amplitude is constant, the amplitude of this "sliding" wave B is largest for synchronous motion and decreases with the wavelength (see Fig. 6.2):

$$B = \max_{k\in[1;N_{rods}-1]} \left[A \frac{\sin\left(k\frac{\Delta\phi}{2}\right)}{\sin\left(\frac{\Delta\phi}{2}\right)} \right] \tag{6.5}$$

$$= \max_{k\in[1;N_{rods}-1]} \left[A \frac{\sin\left(k\frac{2\pi N_\lambda}{N_{rods-1}}\right)}{\sin\left(\frac{2\pi N_\lambda}{N_{rods-1}}\right)} \right]. \tag{6.6}$$

We study the effect of the colony size N_{rods}, the cell aspect ratio L/H and N_λ on the swimming speed, direction and efficiency of the colony. We define the dimensionless period-averaged swimming velocity $\tilde{\boldsymbol{V}}_{swim} = \frac{T}{L_c}\langle \boldsymbol{V}_{COM}\rangle$, which corresponds to the number of chain lengths traveled per sliding period, where $\langle \boldsymbol{V}_{COM}\rangle = \frac{1}{T}\int_0^T \boldsymbol{V}_{COM}(t)dt$ is the mean velocity of the colony center of mass over one period $T = 1/f$.

Figure 6.3 shows the center of mass trajectories and snapshots of a colony with $N_{rods} = 20$ and cell aspect ratio $L/H = 8.7$ together with the flow field during a swimming period for four values of N_λ. The resulting swimming speed as a function of N_λ for various colony sizes N_{rods} (but fixed cell aspect ratio $L/H = 8.7$) is reported in Fig. 6.4a. When $N_\lambda = 0$ the diatom chain expands and contracts symmetrically, leading to zero net velocity. The angle between two fully extended configurations, at $t/T = 0.25$ i.e. between $t/T = 0.75$, is $\alpha \approx \pi/5$, similar to what is observed in experiments. In the absence of hydrodynamic interactions between the rods this angle would be $\alpha = \pi$. When $N_\lambda > 0$, the colony breaks Stokes's reversibility and exhibits a rich variety of trajectories and a swimming speed that varies nonmonotonically with N_λ. For $N_\lambda < 0.6$ the chain travels *in the direction* of the deformation wave, with a maximum swimming speed obtained at $N_\lambda = 0.2$ ($\lambda = 5L_c$) where the colony travels up to 130% its length per sliding period. At $N_\lambda \approx 0.6$ even though the colony performs a non-reciprocal motion it oscillates without swimming. Beyond that value, the colony swims in the direction opposite to the deformation wave, just like a slender beating flagellum. The dimensionless speed reaches a secondary maximum at $N_\lambda \approx 1 - 1.2$, for which the micro-swimmer travels up to 40% of its length per sliding period. These local maxima and minima are repeated with a period of approximately one wavelength: $N_{\lambda,\min\,/\,\max} = 0.6/1.2 + k$, $k \in \mathbb{N}$ (not shown).
While we do not have yet a detailed explanation as to why $N_\lambda = 0.2$ is the fastest swimming mode, it is clear mathematically that the swimming speed must go through a maximum between the two zeros at $N_\lambda = 0$ and $N_\lambda \approx 0.6$. In addition, the amplitude of the deformation B is larger at $N_\lambda = 0.2$ than for $N_\lambda > 0.6$ (see Fig. 6.2), which could explain why $N_\lambda = 0.2$ is a global maximum for the swimming speed.

To determine which of these modes is the most energetically efficient, we compute the swimming efficiency η as the ratio of the average power required to pull the particle at its swimming

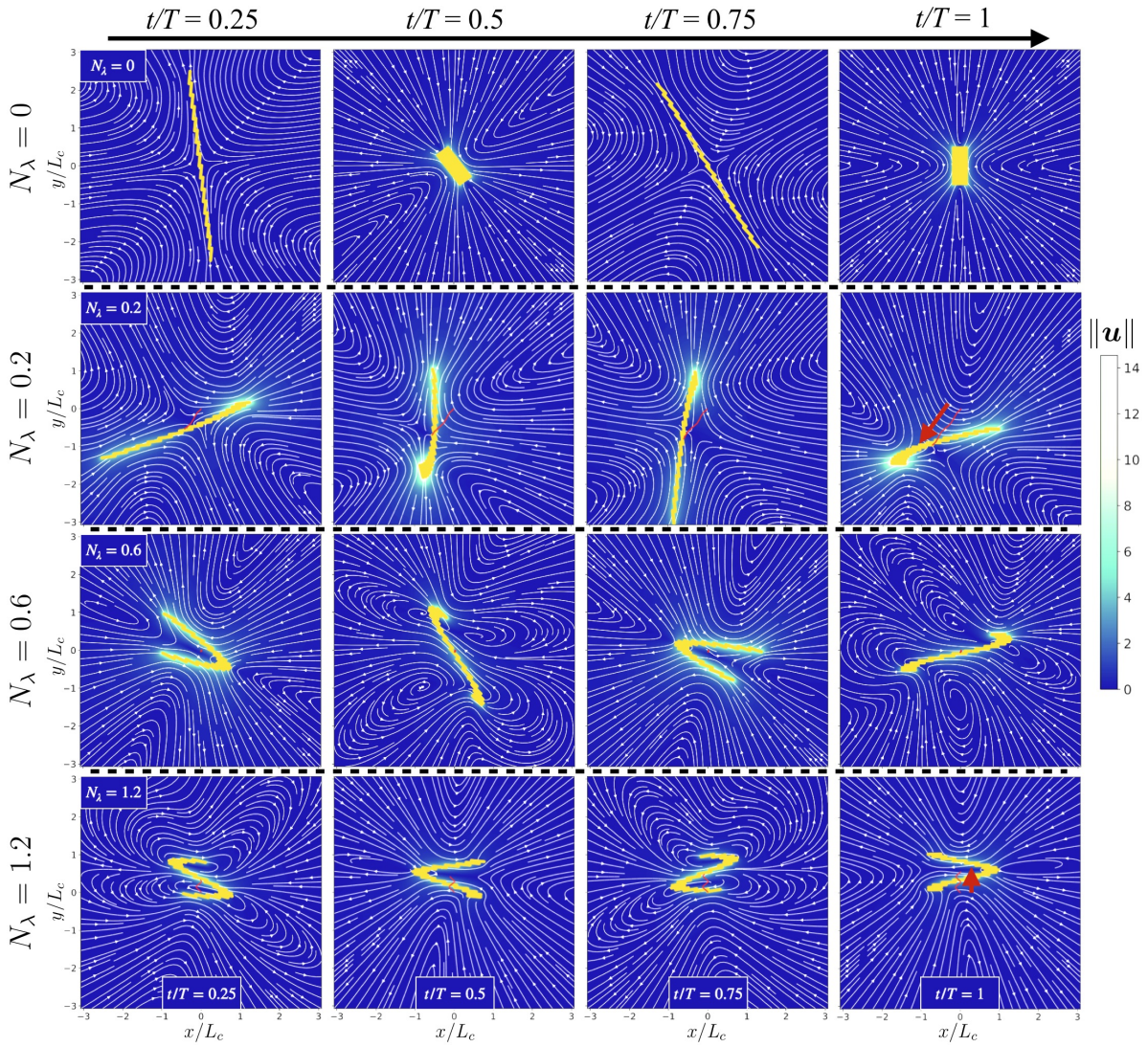

Figure 6.3: Flow field and motion of a colony with $N_{rods} = 20$ and cell aspect ratio $L/H = 8.7$ over one swimming period for $N_\lambda = 0$, 0.2, 0.6, 1.2. Red line: center of mass trajectory. Red arrow: magnitude and direction of motion. Colorbar: magnitude of the fluid velocity normalize by the swimming speed.

speed over the power required to swim, i.e. to perform the sliding motion:

$$\eta = \frac{P_{pull}}{P_{swim}} \tag{6.7}$$

with

$$P_{pull} = f^2 L_c^2 \left(\tilde{\boldsymbol{V}}_{swim} \cdot \langle \boldsymbol{R}^{FU} \rangle \cdot \tilde{\boldsymbol{V}}_{swim} \right) \tag{6.8}$$

and

$$P_{swim} = \frac{1}{T} \int_0^T \boldsymbol{F}^C(t) \cdot \boldsymbol{U}(t) dt = \frac{1}{T} \int_0^T \boldsymbol{\phi}(t) \cdot \boldsymbol{B}(t) dt \tag{6.9}$$

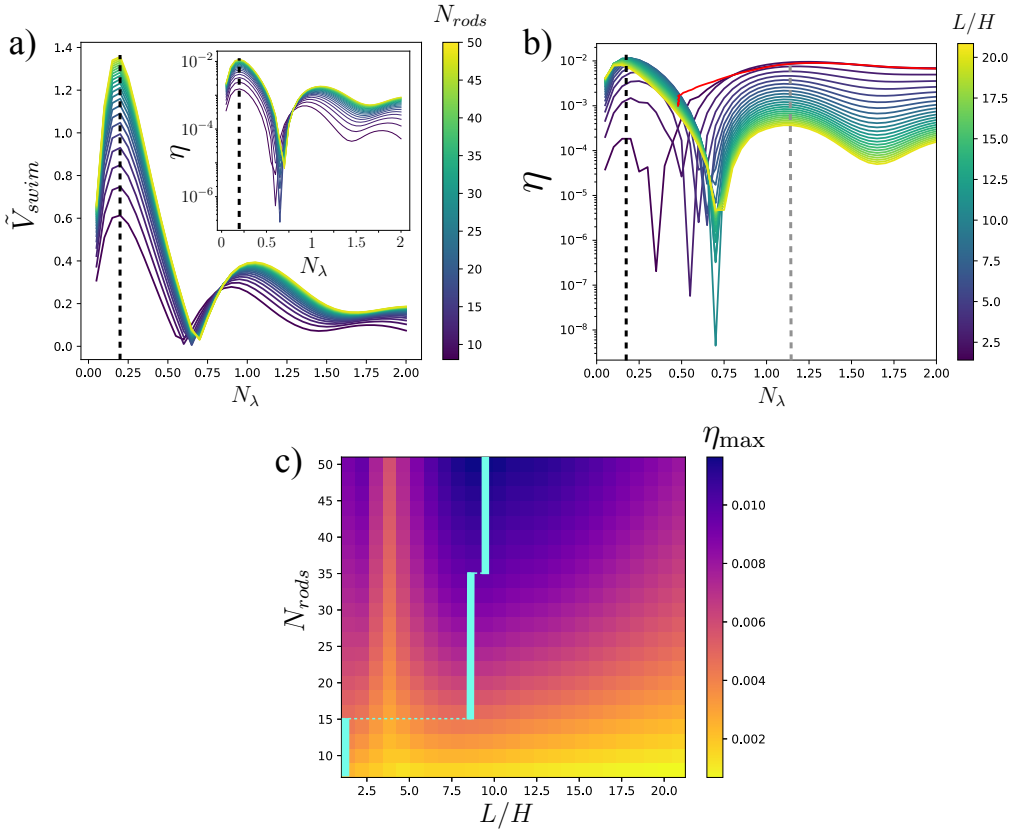

Figure 6.4: (a) Normalized swimming speed of the colony as a function of N_λ for various colony sizes N_{rods} (colorbar) and fixed cell aspect ratio $L/H = 8.7$. Black dashed line: position of the maximum $N_\lambda \approx 0.2$. Inset: Swimming efficiency (6.7). (b) Swimming efficiency (6.7) as a function of N_λ for various cell aspect ratio L/H (colorbar) and $N_{rods} = 50$. Black/grey dashed line: position of the first/second maximum $N_\lambda \approx 0.2/1.2$. Red line: efficiency for flagellar beating extracted from Higdon (Higdon, 1979*b*). (c) Maximal efficiency (colorbar) as a function of cell aspect ratio L/H and colony size N_{rods}. Blue lines: position of the maximum.

where $\langle \boldsymbol{R}^{FU} \rangle = \frac{1}{T}\int_0^T \boldsymbol{R}^{FU}(t)dt$ is the period-averaged resistance matrix of the colony, $\boldsymbol{U}(t)$ is the instantaneous rods' velocity, $\boldsymbol{\phi}(t)$ are the Lagrange multipliers (forces) to satisfy the sliding velocity constraints (3.31) and $\boldsymbol{B}(t)$ is the relative sliding speed between pairs of rods (see last row of Table 3.1). The inset of Figure 6.4a shows that, for a fixed cell aspect ratio $L/H = 8.7$, the efficiency follows a similar trend to the swimming speed: the fastest swimming mode, obtained for $N_\lambda = 0.2$, is also the most efficient one.

In order to investigate the effect of the cell geometry on the swimming efficiency, we fix the number of rods ($N_{rods} = 50$) and vary their aspect ratio L/H. As shown on Fig. 6.4b the optimal wavelength jumps from $N_\lambda \approx 1.2$ for $L/H < 4.5$ to $N_\lambda \approx 0.2$ when $L/H > 4.5$. The optimal value $N_\lambda \approx 1.2$ is close to the one obtained by Higdon (Higdon, 1979*b*) and Dresdner (Dresdner *et al.*, 1980) for slender flagella deforming with a sinusoidal traveling wave (red line). The resemblance with flagellar dynamics at small aspect ratio is not so surprising since in the limit $L/H = 1$ the drag anisotropy of the colony is similar to that of slender filaments. Figure

6.4c shows the maximal efficiency as a function of the rod aspect ratio and colony size. For large enough colonies ($N_{rods} \geq 15$), the optimal aspect ratio stabilizes around $L/H = 9$, which is of the same order of magnitude as the one measured in natural cells ($\approx 6 - 20$).

To conclude, our toy model with a simple sinusoidal sliding motion exhibits new behaviors compared to classical flagellar dynamics:

- we have found a new optimal swimming mode where the colony travels *fast* (up to 1.3 colony length per sliding period) *in the direction* of the traveling wave with *a large wavelength* ($\lambda \approx 5L_c$).
- due to hydrodynamic interactions between the rod-like cells, non-reciprocal motion can lead to zero swimming speed ($N_\lambda \approx 0.6$).
- the optimal swimming mode and swimming efficiency are highly dependent on the rod aspect ratio, and the colony behaves like a flagellum when $L/H \to 1$.

While we do not have yet simple physical arguments to explain all these new features, we believe that the drag anisotropy between the normal and tangent directions to the colony centerline plays a crucial role. For a filament waving sinusoidally along the $x-$direction, the swimming speed is proportional to the difference between the tangential and normal drag coefficients: $\boldsymbol{V}_{swim} \sim (\xi_\parallel - \xi_\perp)\boldsymbol{e}_x$ (Lauga & Powers, 2009). For a slender object the drag anistropy is such that the filament always moves in the direction opposite to the wave: $\xi_\parallel - \xi_\perp \approx -\frac{1}{2}\xi_\perp < 0$. However, as the filament "thickens", i.e. when the cell aspect ratio L/H increases, the longitudinal drag can overcome the normal one ($\xi_\parallel > \xi_\perp$), which leads to a change in direction and swimming speed. This motion reversal has been observed for zoospores (Tran *et al.*, 2022). Zoospores are motile spore cells with a beating flagellum covered by semi-rigid rods, called mastigonemes, whose distribution along the centerline can change the longitudinal drag and thus the direction of motion of the microorganism.

6.3 Data extraction and comparisons with experiments

While instructive, the toy model introduced above does not reproduce the diversity conformations of *B. Paxillifer*. In order to model more realistic cell motion and colony motility, we developed a simple method to extract the sliding motion from experimental videos and then used them as kinematic constraints in simulations. The resulting motion of the colony can then be compared with experiments.

6.3.1 Extracting sliding motion from experiments

In order to extract the relative sliding motion between cells, we designed a minimization algorithm that represents the colony as a collection of N_{rods} coplanar rectangular rods with identical length L and height H. The rods all have the same orientation angle θ and are constrained to remain at a fixed normal distance H from each other. Given these constraints, the position of any rod i within the colony can be determined with the position of the first rod and the relative

sliding distances L_{pq} (see Fig. 6.5b):

$$\begin{pmatrix} x_i \\ y_i \end{pmatrix} = \begin{pmatrix} x_1 \\ y_1 \end{pmatrix} + \sum_{j=2}^{i} \boldsymbol{R}(\theta) \cdot \begin{pmatrix} L_{j-1,j} \\ H \end{pmatrix}, \tag{6.10}$$

where $\boldsymbol{R}(\theta)$ is a rotation matrix.

We define the set of known, time-independent, parameters that are intrinsic to the colony and easily measurable

$$\boldsymbol{P} = \begin{pmatrix} N_{rods} \\ L \\ H \end{pmatrix}, \tag{6.11}$$

and the set of unknown, time-dependent, variables

$$\boldsymbol{X} = \begin{pmatrix} x_1 \\ y_1 \\ L_{12} \\ L_{23} \\ \vdots \\ L_{N_{rods}-1,N_{rods}} \\ \theta \end{pmatrix}. \tag{6.12}$$

Our algorithm seeks to minimize, at each frame, the difference between the binarized experimental image I^{exp} and the synthetic one I^{num} generated with rectangular cells:

$$\boldsymbol{X}^{\star} = \arg\min_{\boldsymbol{X}} \left[\sum_{i,j} \left(I_{ij}^{exp} - I_{ij}^{num}(\boldsymbol{X}, \boldsymbol{P}) \right)^2 \right]. \tag{6.13}$$

The sliding motions extracted at each frame from the minimization algorithm are then interpolated in time with Fourier series. The resulting mathematical expressions $L_{pq}(t)$ are then directly plugged into the kinematic constraints (6.1)-(6.3) which are read by the code from a single input file. Figure 6.5 provides a diagram that illustrates the whole extraction process (the interpolated sliding motion is shown only for two pairs of rods).

6.3.2 Preliminary comparisons with experiments

Figure 6.6 presents a comparison of the orientational and translational dynamics measured in a YouTube video (`https://www.youtube.com/watch?v=4r8rEIxBkVc`, 7min34), for which the experimental conditions are unknown, against numerical simulations, where the relative sliding motion has been extracted from the video, in an unbounded fluid in the absence of external forces and torques. The simulations accurately reproduce the rotation of the colony (panel (a)); however, the predicted trajectory of the colony center of mass significantly diverges from the experimental one (panel (b)). An examination of the experimental trajectory of each cell in panel (d) reveals that some rods exhibit minimal movement within the colony, as if they were

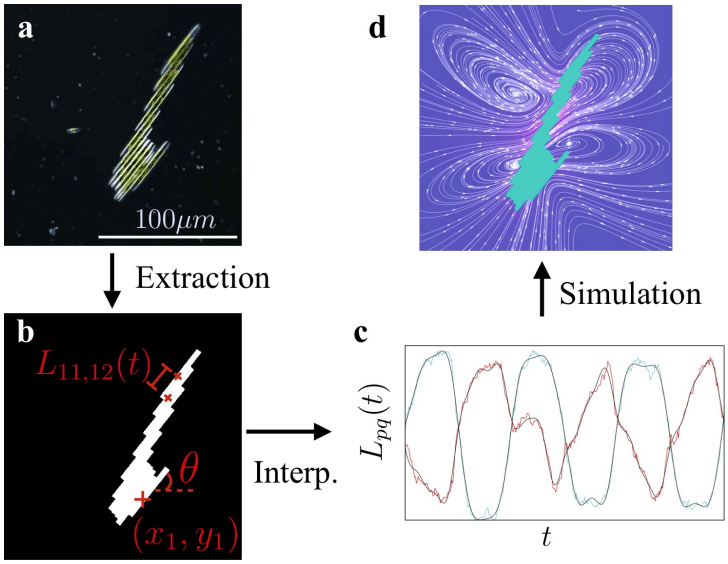

Figure 6.5: Schematic of the extraction process. (a) Raw Youtube video (https://www.youtube.com/watch?v=4r8rEIxBkVc, 7min34). (b) Reconstructed video with identical rods using the minimization algorithm. (c) Sliding motion of two pairs of rods extracted from the reconstruction. Red and blue lines: extracted data for two pairs of rods. Black lines: interpolated signal using Fourier decomposition. (d) Snapshot of a numerical simulation using the interpolated signal $L_{pq}(t)$.

fixed or adhering to a substrate below. This discrepancy may be attributed to lubrication forces and/or adhesive forces induced by the mucilage excreted from the lateral raphes of the cells above the substrate. However, the lack of knowledge regarding the experimental conditions precludes further comparisons.

Nevertheless these first results are encouraging and suggest several avenues for future investigation, which we outline below.

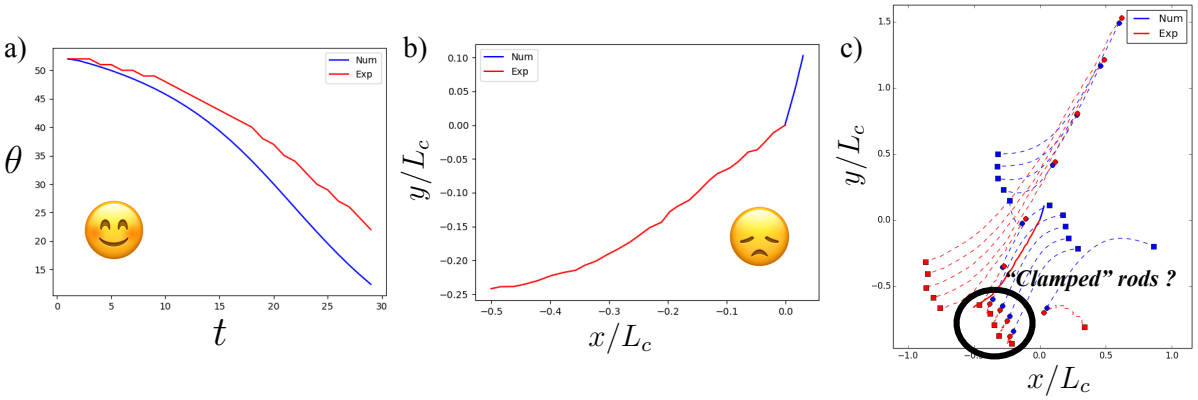

Figure 6.6: (a) Time evolution of the colony orientation. Red line: experiments. Blue line: numerical simulation. (b) Trajectory of the colony center of mass. (c) Motion of the rods' center of mass. Diamonds: initial positions. Squares: final positions.

6.4 Perspectives

1. **Infer adhesive and active forces by combining numerics and experiments.** The mechanisms underlying cell adhesion and sliding, as well as their interactions with a substrate, are poorly understood. Therefore, our numerical model with prescribed kinematics could be used to infer the adhesive and active stresses acting on the cells. The constraint forces computed in the simulations to prescribe the sliding motion extracted from experiments (3.32) provide an estimate of the active and adhesive forces at play between adjacent cells. Similarly, interaction forces with the substrate could be inferred by using the experimentally observed kinematics in simulations above a no-slip boundary (Kurjahn *et al.*, 2024).

2. **Measuring and comparing the induced flow fields.** The flow generated by the sliding cells not only propels the cells forward but also disrupts the motion of surrounding particles. This is of particular importance in the context of marine snow aggregates, where diatoms interact with a multitude of other objects, including bacteria, algae, microbes, detritus, and inorganic matter (Alldredge & Silver, 1988). A direct comparison of the flow field between simulations and experiments will also be useful for evaluating the accuracy of the model. Thus far, we have been able to seed the fluid around *B. Paxillifer* with small tracer particles in our preliminary experiments at a fluid-fluid interface. However our cultures did not survive more than a few days, and strong spurious Marangoni flows developed at the interface. More well-controlled experiments are required for further comparisons. Additionally, the collection of viable samples of *B. Paxillifer* is challenging due to the lack of knowledge regarding their seasonal and spatial distribution patterns. Fortunately, Jean-Luc Coulon, president of the "Chemins de Camargue" hiking club, whom we contacted by email, kindly agreed to collect some samples with live diatoms in Aigues-Mortes, which we were able to use for our preliminary experiments (see Fig. 6.7).

3. **Sedimentation and dynamics in background flows.** Due to their dense silica shells, diatoms are not only transported by the background flow but also sediment. The sedimentation of passive rigid objects with complex shapes at low Reynolds numbers leads to non-trivial trajectories and is only beginning to be investigated (Miara *et al.*, 2024; Huseby *et al.*, 2024). The settling dynamics of actively deforming particles is still awaiting further investigations. The objective of this study is to examine the impact of colony geometry (cell aspect ratio, number of cells) and sliding motion on their trajectory. Given the inherent variability in drag experienced by deforming colonies, it is anticipated that complex trajectories will be observed. To further elucidate the sinking dynamics of these colonies in more realistic conditions, different types of background flows will be introduced. The findings of this study will contribute to a deeper understanding of the fate of diatoms, and by extension marine snow aggregates, as they sediment towards the ocean depths.

4. **Optimizing the sliding motion.** The optimization of microswimmer swimming gaits represents a long-standing yet still active research topic. Our objective is to advance beyond the simplistic sinusoidal toy model to explore the diverse optimal swimming gaits enabled by the sliding motion between cells. The first objective is to maximize the swim-

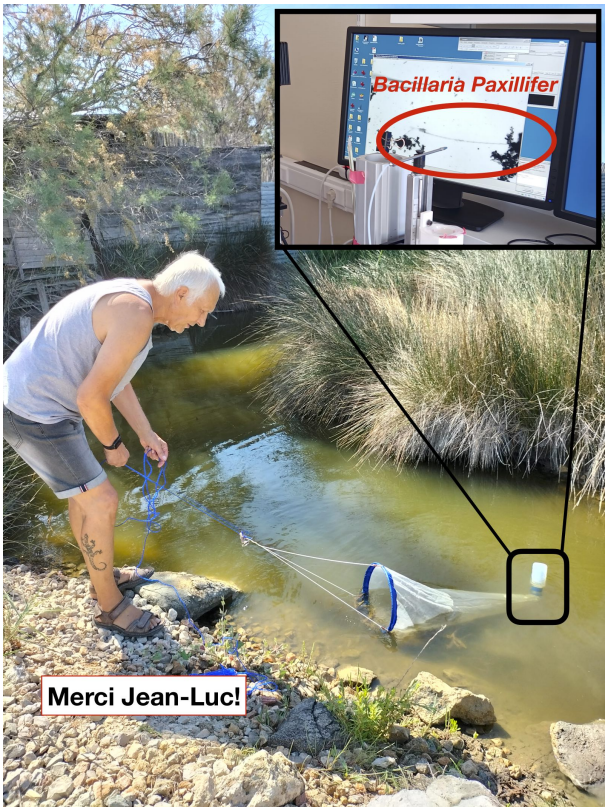

Figure 6.7: Jean-Luc Coulon collecting water samples in Camargue for the sake of Science. Merci Jean-Luc!

ming efficiency by tuning the coefficients of the Fourier decomposition of a periodic sliding motion (Tam & Hosoi, 2011). Subsequently, more sophisticated techniques, such as reinforcement learning (Zou *et al.*, 2022) or optimal control (Giraldi *et al.*, 2013), will be employed to investigate more complex, aperiodic, sliding motions. These approaches will facilitate the discovery of new optimal strategies that maximize the swimming efficiency or enable the completion of specific tasks, such as reaching a target destination.

Chapter 7

Conclusions

In the coming years, I will continue to work on the development of mathematical and numerical methods to model fluid-structure interactions and complex suspensions in collaboration with applied mathematicians. As outlined in the perspectives of Chapter 2, a number of approaches will be investigated with the aim of improving the accuracy of the rigid multiblob model. In particular, developing smart quadrature techniques that can balance the regularization error to achieve higher convergence while preserving the efficiency and robustness of the rigid multiblob method is a line of research that I find exciting.

In parallel with these developments, I will continue to investigate the physics of complex suspensions in collaboration with theoreticians and experimentalists. While a few remaining questions require further investigation, my involvement in the study of microroller suspensions will gradually diminish in the coming years. Regarding the motion of flexible fibers in structured and porous media, the TransClog project has yielded new insights and prompted further questions regarding the sorting potential of pillar arrays with different driving fields, their efficiency, and their applicability in real-life systems. As evidenced by the bullet list in the conclusions of Chapter 4, numerous fundamental and technological questions remain to be addressed. Additional funding will be needed to work on these topics as the ANR grant will end in September 2024. Finally, the *Bacillaria* project, at the interface of biology and fluid mechanics, is just beginning. The doctoral work of Julien le Dreff will start on October 1st. His initial focus will be on finalizing the analysis of the toy model and then moving on to comparisons with experiments for inferring the sliding and adhesive forces between cells or on a substrate. The remaining research directions outlined in the final section of Chapter 5 (optimization of the sliding motion, sedimentation and motion in background flows) will be addressed in a subsequent phase.

In the meantime, new research directions have emerged from discussions with other colleagues. I am starting a joint project involving experiments, theory and simulations, with Joshua McGraw (CR CNRS, Gulliver, ESPCI) and Thomas Salez (DR CNRS, LOMA, Bordeaux). Our objective is to investigate the collective diffusion of sheared colloidal suspensions near interfaces. An intern from ESPCI, Ruben Levy-Arditi, recently conducted preliminary simulations with the code that I co-develop (`https://github.com/stochasticHydroTools/RigidMultiblobsWall`) and corroborated the experimental results, demonstrating that particle diffusion is enhanced with increasing shear rate and volume fraction in a non-trivial manner. A PhD student from Bordeaux, Juliette Lacherez, will take over to rationalize these findings and explore other collective-diffusion-related questions in the vicinity of interfaces.

Together with Sebastien Michelin (LadHyX) and Florencio Balboa-Usabiaga (BCAM) we are planning to investigate the rheology of phoretic particles with complex shapes and/or sur-

face coatings. Our goal is to analyse the effective rheology and dynamic response of phoretic suspensions to mechanical forcing (e.g. shear flow). The surface coating and shape of a phoretic particle can be designed to encode a given hydro-chemical response. This provides a route for controlling their behavior at the collective level and the effective physical properties of a whole suspension, such as rheology. The project will exploit our numerical developments, presented in Chapter 2, to study in detail the evolution of the suspension's rheology with particle density, shape and surface properties, as well as its response to chemical signaling.

Bibliography

Alldredge, Alice L & Silver, Mary W 1988 Characteristics, dynamics and significance of marine snow. *Progress in oceanography* **20** (1), 41–82. (Cited on page 104.)

Anderson, J L 1989 Colloid transport by interfacial forces. *Annu. Rev. Fluid Mech.* **21** (1), 61–99. (Cited on pages 7 and 14.)

Ando, Tadashi, Chow, Edmond, Saad, Yousef & Skolnick, Jeffrey 2012 Krylov subspace methods for computing hydrodynamic interactions in brownian dynamics simulations. *The Journal of chemical physics* **137** (6), 064106. (Cited on pages 11 and 23.)

Ando, Tadashi, Chow, Edmond & Skolnick, Jeffrey 2013 Dynamic simulation of concentrated macromolecular solutions with screened long-range hydrodynamic interactions: Algorithm and limitations. *The Journal of chemical physics* **139** (12), 121922. (Cited on page 11.)

Aponte-Rivera, Christian & Zia, Roseanna N 2016 Simulation of hydrodynamically interacting particles confined by a spherical cavity. *Physical Review Fluids* **1** (2), 023301. (Cited on page 19.)

Balboa Usabiaga, Florencio & Delmotte, Blaise 2022 A numerical method for suspensions of articulated bodies in viscous flows. *Journal of Computational Physics* **464**, 111365. (Cited on pages 33 and 35.)

Balboa Usabiaga, Florencio, Delmotte, Blaise & Donev, Aleksandar 2017 Brownian dynamics of confined suspensions of active microrollers. *The Journal of Chemical Physics* **146** (13), 134104, software available at `https://github.com/stochasticHydroTools/RigidMultiblobsWall`, arXiv: http://dx.doi.org/10.1063/1.4979494. (Cited on page 49.)

Balboa Usabiaga, F & Ellero, M 2024 Rheology of moderated dilute suspensions of star colloids: The shape factor. *Physics of Fluids* **36** (5). (Cited on page 18.)

Beatus, Tsevi, Bar-Ziv, Roy H & Tlusty, Tsvi 2012 The physics of 2d microfluidic droplet ensembles. *Physics reports* **516** (3), 103–145. (Cited on page 48.)

Beatus, Tsevi, Tlusty, Tsvi & Bar-Ziv, Roy 2009 Burgers shock waves and sound in a 2d microfluidic droplets ensemble. *Physical review letters* **103** (11), 114502. (Cited on page 50.)

Beech, Jason P, Ho, Bao Dang, Garriss, Geneviève, Oliveira, Vitor, Henriques-Normark, Birgitta & Tegenfeldt, Jonas O 2018 Separation of pathogenic bacteria by chain length. *Analytica chimica acta* **1000**, 223–231. (Cited on page 66.)

Bell, John B, Dawson, Clint N & Shubin, Gregory R 1988 An unsplit, higher order godunov method for scalar conservation laws in multiple dimensions. *Journal of Computational Physics* **74** (1), 1–24. (Cited on page 53.)

Bender, Carl M. & Orszag, Steven A. 1999 *Advanced Mathematical Methods for Scientists and Engineers I*. New York, NY: Springer New York. (Cited on page 72.)

Berg, Howard C. & Anderson, Robert A. 1973 Bacteria Swim by Rotating their Flagellar Filaments. *Nature* **245** (5425), 380–382, bandiera_abtest: a Cg_type: Nature Research Journals Number: 5425 Primary_atype: Research Publisher: Nature Publishing Group. (Cited on page 11.)

Bhalla, Amneet Pal Singh, Griffith, Boyce E., Patankar, Neelesh A. & Donev, Aleksandar 2013 A minimally-resolved immersed boundary model for reaction-diffusion problems. *The Journal of Chemical Physics* **139**, 214112. (Cited on page 14.)

Bielinski, Clément, Li, Zhibo, Lindner, Anke, Delmotte, Blaise & du Roure, Olivia 2024 Optimized separation of flexible fibers by deterministic lateral displacement. *In preparation* . (Cited on pages 2 and 83.)

Bililign, Ephraim S, Balboa Usabiaga, Florencio, Ganan, Yehuda A, Poncet, Alexis, Soni, Vishal, Magkiriadou, Sofia, Shelley, Michael J, Bartolo, Denis & Irvine, William TM 2022 Motile dislocations knead odd crystals into whorls. *Nature Physics* **18** (2), 212–218. (Cited on page 18.)

Blake, JR 1971*a* A spherical envelope approach to ciliary propulsion. *Journal of Fluid Mechanics* **46** (01), 199–208. (Cited on page 7.)

Blake, JR & Chwang, AT 1974 Fundamental singularities of viscous flow. *Journal of Engineering Mathematics* **8** (1), 23–29. (Cited on pages 48, 57 and 60.)

Blake, J. R. 1971*b* A spherical envelope approach to ciliary propulsion. *J. Fluid Mech.* **46** (1), 199–208. (Cited on page 27.)

Boegh, Marie & Nielsen, Hanne Mørck 2015 Mucus as a barrier to drug delivery–understanding and mimicking the barrier properties. *Basic & clinical pharmacology & toxicology* **116** (3), 179–186. (Cited on page 92.)

Bourrianne, Philippe, Niggel, Vincent, Polly, Gatien, Divoux, Thibaut & McKinley, Gareth H 2022 Tuning the shear thickening of suspensions through surface roughness and physico-chemical interactions. *Physical Review Research* **4** (3), 033062. (Cited on pages 2 and 22.)

Bozuyuk, Ugur, Suadiye, Eylul, Aghakhani, Amirreza, Dogan, Nihal Olcay, Lazovic, Jelena, Tiryaki, Mehmet Efe, Schneider, Martina, Karacakol, Alp Can, Demir, Sinan Ozgun, Richter, Gunther & others 2022 High-performance magnetic fept (l10) surface microrollers towards medical imaging-guided endovascular delivery applications. *Advanced Functional Materials* **32** (8), 2109741. (Cited on page 45.)

Brady, J F & Bossis, G 1988 Stokesian dynamics. *Annu. Rev. Fluid Mech.* **20** (1), 111–157. (Cited on page 9.)

Bricard, Antoine, Caussin, Jean-Baptiste, Desreumaux, Nicolas, Dauchot, Olivier & Bartolo, Denis 2013 Emergence of macroscopic directed motion in populations of motile colloids. *Nature* **503** (7474), 95–98. (Cited on page 45.)

Bringley, Thomas T. & Peskin, Charles S. 2008 Validation of a simple method for representing spheres and slender bodies in an immersed boundary method for stokes flow on an unbounded domain. *Journal of Computational Physics* **227**, 5397. (Cited on page 97.)

Brokaw, CJ 1965 Non-sinusoidal bending waves of sperm flagella. *J. exp. Biol* **43** (1), 155–169. (Cited on page 96.)

Broms, Anna, Sandberg, Mattias & Tornberg, Anna-Karin 2023 A locally corrected multiblob method with hydrodynamically matched grids for the stokes mobility problem. *Journal of Computational Physics* **487**, 112172. (Cited on page 26.)

Brooks, Allan M, Tasinkevych, Mykola, Sabrina, Syeda, Velegol, Darrell, Sen, Ayusman & Bishop, Kyle JM 2019 Shape-directed rotation of homogeneous micromotors via catalytic self-electrophoresis. *Nature communications* **10** (1), 495. (Cited on page 32.)

Brosseau, Quentin, Usabiaga, Florencio Balboa, Lushi, Enkeleida, Wu, Yang, Ristroph, Leif, Ward, Michael D, Shelley, Michael J & Zhang, Jun 2021 Metallic microswimmers driven up the wall by gravity. *Soft Matter* **17** (27), 6597–6602. (Cited on pages 18 and 31.)

Brosseau, Quentin, Usabiaga, Florencio Balboa, Lushi, Enkeleida, Wu, Yang, Ristroph, Leif, Zhang, Jun, Ward, Michael & Shelley, Michael J 2019 Relating rheotaxis and hydrodynamic actuation using asymmetric gold-platinum phoretic rods. *Physical review letters* **123** (17), 178004. (Cited on page 18.)

Brotto, Tommaso, Caussin, Jean-Baptiste, Lauga, Eric & Bartolo, Denis 2013 Hydrodynamics of confined active fluids. *Physical review letters* **110** (3), 038101. (Cited on page 48.)

Brouzet, Christophe, Verhille, Gautier & Le Gal, Patrice 2014 Flexible fiber in a turbulent flow: a macroscopic polymer. *Physical review letters* **112** (7), 074501. (Cited on page 4.)

Chakrabarti, Brato, Gaillard, Charles & Saintillan, David 2020*a* Trapping, gliding, vaulting: transport of semiflexible polymers in periodic post arrays. *Soft Matter* **16** (23), 5534–5544, publisher: The Royal Society of Chemistry. (Cited on pages 66 and 77.)

Chakrabarti, Brato, Liu, Yanan, LaGrone, John, Cortez, Ricardo, Fauci, Lisa, Du Roure, Olivia, Saintillan, David & Lindner, Anke 2020*b* Flexible filaments buckle into helicoidal shapes in strong compressional flows. *Nature Physics* **16** (6), 689–694. (Cited on pages 84 and 85.)

Chamolly, Alexander, Lauga, Eric & Tottori, Soichiro 2020 Irreversible hydrodynamic trapping by surface rollers. *Soft matter* **16** (10), 2611–2620. (Cited on page 45.)

Champagne, Nicolas, Lauga, Eric & Bartolo, Denis 2011 Stability and non-linear response of 1d microfluidic-particle streams. *Soft Matter* **7** (23), 11082–11085. (Cited on page 50.)

Chelakkot, Raghunath, Winkler, Roland G & Gompper, Gerhard 2012 Flow-induced helical coiling of semiflexible polymers in structured microchannels. *Physical review letters* **109** (17), 178101. (Cited on page 85.)

Chen, Yu, Abrams, Ezra S., Boles, T. Christian, Pedersen, Jonas N., Flyvbjerg, Henrik, Austin, Robert H. & Sturm, James C. 2015 Concentrating genomic length DNA in a microfabricated array. *Physical Review Letters* **114** (19), 198303. (Cited on page 66.)

Chow, Edmond & Saad, Yousef 2014 Preconditioned Krylov Subspace Methods for Sampling Multivariate Gaussian Distributions. *SIAM Journal on Scientific Computing* **36** (2), A588–A608. (Cited on pages 11 and 23.)

Cortez, R 2001 The method of regularized Stokeslets. *SIAM J. Sci. Comput.* **23** (4), 1204–1225. (Cited on page 11.)

Cui, Bianxiao, Diamant, Haim, Lin, Binhua & Rice, Stuart A 2004 Anomalous hydrodynamic interaction in a quasi-two-dimensional suspension. *Physical review letters* **92** (25), 258301. (Cited on page 48.)

Cunha, Lucas H. P., Zhao, Jingjing, MacKintosh, Fred C. & Biswal, Sibani Lisa 2022 Settling dynamics of Brownian chains in viscous fluids. *Physical Review Fluids* **7** (3), 034303. (Cited on page 67.)

Delmotte, Blaise 2019 Hydrodynamically bound states of a pair of microrollers: A dynamical system insight. *Physical Review Fluids* **4** (4), 044302. (Cited on page 44.)

Delmotte, Blaise 2023 Viscosity ratio across interfaces controls the stability and self-assembly of microrollers. *Physical Review Fluids* **8** (6), L062302. (Cited on pages 19 and 56.)

Delmotte, Blaise, Climent, Eric & Plouraboué, Franck 2015*a* A general formulation of bead models applied to flexible fibers and active filaments at low reynolds number. *Journal of Computational Physics* **286**, 14 – 37. (Cited on page 33.)

Delmotte, Blaise, Donev, Aleksandar, Driscoll, Michelle & Chaikin, Paul 2017*a* Minimal model for a hydrodynamic fingering instability in microroller suspensions. *Physical Review Fluids* **2** (11), 114301. (Cited on pages 49 and 54.)

Delmotte, Blaise, Driscoll, Michelle, Chaikin, Paul & Donev, Aleksandar 2017*b* Hydrodynamic shocks in microroller suspensions. *Physical Review Fluids* **2** (9), 092301(R). (Cited on pages 46 and 49.)

Delmotte, Blaise & Keaveny, Eric E 2015 Simulating brownian suspensions with fluctuating hydrodynamics. *The Journal of chemical physics* **143** (24), 244109. (Cited on pages 10, 11, 24 and 25.)

Delmotte, Blaise, Keaveny, Eric E., Plouraboue, Franck & Climent, Eric 2015*b* Large-scale simulation of steady and time-dependent active suspensions with the force-coupling method. *Journal of Computational Physics* **302**, 524 – 547. (Cited on page 25.)

Delmotte, Blaise & Usabiaga, Florencio Balboa 2024 A scalable method to model large suspensions of colloidal phoretic particles with arbitrary shapes. *arXiv preprint arXiv:2403.05337* . (Cited on pages 18, 25, 26, 27, 28, 30 and 39.)

Delong, Steven, Usabiaga, Florencio Balboa, Delgado-Buscalioni, Rafael, Griffith, Boyce E & Donev, Aleksandar 2014 Brownian dynamics without green's functions. *The Journal of chemical physics* **140** (13), 134110. (Cited on pages 10, 11, 21 and 24.)

Delong, Steven, Usabiaga, Florencio Balboa & Donev, Aleksandar 2015 Brownian dynamics of confined rigid bodies. *The Journal of chemical physics* **143** (14), 144107. (Cited on pages 8 and 19.)

Demirörs, Ahmet F, Stauffer, Alex, Lauener, Carmen, Cossu, Jacopo, Ramakrishna, Shivaprakash N, de Graaf, Joost, Alcantara, Carlos CJ, Pané, Salvador, Spencer, Nicholas & Studart, André R 2021 Magnetic propulsion of colloidal microrollers controlled by electrically modulated friction. *Soft Matter* **17** (4), 1037–1047. (Cited on page 45.)

Desreumaux, Nicolas, Caussin, Jean-Baptiste, Jeanneret, Raphael, Lauga, Eric & Bartolo, Denis 2013 Hydrodynamic fluctuations in confined particle-laden fluids. *Physical review letters* **111** (11), 118301. (Cited on pages 48 and 49.)

Długosz, Maciej, Cichocki, Bogdan & Szymczak, Piotr 2022 Estimating near-wall diffusion coefficients of arbitrarily shaped rigid macromolecules. *Physical Review E* **106** (1), 014407. (Cited on page 18.)

Długosz, Maciej, Cichocki, Bogdan & Szymczak, Piotr 2023 First coarse grain then scale: How to estimate diffusion coefficients of confined molecules. *The Journal of Chemical Physics* **159** (21). (Cited on page 18.)

Dombrowski, Thomas, Jones, Shannon K, Katsikis, Georgios, Bhalla, Amneet Pal Singh, Griffith, Boyce E & Klotsa, Daphne 2019 Transition in swimming direction in a model self-propelled inertial swimmer. *Physical Review Fluids* **4** (2), 021101. (Cited on page 18.)

Dombrowski, Thomas & Klotsa, Daphne 2020 Kinematics of a simple reciprocal model swimmer at intermediate reynolds numbers. *Physical Review Fluids* **5** (6), 063103. (Cited on page 18.)

Domínguez, Alvaro & Popescu, Mihail N 2022 A fresh view on phoresis and self-phoresis. *Current Opinion in Colloid & Interface Science* p. 101610. (Cited on page 13.)

Douglas, Ross G, Amino, Rogerio, Sinnis, Photini & Frischknecht, Freddy 2015 Active migration and passive transport of malaria parasites. *Trends in parasitology* **31** (8), 357–362. (Cited on page 92.)

Drescher, Knut, Shen, Yi, Bassler, Bonnie L. & Stone, Howard A. 2013 Biofilm streamers cause catastrophic disruption of flow with consequences for environmental and medical systems. *Proceedings of the National Academy of Sciences* **110** (11), 4345–4350. (Cited on page 65.)

Dresdner, RD, Katz, DF & Berger, SA 1980 The propulsion by large amplitude waves of uniflagellar micro-organisms of finite length. *Journal of Fluid Mechanics* **97** (3), 591–621. (Cited on pages 96 and 100.)

Dreyfus, Rémi, Baudry, Jean, Roper, Marcus L., Fermigier, Marc, Stone, Howard A. & Bibette, Jérôme 2005 Microscopic artificial swimmers. *Nature* **437** (7060), 862–865. (Cited on page 11.)

Driscoll, Michelle & Delmotte, Blaise 2018 Leveraging collective effects in externally driven colloidal suspensions: Experiments and simulations. *Current Opinion in Colloid & Interface Science* . (Cited on pages 46 and 49.)

Driscoll, Michelle, Delmotte, Blaise, Youssef, Mena, Sacanna, Stefano, Donev, Aleksandar & Chaikin, Paul 2016 Unstable fronts and motile structures formed by microrollers. *Nature Physics* . (Cited on pages 2, 44, 46 and 49.)

Du Roure, O, Lindner, A., Nazockdast, E N & Shelley, M J 2019 Dynamics of flexible fibers in viscous flows and fluids. *Annual Review of Fluid Mechanics* Publisher: Annual Reviews. (Cited on pages 77 and 85.)

D'Angelo, M. V., Semin, B., Picard, G., Poitzsch, M. E., Hulin, J. P. & Auradou, H. 2010 Single Fiber Transport in a Fracture Slit: Influence of the Wall Roughness and of the Fiber Flexibility. *Transport in Porous Media* **84** (2), 389–408. (Cited on page 65.)

Engdahl, Nicholas B. 2018 Simulating the mobility of micro-plastics and other fiber-like objects in saturated porous media using constrained random walks. *Advances in Water Resources* **121**, 277–284. (Cited on page 65.)

Ermak, Donald L. & McCammon, J. A. 1978 Brownian dynamics with hydrodynamic interactions. *The Journal of Chemical Physics* **69** (4), 1352–1360. (Cited on page 10.)

Fabritiis, G. De, Serrano, M., Delgado-Buscalioni, R. & Coveney, P. V. 2007 Fluctuating hydrodynamic modeling of fluids at the nanoscale. *Physical Review E* **75**, 026307. (Cited on page 10.)

Featherstone, Roy 1987 *Robot Dynamics Algorithms*, *Robotics: Vision, Manipulation and Sensors*, vol. 22. Springer US. (Cited on page 13.)

Fei, Wenjie, Gu, Yang & Bishop, Kyle JM 2017 Active colloidal particles at fluid-fluid interfaces. *Current opinion in colloid & interface science* **32**, 57–68. (Cited on page 64.)

Fei, Wenjie, Tzelios, Peter M & Bishop, Kyle JM 2020 Magneto-capillary particle dynamics at curved interfaces: time-varying fields and drop mixing. *Langmuir* . (Cited on page 64.)

Fiore, Andrew M, Balboa Usabiaga, Florencio, Donev, Aleksandar & Swan, James W 2017 Rapid sampling of stochastic displacements in brownian dynamics simulations. *The Journal of chemical physics* **146** (12), 124116. (Cited on pages 23 and 74.)

Fiore, Andrew M & Swan, James W 2018 Rapid sampling of stochastic displacements in brownian dynamics simulations with stresslet constraints. *The Journal of chemical physics* **148** (4), 044114. (Cited on page 23.)

Fixman, Marshall 1978 Simulation of polymer dynamics. I. General theory. *The Journal of Chemical Physics* **69** (4), 1527–1537. (Cited on page 11.)

Fixman, Marshall 1986 Construction of Langevin forces in the simulation of hydrodynamic interaction. *Macromolecules* **19** (4), 1204–1207. (Cited on page 11.)

Fuentes, Yuris O, Kim, Sangtae & Jeffrey, David J 1989 Mobility functions for two unequal viscous drops in stokes flow. ii. asymmetric motions. *Physics of Fluids A: Fluid Dynamics* **1** (1), 61–76. (Cited on page 57.)

Gao, Yan, Sprinkle, Brennan, Springer, Ela, Marr, David WM & Wu, Ning 2023 Rolling of soft microbots with tunable traction. *Science Advances* **9** (16), eadg0919. (Cited on page 18.)

Gidituri, H, Ellero, M & Usabiaga, F Balboa 2023 Swimming efficiently by wrapping. *arXiv preprint arXiv:2307.04243* . (Cited on page 18.)

Gidituri, Harinadha, Kabacaoğlu, Gökberk, Ellero, Marco & Usabiaga, Florencio Balboa 2024 Mapping flagellated swimmers to surface-slip driven swimmers. *Journal of Computational Physics* **510**, 113081. (Cited on pages 18 and 19.)

Giraldi, Laetitia, Martinon, Pierre & Zoppello, Marta 2013 Controllability and optimal strokes for n-link microswimmer. In *52nd IEEE Conference on Decision and Control*, pp. 3870–3875. IEEE. (Cited on page 105.)

Goldstein, Herbert, Poole, Charles & Safko, John 2001 *Classical mechanics (3rd ed.)*. Addison-Wesley. (Cited on page 33.)

Golestanian, Ramin, Liverpool, TB & Ajdari, A 2007 Designing phoretic micro-and nano-swimmers. *New Journal of Physics* **9** (5), 126. (Cited on pages 7 and 13.)

Gordon, Richard 2016 Partial synchronization of the colonial diatom Bacillaria "paradoxa". *Research Ideas and Outcomes* **2**, e7869, publisher: Pensoft Publishers. (Cited on pages 11 and 95.)

Grassia, P. S., Hinch, E. J. & Nitsche, L. C. 1995 Computer simulations of Brownian motion of complex systems. *Journal of Fluid Mechanics* **282**, 373–403. (Cited on page 11.)

Grzybowski, Bartosz A, Stone, Howard A & Whitesides, George M 2000 Dynamic self-assembly of magnetized, millimetre-sized objects rotating at a liquid–air interface. *Nature* **405** (6790), 1033–1036. (Cited on page 45.)

Gustavsson, K. & Tornberg, A.-K. 2009 Gravity induced sedimentation of slender fibers. *Physics of Fluids* **21** (12), 123301. (Cited on page 92.)

Hansen, Nikolaus & Ostermeier, Andreas 2001 Completely derandomized self-adaptation in evolution strategies. *Evolutionary computation* **9** (2), 159–195. (Cited on page 90.)

Harbich, Thomas 2023 Modeling the synchronization of the movement of bacillaria paxillifer by a kuramoto model with time delay. *The Mathematical Biology of Diatoms* pp. 193–228. (Cited on pages 95 and 96.)

Hashemi, Aref, Peláez, Raúl P, Natesh, Sachin, Sprinkle, Brennan, Maxian, Ondrej, Gan, Zecheng & Donev, Aleksandar 2023 Computing hydrodynamic interactions in confined doubly periodic geometries in linear time. *The Journal of Chemical Physics* **158** (15). (Cited on page 25.)

Herzhaft, Benjamin & Guazzelli, Élisabeth 1999 Experimental study of the sedimentation of dilute and semi-dilute suspensions of fibres. *Journal of Fluid Mechanics* **384**, 133–158. (Cited on page 92.)

Higdon, JJL 1979*a* The hydrodynamics of flagellar propulsion: helical waves. *Journal of Fluid Mechanics* **94** (2), 331–351. (Cited on pages 35, 36 and 96.)

Higdon, J. J. L. 1979*b* A hydrodynamic analysis of flagellar propulsion. *Journal of Fluid Mechanics* **90** (04), 685. (Cited on pages 96 and 100.)

Hinch, E. J. 1975 Application of the langevin equation to fluid suspensions. *Journal of Fluid Mechanics* **72**, 499–511. (Cited on page 10.)

Hinch, E. J. 1991 *Perturbation Methods*. Cambridge: Cambridge University Press. (Cited on page 72.)

Hoeger, Kentaro & Ursell, Tristan 2021 Steric scattering of rod-like swimmers in low reynolds number environments. *Soft Matter* **17** (9), 2479–2489. (Cited on page 61.)

Holm, Stefan H, Beech, Jason P, Barrett, Michael P & Tegenfeldt, Jonas O 2011 Separation of parasites from human blood using deterministic lateral displacement. *Lab on a Chip* **11** (7), 1326–1332. (Cited on page 66.)

Holm, Stefan H, Zhang, Zunmin, Beech, Jason P, Gompper, Gerhard, Fedosov, Dmitry A & Tegenfeldt, Jonas O 2019 Microfluidic particle sorting in concentrated erythrocyte suspensions. *Physical Review Applied* **12** (1), 014051. (Cited on page 66.)

Howard, P.R., King, M.T., Morris, M., Feraud, J-P, Slusher, G. & Lipari, S. 1995 Fiber/proppant mixtures control proppant flowback in south texas. *SPE Annual Technical Conference and Exhibition*, vol. All Days. SPE-30495-MS. (Cited on page 65.)

Huang, Lotien Richard, Cox, Edward C, Austin, Robert H & Sturm, James C 2004 Continuous particle separation through deterministic lateral displacement. *Science* **304** (5673), 987–990. (Cited on page 65.)

Huseby, Elias, Gissinger, Josephine, Candelier, Fabien, Pujara, Nimish, Verhille, Gautier, Mehlig, Bernhard & Voth, Greg 2024 Helical ribbons: Simple chiral sedimentation. *arXiv preprint arXiv:2403.18157* . (Cited on page 104.)

Illien, Pierre, Golestanian, Ramin & Sen, Ayusman 2017 'fuelled'motion: phoretic motility and collective behaviour of active colloids. *Chemical Society Reviews* **46** (18), 5508–5518. (Cited on page 13.)

iNaturalist 2017 Photo 11624974, https://www.inaturalist.org/photos/11624974. (Cited on pages 2 and 96.)

Jang, Bumjin, Gutman, Emiliya, Stucki, Nicolai, Seitz, Benedikt F, Wendel-García, Pedro D, Newton, Taylor, Pokki, Juho, Ergeneman, Olgaç, Pané, Salvador, Or, Yizhar & others 2015 Undulatory locomotion of magnetic multilink nanoswimmers. *Nano letters* **15** (7), 4829–4833. (Cited on page 11.)

Johnson, Russell C 1977 The spirochetes. *Annual Reviews in Microbiology* **31** (1), 89–106. (Cited on page 92.)

Johnson, Robert E. 1980 An improved slender-body theory for Stokes flow. *Journal of Fluid Mechanics* **99** (2), 411–431, publisher: Cambridge University Press. (Cited on page 72.)

Kabacaoğlu, Gökberk & Biros, George 2018 Optimal design of deterministic lateral displacement device for viscosity-contrast-based cell sorting. *Physical Review Fluids* **3** (12), 124201. (Cited on page 66.)

Kapinga, Margaret R. M. & Gordon, Richard 1992 Cell attachment in the motile colonial diatom bacillaria paxillifer. *Diatom Research* **7** (2), 215–220, publisher: Taylor & Francis. (Cited on pages 11, 95 and 96.)

Karani, Hamid, Pradillo, Gerardo E & Vlahovska, Petia M 2019 Tuning the random walk of active colloids: From individual run-and-tumble to dynamic clustering. *Physical review letters* **123** (20), 208002. (Cited on page 45.)

Kawale, Durgesh, Bouwman, Gelmer, Sachdev, Shaurya, Zitha, Pacelli L. J., Kreutzer, Michiel T., Rossen, William R. & Boukany, Pouyan E. 2017 Polymer conformation during flow in porous media. *Soft Matter* **13** (46), 8745–8755. (Cited on page 77.)

Keaveny, Eric E 2014 Fluctuating force-coupling method for simulations of colloidal suspensions. *Journal of Computational Physics* **269**, 61–79. (Cited on pages 11, 24 and 25.)

Keller, Joseph B. & Rubinow, Sol I. 1976 Slender-body theory for slow viscous flow. *Journal of Fluid Mechanics* **75** (4), 705–714. (Cited on page 72.)

Ketzetzi, Stefania, Rinaldin, Melissa, Dröge, Pim, Graaf, Joost de & Kraft, Daniela J 2022 Activity-induced interactions and cooperation of artificial microswimmers in one-dimensional environments. *Nature Communications* **13** (1), 1–10. (Cited on page 61.)

Kim, Sangtae & Karrila, Seppo J 1991 *Microhydrodynamics: principles and selected applications*. Courier Dover Publications. (Cited on pages 7, 57 and 83.)

Kirch, Julian, Schneider, Andreas, Abou, Bérengère, Hopf, Alexander, Schaefer, Ulrich F, Schneider, Marc, Schall, Christian, Wagner, Christian & Lehr, Claus-Michael 2012 Optical tweezers reveal relationship between microstructure and nanoparticle penetration of pulmonary mucus. *Proceedings of the National Academy of Sciences* **109** (45), 18355–18360. (Cited on page 92.)

Krueger, Timm, Kusumaatmaja, Halim, Kuzmin, Alexandr, Shardt, Orest, Silva, Goncalo & Viggen, Erlend Magnus 2016 *The Lattice Boltzmann Method: Principles and Practice*. Springer. (Cited on page 78.)

Kumar, Piyush, Zhang, Yi, Ebbens, Stephen J & Zhao, Xiubo 2022 3d inkjet printed self-propelled motors for micro-stirring. *Journal of Colloid and Interface Science* **623**, 96–108. (Cited on page 32.)

Kurjahn, Maximilian, Deka, Antaran, Girot, Antoine, Abbaspour, Leila, Klumpp, Stefan, Lorenz, Maike, Bäumchen, Oliver & Karpitschka, Stefan 2024 Quantifying gliding forces of filamentous cyanobacteria by self-buckling. *Elife* **12**, RP87450. (Cited on page 104.)

Landau, L.D. & Lifshitz, E.M. 1959 *Fluid Mechanics*. Pergamon Press. (Cited on pages 10 and 24.)

Lauga, Eric 2020 Traveling waves are hydrodynamically optimal for long-wavelength flagella. *Physical Review Fluids* **5** (12), 123101. (Cited on page 96.)

Lauga, Eric, DiLuzio, Willow R., Whitesides, George M. & Stone, Howard A. 2006 Swimming in circles: Motion of bacteria near solid boundaries. *Biophysical Journal* **90** (2), 400–412. (Cited on page 37.)

Lauga, Eric & Eloy, Christophe 2013 Shape of optimal active flagella. *Journal of Fluid Mechanics* **730**, R1. (Cited on page 96.)

Lauga, E. & Powers, T. R 2009 The hydrodynamics of swimming microorganisms. *Rep. Prog. Phys.* **72** (9), 096601. (Cited on page 101.)

Lauga, Eric & Squires, Todd M 2005 Brownian motion near a partial-slip boundary: A local probe of the no-slip condition. *Physics of Fluids* **17** (10), 103102. (Cited on page 64.)

Le Dreff, Julien & Delmotte, Blaise 2024 Nontrivial optimal swimming gaits of a model diatom colony. *In preparation* . (Cited on page 96.)

Lee, SH, Chadwick, RS & Leal, L Gary 1979 Motion of a sphere in the presence of a plane interface. part 1. an approximate solution by generalization of the method of lorentz. *Journal of Fluid Mechanics* **93** (4), 705–726. (Cited on page 57.)

Lefauve, Adrien & Saintillan, David 2014 Globally aligned states and hydrodynamic traffic jams in confined suspensions of active asymmetric particles. *Physical Review E* **89** (2), 021002. (Cited on page 50.)

Leishangthem, Premkumar & Xu, Xinliang 2024 Thermodynamic effects are essential for surface entrapment of bacteria. *Physical Review Letters* **132** (23), 238302. (Cited on page 10.)

Li, Lei, Manikantan, Harishankar, Saintillan, David & Spagnolie, Saverio E. 2013 The sedimentation of flexible filaments. *Journal of Fluid Mechanics* **735**, 705–736, publisher: Cambridge University Press. (Cited on pages 67, 72 and 75.)

Li, Zhibo 2023 Dynamics of rigid and flexible fibers in complex microfluidic environment. PhD thesis, Université Sorbonne Paris Cité. (Cited on page 85.)

Li, Zhibo, Bielinski, Clément, Lindner, Anke, du Roure, Olivia & Delmotte, Blaise 2024 Dynamics of rigid fibers interacting with triangular obstacles in microchannel flows. *Physical Review Fluids* **9** (4), 044302. (Cited on pages 77, 78 and 81.)

Liang, Zhi, Gimbutas, Zydrunas, Greengard, Leslie, Huang, Jingfang & Jiang, Shidong 2013 A fast multipole method for the rotne–prager–yamakawa tensor and its applications. *Journal of Computational Physics* **234**, 133–139. (Cited on page 23.)

Liao, Pan, Xing, Liuxi, Zhang, Shiwu & Sun, Dong 2019 Magnetically driven undulatory microswimmers integrating multiple rigid segments. *Small* **15** (36), 1901197. (Cited on page 11.)

Lieleg, Oliver & Ribbeck, Katharina 2011 Biological hydrogels as selective diffusion barriers. *Trends in cell biology* **21** (9), 543–551. (Cited on page 92.)

Lighthill, Michael J 1952 On the squirming motion of nearly spherical deformable bodies through liquids at very small reynolds numbers. *Communications on pure and applied mathematics* **5** (2), 109–118. (Cited on page 27.)

Liu, Yanan 2018 Dynamics of flexible and Brownian filaments in viscous flow. PhD thesis, Université Sorbonne Paris Cité. (Cited on page 84.)

Liu, Yanan, Chakrabarti, Brato, Saintillan, David, Lindner, Anke & Du Roure, Olivia 2018 Morphological transitions of elastic filaments in shear flow. *Proceedings of the National Academy of Sciences of the United States of America* **115** (38), 9438–9443. (Cited on page 84.)

Loutherback, Kevin, D'Silva, Joseph, Liu, Liyu, Wu, Amy, Austin, Robert H & Sturm, James C 2012 Deterministic separation of cancer cells from blood at 10 ml/min. *AIP advances* **2** (4). (Cited on page 66.)

Lu, Shih-Yuan 1998 Diffusion and reaction in regular arrays of spheres. *The Journal of Chemical Physics* **109** (12), 4985–4989, arXiv: https://doi.org/10.1063/1.477110. (Cited on page 13.)

Lundell, Fredrik, Söderberg, L Daniel & Alfredsson, P Henrik 2011 Fluid mechanics of papermaking. *Annual Review of Fluid Mechanics* **43**, 195–217. (Cited on page 65.)

Lushi, Enkeleida 2016 Stability and dynamics of anisotropically tumbling chemotactic swimmers. *Phys. Rev. E* **94**, 022414. (Cited on page 37.)

Lushi, Enkeleida, Wioland, Hugo & Goldstein, Raymond E. 2014 Fluid flows created by swimming bacteria drive self-organization in confined suspensions. *Proceedings of the National Academy of Sciences* **111** (27), 9733–9738, arXiv: http://www.pnas.org/content/111/27/9733.full.pdf. (Cited on page 37.)

Maeda, K, Imae, Y, Shioi, J I & Oosawa, F 1976 Effect of temperature on motility and chemotaxis of escherichia coli. *Journal of Bacteriology* **127** (3), 1039–1046, arXiv: https://journals.asm.org/doi/pdf/10.1128/jb.127.3.1039-1046.1976. (Cited on page 37.)

Makanga, Ursy, Duprat, Camille & Delmotte, Blaise 2024*a* Device for sorting fibres by differentiated lateral displacement. *Patent FR2206968A / WO2024008947A1* . (Cited on pages 66, 73 and 77.)

Makanga, Ursy, Duprat, Camille & Delmotte, Blaise 2024*b* Sedimentation of flexible fibers through ordered arrays of pillars. *To be submitted* . (Cited on pages 18 and 73.)

Makanga, Ursy, Sepahi, Mohammadreza, Duprat, Camille & Delmotte, Blaise 2023 Obstacle-induced lateral dispersion and nontrivial trapping of flexible fibers settling in a viscous fluid. *Physical Review Fluids* **8** (4), 044303. (Cited on pages 18, 67, 69 and 70.)

Maldarelli, Charles, Donovan, Nicole T, Ganesh, Subramaniam Chembai, Das, Subhabrata & Koplik, Joel 2022 Continuum and molecular dynamics studies of the hydrodynamics of colloids straddling a fluid interface. *Annual Review of Fluid Mechanics* **54**, 495–523. (Cited on page 64.)

Marbach, Sophie & Bocquet, Lydéric 2019 Osmosis, from molecular insights to large-scale applications. *Chemical Society Reviews* **48** (11), 3102–3144. (Cited on page 14.)

Marchetti, Benjamin, Raspa, Veronica, Lindner, Anke, du Roure, Olivia, Bergougnoux, Laurence, Guazzelli, Elisabeth & Duprat, Camille 2018 Deformation of a flexible fiber settling in a quiescent viscous fluid. *Physical Review Fluids* **3** (10), 104102, publisher: American Physical Society. (Cited on pages 67 and 68.)

Martinez-Pedrero, Fernando, Ortiz-Ambriz, Antonio, Pagonabarraga, Ignacio & Tierno, Pietro 2015 Colloidal microworms propelling via a cooperative hydrodynamic conveyor belt. *Physical review letters* **115** (13), 138301. (Cited on pages 45, 57 and 58.)

Maxey, MR & Patel, BK 2001 Localized force representations for particles sedimenting in Stokes flow. *Int. J. Multiph. Flow* **27** (9), 1603–1626. (Cited on pages 19 and 24.)

May, Sandra, Nonaka, Andrew, Almgren, Ann & Bell, John 2011 An unsplit, higher-order godunov method using quadratic reconstruction for advection in two dimensions. *Communications in Applied Mathematics and Computational Science* **6** (1), 27–61. (Cited on page 53.)

McGrath, J, Jimenez, M & Bridle, H 2014 Deterministic lateral displacement for particle separation: a review. *Lab on a Chip* **14** (21), 4139–4158. (Cited on page 65.)

McMullen, Angus, Holmes-Cerfon, Miranda, Sciortino, Francesco, Grosberg, Alexander Y. & Brujic, Jasna 2018 Freely Jointed Polymers Made of Droplets. *Physical Review Letters* **121** (13), 138002. (Cited on page 11.)

Metzger, Bloen, Guazzelli, Elisabeth & Butler, Jason E 2005 Large-scale streamers in the sedimentation of a dilute fiber suspension. *Physical review letters* **95** (16), 164506. (Cited on page 92.)

Metzger, Bloen, Nicolas, Maxime & Guazzelli, Elisabeth 2007 Falling clouds of particles in viscous fluids. *Journal of Fluid Mechanics* **580**, 283–301. (Cited on page 56.)

Miara, Tymoteusz, Vaquero-Stainer, Christian, Pihler-Puzović, Draga, Heil, Matthias & Juel, Anne 2024 Dynamics of inertialess sedimentation of a rigid u-shaped disk. *Communications Physics* **7** (1), 47. (Cited on page 104.)

Michelin, S. & Lauga, E. 2014 Phoretic self-propulsion at finite Péclet numbers. *J. Fluid Mech.* **747**, 572–604. (Cited on pages 13, 30 and 31.)

Montenegro-Johnson, Thomas D, Michelin, Sébastien & Lauga, Eric 2015 A regularised singularity approach to phoretic problems. *The European Physical Journal E* **38** (12), 139. (Cited on page 28.)

Moran, J. L. & Posner, J. D. 2017 Phoretic self-propulsion. *Annu. Rev. Fluid Mech.* **49**, 511–540. (Cited on page 13.)

Moreno, Nicolas, Moreno-Chaparro, Daniela, Usabiaga, Florencio Balboa & Ellero, Marco 2022 Hydrodynamics of spike proteins dictate a transport-affinity competition for sars-cov-2 and other enveloped viruses. *Scientific Reports* **12** (1), 11080. (Cited on pages 18 and 19.)

Moreno, Nicolas, Vazquez-Cortes, David & Fried, Eliot 2024 Sedimentation dynamics of triply-twisted möbius bands: Geometry versus topology. *arXiv preprint arXiv:2402.13017* . (Cited on pages 18 and 19.)

Moreno-Chaparro, Daniela, Moreno, Nicolas, Usabiaga, Florencio Balboa & Ellero, Marco 2023 Computational modeling of passive transport of functionalized nanoparticles. *The Journal of Chemical Physics* **158** (10). (Cited on page 18.)

Müller, Otto Frederik 1782 *Kleine Schriften aus der Naturhistorie*, , vol. 1. Buchhandlung der Gelehrten. (Cited on pages 11, 95 and 96.)

Murgia, Xabier, Loretz, Brigitta, Hartwig, Olga, Hittinger, Marius & Lehr, Claus-Michael 2018 The role of mucus on drug transport and its potential to affect therapeutic outcomes. *Advanced drug delivery reviews* **124**, 82–97. (Cited on page 92.)

Napper, Imogen E & Thompson, Richard C 2016 Release of synthetic microplastic plastic fibres from domestic washing machines: Effects of fabric type and washing conditions. *Marine pollution bulletin* **112** (1-2), 39–45. (Cited on page 65.)

Nguyen, Hoa & Fauci, Lisa 2014 Hydrodynamics of diatom chains and semiflexible fibres. *Journal of The Royal Society Interface* **11** (96), 20140314. (Cited on page 85.)

Noetinger, Benoît 1990 Fluctuating hydrodynamics and brownian motion. *Physica A: Statistical Mechanics and its Applications* **163** (2), 545–558. (Cited on page 10.)

Pak, O. S. & Lauga, E. 2014 Generalized squirming motion of a sphere. *J. Eng. Math.* **88**, 1–28. (Cited on page 27.)

Paul, Richard EL, Brey, Paul T & Robert, Vincent 2002 Plasmodium sex determination and transmission to mosquitoes. *Trends in parasitology* **18** (1), 32–38. (Cited on page 92.)

Pedley, Timothy J 2016 Spherical squirmers: models for swimming micro-organisms. *IMA Journal of Applied Mathematics* **81** (3), 488–521. (Cited on page 27.)

Pérez Peláez, Raúl 2022 Complex fluids in the Gpu era: Algorithms and simulations. http://purl.org/dc/dcmitype/Text, Universidad Autónoma de Madrid. (Cited on page 74.)

Peskin, C.S. 2002 The immersed boundary method. *Acta Numerica* **11**, 479–517. (Cited on pages 19 and 24.)

Pozrikidis, C. 1992 *Boundary Integral and Singularity Methods for Linearized Viscous Flow*. Cambridge University Press. (Cited on pages 9, 11, 18 and 29.)

Qi, Kai, Westphal, Elmar, Gompper, Gerhard & Winkler, Roland G 2022 Emergence of active turbulence in microswimmer suspensions due to active hydrodynamic stress and volume exclusion. *Communications Physics* **5** (1), 1–12. (Cited on page 37.)

Quennouz, N., Shelley, M., du Roure, O. & Lindner, A. 2015 Transport and buckling dynamics of an elastic fibre in a viscous cellular flow. *Journal of Fluid Mechanics* **769**, 387–402. (Cited on page 77.)

Rallabandi, Bhargav, Hilgenfeldt, Sascha & Stone, Howard A 2017 Hydrodynamic force on a sphere normal to an obstacle due to a non-uniform flow. *Journal of Fluid Mechanics* **818**, 407–434. (Cited on page 83.)

Re, Viviana 2019 Shedding light on the invisible: addressing the potential for groundwater contamination by plastic microfibers. *Hydrogeology Journal* **27** (7), 2719–2727. (Cited on page 65.)

Rojas-Pérez, Francisco, Delmotte, Blaise & Michelin, Sébastien 2021 Hydrochemical interactions of phoretic particles: a regularized multipole framework. *Journal of Fluid Mechanics* **919**, A22. (Cited on pages 2, 31 and 38.)

Rotne, Jens & Prager, Stephen 1969 Variational treatment of hydrodynamic interaction in polymers. *Journal of Chemical Physics* **50**, 4831. (Cited on page 19.)

Roux, Jean-Noël 1992 Brownian particles at different times scales: a new derivation of the smoluchowski equation. *Physica A: Statistical Mechanics and its Applications* **188** (4), 526–552. (Cited on page 10.)

Rusconi, Roberto, Lecuyer, Sigolene, Guglielmini, Laura & Stone, Howard A. 2010 Laminar flow around corners triggers the formation of biofilm streamers. *Journal of The Royal Society Interface* **7** (50), 1293–1299. (Cited on page 65.)

Sabrio, Alexandra & Rasoulzadeh, Mojdeh 2022 Main modes of microfilament particles deformation in rough channels. *Physics of Fluids* **34** (1), 013320. (Cited on page 77.)

Sacanna, Stefano, Irvine, William TM, Chaikin, Paul M & Pine, David J 2010 Lock and key colloids. *Nature* **464** (7288), 575–578. (Cited on page 11.)

Saggiorato, Guglielmo, Elgeti, Jens, Winkler, Roland G & Gompper, Gerhard 2015 Conformations, hydrodynamic interactions, and instabilities of sedimenting semiflexible filaments. *Soft matter* **11** (37), 7337–7344. (Cited on page 67.)

Saintillan, David, Darve, Eric & Shaqfeh, Eric S. G. 2005 A smooth particle-mesh ewald algorithm for stokes suspension simulations: The sedimentation of fibers. *Physics of Fluids* **17** (3), 033301. (Cited on page 92.)

Saintillan, David & Shelley, Michael J. 2008 Instabilities and pattern formation in active particle suspensions: Kinetic theory and continuum simulations. *Phys. Rev. Lett.* **100**, 178103. (Cited on page 37.)

Salafi, Thoriq, Zhang, Yi & Zhang, Yong 2019 A review on deterministic lateral displacement for particle separation and detection. *Nano-Micro Letters* **11** (1), 77. (Cited on page 65.)

Scagliarini, Andrea & Pagonabarraga, Ignacio 2022 Hydrodynamic and geometric effects in the sedimentation of model run-and-tumble microswimmers. *Soft Matter* pp. –. (Cited on page 37.)

Schoeller, Simon F, Townsend, Adam K, Westwood, Timothy A & Keaveny, Eric E 2021 Methods for suspensions of passive and active filaments. *Journal of Computational Physics* **424**, 109846. (Cited on page 13.)

Shum, H., Gaffney, E. A. & Smith, D. J. 2010 Modelling bacterial behaviour close to a no-slip plane boundary: the influence of bacterial geometry. *Proceedings of the Royal Society A: Mathematical, Physical and Engineering Sciences* **466** (2118), 1725–1748. (Cited on page 13.)

Shum, Henry & Yeomans, Julia M. 2017 Entrainment and scattering in microswimmer-colloid interactions. *Physical Review Fluids* **2** (11), 113101. (Cited on page 13.)

Simmchen, Juliane, Katuri, Jaideep, Uspal, William E, Popescu, Mihail N, Tasinkevych, Mykola & Sánchez, Samuel 2016 Topographical pathways guide chemical microswimmers. *Nature communications* **7**, 10598. (Cited on page 61.)

Sing, Charles E, Schmid, Lothar, Schneider, Matthias F, Franke, Thomas & Alexander-Katz, Alfredo 2010 Controlled surface-induced flows from the motion of self-assembled colloidal walkers. *Proceedings of the National Academy of Sciences* **107** (2), 535–540. (Cited on page 45.)

Smith, David J, Gallagher, Meurig T, Schuech, Rudi & Montenegro-Johnson, Thomas D 2021 The role of the double-layer potential in regularised stokeslet models of self-propulsion. *Fluids* **6** (11), 411. (Cited on page 27.)

Snezhko, Alexey 2016 Complex collective dynamics of active torque-driven colloids at interfaces. *Current Opinion in Colloid & Interface Science* **21**, 65–75. (Cited on page 45.)

Spagnolie, Saverio E & Lauga, Eric 2010 The optimal elastic flagellum. *Physics of Fluids* **22** (3). (Cited on page 96.)

Spagnolie, Saverio E, Moreno-Flores, Gregorio R, Bartolo, Denis & Lauga, Eric 2015 Geometric capture and escape of a microswimmer colliding with an obstacle. *Soft Matter* **11** (17), 3396–3411. (Cited on page 61.)

Sprinkle, Brennan, Balboa Usabiaga, Florencio, Patankar, Neelesh A. & Donev, Aleksandar 2017 Large scale brownian dynamics of confined suspensions of rigid particles. *The Journal of Chemical Physics* **147** (24), 244103, arXiv: https://doi.org/10.1063/1.5003833. (Cited on pages 10, 20, 21 and 22.)

Sprinkle, Brennan, Donev, Aleksandar, Bhalla, Amneet Pal Singh & Patankar, Neelesh 2019 Brownian dynamics of fully confined suspensions of rigid particles without green's functions. *The Journal of chemical physics* **150** (16), 164116. (Cited on page 21.)

Sprinkle, Brennan, Van Der Wee, Ernest B, Luo, Yixiang, Driscoll, Michelle M & Donev, Aleksandar 2020 Driven dynamics in dense suspensions of microrollers. *Soft Matter* **16** (34), 7982–8001. (Cited on page 18.)

Sprinkle, Brennan, Wilken, Sam, Karapetyan, Shake, Tanaka, Michio, Chen, Zhe, Cruise, Joseph R, Delmotte, Blaise, Driscoll, Michelle M, Chaikin, Paul & Donev, Aleksandar 2021 Sedimentation of a colloidal monolayer down an inclined plane. *Physical Review Fluids* **6** (3), 034202. (Cited on pages 3, 18 and 51.)

Stark, Holger 2018 Artificial chemotaxis of self-phoretic active colloids: collective behavior. *Accounts of chemical research* **51** (11), 2681–2688. (Cited on page 13.)

Stone, H. A. & Samuel, A. D. T. 1996 Propulsion of microorganisms by surface distortions. *Phys. Rev. Lett.* **77**, 4102. (Cited on page 9.)

Storn, Rainer & Price, Kenneth 1997 Differential evolution–a simple and efficient heuristic for global optimization over continuous spaces. *Journal of global optimization* **11**, 341–359. (Cited on page 27.)

Succi, Sauro 2001 *The Lattice Boltzmann Equation for Fluid Dynamics and Beyond*. Oxford: Clarendon Press. (Cited on page 78.)

Sulaiman, Mostafa, Climent, Eric, Delmotte, Blaise, Fede, Pascal, Plouraboué, Franck & Verhille, Gautier 2019 Numerical modelling of long flexible fibers in homogeneous isotropic turbulence. *The European Physical Journal E* **42**, 1–11. (Cited on page 4.)

Swan, James W & Brady, John F 2007 Simulation of hydrodynamically interacting particles near a no-slip boundary. *Physics of Fluids (1994-present)* **19** (11), 113306. (Cited on pages 19, 45 and 57.)

Swan, James W, Brady, John F, Moore, Rachel S & others 2011 Modeling hydrodynamic self-propulsion with stokesian dynamics. or teaching stokesian dynamics to swim. *Physics of Fluids* **23** (7). (Cited on page 9.)

Swan, James W. & Wang, Gang 2016 Rapid calculation of hydrodynamic and transport properties in concentrated solutions of colloidal particles and macromolecules. *Physics of Fluids* **28** (1), 011902. (Cited on page 27.)

Takagi, Daisuke, Palacci, Jérémie, Braunschweig, Adam B, Shelley, Michael J & Zhang, Jun 2014 Hydrodynamic capture of microswimmers into sphere-bound orbits. *Soft Matter* **10** (11), 1784–1789. (Cited on page 61.)

Takaha, Yuki & Nishiguchi, Daiki 2022 Quasi-two-dimensional bacterial swimming around pillars: enhanced trapping efficiency and curvature dependence. *arXiv preprint arXiv:2203.16017* . (Cited on page 61.)

Tam, Daniel & Hosoi, AE 2011 Optimal kinematics and morphologies for spermatozoa. *Physical Review E—Statistical, Nonlinear, and Soft Matter Physics* **83** (4), 045303. (Cited on pages 96 and 105.)

Theurkauff, I., Cottin-Bizonne, C., Palacci, J., Ybert, C. & Bocquet, L. 2012 Dynamic clustering in active colloidal suspensions with chemical signaling. *Phys. Rev. Lett.* **108**, 268303. (Cited on page 14.)

Tornberg, Anna-Karin & Shelley, Michael J. 2004 Simulating the dynamics and interactions of flexible fibers in Stokes flows. *Journal of Computational Physics* **196** (1), 8–40. (Cited on page 72.)

Trachtenberg, Shlomo & Hammel, Ilan 1992 The rigidity of bacterial flagellar filaments and its relation to filament polymorphism. *Journal of structural biology* **109** (1), 18–27. (Cited on page 11.)

Tran, Quang D, Galiana, Eric, Thomen, Philippe, Cohen, Céline, Orange, François, Peruani, Fernando & Noblin, Xavier 2022 Coordination of two opposite flagella allows high-speed swimming and active turning of individual zoospores. *Elife* **11**, e71227. (Cited on page 101.)

Tsang, Alan Cheng Hou & Kanso, Eva 2016 Density shock waves in confined microswimmers. *Physical review letters* **116** (4), 048101. (Cited on page 50.)

Usabiaga, F Balboa, Kallemov, Bakytzhan, Delmotte, Blaise, Bhalla, A, Griffith, Boyce E & Donev, Aleksandar 2016 Hydrodynamics of suspensions of passive and active rigid particles: A rigid multiblob approach. Preprint at http://arxiv.org/abs/1602.02170 . (Cited on pages 18, 23, 26, 27 and 97.)

Vakil, Ali & Green, Sheldon I. 2011 Flexible fiber motion in the flow field of a cylinder. *International Journal of Multiphase Flow* **37** (2), 173–186. (Cited on page 65.)

Wajnryb, Eligiusz, Mizerski, Krzysztof A., Zuk, Pawel J. & Szymczak, Piotr 2013 Generalization of the rotne–prager–yamakawa mobility and shear disturbance tensors. *Journal of Fluid Mechanics* **731**, R3. (Cited on page 19.)

Walker, Benjamin J., Wheeler, Richard J., Ishimoto, Kenta & Gaffney, Eamonn A. 2019 Boundary behaviours of Leishmania mexicana: A hydrodynamic simulation study. *Journal of Theoretical Biology* **462**, 311–320. (Cited on page 13.)

Wandersman, Elie, Quennouz, Nawal, Fermigier, Marc, Lindner, Anke & Du Roure, O 2010 Buckled in translation. *Soft matter* **6** (22), 5715–5719. (Cited on page 77.)

Wang, Chao, Bruce, Robert L., Duch, Elizabeth A., Patel, Jyotica V., Smith, Joshua T., Astier, Yann, Wunsch, Benjamin H., Meshram, Siddharth, Galan, Armand, Scerbo, Chris, Pereira, Michael A., Wang, Deqiang, Colgan, Evan G., Lin, Qinghuang & Stolovitzky, Gustavo 2015 Hydrodynamics of diamond-shaped gradient nanopillar arrays for effective DNA translocation into nanochannels. *ACS Nano* **9** (2), 1206–1218. (Cited on page 66.)

Wang, Xiaoyu, Sprinkle, Brennan, Bisoyi, Hari Krishna, Yang, Tao, Chen, Lixiang, Huang, Shuai & Li, Quan 2023 Colloidal tubular microrobots for cargo transport and compression. *Proceedings of the National Academy of Sciences* **120** (37), e2304685120. (Cited on page 18.)

van der Wee, Ernest B, Blackwell, Brendan C, Balboa Usabiaga, Florencio, Sokolov, Andrey, Katz, Isaiah T, Delmotte, Blaise & Driscoll, Michelle M 2023 A simple catch: Fluctuations enable hydrodynamic trapping of microrollers by obstacles. *Science Advances* **9** (10), eade0320. (Cited on pages 18 and 60.)

Westwood, Timothy A., Delmotte, Blaise & Keaveny, Eric E. 2021 A generalised drift-correcting time integration scheme for Brownian suspensions of rigid particles with arbitrary shape. *arXiv:2106.00449 [physics]* ArXiv: 2106.00449. (Cited on page 18.)

Westwood, Timothy A., Delmotte, Blaise & Keaveny, Eric E. 2022 A generalised drift-correcting time integration scheme for brownian suspensions of rigid particles with arbitrary shape. *Journal of Computational Physics* **467**, 111437. (Cited on pages 8, 18, 20 and 23.)

Wykes, Megan S Davies, Zhong, Xiao, Tong, Jiajun, Adachi, Takuji, Liu, Yanpeng, Ristroph, Leif, Ward, Michael D, Shelley, Michael J & Zhang, Jun 2017 Guiding

microscale swimmers using teardrop-shaped posts. *Soft Matter* **13** (27), 4681–4688. (Cited on page 61.)

Xu, Xianghua & Nadim, Ali 1994 Deformation and orientation of an elastic slender body sedimenting in a viscous liquid. *Physics of Fluids* **6** (9), 2889–2893. (Cited on page 67.)

Xue, Nan, Nunes, Janine K. & Stone, Howard A. 2022 Shear-induced migration of confined flexible fibers. *Soft Matter* **18** (3), 514–525. (Cited on page 77.)

Yan, W. & Blackwell, R. 2020 Kernel aggregated fast multipole method: Efficient summation of laplace and stokes kernel functions. *arXiv preprint arXiv:2010.15155* . (Cited on pages 30 and 37.)

Yan, Wen & Blackwell, Robert 2021 Kernel aggregated fast multipole method: Efficient summation of laplace and stokes kernel functions. *Advances in Computational Mathematics* **47** (5), 69. (Cited on pages 19 and 23.)

Yan, Wen & Shelley, Michael 2018 Universal image system for non-periodic and periodic stokes flows above a no-slip wall. *Journal of Computational Physics* **375**, 263–270. (Cited on pages 19, 23 and 37.)

Yang, Tao, Sprinkle, Brennan, Guo, Yang, Qian, Jun, Hua, Daoben, Donev, Aleksandar, Marr, David WM & Wu, Ning 2020 Reconfigurable microbots folded from simple colloidal chains. *Proceedings of the National Academy of Sciences* **117** (31), 18186–18193. (Cited on page 18.)

Young, Y.-N. & Shelley, Michael J. 2007 Stretch-coil transition and transport of fibers in cellular flows. *Phys. Rev. Lett.* **99**, 058303. (Cited on page 84.)

Zhang, Yu, Gregory, David A, Zhang, Yi, Smith, Patrick J, Ebbens, Stephen J & Zhao, Xiubo 2019 Reactive inkjet printing of functional silk stirrers for enhanced mixing and sensing. *Small* **15** (1), 1804213. (Cited on page 32.)

Zöttl, Andreas & Stark, Holger 2023 Modeling active colloids: From active brownian particles to hydrodynamic and chemical fields. *Annual Review of Condensed Matter Physics* **14**, 109–127. (Cited on page 13.)

Zou, Zonghao, Liu, Yuexin, Young, Y-N, Pak, On Shun & Tsang, Alan CH 2022 Gait switching and targeted navigation of microswimmers via deep reinforcement learning. *Communications Physics* **5** (1), 158. (Cited on page 105.)

Zuk, P. J., Wajnryb, E., Mizerski, K. A. & Szymczak, P. 2014 Rotne–Prager–Yamakawa approximation for different-sized particles in application to macromolecular bead models. *Journal of Fluid Mechanics* **741**. (Cited on page 19.)

Curriculum Vitae

État civil

Nom : **Delmotte**, prénom : **Blaise**.
Né le 18 Janvier 1988 (36 ans), à Prades (Pyrénées-Orientales).
Adresse Professionnelle : LadHyX, 9 Boulevard des Maréchaux, 91120 Palaiseau, France
Tél : 01 69 33 52 50
E-mail : blaise.delmotte@ladhyx.polytechnique.fr
Page web : `https://sites.google.com/site/blaisedelmotte/`

Postes occupés

09/2020 - ...	**Professeur Chargé de Cours à temps incomplet**, Département Mécanique, École Polytechnique
10/2018 - ...	**Chargé de Recherche**, CNRS, LadHyX, École Polytechnique
10/2015 - 07/2018	**Instructor/Visiting Assistant Professor**, Courant Institute of Mathematical Sciences, New York University (NYU), USA

Formation

10/2012 - 09/2015	**Doctorat de Dynamique des Fluides**, Institut de Mécanique des Fluides de Toulouse. *Soutenu le 21 Septembre 2015*
09/2011 - 09/2012	**Master 2 Recherche, Dynamique des Fluides, option Mécanique des Fluides Environnementale**, *Mention Très Bien*, classé 2^{nd}, Université Paul Sabatier, Toulouse
09/2006 - 09/2011	**Diplôme d'Ingénieur, Mathématiques et Modélisation Numérique**, Institut National des Sciences Appliquées (INSA), Toulouse
09/2009 - 02/2010	Semestre d'étude au sein du département de Mathématiques de l'Universidad de Valencia, Espagne

Expériences d'enseignement et d'encadrement

09/2020 - ... **Professeur Chargé de Cours à temps incomplet**, Département Mécanique, École Polytechnique

01/2020 **Vacataire**, Petites Classes du cours "Hydrodynamique pour l'Environnement" (MEC567), École Polytechnique.

10/2015 - 07/2018 **Instructor/Visiting Assistant Professor**, Courant Institute of Mathematical Sciences, New York University (NYU), USA
Responsable de cours (environ 180 HETD/an).

10/2012 - 10/2014 **Moniteur - Chargé d'enseignement**, ENSEEIHT, Institut National Polytechnique de Toulouse.
Chargé de TD et supervision de projets (environ 64 HETD/an)

Résumé de mes enseignements

Discipline	Niveau	Établissement	Années	Cours	PC/TD/Projets
Solid Mechanics (PHY304)	L3-M1	X	2024-2025		40h
Mécanique des Fluides (MEC432)	L3-M1	X	2020-2025		200h
Hydro. pour l'Environnement (MEC567)	M1	X	2020-2024		132h
Algèbre Linéaire et Numérique	L3	NYU	2015-2018	225h	90h
Calcul Multi-variables	L1	NYU	2017/2018	75h	30h
EDO et Sys. Dynamiques	L3	NYU	2016/2017	56.25h	30h
Projets Méca. Flu.	M2	INSA Toulouse	2013/2014		20h
Volumes Finis	M1	ENSEEIHT	2012-2014		52h
Méth. Num. pour les EDP	M1	ENSEEIHT	2012-2014		31.5h
Optimisation Hydraulique	L3	ENSEEIHT	2012-2014		28h
Introduction Matlab	L3	ENSEEIHT	2012-2014		17.5h

Résumé de mes encadrements

Nom	Niveau	Établissement	Années	Sujet
J. Le Dreff	M1/M2/PhD	X	2022-2027	Modelling the diatom chain *B. Paxillifer*
C. Bielinski	Post-Doc	X	2021-2024	Sorting of elastic objects in porous media
M. Sepahi	M2	X	2021	Sedimentation of fibers against obstacles
U. Makanga	M2/PhD	X	2020-2023	Simulating transport and clogging of elastic fibers in structured environments
F. Rojas	M2/PhD	X	2019-2022	Modeling collective motion in reactive suspensions
A. Ivaldi	M2	X	2019	Particle transport and mixing by micro-swimmers
J. Cruise	L3	NYU	2018	Sedimentation of colloidal suspensions near boundaries
Z. Chen	M1	NYU	2017	Particle collective diffusion above a no-slip boundary
P. Mooney	L3	NYU	2016	Monte-Carlo simulation of confined particles with arbitrary shape
M. Sulaiman	M2	IMFT	2015	Simulating flexible fibers in turbulent flows
I. Thiam	M2	IMFT	2014	Identification of internal properties of fibers and micro-swimmers
E. Delclaux	M1	IMFT	2014	Modelling sperm beating patterns

Formations à l'encadrement

- Formation des encadrants de thèse à la prévention des risques psycho-sociaux: "L'impact de votre encadrement sur le projet et la relation doctorale". CNRS, campus de Gif-sur-Yvette, 24/11-25/11/2022.

Expériences de recherche

10/2015 - 07/2018 **Instructor/Visiting Assistant Professor**, Courant Institute of Mathematical Sciences, New York University (NYU), USA
Collaborateurs : Aleksandar Donev (Associate Prof. NYU), Michelle Driscoll (Assistant Prof. Northwestern University), Paul Chaikin (Silver Prof. NYU, Emeritus Prof. Princeton)
Mots clefs : suspensions, instabilités, ondes, méthodes numériques, modèles continus, calcul haute performance

01/2014 - 01/2015 **Chercheur invité**, Department of Mathematics, Imperial College, Londres (3×1 mois).
Collaborateur : Eric Keaveny (Senior Lecturer, Imperial College)
Sujet : "Simulating Brownian suspensions with fluctuating hydrodynamics"
Mots clefs : suspensions colloïdales, gels, systèmes stochastiques, méthodes numériques

10/2012 - 09/2015 **Doctorat de Dynamique des Fluides**, Institut de Mécanique des Fluides de Toulouse (IMFT), France
Sujet : "Modélisation et Simulation Numérique des Mécanismes de Nage Individuels et Collectifs dans les Suspensions Actives"
Directeurs de thèse : Pr. Eric Climent (Prof. INP/IMFT), Pr. Pierre Degond (Chair Prof. Imperial College)
Mots clefs : suspensions actives, locomotion, méthodes numériques, calcul haute performance

02/2012 - 08/2012 **Stage de Master Recherche**, IMFT, Toulouse, France
Encadrants : Pr. Eric Climent (Prof. INP/IMFT), Franck Plouraboué (Directeur de Recherche, CNRS/IMFT)
Sujet : "Modélisation des Suspensions de Spermatozoïdes"

02/2011 - 08/2011 **Stage de recherche**, CERFACS, Toulouse - University of Maryland, USA
Encadrants : Sophie Ricci (CERFACS), Bénédicte Cuenot (CERFACS), Arnaud Trouvé (Prof. Univ. Maryland)
Sujet : "Assimilation de Données pour la Propagation des Feux de Forêt"

06/2010 - 09/2010 **Stage de recherche**, HydroSciences, Montpellier, France
Encadrants : Carole Delenne (MCF, Univ. Montpellier), Vincent Guinot (Prof. Univ. Montpellier)
Sujet: "Modélisation de la Dégradation des Polluants dans les Lagunages"

Financements, distinctions et bourses

2022-2024	**Lauréat du Partenariat Hubert Curien-PROCORE avec Hong-Kong** "Experimental and computational investigation on the collective phototaxis of colonial swimming microorganisms". Co-PI : Alan Cheng Hou-Tsang (Assist. Prof. HKU), 10 000 euros.
2020-2024	**PI ANR JCJC**, "Transport and clogging of deformable objects in porous media" (ANR-20-CE30-0006), 170 000 euros.
2018-2019	**NVidia Academic Partnership Program**, bourse attribuée sous la forme de dons de cartes graphiques haute performance (Titan V).
2017-2018	**Lauréat du prix Joseph B. Keller**, bourse attribuée à un post-doctorant par an au Courant Institute pour la qualité de sa recherche.
2017-2021	**Co-PI NSF Grant**, "Magnetic microrollers as a platform for active transport" (PMP-1706562). Collaborateurs: Driscoll (Assist. Prof. NorthWestern University, Co-PI) et Aleksandar Donev (Prof. Courant Institute, NYU, PI), $420 000.
2015-2017	**Bourse NYU** MRSEC DMR-1420073 pour le financement de ma recherche.
2015	**Lauréat du Prix Léopold Escande**, récompense les meilleures thèses de l'Institut National Polytechnique (INP) de Toulouse.
04/2015	**Bourse STSM** du COST Action MP1305 pour une mobilité à l'Imperial College.
06 & 10/2014	**Bourse INPT** BQR-SMI pour des séjours à l'Imperial College.
05-08/2011	**Bourse CERFACS** pour une mobilité à l'University of Maryland.

Responsabilités et services

Responsabilités scientifiques

- Co-responsable des visites d'entreprises pour les élèves ingénieurs polytechniciens (2024-...)
- Co-organisateur du colloquium Euromech "Nonlinear dynamics at low Reynolds number" avec E. Keaveny (Imperial College), Londres, 05/2024.
- Membres de plusieurs groupes de travail sur les enseignements de Mécanique à l'École Polytechnique (2023-...)
- Responsable de la communication scientifique du LadHyX (06/2023-...)
- Organisateur du Minisymposium"Numerical Methods for Particle Suspensions and Fluid-Structure Interactions at Small Scales", SIAM CSE Meeting, Amsterdam, 27/02-03/03/2023.
- Responsable des séminaires du LadHyX (05/2019-06/2023).
- Organisateur de la journée du LadHyX : APS@LadHyXa (11/2019-...).
- Co-fondateur et secrétaire de Doct'Eau, l'association des doctorants et post-doctorants de l'IMFT (2013-2015).
- Bénévole au 10th International Symposium on Fire Safety Science, University of Maryland, USA (06/2011).

Relecture pour des journaux internationaux

- Proceedings of the National Academy of Sciences,
- Physical Review Letters,
- Journal of Fluid Mechanics,
- Physical Review Fluids,
- Journal of Computational Physics,
- New Journal of Physics,
- Journal of Fluids and Structures,
- Journal of Physics: Condensed Matter,
- Physical Review E,
- Advances in Computational Mathematics.
- European Journal of Mechanics /B Fluids.

Jury de thèse

- Thomas Mabit, Institut de Physique de Rennes, ENS-Rennes, December 2024 *(Examiner)*
- Anna Broms, Math Dept. KTH, Stockholm, April 2024 *(Examiner)*
- Zhibo Li, PMMH, Paris, September 2023 *(invited member)*
- Marvin Brun-Cosme-Bruny, LiPhy, Grenoble, October 2019 *(examiner)*

Publications

Journaux internationaux à comité de lecture

1. Delmotte, B.*, Usabiaga, F. B.* A scalable method to model large suspensions of colloidal phoretic particles with arbitrary shapes. *to appear in Journal of Computational Physics* (2024).
2. Li, Z.*, Bielinski, C.*, Lindner, A., du Roure, O., Delmotte, B. Non-trivial dynamics of rigid fibers interacting with triangular obstacles in microchannel flows. *Physical Review Fluids* (2024).
3. Delmotte, B. Viscosity ratio across interfaces controls the stability and self-assembly of microrollers. *Physical Review Fluids* (2023).
4. Makanga, U., Sepahi, M., Duprat, C., Delmotte, B. Obstacle-induced lateral dispersion and nontrivial trapping of flexible fibers settling in a viscous fluid. *Physical Review Fluids* (2023).
5. van der Wee, E.* , Blackwell, B., Usabiaga, F.B., Sokolov, A., Katz, I., Delmotte, B.*, Driscoll, M.*. A simple catch: thermal fluctuations enable hydrodynamic trapping of microrollers by obstacles. *Science Advances* (2023).
   - Dans les médias: Northwestern News : "A surprising way to trap a microparticle", Journal du CNRS : "Un piégeage de particules grâce au mouvement brownien"
6. Usabiaga, F. B.*, Delmotte, B.*. A numerical method for suspensions of articulated bodies in viscous flows, *Journal of Computational Physics* (2022).
7. Westwood, T. A., Delmotte, B., Keaveny, E. E. A generalised drift-correcting time integration scheme for Brownian suspensions of rigid particles with arbitrary shape, *Journal of Computational Physics* (2022).

8. Rojas-Pérez, F., Delmotte, B., Michelin, S. Hydrochemical interactions of phoretic particles: a regularized multipole framework. *Journal of Fluid Mechanics* (2021).
9. Sprinkle, B., Wilken, S., Karapetyan, S., Tanaka, M., Chen, Z., Cruise, JR., Delmotte, B., Driscoll, M., Chaikin, P., Donev, A. Sedimentation of a colloidal monolayer down an inclined plane. *Physical Review Fluids* (2021).
10. M. Sulaiman, E. Climent, B. Delmotte, P. Fede, F. Plouraboué, G. Verhille, "Numerical modelling of long flexible fibers in homogeneous isotropic turbulence", *The European Physical Journal E* (2019).
11. B. Delmotte, "Hydrodynamically-bound states of a pair of microrollers: a dynamical system insight", *Physical Review Fluids* (2019).
12. M. Driscoll*, B. Delmotte*, "Leveraging Collective Effects in Externally Driven Colloidal Suspensions: Experiments and Simulations", *Current Opinion in Colloid and Interface Science* (2018).
13. B. Delmotte, E.E. Keaveny, E. Climent, F. Plouraboué, "Simulations of Brownian tracer transport in squirmer suspensions", *IMA Journal of Applied Mathematics* (2018)
14. B. Delmotte, M. Driscoll, P. Chaikin, A. Donev, "A minimal model for a hydrodynamic fingering instability in microroller suspensions", *Physical Review Fluids* (2017).
15. B. Delmotte, M. Driscoll, P. Chaikin, A. Donev, "Hydrodynamic Shocks in Microroller Suspensions", *Physical Review Fluids* (2017).
16. F. Balboa-Usabiaga, B. Delmotte, A . Donev, "Brownian dynamics of confined suspensions of active microrollers", *Journal of Chemical Physics* (2017).
17. F. Plouraboué, E. Ibrahima, B. Delmotte, E. Climent, "Identification of internal properties of fibers and micro-swimmers". *Proceedings of the Royal Society A* (2017).
18. M. Driscoll*, B. Delmotte*, M. Youssef, S. Saccana, A. Donev, P. Chaikin, "Unstable Fronts and Stable Motile Structures formed by Microrollers", *Nature Physics* (2017).
    - Dans les médias: P. Tierno, "Colloids: a microscopic army", *Nature Physics* (2017).
    - Vidéo présentée au 69^{th} APS-DFD meeting: "The Hydrodynamic Genesis of Critters", `https://www.youtube.com/watch?v=V1GTbao_noU`.
19. F. Balboa-Usabiaga, B. Kallemov, B. Delmotte, A. Pal Singh Balla, B. Griffith and A. Donev, "Hydrodynamics of Suspensions of Passive and Active Rigid Particles: a Rigid Multiblob Approach", *Communications in Applied Mathematics and Computational Science* (2016).
20. B. Delmotte, E. Keaveny, "Simulating Brownian Suspensions with Fluctuating Hydrodynamics", *Journal of Chemical Physics* (2015).
21. B. Delmotte, E. Keaveny, F. Plouraboué and E. Climent, "Large-scale Simulation of Steady and Time-dependent Active Suspensions with the Force Coupling Method", *Journal of Computational Physics* (2015).
22. B. Delmotte, F. Plouraboué and E. Climent, "A General Formulation of Bead Models Applied to Flexible Fibers and Active Filaments at Low Reynolds Number", *Journal of Computational Physics* (2015).
23. B. Delmotte, F. Plouraboué and E. Climent, "Hydrodynamic Interactions among Large Populations of Swimming Microorganisms", *Computer Methods in Biomechanics and Biomedical Engineering* (2013).

24. M.C. Rochoux, B. Delmotte, B. Cuenot, S. Ricci, A. Trouvé, "Regional-scale Simulations of Wildland Fire Spread Informed by Real-time Flame Front Observations", *Proceedings of the Combustion Institute* (2013).
25. M.C. Rochoux, B. Cuenot, S. Ricci, A. Trouvé, B. Delmotte, S. Massart, R. Paoli, R. Paugam, "Data Assimilation Applied to Combustion", *Comptes Rendus Mécanique* (2013).

Brevets

Makanga, U.*, Delmotte, B.*, Duprat, C.* "Device for sorting fibres by differentiated lateral displacement and method for sorting fibres", FR2206968A/WO2024008947A1, (2024).

Thèse de doctorat

1. "Modélisation et Simulation Numérique des Mécanismes de Nage Individuels et Collectifs dans les Suspensions Actives", 09/2015, IMFT, Institut National Polytechnique de Toulouse, *rédigée en anglais.*

Communications

Séminaires invités

1. Laboratoire de Génie Chimique, Toulouse, May 2024
2. "Confluence", Institut de Mécanique des Fluides, Toulouse, France, May 2024
3. IRPHE, Marseille, March 2024
4. Séminaire du Dept. Mécanique, ENSTA, 08/11/2022
5. Séminaire du PMMH, ESPCI, 23/09/2022
6. Network Seminar, Centre de Recherche Interdisciplinaire, Paris, 28/11/2019
7. Séminaire MSC, Laboratoire Matière et Systèmes Complexes, Paris, 16/09/2019
8. Maths Seminar, Imperial College, Londres, 17/05/2019
9. Physics and Astronomy Complex Systems Seminars, Northwestern University, Evanston, USA, 15/11/2018
10. Fluids and Waves Seminar, New Jersey Institute of Technology, USA 02/04/2018
11. Séminaire Externe, LadHyX, École Polytechnique 15/03/2018
12. MSC seminars, Courant Institute, NYU, USA, 24/10/2017
13. LiPhy, Grenoble, France, 25/09/2017
14. Institut de Mécanique des Fluides de Toulouse (IMFT), France, 03/01/2017
15. Applied Mathematics Seminar, Courant Institute of Mathematical Sciences, NYU, USA, 10/11/2016
16. Center for Soft Matter Research, NYU, USA, 12/10/2016
17. Levich Institute Seminars, Levich Institute, CUNY, New York, USA, 19/04/2016
18. Applied Mathematics Seminar, Courant Institute of Mathematical Sciences, NYU, USA, 12/11/2015
19. Junior Applied Mathematics Seminar, Imperial College, Londres, UK, 28/10/2014
20. Biolunch, Department of Applied Mathematics and Theoretical Physics, Cambridge, UK, 22/06/2014

Présentations invitées (keynote) lors de conférences ou workshops

1. IUTAM Symposium : "From Stokesian suspensions dynamics to particulate flows in turbulence", IMFT, Toulouse, 29/08-02/09/2022
2. CECAM Workshop : "Computational methods and tools for complex suspensions", Bilbao, Espagne, 23-27/05/2022.

Présentations effectuées lors de conférences ou workshops

1. Euromech Colloquium: "Nonlinear dynamics at zero Reynolds number", London, May 21-23, 2024
2. Euromech Colloquium, "Suspension flows and rheology", 26/06-30/06/2023, Nice
3. GDR MicroNanoFluidique, Lyon, 03/04-04/04/2023
4. SIAM CSE Meeting, Amsterdam, 27/02-03/03/2023
5. Workshop, "Physics of Microbial Motility", ESPCI, Paris, November 2/11-4/11/2022
6. GDR Navier-Stokes 2.0, Univ. Paris-Saclay, 27-29/10/2021
7. Micro and Nanoscale Flows 2021, Imperial College, London (Zoom), 20-23/05/2021
8. 9th International Congress on Industrial and Applied Mathematics, Valencia, Espagne, 15-19/07/2019
9. Colloidal Sciences and Metamaterials, Paris, 25-27/02/2019
10. Journée de Mécanique des Fluides du Plateau de Saclay, ëcole Centrale, 28/01/2019
11. 71^{th} APS DFD Meeting, Atlanta, USA, 18-20/11/2018
12. IUTAM Symposium on Motile Cells in Complex Environments, Udine, Italie, 15-18/05/2018
13. 70^{th} APS DFD Meeting, Denver, USA, 19-21/11/2017
14. APS March Meeting, New Orleans, USA, 13-17/03/2017
15. SIAM Conference on Computational Science and Engineering, Atlanta,USA, 27/02 - 03/03/2017
16. 69^{th} APS DFD Meeting, Portland, USA, 20-22/11/2016
17. Active and Smart Matter: A New Frontier for Science and Engineering, Syracuse University, USA, 20-23/06/2016
18. SIAM Conference on Mathematical Aspects of Material Sciences , Philadelphia, USA, 05/2016
19. 68^{th} Annual Meeting of the APS Division of Fluid Dynamics, Boston, USA, 23 - 25/11/2015
20. Molecular Dynamics meets Fluctuating Hydrodynamics, Madrid, Espagne, 05/2015
21. 67^{th} Annual Meeting of the APS Division of Fluid Dynamics, San Francisco, USA, 23 - 25/11/2014
22. Flowing Soft Matter: Bridging the Gap between Statistical Physics and Fluid Mechanics, International Center for Mechanical Sciences, Udine, Italie, 30/06 - 4/07/2014
23. 17^{th} U.S. National Congress on Theoretical and Applied Mechanics, Lansing, USA, 15 - 20/06/2014
24. Active Fluids New Challenges from Experiments to High-Performance Computing, Marienham, Finlande, 28 - 31/05/2014
25. GDR MéPhy: Active Fluids, ESPCI, Paris, France, 7/04/2014
26. Workshop: Collective motion of active swimmers, Université de Nice Sophia Antipolis, Nice, France, 25 - 26/09/2013
27. 38^{th} Congress of the Biomechanics Society, Marseille, France, 4 - 6/09/2013